THE UNIVERSITY *of* EDINBURGH

A mafic rock perspective on the magmatic maturation of a large scale silicic system: A multidisciplinary study of basalt in the Taupo Volcanic Zone, New Zealand.

SALLY LAW

A thesis presented for the degree of Doctor of Philosophy

THE UNIVERSITY OF EDINBURGH

2020

Abstract

Large-scale silicic systems are characterised by eruption of rhyolite composition magma in caldera-forming events. This often produces pyroclastic flows, which can travel >100km from the vent. A key question in volcanology is understanding how and why some magmatic systems evolve into producing large volumes of eruptible silicic magma, and others do not. The flux of magma over time must be sufficiently high to allow accumulation of large bodies of partially molten, eruptible material within the crust, as opposed to forming fully solidified plutons. First, priming of the system must occur, by repeated injection of mantle-derived mafic magma into the crust. Therefore, a great volume of mafic material is stored at depth beneath silicic systems, driving the production of silicic magma. However, the dominant erupted products in silicic systems are overwhelmingly rhyolitic in composition, and are subject to large amounts of crustal processing, obscuring primitive mantle-derived features. Therefore, in comparison to our knowledge on silicic processes, our knowledge on the primitive, mafic portion of the magmatic system is limited.

The Taupo Volcanic Zone (TVZ), New Zealand (NZ) is one of the most productive silicic systems worldwide. It is a rifted continental arc, where both fluids derived from the subducting slab and decompression from rifting drive production of magma. Rifting aids the eruption of volumetrically minor amounts of basalt, which rise from depth along faults parallel to the main rift axis, and caldera rims. Large amounts of mafic magma in the crust are required to drive the production of silicic magma, but are too dense to erupt without the help of normal faulting. This means that although basalt

is volumetrically minor at the surface, its composition and crystal cargo can be used to infer much broader processes occurring in the primitive portions of the magmatic plumbing system.

The TVZ is also one of the clearest examples of maturation of a magmatic system, where the shift from andesitic continental arc-type volcanism to rhyolitic volcanism is both spatial and temporal. The arc is propagating southwards with time, and is split into north, central and southern segments. Andesitic volcanism is precursory to rhyolitic volcanism in the TVZ and dominates the south TVZ (S-TVZ), where the onset of volcanism is more recent in comparison with the central TVZ (C-TVZ). Coeval mafic rocks show a shift in whole rock composition coinciding with the shift from andesitic to rhyolitic volcanism.

This thesis uses a multidisciplinary geochemical approach to resolve the shift in mafic rock composition between the different segments of the TVZ. We find that basalt in monogenetic eruptions is much more texturally complex than previously assumed. TVZ basalt inherits antecrysts and xenocrysts from a range of sources, including the lithospheric mantle, cognate cumulate mushes, and hydrothermally altered rhyolites. The type of crystals inherited vary between different segments of the arc, allowing us to attribute shifts in the basalt composition to changes in the maturation of the magmatic system. Finally, we successfully reproduce the observed changes in basalt composition through a series of high pressure/temperature experiments. This PhD project gives insight into changes within the mafic portion of the transcrustal magma system through the waxing and waning of one of the most productive large-scale silicic systems on Earth.

Lay Summary

Volcanoes around the world vary hugely in how big and how explosive their eruptions are. Some volcanoes have frequent, small eruptions of lava (molten rock) that does not flow far from the volcanic vent. Others, such as Yellowstone (USA), erupt relatively infrequently on human timescales but, when they do they explosively erupt enormous volumes of material in kilometre-high columns of fragments of hot ash and rock, and avalanches of the same (pyroclastic density currents), which can travel for tens of kilometres and cause huge damage to infrastructure, livestock and human life.

Much of the variation in the way a volcano erupts is due to the composition, or chemical makeup of the magma that is being erupted. All volcanoes source their magma from a layer of partially molten rock that lies just beneath the crust of the Earth, called the mantle. Volcanoes that erupt non-viscous, runny lava flows tend to have basaltic composition magma. This type of magma is often sourced relatively directly from its source in the mantle beneath. Volcanoes that erupt in an explosive way tend to have silicic compostion magma. This is much more viscous than basaltic magma and tends to fragment when erupted, causing the explosive style. Silicic magma is essentially a 'distilled' version of basaltic magma, meaning that when a basalt magma crystallises in the crust, the leftover liquid tends towards silicic compositions. This means that silicic magma is made from basaltic magma.

However, there are many ways in which basaltic magma changes to silicic magma, and the exact way that basalt produces silica rich magmas is not clear. Because silicic eruptions are so hazardous, we need to understand the way in which basaltic magma

changes in composition and drives production of silicic magma. Unfortunately, this is often hard to observe, as these processes occur underground and we cannot directly sample molten rock. At the surface, because silicic eruptions are so large, they tend to dominate the volcanic landscape, meaning that if any basalt was erupted nearby, it is usually buried beneath thick pyroclastic flows.

This thesis takes a rare opportunity to study the link between basaltic and silicic magma in the Taupo Volcanic Zone (TVZ), New Zealand. This area is dominated by silicic composition eruptions, but small eruptions of basalt co-exist. The basalt provides a unique 'window', to see back to the starting compositions of magmas sourced from the mantle in the TVZ, and are a link between the mantle, the source of all magma, and the final erupted product - the explosive silicic material. From the compositional variation in basalt and the crystals they contain, we are able to provide vital insights on the conditions that favour production of silicic magma, and why some volcanoes produce explosive silicic eruptions, and others do not.

Declaration

I declare that this thesis has been composed solely by myself and that it has not been submitted, in whole or in part, in any previous application for a degree. Except where states otherwise by reference or acknowledgement, the work presented is entirely my own.

Sally Law, December 2020

Acknowledgements

This thesis is the culmination of 4 years of hard work, fun, constant learning, and most importantly - melting stuff, and there are many people that I want to thank for contributing along the way.

First and foremost, my thanks go to my supervisor, Geoff Bromiley. I know initially you were really only in it for the melting stuff part, but throughout everything, and especially when things got pretty tough back in 2nd/3rd year, you've always had my back, and I cannot thank you enough for that. Without your moral support, I would never have been able to complete this PhD, and do all the cool science we've ended up doing. Thank you for always taking time (or making time) to read my work, respond to my sometimes excessive barrage of emails, and my hastily typed whatsapps with images of the piston-cylinder apparatus asking 'Am I going to electrocute myself if I touch this??'.

My secondary supervisors: Geoff Kilgour, from the other side of the world, I don't think a supervisor could have been as top-rate as you have been. Thank you for all the late-night/early morning skype meetings, your fantastic ideas, and of course, your help with the trickier Māori pronunciations - Rerewhakaiitu is now forever imprinted on my brain. Godfrey Fitton, since you came on board in my 3rd year, your knowledge has been invaluable - Little conversations can go a long way if they're about the right thing! Lastly Adrian Boyce, for giving me access to your fantastic lab at SUERC, and getting me the amazing dataset I did, your input has been truly appreciated.

I also want to acknowledge all the other fantastic academics and scientists that have

made this PhD possible. Chris Hayward, for all your help on the electron microprobe; Nicola Cayzer, not only for your help with the SEM, but for bending over backwards to help these last few months - without you, I would not be submitting this thesis before Christmas; John Craven, for all your help with access to sample prep facilities, for your general wisdom in the micro-analytical world, and for donating me the best pair of tweezers in the whole Geosciences department - picking crystals was never a chore with those! Nic Odling, for help with crushing and grinding facilities, and our chats in the XRF lab about all things piston-cylinder experiments; Mike Hall and Ivan Febbrari, for their help with sample preparation, and Alison McDonald, for showing me how to use the laser fluorination line. I also want to thank Ery Hughes, for paving the way with your work on Okataina basalts, for donating me all your fantastic OVC samples, and for the hugely helpful discussions we've had over the last few years. Lastly, I want to thank everyone who I have had the joy of working with in the solid media lab at Edinburgh, even though its currently a one-man-band, the friendship, support and help in the early years was the best part of my PhD. Specifically, I have to thank Nicci Potts, for showing me the ropes, and for being an amazing role model of a young strong female academic; and Tom Stokes, even though you hindered Nicci's teaching slightly with your snatching habits, you helped enormously by showing me what not to do - namely never put acetone in a 600°C furnace. Side note: If you do, and the furnace sets fire, just shut the door and pretend its not happening. That will fix it.

Following that, the past 4 years of coffee times, pints, running clubs, weekends away and more with all you lovely PhD lot has been amazing. Special thanks goes to all members of Grant Attic booth 4 - the best booth - but in particular Kirsty, even if I missed out this year on the motivational citrus fruit, and Amy, I couldn't have asked for better booth buddies! To Hannah, Isla, Sophie, Amy, Rachel, and all other members, past and present (male or female), of the Grant attic Women's Institute, it wouldn't have been the same without you! Special thanks to Sophie, for your incessant optimism, energy, trash TV chat and prosecco habit, your friendship has been the perfect antidote

to all the sciencing.

Lastly, to my family, for the continued moral support they have shown me throughout this adventure. To Mum, for everything she has done for both me and my brother, for valuing education, and giving me the support and freedom to take that as far as I can go; My brother Ben, my absolute best friend and always being there no matter what; Dad, for your support, and for steering me the long way round my childhood dream of having a horse - now I can have a job, and a pony!; And to Justin, for doing all the dishes, cooking, and general maintenance of my life these last few weeks, for learning the word olivine, and the appropriate time to drop it into PhD conversation - e.g.'Yes Sal, I hear your point, but what is the *olivine* telling you?'. You are kindest and the most supportive partner I could ask for.

Contents

List of Figures

List of Tables

Chapter 1

Introduction

1.1 Generating silicic magma

A key question in volcanology is understanding how and why some magmatic systems develop into being able to produce large volumes of eruptible silicic magma, and others do not. Large volumes of silicic magma are most commonly evacuated in caldera-forming eruptions as pyroclastic flows that can travel >100km from the source vent (Streck and Grunder, 1995; Wilson et al., 1995a). Early research into generating silicic magma envisioned large, long-lived liquid-dominated chambers of melt, residing in the crust, and ready to erupt at any given moment. However, common observations from multiple settings challenge the 'big tank' model. Voluminous ignimbrites are often zoned, i.e, they are characterised by relatively crystal poor units that grade into crystal rich upper units. This led to an interpretation that the melt-rich cap is first evacuated, followed by entrainment of silicic cumulate toward the base of the eruptible portion of the chamber (Bachmann et al., 2014; Deering et al., 2011b; Wolff et al., 2015). To accumulate these vast magma volumes, some authors (Huppert and Sparks, 1988) suggested that a heat source was required to maintain high melt fractions. However, this paradigm has shifted after the recognition of intra-eruptive geochemical complexity, coupled with geophysical inversions. For example, geophysical studies commonly identify large, low seismic velocity zones and conductive magneto-telluric

(MT) areas under calderas (Comeau et al., 2015; Farrell et al., 2014; Heise et al., 2010), interpreted as the presence of low melt fraction, near-solidus magma bodies with variable crystal to melt ratios. These observations have led to the idea that large silicic magma bodies spend long periods of their evolution in a crystal rich, uneruptible state, with melt fractions (<50%) trapped as interstitial pockets between crystalline phases, and is known as the 'mush model' (Bachmann and Bergantz, 2004; Cooper and Kent, 2014). Crystal mush then needs a process of remobilisation or 'defrosting', such as magma recharge, to increase the melt fraction resulting in a body of magma capable of eruption. A key question relating to the mush model, is how magmatic systems grow and thermally mature over time, in order of being capable of producing large volumes of silicic melt.

Field, geochronological and numerical studies have shown that large igneous bodies grow incrementally from repeated small intrusions of magma (Annen, 2009; Barboni et al., 2015; Coleman et al., 2004; Lipman, 2007; Miller et al., 2011), with the rate of magma flux controlling the heat input, and therefore the rate at which the magma solidifies (Annen, 2011; Karakas et al., 2019). Liquid portions of magma only accumulate at elevated rates of flux (Annen et al., 2015; Karakas et al., 2017). Therefore, magma systems that are capable of producing large silicic eruptions require time to thermally mature, through long-term magmatism on the orders of 10^5 to 10^6 years (de Silva et al., 2006; de Silva and Gregg, 2014). Often, this is characterised by a shift from relatively small but frequent eruptions of andesitic composition magma during the priming of the crust, to infrequent but large eruptions of silicic composition magma when the system thermally matures.

As the dominant erupted products of a mature silicic system are highly evolved melts, usually erupted in hazardous ignimbrite-forming eruptions, much research focus has been on the incremental growth of shallow crystal mush, and the processes that serve to remobilise the mush and separate out large fractions of silicic melt. However, the mature silicic system is vertically extensive and should be viewed as a transcrustal

magma system, with processes occurring in the mafic roots of the system ultimately controlling generation of magma in the upper crust (Cashman et al., 2017). Unfortunately though, sampling the mafic roots of silicic systems is not easy; as little to no basalt can rise through a heavily intruded crust without modification (Lipman, 2007). The exception to this is in extensional regimes, where normal faulting aids the tapping of otherwise trapped mafic magma.

Flux and subsequent storage of mafic mantle derived magma is key in driving the maturation of magmatic systems toward silicic compositions. However, the mafic roots of these systems are difficult to sample, and therefore poorly understood in relation to their silicic counterparts. Extensional tectonics are key in that they allow otherwise too-dense basaltic magma to erupt at the surface. The Taupo Volcanic Zone (TVZ) in New Zealand is one of the world's most productive silicic systems, having erupted an estimated 15,000 km^3 of silicic magma since the onset of volcanism at 2Ma (Wilson et al., 1995b; Wilson and Rowland, 2016). It is a rifted arc, and consequently small eruptions of basalt occur along faults and caldera rims. Furthermore, small basalt eruptives are located throughout the TVZ, providing a broad spatial sample of the roots of this hyper-active silicic system. For these reasons, this thesis seeks to understand the conditions and drivers of basalt magma generation and propensity to interact and accentuate silicic volcanism.

1.2 Thesis Aims

The main aim of this thesis is to use mafic rocks to provide insight into the maturation of the magmatic system in the Taupo Volcanic Zone, from pre-caldera-forming volcanism, to caldera-forming volcanism, to the eventual waning of the system and post-caldera-forming volcanism.

This project uses a multi-disciplinary geochemical approach to reconstruct changes in the mafic magma plumbing system and the mantle source region throughout the life

cycle of the caldera-forming system. Therefore the project is split into distinct sections, which compiled, provide an overview of the mafic system as a whole. Specifically, these sections are:

- Investigate crustal assimilation into mafic magmas, using oxygen isotopes and rock textures.
- Investigate changes in pressure, temperature and H_2O contents of the mafic magmas along the arc.
- Use the olivine crystal cargo, along with whole rock trace element geochemistry to investigate mantle melting processes.
- Combine insights from the natural rocks, and attempt to reproduce the observed compositional changes from along the arc in a suite of piston cylinder experiments.

In summary, this thesis provides a unique opportunity to study the mafic roots of a hyper-productive silicic system. The work carried out provides new insights into how the mafic portion of the magmatic system changes throughout the birth and death of a silicic caldera-forming system. Due to the scarcity of coeval basalt eruptions in predominantly silicic caldera-forming systems, this work fills a niche, by looking at the evolution of a silicic system, from the perspective of the mafic rock.

1.3 The Taupo Volcanic Zone - a rifted arc

The Taupo Volcanic Zone is a rifted continental arc, and is the largest present day manifestation of volcanism in the North Island of New Zealand. The TVZ results from the oblique subduction of the Pacific plate beneath the Australian plate. To the north this continues into the Tonga-Kermadec arc and back-arc system, and to the south subduction transitions into the strike-slip system of the Alpine fault, which continues

through the South Island of New Zealand (Figure 1.1). The subducting material is the Hikurangi Plateau (Wilson and Rowland, 2016), which is a section of over-thickened oceanic crust associated with the Ontong Java Plateau (Reyners et al., 2011). The trench is 200-270km east of the North Island (Cole and Lewis, 1981). Volcanism in the TVZ is assisted by rifting, which is happening in the central TVZ at a rate of 7-15mm/year (Wallace et al., 2004).

The TVZ is the current manifestation of silicic Volcanism on the North Island. However, volcanism on the North Island commenced much earlier, around 25Ma (Wilson and Rowland, 2016). Prior to the TVZ, volcanism formed the north-south orientated Coromandel Volcanic Zone (CVZ) from 17-5Ma (Seebeck et al., 2014). Since 2Ma the arc has shifted to the south, resulting in the current formation of the TVZ (Carter et al., 2003; Herzer, 1995; Wilson and Rowland, 2016). The mechanism as to how this occurred originally referred to rotation of the arc due to oblique subduction (Stern, 1987). More recently, the idea that the TVZ is the southward migration of the CVZ is preferred (Seebeck et al., 2014; Wilson and Rowland, 2016), making the CVZ and TVZ contiguous in time and space (Wilson and Rowland, 2016).

The TVZ is approximately 250km in length, and spans from White Island (Whakaari) in the north, to Ohakune in the south (Figure 1.2). The TVZ is split into 3 segments, the north, central and south. The central TVZ is characterised by the dominance of rhyolitic volcanism, which makes up >98% of the estimated erupted products (Wilson et al., 1995b), although significant buried andesite edifices have been intersected by geothermal drilling (Browne et al., 1992; Rosenberg et al., 2020). This spans the area between (and including) the two currently active caldera centres, Okataina Volcanic Centre (OVC) at the northern point of the central TVZ, and the Taupo Volcanic Centre (TVC) at the southern point of the central TVZ. Basalt comprises approximately 1% of the total erupted volume of the central TVZ (Wilson et al., 1995b), and is mostly erupted along faults (Figure 1.2) and caldera rims (Cole and Lewis, 1981; Hiess et al., 2007; Wilson et al., 1995b), indicating a structural control on eruption of basalt. The north

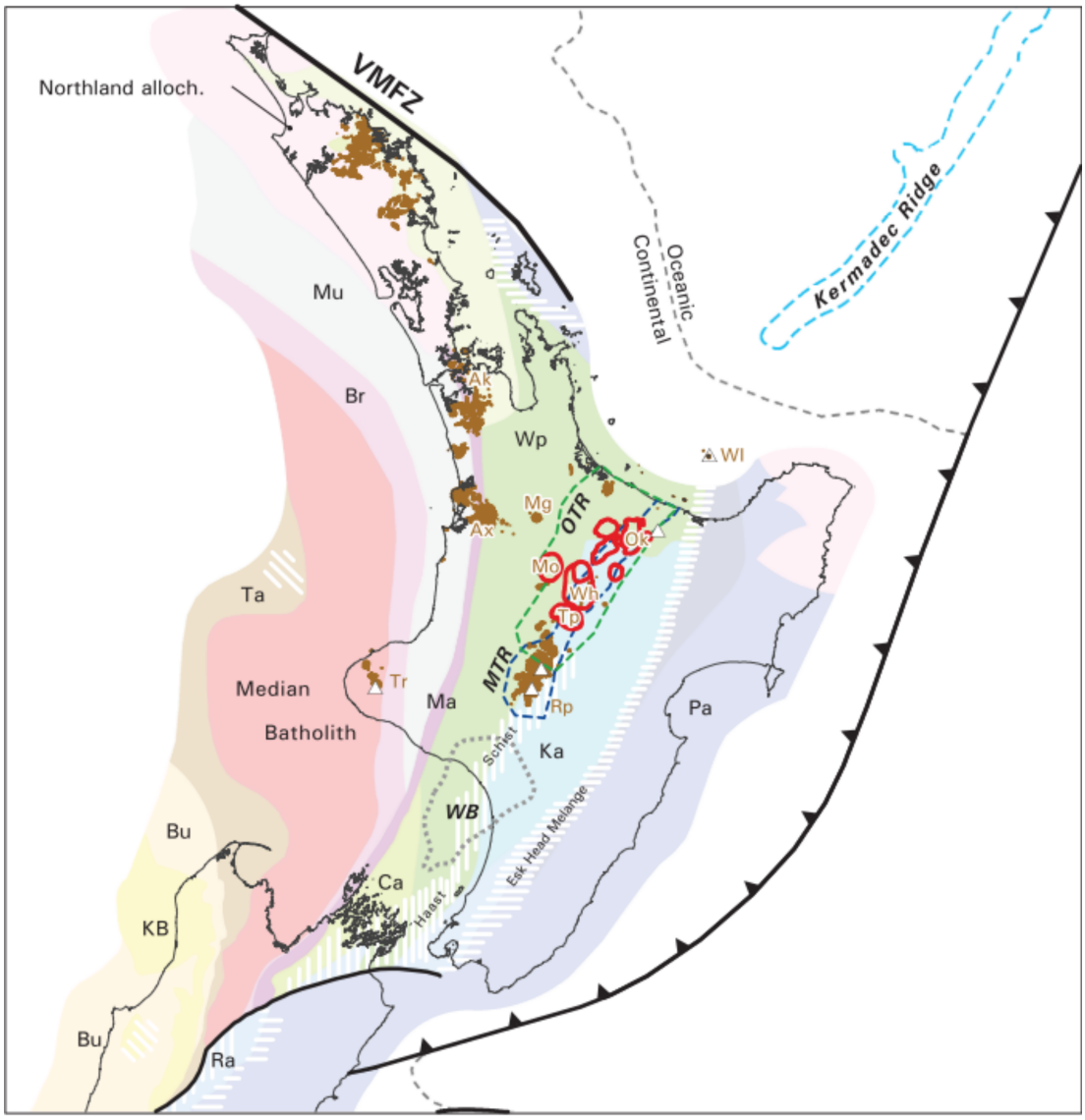

Figure 1.1: Map of the North Island, New Zealand, from Eberhart-Phillips et al. (2020) and references therein. Terranes: Median batholith, Northland allocthon, Murihiku (Mu), Brook Street (Br), Matai (Ma), Waipapa (Wp), Kaweka (Ka), Pahau (Pa), Takaka (Ta), Buller (Bu), Karamea batholith (KB), Rakaia (Ra). Kaweka and Pahau terranes are components of the Torlesse Terrane. Plate boundary shown at subduction trench and South Island Alpine fault zone. Taupo Volcanic Zone shown by Old Taupo Rift (OTR, 2–0.35 Ma) defining the old TVZ (green dashed line), and Modern Taupo Rift (MTR) defining the new TVZ (blue); Volcanic calderas (red), non-silicic (brown, <2 Ma), active andesite volcanoes (triangles) (Leonard et al. 2010; Villamor et al. (2017). Volcanic labels: Ok, Okataina; Mo, Mangakino; Wh, Whakamaru; WI, White Is.; Rp, Ruapehu; Tp, Taupo; Ak, Auckland; Ax, Alexandra; Mg, Maungataurari; Tr, Taranaki. In the oceanic upper plate, volcanism occurs along the Kermadec Ridge (pale blue dashed line).

.

TVZ spans the area north of OVC up to White Island (Figure 1.2), and the south TVZ spans the area south of Lake Taupo to Ohakune, and includes the three stratovolcanoes Tongariro, Ngauruhoe and Ruapehu. Both the north and south TVZ are characterised by andesitic, continental arc style volcanism (Wilson et al., 1995b). Volumetrically minor eruptions of mafic rock also occurs along faults in the south TVZ. However, the composition of mafic rock in the south TVZ is systematically different to that in the central TVZ (Gamble et al., 1990; Graham and Hackett, 1987).

The central TVZ, bounded by the OVC and TVC to the north and south, is otherwise defined by an envelope around the 8 main volcanic centres that have been active in the past 2Ma (Houghton et al., 1995; Wilson et al., 2009; Wilson and Rowland, 2016). These 8 caldera centres are shown in Figure 1.2. The 8 caldera boundaries are representative of individual caldera-forming events. The Reporoa and Rotorua caldera were formed from single caldera collapse episodes. Maroa, Okataina, Taupo and Whakamaru are formed from overlapping collapses, within relatively short timescales, whereas Mangakino and Kapenga centres are formed from separate episodes of magmatism, that occurred in similar geographic positions (Wilson et al., 1995b) (Figure 1.3). The caldera centres of the central TVZ are also divided by age, with the 0.34Ma formation of the Whakamaru ignimbrites dividing eruptions in the old TVZ, to the young TVZ (Figure 1.3). Of the 8 caldera centres, 7 have been active more recently than the formation of the Whakamaru ignimbrites (Figure 1.3). Mangakino caldera was only active in the old TVZ. Only OVC and TVC are currently still active. There is no correlation between the location and timing of caldera forming events, or between geographical location and the nature of a caldera forming event. The rhyolites also do not show any compositional trends with time (Graham et al., 1995), emphasising the segmented and discontinuous nature of volcanism in the TVZ. The reason for this segmentation within the central TVZ is still unclear, but it is suggested that it is proportional to the variable amounts of rifting within the zone (Wilson et al., 2009). When examining the TVZ as a whole, segments of the TVZ that show the greatest proportions

of extension coincide with the currently active caldera centres (OVC, TVC), whereas zones subject to greater transtensional forces are linked to andesitic stratovolcanoes, which are volumetrically less active, supporting an integral link between tectonism and volcanism in the TVZ (Wilson et al., 1995b, 2009).

Eruptions of mafic magma in the TVZ are small and relatively rare, with the largest eruption, the 1886 eruption of Tarawera producing only $1km^3$ of erupted product (Wilson et al., 1995b), up to three orders of magnitude smaller than the largest rhyolitic eruptions (Wilson et al., 1995b). Basaltic magma is often erupted in monogenetic eruptions, forming scoria cones, tuff rings and maars, which are commonly aligned along faults (Cole, 1973; Hiess et al., 2007). Mafic clasts and enclaves are also erupted in silicic magmas, and injection of basaltic magma is a likely eruption trigger for many silicic mush bodies (Barker et al., 2020; Leonard et al., 2002; Shane et al., 2008). Basalts are concentrated in young TVZ, but this hints at the poor preservation potential of basalt, as opposed to an increase in basaltic eruptions over time. Older basalt is likely buried beneath the 0.34Ma Whakamaru ignimbrites.

Magma generation in the TVZ is driven both by fluids derived from the subducting slab, and decompression from rifting. Variations in volcanic productivity along the TVZ are influenced by heterogeneity in both the subducting slab, and the mantle wedge (Eberhart-Phillips et al., 2020). The subducting slab is strong and old (120Ma), however the thickened Hikurangi Plateau is relatively buoyant and has subducted to a depth of 150km south of Taranaki in the west of the North Island (Reyners et al., 2011). The slab is subducting more shallowly at depths <150km. Beneath OVC in the northern part of the central TVZ, the surface of the slab is at a depth of approximately 80-140km (Eberhart-Phillips et al., 2005), whereas beneath Mt. Ruapehu at the southern edge of the TVZ, the surface of the slab is at a depth of approximately 60-120km. A zone of dehydration-related partial melt is inferred at a depth of 65km beneath the central TVZ from low values of Q_S (Eberhart-Phillips et al., 2020), suggesting melt ascent under the central rift structure of the TVZ. Additionally, V_P is lowest directly west of Taupo

caldera and interpreted as a region of high melt generation (Reyners et al., 2007). The low Q*s* zone in the mantle wedge becomes deeper and weaker beneath Ruapehu, and the lithosphere becomes progressively thicker and stronger southwest toward Mt. Taranaki. The weakening of this signal is suggested to mean lower fluid or melt fractions toward the south TVZ (Eberhart-Phillips et al., 2020). There is no low *Vp* zone south west of Ruapehu, and this is suggested to indicate an absence of upward return flow in the mantle, explaining the cessation of volcanism southwards of Ruapehu (Reyners et al., 2007). Cessation of corner flow at Ruapehu is also suggested to promote lateral fluid flow, resulting in more partial melt to the north east, at TVC.

Within the crust, the shallowest seismicity occurs at depths of approximately 10km in the central TVZ (Hurst et al., 2016; Reyners et al., 2007). The interpreted brittle-ductile transition deepens toward Ruapehu to depths of 25km, with some seismicity down to 30-40km (Reyners et al., 2007). These earthquakes also occur in swarms, which is thought to represent a rift margin zone of weakening through migration of hot fluids from the mantle wedge (Reyners et al., 2007). This deepening seismicity towards the south TVZ mirrors patterns of lithospheric thickening in the south TVZ and thinning in the central TVZ (Stern et al., 2010). The crust directly east of the TVZ is approximately 35km thick, but thinning of the crust to approximately 15-25km is reported beneath the central TVZ (Stern et al., 2006, 2010; Stratford and Stern, 2006) (Figure 1.4), due to the ongoing rifting (Wallace et al., 2004). Rifting is the second driver of volcanism, along with subduction and fluid induced melting, and exerts a control on the volcanic productivity of the region. The south TVZ is not subject to extensive crustal thinning (Stern et al., 2006, 2010) (Figure 1.5). In the central TVZ, low *Qp* at approximately 18km depth strongly suggests underplating of new crust (Stern et al., 2006, 2010). The upper mantle here strongly suggests asthenosphere not lithosphere (presence of 1-4% melt) and is consistent with removal of mantle lithosphere (Stern et al., 2010). Above this, the crust is heavily extended and intruded (Figure 1.4) (Stratford and Stern, 2006; Stern et al., 2006). Magneto-telluric imaging of melt fractions in the central TVZ show

that conductivity abruptly increases at depths of 10km, interpreted as a roughly 4% interconnected melt fraction (Heise et al., 2007, 2010). The lowest resistivity within the conductive zones is beneath Okataina and Maroa calderas, however no pluton-scale bodies of partial melt have been imaged anywhere beneath the TVZ (Heise et al., 2010), consistent with the idea that much of the high-level magmatic system spends most of its time as highly crystalline mush bodies.

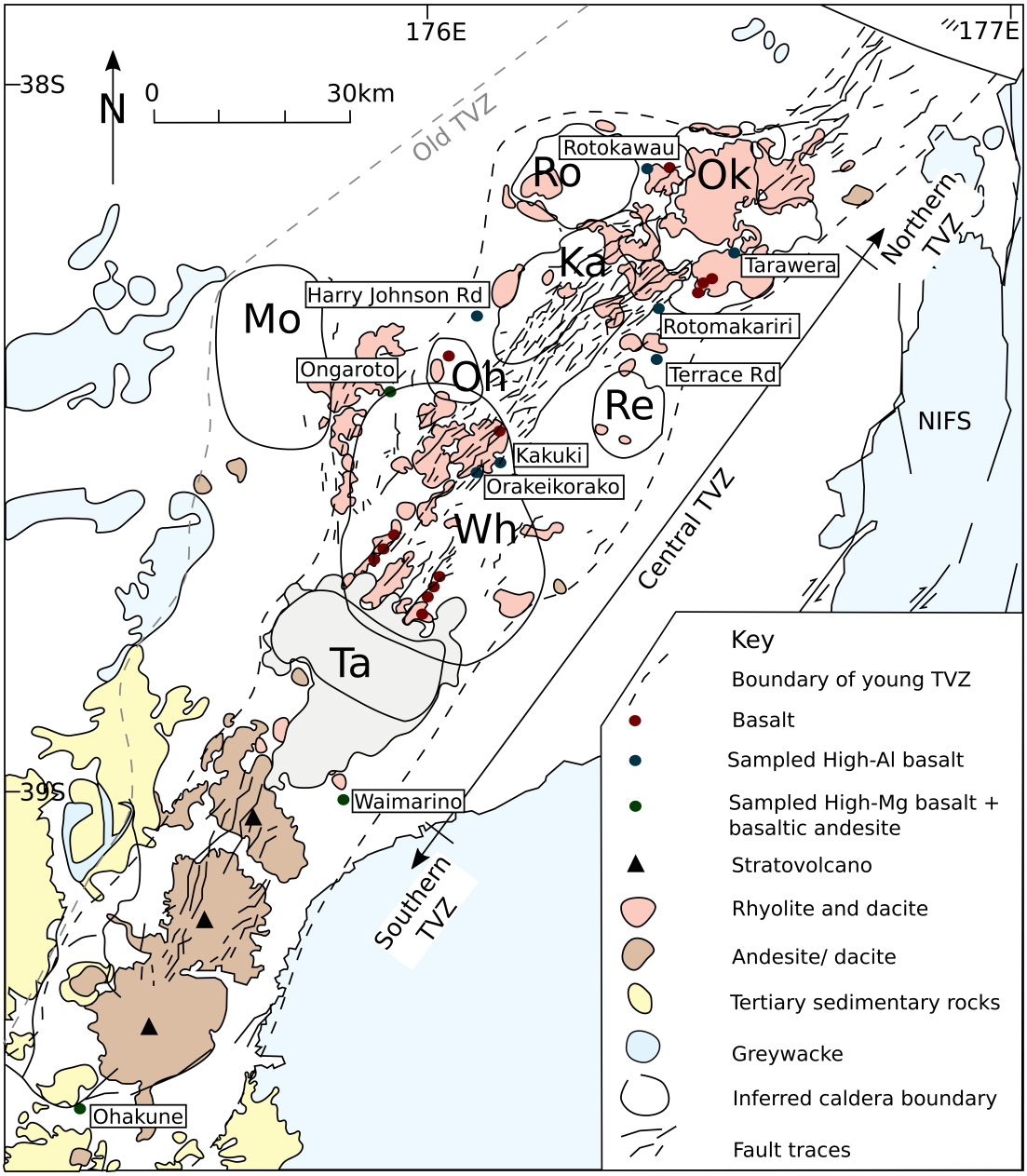

Figure 1.2: Map of the TVZ, modified from Wilson and Rowland (2016) and references therein. Ka - Kapenga, Mo - Mangakino, Oh - Ohakuri, Ok - Okataina, Re - Reporoa, Ta - Taupo, Wh - Whakamaru. NIFS - North Island Fault System.

.

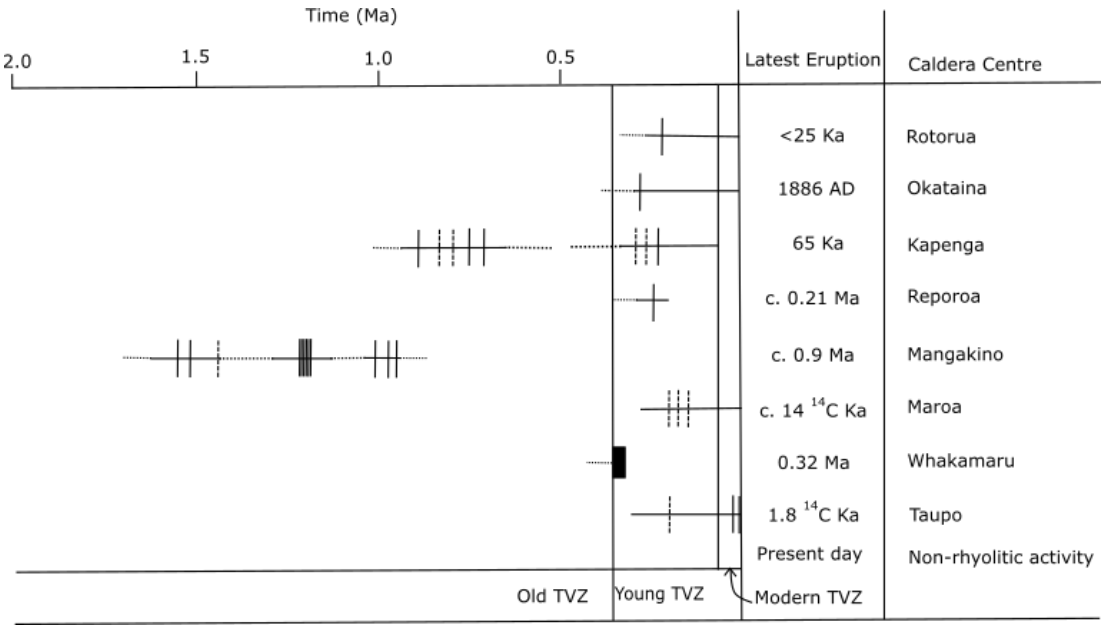

Figure 1.3: Timeline of caldera collapse events in the TVZ. Redrawn from Wilson et al. (1995b).

.

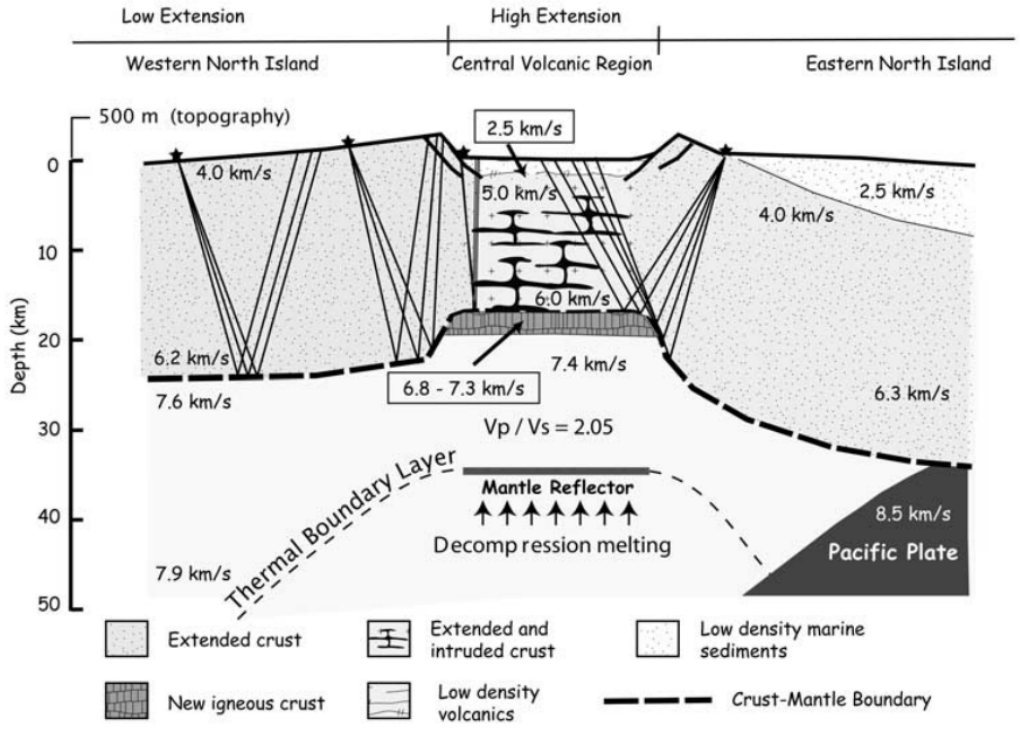

Figure 1.4: Schematic diagram illustrating crustal thinning and formation of new igneous crust in the central TVZ. Taken directly from Stern et al. (2006), and after (Stratford and Stern, 2006).

.

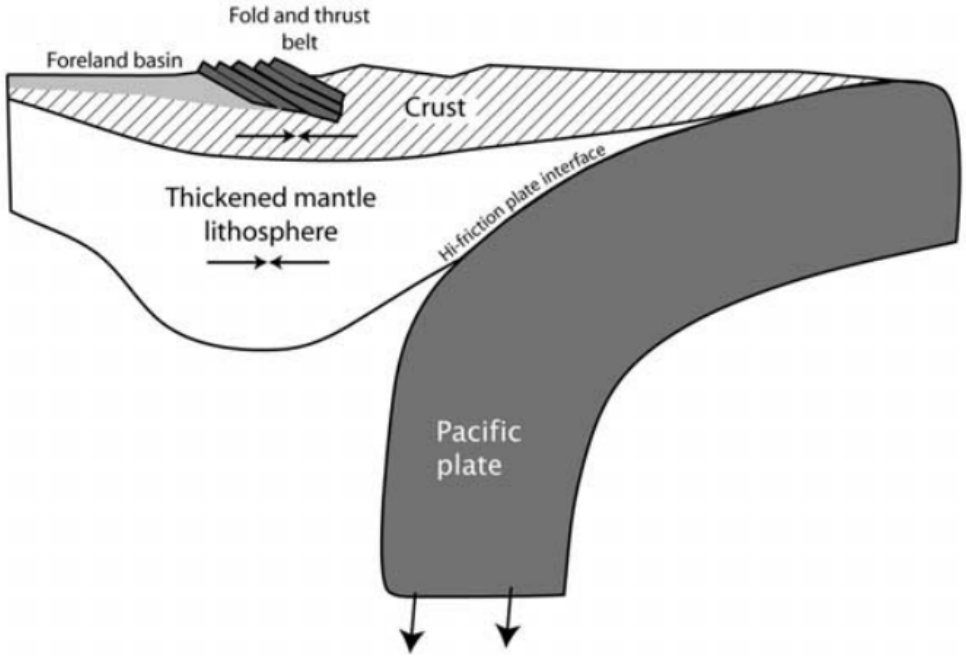

Figure 1.5: Schematic diagram illustrating thickening of the mantle lithosphere suggested to be occurring south of the TVZ in the Wanganui basin. Taken directly from Stern et al. (2006).

.

1.3.1 Basalt in the context of andesite and rhyolite

Compositions of erupted products vary along the arc. In its simplest form, this means that andesite is the dominant erupted product in the south TVZ, whilst rhyolite is the dominant erupted product in the central TVZ. Andesite volcanism is precursory to rhyolitic volcanism in the TVZ. The arc is propagating southwards with time (Villamor and Berryman, 2006), and andesite lava is found buried underneath rhyolite in the central TVZ (Browne et al., 1992; Chambefort et al., 2014). As the onset of volcanism in the south TVZ is more recent than in the central TVZ, andesitic volcanism is dominant, as it is yet to thermally mature. This transition, from andesite eruptions in the early stages of magmatism to rhyolite in the mature stages of magmatism, is also associated with the extent of rifting, and the amount of crustal thinning. Generation of silicic magma also requires episodic injection of magma over time (Annen, 2009, 2011), in order to thermally mature (Annen et al., 2015).

Early basalt studies in the TVZ

Mafic rock compositions co-vary with the andesite-rhyolite shift. Mafic rocks from the central TVZ are mostly high-Alumina basalt (HAB) (Cole, 1973; Gamble et al., 1990). Plagioclase is the dominant crystallising phase, ± olivine, ± clinopyroxene (Gamble et al., 1990). High-Magnesium basalt (HMB) also occurs in the central TVZ, with olivine as the major crystallising phase, but is much rarer than HAB (Gamble et al., 1990). Mafic rocks in the south TVZ are HMB and high-Mg basaltic andesite (HMBA) (Gamble et al., 1990; Graham and Hackett, 1987; Hackett, 1985). HMB in the south TVZ has olivine + clinopyroxene as the dominant crystallising phases, whereas HMBA is composed of mostly clinopyroxene + orthopyroxene with minor olivine (Graham and Hackett, 1987; Hackett, 1985).

For a long time, research has recognised the potential importance of the small outcrops of basalt in the TVZ. The initial study into central TVZ basalt (Cole, 1973)

sampled 8 basalts and provided the first geochemical classification, as high-Alumina basalt. The basalt sampled was Rotokawau and Tarawera from OVC, Ongaroto, Kakuki, Orakeikorako and Harry Johnson's Rd from Maroa, and K-Trig, Ben Lomond and Punatekahi from TVC. It was noted that basalt was erupted along fault lines, and likely ascended relatively rapidly from depth, and that aphyric samples like Tarawera, likely ascended faster than highly porphyritic samples, like Ongaroto. It was suggested that due to their similar major element composition, and modal mineral assemblages, that they shared a common source in the mantle. However, systematic differences in certain elements, such as TiO_2, between basalt from Okataina and Maroa calderas suggested differences in the initial composition of the magma (Cole, 1973).

Gamble et al. (1990) and Gamble et al. (1993) expanded the dataset on high-Al basalt in the central TVZ to also include basalt samples from the south TVZ, and drew comparisons between these and basalt from the Kermadec arc and the Havre Trough (KAHT). Again, similarities in modal mineralogy and petrology of TVZ HABs and KAHT samples lead to the interpretations that both sets of samples share a similar mantle source mineralogy (Gamble et al., 1990), and that differences in individual sample mineralogy is associated with differences in the subsequent crustal processing and magma storage each rock had undergone. It was at this point, that the Kakuki sample was identified as the 'most primitive' TVZ HAB, with only olivine and plagioclase as fractionating phases, and low SiO_2 and high MgO major element composition. Trace element and $^{87}Sr/^{86}Sr$ and $^{143}Nd/^{144}Nd$ data (Gamble et al., 1993) showed variation that was attributable to both differences in tectonic setting and source heterogeneity. Isotope data from the KA and TVZ basalt plots on an isotopic mixing line between MORB and the basement rocks of New Zealand (Torlesse Terrane metasediments). Additionally, the most primitive (MORB-like) isotopic signatures of both KA and TVZ basalt overlap, suggesting isotopically similar sources. KA and TVZ basalt show enrichments in large ion lithophile elements (LILE) and depletions in high field strength elements (HFSE), typical of a subduction zone signature. However, incompatible element concentrations

and ratios show Kakuki basalt to plot in the centre of the TVZ basalt array. This suggests that variation in trace element composition of the TVZ basalt is not entirely controlled by crustal processes, and instead reflect some degree of source heterogeneity, or variation in mantle melt fractions (Gamble et al., 1993).

The idea that primitive magma compositional variation in the TVZ reflects source heterogeneity is strengthened when considering mafic rocks of the south TVZ that were not included as a part of Gamble et al. (1993). In a wider study of Ruapehu and associated vents, Graham and Hackett (1987) identified a series of clinopyroxene and olivine phyric andesites, which were named type 5 andesites. These are suggested to have a parental magma similar to the Waimarino basalt (Graham and Hackett, 1987), which is olivine and clinopyroxene phyric, with whole rock $Mg\#_{77}$ (Gamble et al., 1990; Graham and Hackett, 1987), and does not follow the crystallisation sequence identified in Gamble et al. (1990). Additionally, Graham and Hackett (1987) report the occurrence of highly forsteritic olivine (Fo_{94}), suggesting that crustal processes cannot explain the differences between the major element compositions of Kakuki and Waimarino basalt. Examples of type 5 andesites are found at Hauhungatahi, Ohakune, Pukekaikiore and Waimarino.

Linking basalt to rhyolite

Since the early whole rock geochemical studies on mafic rocks in the TVZ, research focus has mostly been driven toward the comparison of basalt with their rhyolitic counterparts.

Numerous studies have shown that eruption of rhyolite in the TVZ is induced by partial melting, or remobilisation, of much longer-lived crystal mushes that reside in the shallow crust (Allan et al., 2013; Brown et al., 1998; Charlier et al., 2005, 2008, 2010; Cole et al., 2014; Cooper and Wilson, 2014; Cooper et al., 2017; Deering et al., 2011b). However, whilst it is clear that most rhyolite eruptions occur through crystal mush re-

mobilisation, like the basalt, there are compositional differences between rhyolites from different portions of the central TVZ that cannot be explained by shallow differentiation and partial melting processes. i.e, different rhyolite centres have distinct geochemical trends that they must have inherited from their parental melts, and cannot be a result of pre-eruptive processes e.g. mafic magma intrusion/mixing. Rhyolite from the northern part of the central TVZ, at OVC has predominantly hydrous ferromagnesian minerals (hornblende, biotite), low FeO/MgO, enriched Sr, low Zr and Y (Deering et al., 2008, 2010), and high Ba/La (Rooney and Deering, 2014), whereas rhyolite from the south part of the central TVZ, at TVC has predominantly anhydrous ferromagnesian minerals (orthopyroxene, clinopyroxene), high FeO/MgO, low Sr, high Zr and Y (Deering et al., 2008, 2010) and low Ba/La (Rooney and Deering, 2014). This compositional continuum is interpreted as reflecting cold-wet-oxidising conditions, and hot-dry-reducing conditions, respectively. Initial modelling showed that varying temperature, fO_2, and H_2O concentrations in the lower crustal differentiation of mafic magma was able to produce the observed differences in the cold-wet-oxidising to hot-dry-reducing rhyolite trends (Deering et al., 2008). This was later inferred, due to fundamental differences in the trace element ratios of basalt associated with the cold-wet-oxidising and hot-dry-reducing rhyolite, to mean differences in the slab derived fluid contributions in the mantle source (Rooney and Deering, 2014).

Two recent studies have greatly developed our understanding of basalt in the TVZ. Barker et al. (2020) sampled basalt associated with currently active caldera centres, and basalt from regions between active caldera centres to investigate changes in primitive magma composition between the two settings. Major and trace element compositions from primitive olivine-hosted melt inclusions showed that basalt from intra-caldera settings sampled more hydrous, fertile and shallow mantle than basalt from inter-caldera settings (Barker et al., 2020). Melt fractions from the mantle are larger in intra-caldera basalt than inter-caldera basalt, and this is suggested to relate to whether a volcanic centre was capable of producing caldera-forming volcanism or not. Larger

melt fractions drive production of silicic magma, whereas inter-caldera regions are areas where caldera-forming volcanism has ceased. Therefore, to add a temporal context, intra-caldera basalt can also be referred to as syn-caldera basalt, and inter-caldera basalt as post-caldera basalt. The basalt interpreted as forming from smaller drier melt fractions relates to the hot-dry-reducing trends observed in the rhyolites (Deering et al., 2008), whereas the basalt interpreted as forming from larger, more hydrous melt fractions relates to the cold-wet-oxidising rhyolite trends (Deering et al., 2008). Further context was brought to this by Zellmer et al. (2020), who investigated the mantle source of both central and south TVZ mafic rocks through whole rock trace element compositions. Mafic rocks from the south TVZ sample shallow, hydrous and fertile mantle, similar to intra-caldera basalt (Barker et al., 2020). As the south TVZ is analogous to the central TVZ prior to the onset of caldera-forming volcanism, mafic rocks in the south TVZ can be referred to as pre-caldera basalt. The combination of these studies shows an overall depletion of the mantle with ongoing volcanism through the waxing and waning of the system. In the early stages of magmatism, melt is sourced from shallow and fertile relatively undepleted mantle, in large melt fractions. As the mantle is progressively tapped, the magmatic system becomes primed, and at a tipping point, there is enough heat from magma flux, and enough fusible material stored at near solidus conditions in the crust, that the system becomes capable of producing caldera forming eruptions. As the mantle becomes progressively more depleted, melt fractions become smaller and are sourced deeper in the mantle wedge and the magmatic system begins to wane (Zellmer et al., 2020). The interpretations from these studies provide a vital context within which to examine the basalt data in this thesis.

1.4 A note on style

This project uses a multi-pronged approach to investigate the nature of the basalt in the TVZ. For this reason, my thesis does not lend itself well to a conventional *'review,*

methods, results, discussion, conclusion' structure. Instead, each chapter has its own introduction, methods, results and discussion, consistent with the theme of the chapter. Two of the chapters, Chapter 5 and Chapter 6 are written as manuscripts that are currently under review and published in *Lithos*, respectively. General analytical and experimental setups, along with sample preparation techniques that are universal to the thesis are included in an introductory methods section. However, each chapter should read as a stand-alone piece of work, giving its own insight into the overall aim of the project. Chapters build upon knowledge gained from previous chapters. This is especially true for Chapter 7. At the end, the knowledge gained from each approach is tied together in a final synthesis and conclusions.

Chapter 2

Methods

2.1 Sampling and Sample Localities

Samples have been kindly donated from a range of people and resources. Rotokawau and Kakuki basalts were collected personally in April 2017. Other OVC samples (Rotomakariri, Tarawera and Terrace Road) were kindly donated by Ery Hughes from field seasons in February 2016. Waimarino and extra sample material from Kakuki were collected by Kate Saunders and Geoff Kilgour. All remaining samples (Harry Johnson Rd, Ongaroto, Orakeikorako and Ohakune) were kindly donated by GNS Science NZ. Samples and their localities are listed in Table 2.1. Over time with multiple researchers working on the same deposits, some samples have acquired multiple names. Common alternative names are in brackets with the appropriate authors that have used these names referenced. Additional geochemical classification from Cole (1973); Gamble et al. (1990); Graham and Hackett (1987) is included for reference.

Data on TVZ basalt has been acquired by numerous researchers over many years. This thesis focuses on the addition of mineral-specific data to the dataset on TVZ basalt. When needed for reference, whole rock data from Gamble et al. (1990, 1993) is used for TVZ HABs, Ongaroto and Waimarino; Hiess et al. (2007) for the basaltic andesites Rotomakariri and Terrace Road; and Graham and Hackett (1987) for Ohakune HMBA. The recent new dataset from Zellmer et al. (2020) has also been a great addition to

the TVZ mafic rock database, and has been especially useful for providing a full set of trace element profiles for samples, although due to the relatively recent nature of the publication was not used as the official reference dataset for my PhD. As most basalt eruptions are <1km^3 in volume, monogenetic in nature and have not been reported to show significant diversity in composition within deposits, I believe it is reasonable to use whole rock data from these authors as reference values, and not acquire a new set of whole rock analyses as a part of this project.

Table 2.1: **Sample names, location and geochemical classification**

Sample Name	Code	Lat.	Long.	Classification [a]
Rotokawau	SL4	-38.07405	176.37241	HAB
Rotomakariri	9UZ-008	-38.255972	176.450639	BA
Tarawera	9UZ-009	-38.19584	176.53517	HAB
Terrace Rd	9UZ-004	-38.347783	176.418214	BA
Harry Johnson Rd (Atiamuri)[a]	4/11	-38.29518	176.11301	HAB
Ongaroto	EO28	-38.40187	175.9333	HMB
Kakuki	KSGK2	-38.50017	176.1336	HAB
Orakei Korako (Tatua)[a]	EO27	-38.51028	176.09389	HAB
Waimarino	KSGK8	-39.02467	175.93771	HMB
Ohakune	2/H/9	-39.400667	175.409028	HMBA

[a]Cole (1973); Gamble et al. (1990)

2.2 EPMA

Major and minor element analyses of minerals and glass were conducted by electron microprobe analysis (EMPA) at the University of Edinburgh using a Cameca SX100 instrument. Samples - thin sections for natural samples, Indium mounts for experimental samples - were carbon coated before analysis. Analysing conditions were tailored to each phase, see Tables 2.2, 2.3, 2.4, 2.5, as was spot size, which size varied from 2 to 8μm. kV was set at 15. Current (nA) varied between 2 to 100 depending on phase and element being analysed. Low currents and diffuse beams were used when analysing glass and plagioclase, to avoid Na migration. Peak counting times varied from 20 to

120s and background times varied from 10 to 100s. Data was calibrated using in house mineral standards. Analysing conditions are reported in Tables 2.2, 2.3, 2.4, 2.5 and 2.6. Secondary standards of St John's Island olivine, BCR-2G hydrous basaltic glass, and in-house clinopyroxene and jadeite were used to check for drift. These values are reported in Appendix A.

2.2.1 Analysing conditions

Table 2.2: **Analysing conditions for olivine and orthopyroxene**

Mineral	size	cond.	I (nA)	El.	Pk time (s)	Bg time	Det. (ppm)	Calibration
Ol	4	1	4	Fe	30	15		Fayalite FeSp2 452
				Mg	20	10		Forsterite MgSp5 SiSp4
				Si	20	10		Forsterite MgSp5 SiSp4
	4	2	100	Mn	60	30	170	PuMn BL8 MnSp2
				P	20	10	65	P K4 P Sp1 P Sp3
				Ni	60	30	145	PuNi BL8 NiSp2
				Ca	40	20	45	Wollastonite
				Na	60	30	40	Jadeite BL7 NaSp5
				Al	90	45	38	Spinel

Table 2.3: **Analysing conditions for clinopyroxene**

Mineral	Size	Cond.	I (nA)	Element	Pk time (s)	Bg time	Calibration
Cpx	4	1	4	Mg	20	10	Spinel
				Si	20	10	Wollastonite
				Al	20	10	Spinel
				Ca	20	10	Wollastonite
				Fe	40	20	Fayalite FeSp2 452
	4	2	100	Na	60	30	Jadeite BL7 NaSp5
				K	30	15	Orthoclase BL7 K Sp1 K
				Ti	90	45	Rutile
				Mn	60	30	PuMn BL8 MnSp2
				Ni	60	30	PuNi BL8 NiSp2
				Cr	60	30	PuCr BL8 CrSp2 132

Table 2.4: **Analysing conditions for plagioclase**

Mineral	Size	Cond.	I (nA)	Element	Pk time (s)	Bg time	Calibration
Pl	4	1	4	Si	20	10	Wollastonite
				Ca	20	10	Wollastonite
				Na	20	10	Jadeite BL7 NaSp5
				Al	20	10	Spinel
	4	2	100	K	30	15	Orthoclase BL7 K Sp1 K
				Sr	60	30	Celestite Bl7 SrSp1 SrSp3
				Ti	30	15	Rutile
				Mn	90	45	PuMn BL8 MnSp2
				Mg	80	40	Spinel
				Fe	90	45	Fayalite FeSp2 452

Table 2.5: **Analysing conditions for spinel**

Mineral	Size	Cond.	I (nA)	Element	Pk time (s)	Bg time	Calibration
Sp	4	1	6	Al	30	15	Spinel BL8 MgSp5 AlSp4
				Fe	40	20	Fayalite FeSp2 452
				Mg	30	15	Spinel BL8 MgSp5 AlSp4
				Ti	60	30	Rutile BL8 TiSp1 TiSp3
				Cr	20	10	PuCr BL7 CrSp2
	4	2	100	Mn	60	30	PuMn BL8 MnSp2
				Ni	50	25	PuNi BL8 NiSp2
				Si	60	30	Wollast BL8 SiSp4 CaSp1 CaSp3
				Ca	60	30	Wollast BL8 SiSp4 CaSp1 CaSp3

Table 2.6: **Analysing conditions for glass**

Mineral	Size	Cond.	I (nA)	Element	Pk time (s)	Bg time	Calibration
Glass	4	1	2	Al	20	10	Spinel
				Si	20	10	Wollastonite
				K	20	10	Orthoclase BL7 K Sp1 K
				Ca	20	10	Wollastonite
				Na	20	10	Jadeite BL7 NaSp5
				Mg	20	10	Spinel
				Fe	40	20	Fayalite FeSp2 452
	8	2	80	P	20	10	P K4 P Sp1 P Sp3 193
				Ti	20	10	Rutile
				Mn	60	30	PuMn BL8 MnSp2 304

2.3 SEM - BSE imaging and Quantitative EDS

Back-scatter electron (BSE) images of prepared thin sections and Indium mounts were captured for textural analysis on a Zeiss Sigma field-emission gun (FEG) scanning electron microscope (SEM), using an accelerating voltage of 20kV. Semi-quantitative analyses were recorded using an energy dispersive spectrometer (EDS) to define crystal populations by composition as well as visual characteristics. The instrument was calibrated using a cobalt standard, and a constant working distance of 7mm was used. When obtaining quantitative EDS for analysis of experimental samples, a series of secondary standards were used to check for drift. These are reported in Appendix A.

2.4 Oxygen isotope analysis

Oxygen isotope data obtained in this thesis was collected by laser fluorination at the Scottish Universities Environmental Research Centre (SUERC). Samples were lightly crushed using a jaw crusher, and hammer and anvil to separate out crystals from groundmass, and subsequently sieved into size fractions, ranging from 0-500μm. These were repeatedly cleaned using distilled water in an ultrasonic bath until no visible sediment came off. Each mineral for each sample was handpicked under a binocular microscope, to select pristine grains. 1-2mg aliquots of crystals were weighed, their exact weight recorded, and loaded into a brass holder with 12 ports to contain samples. Oxygen bonded in silicate tetrahedra was released by laser fluorination and subsequently analysed by mass spectrometry according to the methods of Sharp (1990), modified for ClF_3 (Macaulay et al., 2000). The sample was heated by the laser in the presence of ClF_3 (Figure 2.1) to release the oxygen from the silicate minerals. In this setup, the fluoride and other condensibles are collected in the cold trap whilst the oxygen is passed into the glass part of the line (Figure 2.1). Any F leftover is consumed by the mercury diffusion pump. The oxygen (O_2) is then converted to carbon dioxide (CO_2) by passing

over heated graphite in the combustion chamber, whilst the yield is measured with a pressure transducer and subsequently passed into the mass spectrometer to analyse the masses (Figure 2.1). Samples were prefluorinated with a shot of ClF_3 overnight to remove any impurities such as clays. This was discarded and collected in the cold trap before analysis began. Standards were run at the beginning of each day (ports 1 and 2), at the mid point (port 6) and at the end (port 12). Values are reported in Tables 2.7, 2.8 and 2.9. Two standards of YP2 were run at the beginning of each day. The first standard is systematically high, and discarded, whereas the second standard shows remarkable consistency (Table 2.7).

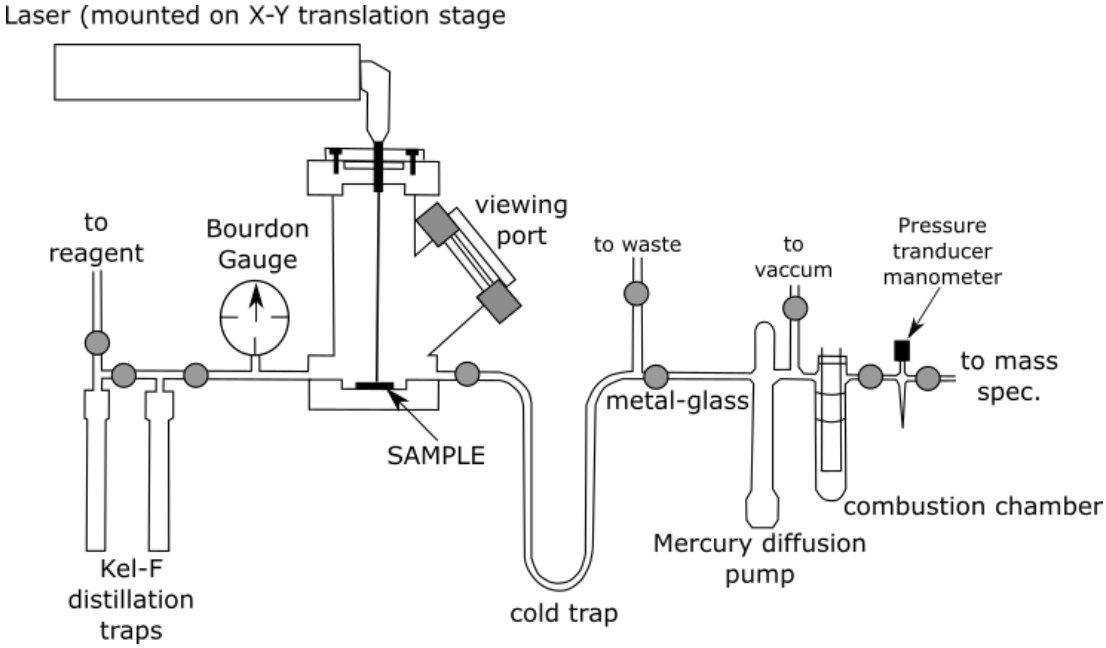

Figure 2.1: Schematic diagram of the laser fluorination system for releasing oxygen from the crystal structure. Adapted from Sharp (1990)

.

2.4.1 Standard Values

Table 2.7: **Standard analyses of YP2 Quartz. Accepted value: 16.4.**

LF No:[a]	Port[b]	Name	$\delta^{18}O_{VSMOW}$	LF No:[a]	Port[b]	Name	$\delta^{18}O_{VSMOW}$
23798	1	YP2	17	23799	2	YP2	16.4
23808	1	YP2	18.5	23809	2	YP2	
18	1	YP2	16.7	19	2	YP2	16.4
30	1	YP2	16.9	31	2	YP2	16.4
42	1	YP2	17.2	43	2	YP2	16.4
54	1	YP2	17.3	55	2	YP2	16.4
66	1	YP2	17.9	67	2	YP2	16.4
78	1	YP2	17.2	76	11	YP2	15.5
24601	1	YP2	21.6	79	2	YP2	16.4
11	1	YP2	16.4	24611	1	YP2	16.4
23	1	YP2	18.4	24	2	YP2	16.4
35	1	YP2	18.1	36	2	YP2	16.4
47	1	YP2	18.8	48	2	YP2	16.4
59	1	YP2	18.2	60	2	YP2	16.4
71	1	YP2	18.3	72	2	YP2	16.4
83	1	YP2	18	84	2	YP2	16.4

[a]Laser fluorination analysis run number
[b]Port refers to the no. analysis on the given day from 1-12

Table 2.8: **Standard analyses of SCXO (San Carlos Olivine) and UWG2 (Garnet). Accepted values: 5.2 & 5.8.**

LF No:[a]	Port[b]	Name	$\delta^{18}O_{VSMOW}$	LF No:[a]	Port[b]	Name	$\delta^{18}O_{VSMOW}$
23803	6	SCXO	5.4	24610	10	UWG2	5.7
13	6	SCXO	5.4	22	12	UWG2	5.6
23	6	SCXO	5.3	34	12	UWG2	5.7
35	6	SCXO	5.3	46	12	UWG2	5.7
47	6	SCXO	5.3	58	12	UWG2	5.6
59	6	SCXO	5.5	70	12	UWG2	5.8
71	6	SCXO	5.5	82	12	UWG2	5.7
83	6	SCXO	5.4	94	12	UWG2	5.6

[a]Laser fluorination analysis run number
[b]Port refers to the no. analysis on the given day from 1-12

Table 2.9: **Standard analyses of GP147. Accepted value: 7.2.**

LF No:[a]	Port[b]	Name	$\delta^{18}O_{VSMOW}$
23807	10	GP147	7.1
17	10	GP147	7
28	11	GP147	7.2
41	12	GP147	7.1
53	12	GP147	7.1
65	12	GP147	6.9
74	9	GP147	6.9
88	11	GP147	7
8	8	GP147	7.2
16	6	GP147	7.4
28	6	GP147	7.2
40	6	GP147	7.2
52	6	GP147	7.4
64	6	GP147	7.2
76	6	GP147	7.2
88	6	GP147	7.3

[a]Laser fluorination analysis run number
[b]Port refers to the no. analysis on the given day from 1-12

2.5 Piston-Cylinder Setup

The piston-cylinder apparatus is a large volume, solid-media device which can be used to replicate pressure-temperature conditions in the mid crust to upper mantle. In this thesis, piston-cylinder experiments were performed (Chapter 7) to provide additional insight into magmatic processes occurring within the TVZ.

2.5.1 Capsule Preparation

For solid-media experiments, samples must be encapsulated to protect them and prevent reaction with components of the sample assembly. Capsules were initially made from 3mm diameter tubes of silver palladium (70%Pd, 30%Ag) cut to 10mm length. However, the melting temperature of silver palladium decreases at lower pressures. In addition, trace amounts of Fe from the melt react with the silver palladium, exacerbating issues with capsule melting at experimental conditions hotter than 1200°C and pressures less than 1GPa. Platinum capsules were used as an alternative. These were 4mm diameter by 10mm length. To avoid Fe loss from the sample into the Pt capsule, the capsules were filled and coated in the starting composition and annealed for 1-2 weeks at 950°C at atmospheric pressure. Recovered capsules were carefully cleaned prior to use. One end of each capsule was triple crimped and welded shut using a Lampert PUK U4 precision welder. The capsule was then filled to approximately 3/4 full with the experimental charge, before the top was triple crimped and welded shut. The capsules were then compressed in a pin press to flatten both ends, resulting in a final capsule length of 5mm (Figure 2.4). Capsules were then loaded into a talc-pyrex 0.5 inch piston-cylinder assemblies (Figure 2.2) that contain internal graphite resistance heaters. During experiments, a current is passed through the graphite base and furnace to produce a stable temperature in the sample volume. An outer sleeve of talc acts as the pressure medium during the experiment, by converting uniaxial compression of the entire assemblage to hydrostatic conditions within the sample volume. A cylinder

of pyrex protects the graphite furnace from the talc, which can dehydrate at high temperatures. Alumina spacer rods centre the capsule inside the assembly to ensure that it lies within the hotspot of the furnace. The upper spacer has a hole into which a thermocouple is inserted, with a small alumina disc protecting the soft Pt capsule from being ruptured by the thermocouple ceramic (Figure 2.2). The sample assembly, once surrounded by a thin sheet of lead foil to act as a lubricant, is placed inside a tungsten carbide bomb with a steel base plug on top (Figure 2.3). Temperature is measured using a R-type Platinum-Rhodium thermocouple inside a 4-bore ceramic thermocouple rod, which is inserted through the base plug and top of the assembly to within 1mm of the capsule, to ensure an accurate record of temperature. Temperature recorded is accurate to ± 10°C. The steel base plug compresses during the experiment to prevent extrusion of the thermocouple, which would prevent accurate recording of run temperature.

2.5.2 Piston Cylinder Apparatus

The piston cylinder is a device that enables a small sample (solid media) to be subject to simultaneous high pressures and temperatures. The apparatus works by stacking multiple components, (bridge, bomb, thermocouple plate and aluminium spacer (Figure 2.3) and applying an initial pressure to stabilise the stack, called the end load. In the middle of the stack is the bomb, which is made up of a tungsten carbide core, with a hole in the centre to allow space for an assembly containing the experimental capsule. Surrounding the core of the bomb are multiple rings of steel; The core is press-fit into these rings, which prevents outward expansion, and failure, of the core when large compressive pressures are applied during experiments. Underneath the bomb is the bridge, which contains a small ram that pushes up a carbide piston into the internal hole in the carbide core of the bomb. This is the primary mechanism by which the press applies pressure to the sample assembly. Sample pressures can be readily determined by accurately measuring oil pressure to the lower ram, and considering

the cross section area of the hydraulic ram and carbide piston. In practice, a small (12%) correction due to loss of pressure by internal friction in the sample assembly is applied. Heat is applied to the capsule by running a current through the press, which travels, due to insulating sheets used in the stack, through the graphite surrounding the capsule in the assembly. Temperature can be controlled by increasing or decreasing the operating power going to the press, and is measured using an R-type platinum-rhodium thermocouple which sits just above the capsule. Temperature recorded is accurate to ± 10°C. Likewise, pressure can be monitored and controlled throughout by varying oil pressure to the hydraulic ram. Pressure accuracy depends on press calibration, which has been previously determined using the quartz-coesite transition, melting point of diopside, kyanite-sillimanite transition and albite = jadeite + quartz reaction, and is accurate to within less than ±5% of the stated value.

2.5.3 Experimental Procedure

Experiments were run at 1065 - 1300°C, and at pressures of 5-10kbar on an end-loaded piston-cylinder press for a run duration of 24 hours. Pressure was initially increased to 1000psi, and then simultaneously increased to 100% of the desired pressure whilst increasing the temperature at a rate of 100°C per minute. Pressure and temperature were continually monitored and controlled throughout each experimental run. Experiments were quenched using the isobaric quench method by shutting off power to the heating circuits and maintaining sample pressure. Experiments were subsequently slowly depressurised by bleeding of oil pressure using a needle valve. Slow depressurisation prevented cracking of the sample.

2.5.4 Preparation for Analysis

Recovered capsules were mounted in crystal bond and subsequently ground down to expose the inside of the sample, before polishing to a fineness of 1μm using diamond

suspensions. They were then prepared for imaging and analysis by dissolving the crystal bond and cleaning in acetone, before embedding into an indium mount using the cold press technique. Capsules were examined under reflected light, before being carbon coated for imaging and analysis on the SEM.

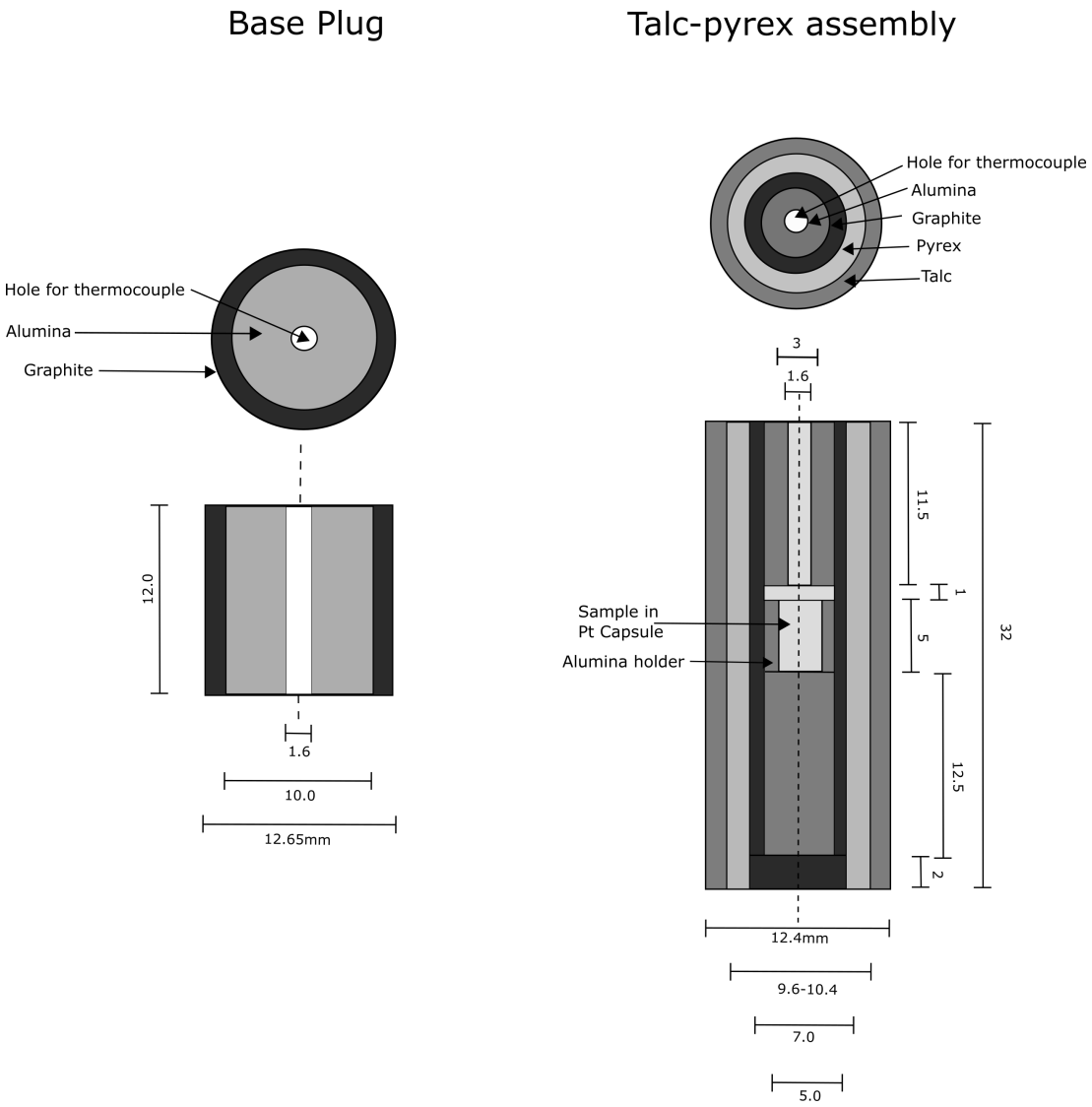

Figure 2.2: Schematic diagram of assembly setup for use in the piston cylinder press. All measurements in mm.

.

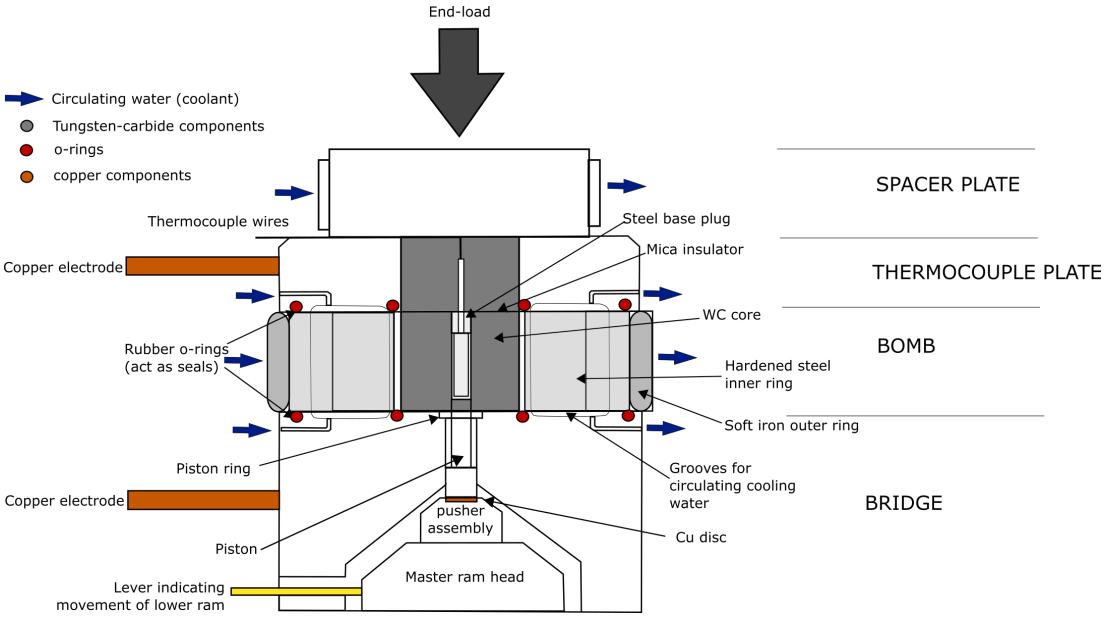

Figure 2.3: Schematic diagram of the piston cylinder apparatus.

.

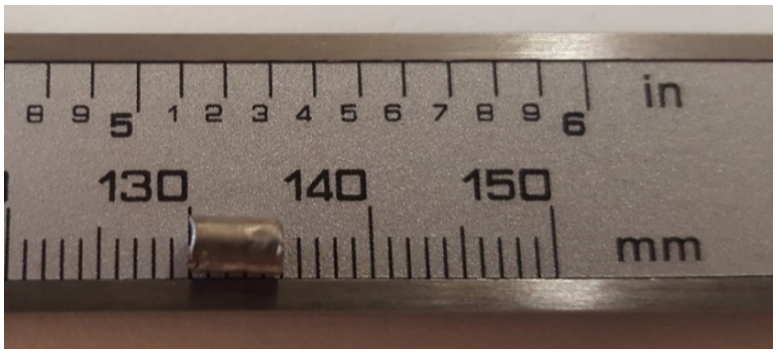

Figure 2.4: Final size of Pt capsule after being filled with sample, triple crimped, welded and flattened on both ends.

.

Chapter 3

Petrology and Mineral Chemistry

3.1 Okataina Volcanic Centre - Northern Central TVZ

3.1.1 Rotokawau (HAB)

Rotokawau scoria in thin section are brown-to-black, homogeneous, and relatively dense, with 10–15 % small vesicles. The sample is porphyritic with microcrystalline groundmass containing plagioclase (65%), clinopyroxene(25%), olivine (8%) and minor orthopyroxene and oxides. It contains phenocrysts of plagioclase, clinopyroxene and olivine, and antecrysts of plagioclase and clinopyroxene. Xenoliths of rhyolitic composition contain albitic plagioclase and quartz (Figure 3.1A). Separated xenocrysts of albitic plagioclase have compositions matching those in the xenoliths. Groundmass texture is heterogeneous, with clear flow alignment of plagioclase from mafic-mafic magma mixing (Figure 3.1B).

Plagioclase phenocrysts are euhedral, lath shaped with aspect ratios of 3.2-6.4, and <250μm. Phenocrysts are An_{83-85} (Figure 3.11) and compositionally unzoned. Clinopyroxene phenocrysts are euhedral to subhedral, equant and <200μm. Phenocrysts are of augitic composition with $Mg\#_{73-79}$ (Figure 3.12) and are compositionally unzoned. Olivine phenocrysts are euhedral to subhedral, but often show significant resorption. Olivine phenocrysts also sometimes show dendritic textures. Crystals are

up to 200μm, but mostly <100μm. Olivine phenocryst compositions are Fo_{71-78} with some crystals showing a thin reverse zone followed by normal zoning toward the rim (Figure 3.1D). Phenocrysts often occur as small glomerocrysts.

There are two types of plagioclase antecryst. Type one plagioclase antecrysts are euhedral and equant, with aspect ratios <3, and up to 500μm (population 1) (Figure 3.1C). Antecryst cores are large, compositionally homogenous with An_{93-96} (Figure 3.11) and some coarse sieving. Antecryst rims are thin (<40μm), euhedral and are An_{82-87}. This population of plagioclase makes up approximately 10% of plagioclase macrocryts and is also present in Terrace Rd and Rotomakariri. Clinopyroxene antecrysts are found along with plagioclase antecrysts. These occur as co-grown glomerocrysts, and are subhedral to euhedral. Clinopyroxene compositions are diopsidic-augitic in composition with $Mg\#_{82-84}$. Antecryst rims are euhedral and augitic in composition with $Mg\#_{73-79}$. Type two plagioclase antecryst are 250μm-1mm and show pervasive coarse sieving in the cores. Measurement on extinction angles indicates approximately An_{50} composition. Rims are euhedral and free from sieving. No compositional data was acquired for these rims, but textures indicate equilibrium with the host basalt.

Xenoliths are rhyolitic in composition and contain abundant small vesicles, showing they were already erupted and cooled when incorporated into the basalt magma. Plagioclase xenocrysts are 250μm-1mm, show weak oscillatory zoning (population 3) and are An_{38}. Xenocrysts in contact with basalt show partial resorption on edges.

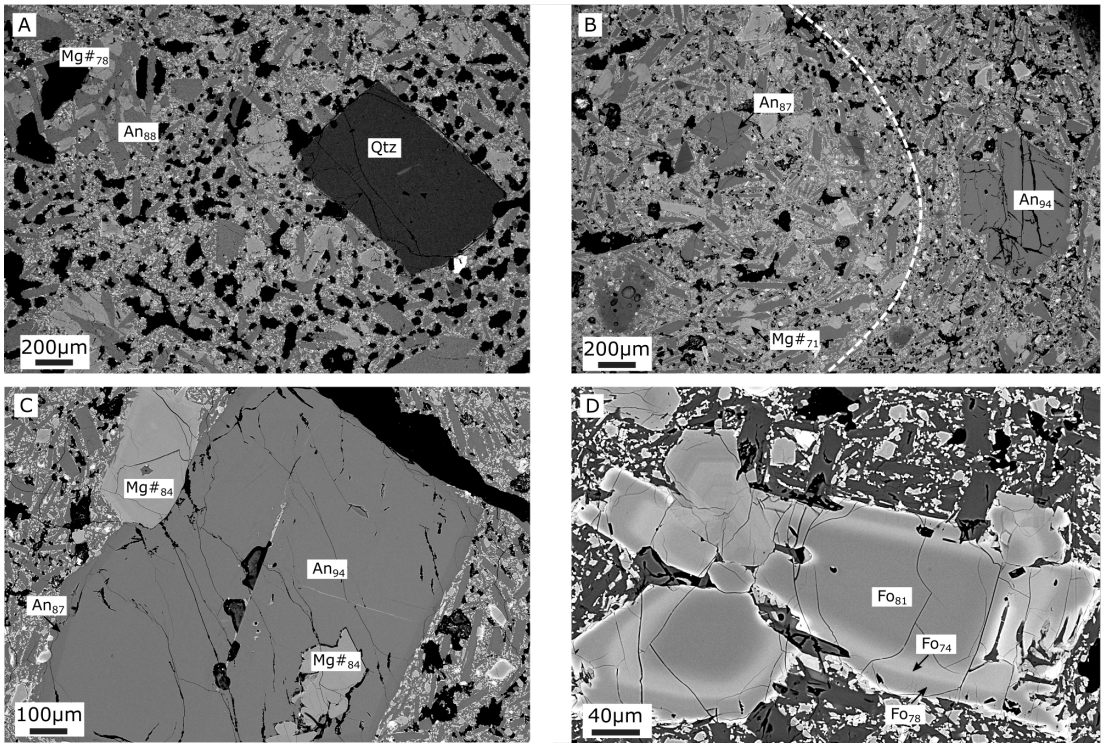

Figure 3.1: Backscatter Electron (BSE) images of representative textures in Rotokawau basalt. A) Microcrystalline groundmass and quartz xenocryst. The top left shows a glomerocryst of unzoned phenocrysts. B) Contrasting groundmass textures with flow alignment of plagioclase along white dashed line. Right side of image shows a high anorthite (An_{94}) antecryst with rim composition matching groundmass plagioclase (An_{87}). C) High anorthite antecryst containing an inclusion of high Mg# clinopyroxene. D) Olivine phenocryst with low Fo zone, followed by a higher Fo zone toward the rim.

3.1.2 Tarawera - 1886 eruption: Plinian phase (HAB)

Tarawera scoria in thin section are brown-black with rare bands of light grey material. The dark material is homogenous throughout and moderately vesicular (20-25%). The sample is aphyric and the groundmass is microcrystalline, composed of approximately 55% plagioclase, 28% clinopyroxene, 14% olivine and minor oxides (Figure 3.2B). Groundmass plagioclase is gradational into microphenocrysts and is 10-200μm, elongate and needle-like, with high aspect ratios (>75% aspect ratio >5 & <10, n=729), and often swallow-tailed. Olivine is 10-50μm and commonly shows hopper texture. Clinopyroxene is 10-50μm and subhedral. The pale grey material is glassy, not vesicular, and contains albitic plagioclase (An_{30}; 30% modal abundance), quartz (5% modal), and minor biotite. The samples also contain plagioclase xenocrysts of similar composition to those in the pale grey material (Figure 3.2A).

The samples contain one population of clinopyroxene and olivine, and both phenocrystic and xenocrystic plagioclase. Unlike Rotokawau, population 1 antecrysts of high-anorthite composition are absent. Phenocrystic plagioclase is An_{85-88} (Figure 3.11), clinopyroxene is $Mg\#_{77-80}$ (Figure 3.12) and olivine is Fo_{80-82}.

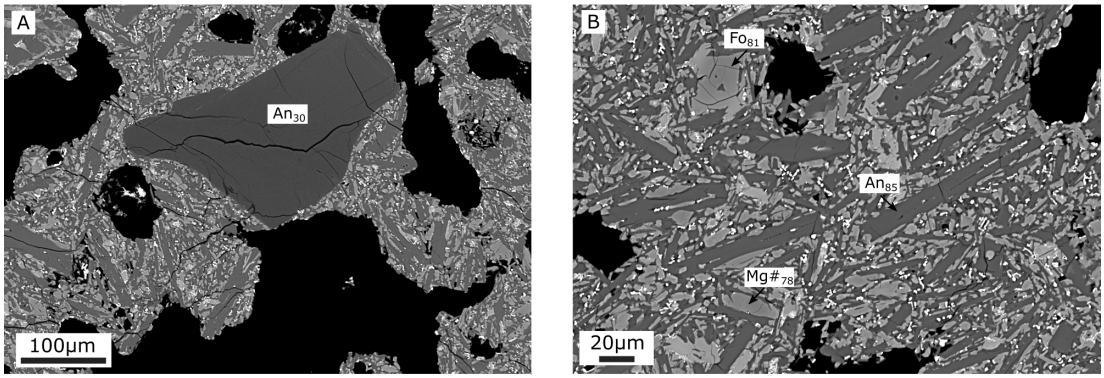

Figure 3.2: Backscatter Electron (BSE) images of representative textures in Tarawera basalt. A) Low anorthite xenocryst in groundmass. B) Groundmass texture. Swallow-tail plagioclase and hopper olivine.

3.1.3 Rotomakariri (BA)

Rotomakariri scoria are homogenous, brown-black and highly vesicular, with 40-50% vesicles with a wide range of sizes. Samples are porphyritic. The groundmass comprises approximately 20% of the total sample (inclusive of pore space), of which 55% is glass, 35% is plagioclase (<5-100μm) and 10% is clinopyroxene (<20μm). It contains phenocrysts of plagioclase and clinopyroxene, and antecrysts of plagioclase, clinopyroxene, orthopyroxene and olivine. The total macrocryst content is approximately 30% of the sample, of which 50% is plagioclase (100-2500μm), 20% clinopyroxene (100-500μm), 20% orthopyroxene (100-500μm) and 10% olivine (100-1000μm).

Plagioclase phenocrysts are lath-shaped, 100-200μm and unzoned with compositions of An_{71-79} (Figure 3.3A). Clinopyroxene phenocrysts are euhedral to subhedral, mostly <100μm, augitic in composition with $Mg\#_{68-73}$ (Figure 3.2A). Larger clinopyroxene phenocrysts (100-200μm) have higher Mg# ($Mg\#_{74-77}$) inherited cores (50-100μm) (Figure 3.3B).

Plagioclase antecrysts are present in two populations. The first population comprises approximately 10% of the total plagioclase cargo, is equant and 250-500μm. Cores of this population are large and homogenous and have very high anorthite content of An_{91-94} (Figure 3.3C, 3.11). Rims are thin (<40μm) and are An_{72-76} (Figure 3.11). This population is similar to high anorthite plagioclase present in Rotokawau, Terrace Rd and Harry Johnson Rd samples. Population two comprises approximately 75% of the plagioclase cargo. These plagioclase crystals are large (mostly 1-2mm), tabular, and often show oscillatory zoning and pervasive coarse sieving. Measurement of anorthite content by extinction angle gives approximately An_{50}. This population of plagioclase is similar to population two plagioclase from Rotokawau basalt. Clinopyroxene antecrysts are 200-400μm and occur as glomerocrysts with plagioclase. They are diopsidic-augitic in composition (Figure 3.12), with $Mg\#_{78-87}$ (Figure 3.3E, F). The highest Mg# compositions are found in glomerocrysts with plagioclase of >An_{90} (Fig-

ure 3.3F). The lower Mg# compositions are present in glomerocrysts with plagioclase of An_{81-88} (Figure 3.3D). The highest Mg# compositions often display normal zoning towards the rim (Figure 3.3D), whereas lower Mg# compositions often display reverse zoning in the rim. Olivine antecrysts are rare and large (200-1000μm) and subhedral to anhedral and display overgrowth textures (Figure 3.3E, F). Overgrowth textures are not uniform. Some olivines have thin overgrowths of microcrystalline orthopyroxene (20-100μm) (Figure 3.3E), others have large, thick overgrowths of orthopyroxene (>200μm), which themselves are overgrown by high Mg# population of clinopyroxene and high anorthite population of plagioclase (Figure 3.3F). Orthopyroxene antecrysts occur in glomerocrysts with plagioclase and clinopyroxene and are reversely zoned, from $Mg\#_{71}$ in the cores to $Mg\#_{76}$ in the rims (Figure 3.3D).

A significant proportion of the crystal cargo is hosted in glomerocrysts. Type one glomerocrysts (2-3 mm across) contain 1–3 olivine nuclei (each 200-1000μm in size) that are overgrown by anhedral orthopyroxene (up to 500μm in size), and clinopyroxene (up to 250μm in size) . In some cases, these are encased in equal proportions of clinopyroxene, orthopyroxene, and plagioclase (similar to population 1), which have euhedral faces and are 250-500μm in size (Figure 3.3F). Type two glomerocrysts (1-2 mm across) contain clinopyroxene, orthopyroxene, and plagioclase only, with grains up 500μm in size. Plagioclase are diffusively normally zoned with distinct clear, rims (An_{83-79}), whilst pyroxenes (clinopyroxene is $Mg\#_{75-78}$ and orthopyroxene is $Mg\#_{71-76}$) can be weakly reversely zoned when in contact with the groundmass (Figure 3.3D).

Hughes et al., *(in prep)*, note that: "Rotomakariri glass analyses (n = 24) are all dacitic in composition and include measurements of melt inclusions (n = 13) and embayments/matrix glass (n = 11). Melt inclusions are hosted in clinopyroxene with $Mg\#_{72-81}$ and low Cr_2O_3 contents (n = 9) and orthopyroxene (n = 5)."

Rotomakariri basaltic andesite, therefore, appears to be a mixture of dacitic melt and crystals derived from dacitic melt, and crystals derived from a basaltic melt (olivine,

high Mg# clinopyroxene, high anorthite content plagioclase). It is unclear whether basaltic melt contributed to the final composition of this sample (i.e. magma mixing), or whether only crystals were incorporated (i.e. plucking of crystals from a mush).

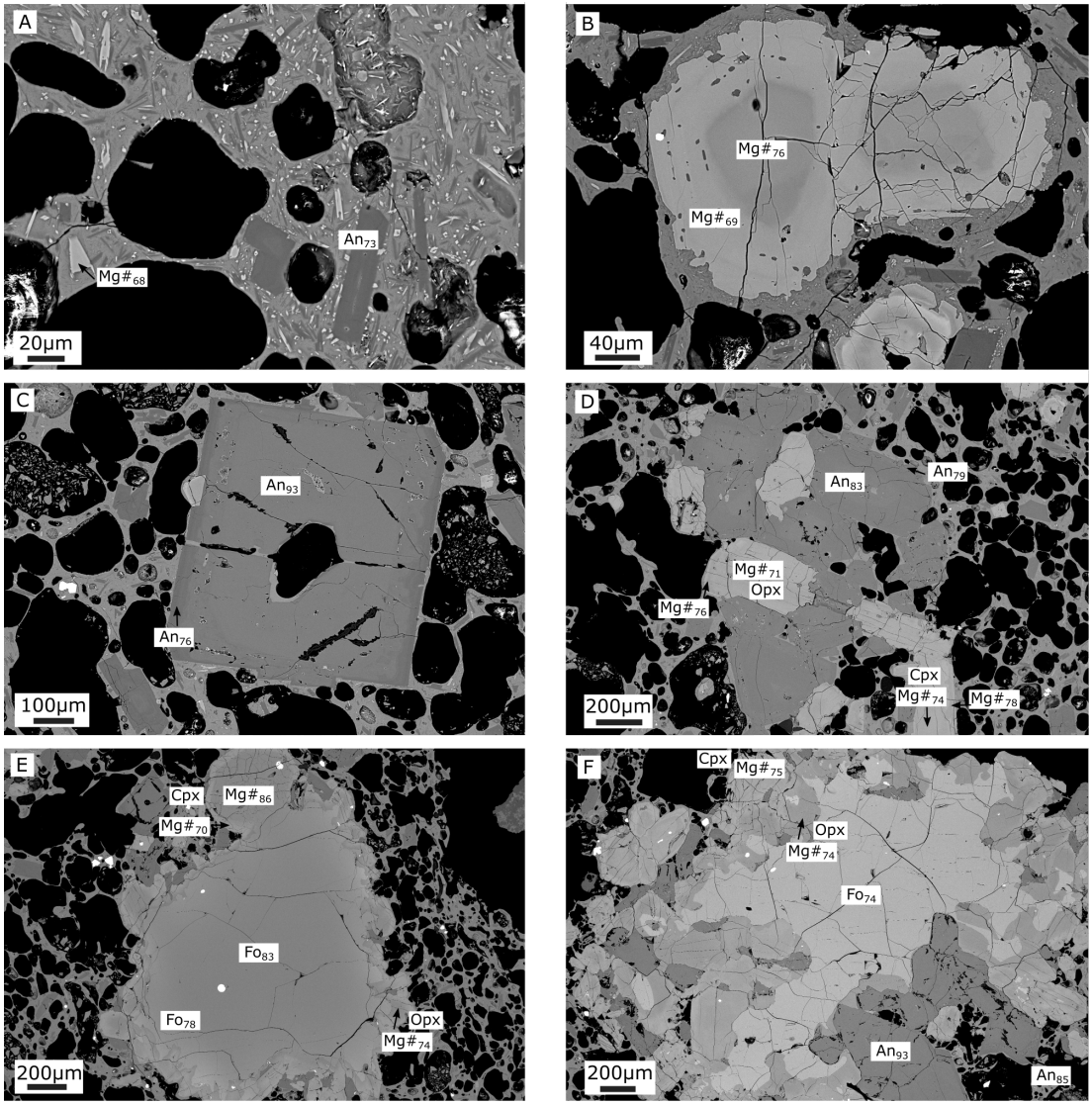

Figure 3.3: Backscatter Electron (BSE) images of representative textures in Rotomakariri basaltic andesite. A) Groundmass texture showing dacitic glass, plagioclase and swallowtail clinopyroxene. B) Clinopyroxene phenocryst with higher Mg# inherited core. Low Mg# outer zone shows numerous small melt inclusions of dacitic composition. Rim is heavily resorbed. C) Population one high-anorthite antecryst with rim in equilibrium with melt. D) Type two glomerocryst containing plagioclase and reversely zoned clino- and orthopyroxene. E) Normally zoned olivine antecryst with microcrystalline orthopyroxene overgrowth and high-Mg# clinopyroxene. F) Type one glomerocryst with large anhedral olivine core, thick orthopyroxene overgrowth, joined by high-Mg# clinopyroxene and high-anorthite plagioclase.

3.1.4 Terrace Road (BA)

Terrace Road scoria are a mixture of dark brown-black and light-mid brown. They are moderately vesicular with no distinct change in vesicularity between dark and light sections. Groundmass plagioclase shows flow alignment along the contacts between darker and lighter areas. Samples are porphyritic, and are approximately 60% microcrystalline groundmass, of which 70% is plagioclase, which is elongate and needle-like in habit (100-10μm), 20% is olivine which is euhedral to subhedral (10-20μm), and 10% is clinopyroxene (<10μm) (Figure 3.4F). It contains phenocrysts of plagioclase, clinopyroxene and olivine. Groundmass plagioclase is gradational with phenocrystic plagioclase in size. It also contains antecrysts of plagioclase, clinopyroxene and orthopyroxene.

Plagioclase phenocrysts are elongate to lath-shaped, 100-200μm and unzoned with compositions of An_{83-87} (Figure 3.11). Clinopyroxene phenocrysts are equant and euhedral, 40-100μm, augitic in composition with $Mg\#_{68-73}$ (Figure 3.12) and often show weak oscillatory zoning. Olivine phenocrysts are subhedral, 20-100μm, unzoned with compositions of Fo_{76-78} and often show dendritic shape. Phenocrysts are commonly grouped together in small glomerocrysts 100-300μm in total size (Figure 3.4C).

One population of plagioclase antecrysts is present. This comprises approximately 20% of the total plagioclase cargo. Plagioclase antecrysts are equant, 250-500μm and have large homogenous cores of An_{92-95} (figure 3.4A, 3.11). The rims of this population of plagioclase are thin (20-40μm) and An_{87-89}. This population of high-anorthite plagioclase is similar to type one plagioclase antecrysts in Rotokawau, Rotomakariri and Harry Johnson Road samples. Clinopyroxene antecrysts are rare and make up <5% modal abundance. They are 250-500μm and are reversely zoned, with cores of Mg#66 – 69 and thick rims (200μm) of $Mg\#_{80-82}$ (Figure 3.4B). The high Mg# zones often contain population one high-anorthite plagioclase, forming glomerocrysts (Figure 3.4B). Orthopyroxene is only present once as a broken fragment of a much larger crystal,

with a newly crystallised clinopyroxene rim (Figure 3.4E). The orthopyroxene is $Mg\#_{76}$ and the clinopyroxene rim is $Mg\#_{74-78}$.

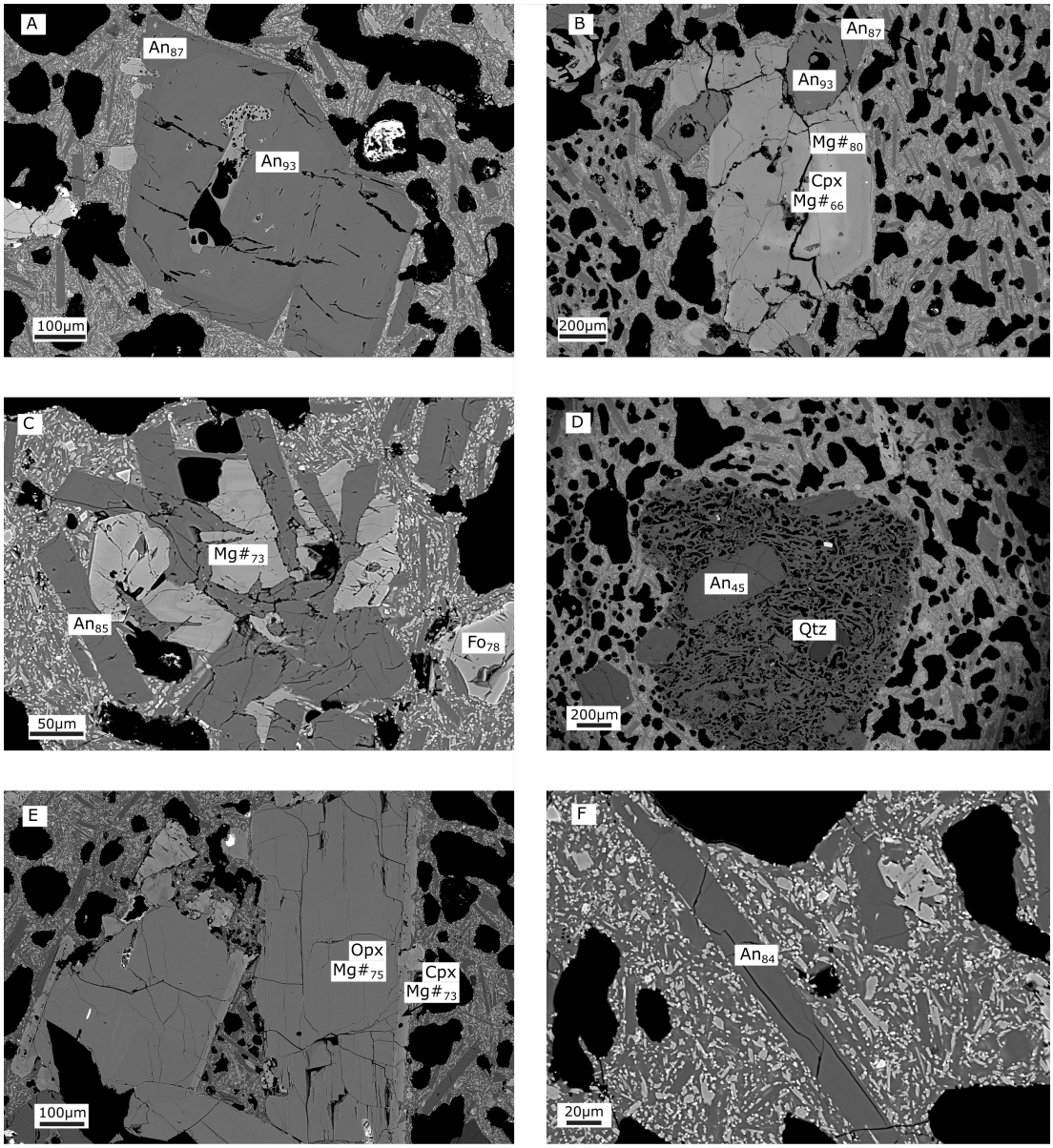

Figure 3.4: Backscatter Electron (BSE) images of representative textures in Terrace Rd basaltic andesite. A) Population one high-anorthite antecryst with rim in equilibrium with melt. B) Clinopyroxene antecryst with lower Mg# inherited core. High Mg# outer zones are co-grown with population one high-anorthite plagioclase. C) Type 1 glomerocryst of phenocrystic plagioclase, olivine and clinopyroxene. D) Rhyolite composition xenolith containing low anorthite plagioclase and quartz. E) Broken orthopyroxene fragment with clinopyroxene rim. F) Groundmass texture showing elongate plagioclase.

3.2 Inter-caldera basalt - Central TVZ

3.2.1 Harry Johnson Road (HAB)

Harry Johnson Road (HJR) scoria in thin section are brown-to-black, homogeneous, and moderately vesicular. Samples are only mildly porphyritic, and contain approximately 80-90% groundmass. Groundmass is microcrystalline with small pockets (<10μm) of devitrified glass, and comprised of plagioclase (55%), which is 10-100μm elongate and lath-shaped, olivine (10%), which is 10-20μm and subhedral, clinopyroxene (20%), which is 10-20μm and subhedral, and glass (15%). It contains phenocrysts of plagioclase, clinopyroxene and olivine, which are gradational in size down to the groundmass.

Plagioclase phenocrysts are 100-200μm in length and lath-shaped. They are unzoned or weakly zoned and have compositions of An_{78-87} (Figure 3.5A, 3.11). Clinopyroxene phenocrysts are subhedral, 30-100μm, augitic in composition with $Mg\#_{70-81}$ (Figure 3.12) and often show weak oscillatory zoning (Figure 3.5A). Olivine phenocrysts are subhedral, 20-100μm, have unzoned cores of Fo_{76-78} and often show dendritic shape. The bright zones near the rim are altered and were not analysed (Figure 3.5A). Phenocrysts occur as single crystals and grouped together in small glomerocrysts 100-300μm in total size.

One population of plagioclase antecrysts is present. This comprises approximately 5% of the total plagioclase cargo. Plagioclase antecrysts are equant, 250-400μm and have large homogenous cores of An_{93-94} (Figure 3.5B). The rims of this population of plagioclase are thin (20-40μm) and An_{86-87}. This population of high-anorthite plagioclase is similar to type one plagioclase antecrysts in Rotokawau, Rotomakariri and Terrace Road samples.

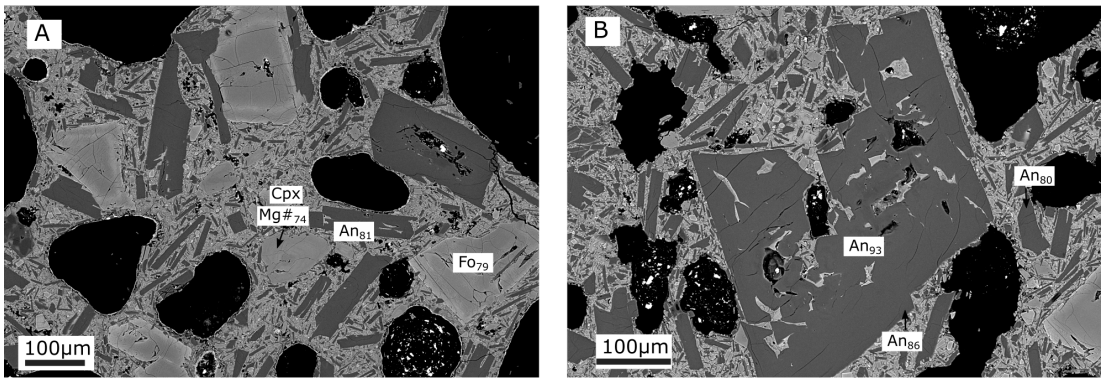

Figure 3.5: Backscatter Electron (BSE) images of representative textures in Harry Johnson Rd basalt. A) Phenocrystic plagioclase, olivine and clinopyroxene in microcrystalline groundmass. B) Population one high anorthite antecryst with lower anorthite rim.

3.2.2 Ongaroto (HMB)

The Ongaroto sample is a lava flow, and is mid-grey in thin section, with visible olivine crystals. Samples are porphyritic, comprising approximately 70% groundmass. Groundmass has a trachytic texture, and is fully crystalline, comprising approximately 65% plagioclase, which is 50-100μm and elongate/lath-shaped, and 35% clinopyroxene, which is 20-100μm and anhedral to subhedral (Figure 3.6C). It contains approximately 30% phenocrysts of olivine.

Phenocrysts of olivine are 200μm to 1mm in length. Olivine displays strong normal zoning and has core compositions up to Fo_{91} in the largest crystals (Figure 3.6A). Cores often contain inclusions of Cr-spinel (Figure 3.6A, B). Olivine rim compositions are Fo_{65-75}. Some olivine rims have thin microcrystalline overgrowths of orthopyroxene of $Mg\#_{67-69}$.

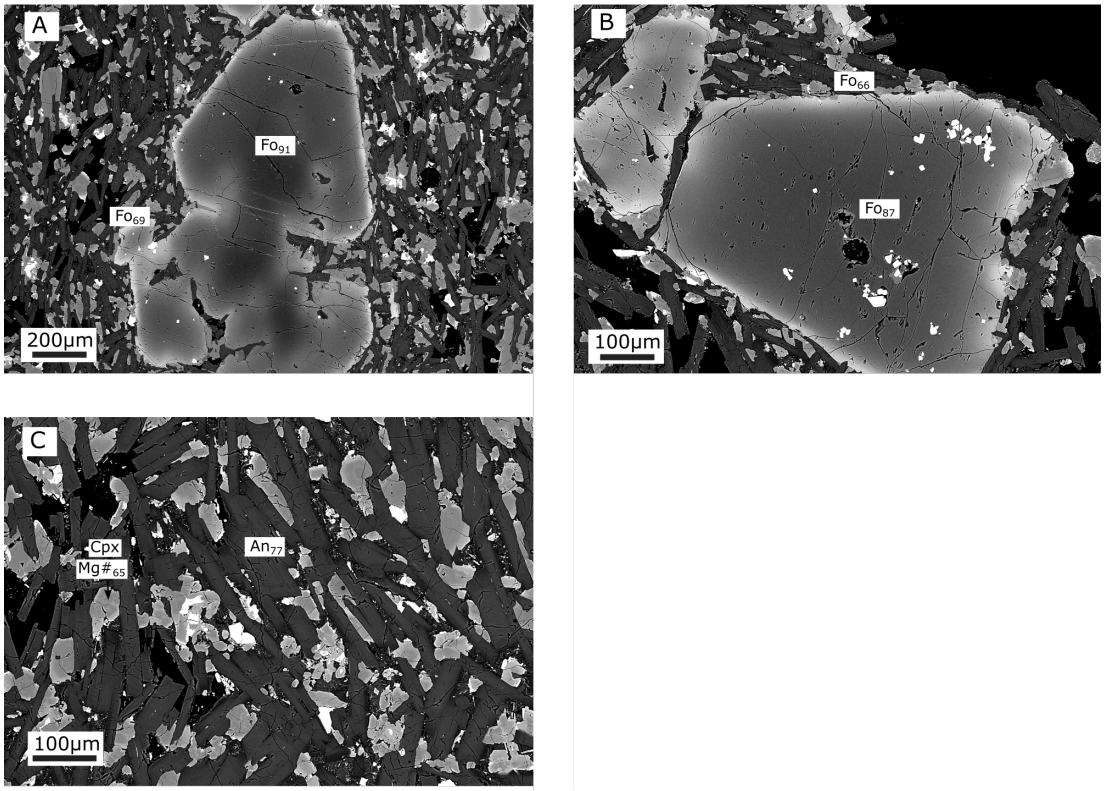

Figure 3.6: Backscatter Electron (BSE) images of representative textures in Ongaroto basalt. A) Large high-forsterite zoned olivine in trachytic groundmass. B) Primitive but lower forsterite olivine with numerous spinel inclusions. C) Groundmass texture of plagioclase and clinopyroxene with minor Fe-Ti oxides.

3.2.3 Kakuki (HAB)

Kakuki scoria in thin section are brown-to-black, homogeneous, and moderately vesicular. Samples are mildly porphyritic, and contain approximately 80-90% groundmass. Groundmass is microcrystalline and comprises plagioclase (60%), which is <10-100μm elongate and lath-shaped, olivine (20%), which is 10-20μm and subhedral, and clinopyroxene (20%), which is 10-20μm and subhedral. It contains phenocrysts of plagioclase and olivine, which are gradational in size down to the groundmass.

Plagioclase phenocrysts are 100-300μm in length and lath-shaped. They are unzoned or weakly zoned and have compositions of An_{76-89} (Figure 3.7A, 3.11). Olivine phenocrysts are euhedral, 20-150μm, and are unzoned or weakly zoned with Fo_{80-85} (Figure 3.7B, C). Phenocrysts occur as single crystals and grouped together in small glomerocrysts 100-500μm in total size (Figure 3.7A).

One population of plagioclase antecryst is present. It is rare (<5% of plagioclase cargo) and comprises a coarsely sieved core of lower anorthite (An_{73-77}) and a rim of the same composition as groundmass plagioclase (An_{80-82}) (Figure 3.7D).

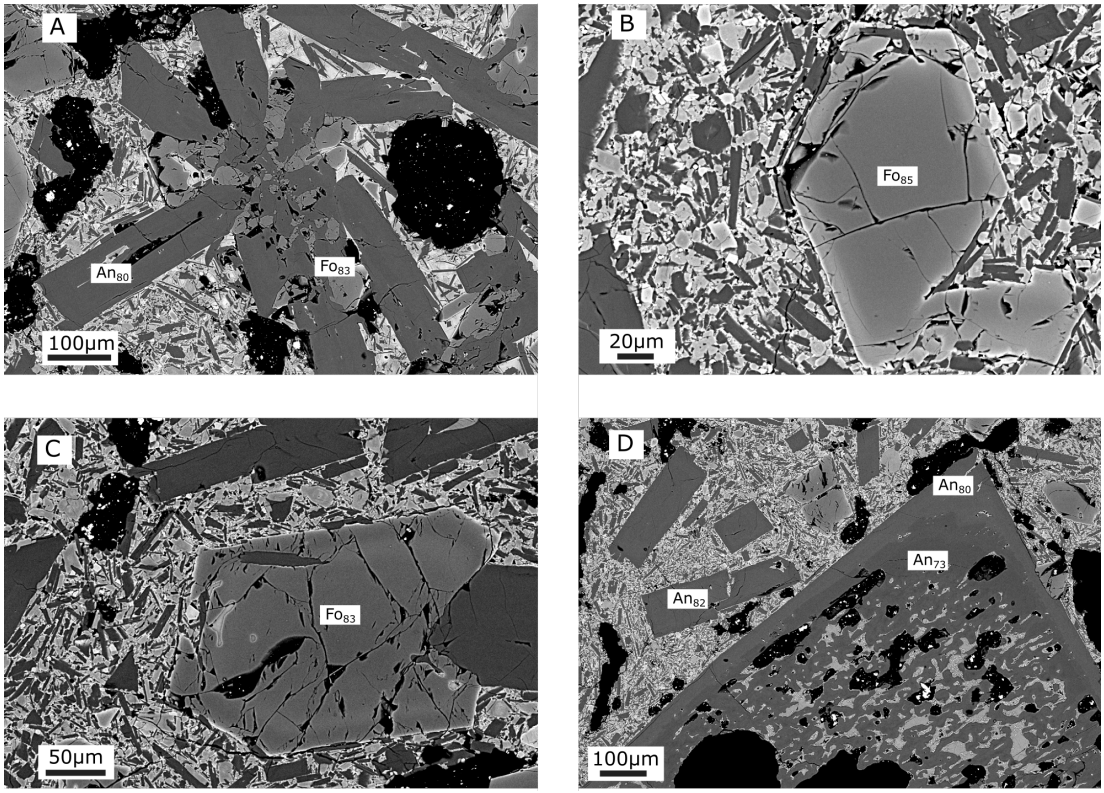

Figure 3.7: Backscatter Electron (BSE) images of representative textures in Kakuki basalt. A) Phenocrystic glomerocryst comprised of olivine and plagioclase. B) olivine phenocryst. C) Olivine phenocryst with weak zoning. D) Rare coarsely sieved reverse zoned plagioclase, with rim of same composition as groundmass plagioclase.

3.2.4 Orakeikorako (HAB)

Orakeikorako lava in thin section are mid-grey and homogenous. Samples are highly porphyritic with coarsely crystalline groundmass which grades into phenocrysts (Figure 3.8A). Groundmass crystals are plagioclase (70%), which is lath-shaped and 20-200μm, clinopyroxene (20%), which is sub-anhedral and 10-100μm and olivine (10%), which is euhedral to subhedral and up to 50μm. Phenocryst content is approximately 40-50%. Plagioclase phenocrysts are 100-300μm, An_{80} (Figure 3.11) and show weak normal zoning toward the rim. Clinopyroxene phenocrysts are 100-150μm, $Mg\#_{74-81}$ (Figure 3.12) and show weak oscillatory zoning. Olivine phenocrysts are up to 300μm and Fo_{78} in the cores with a thin higher forsterite zone of Fo_{80-82} before the rim which shows normal zoning down to Fo_{55-67} (Figure 3.8C).

Both plagioclase and clinopyroxene antecrysts are present (Figure 3.8D). Plagioclase antecrysts are up to 500μm and have lower aspect ratios than groundmass plagioclase. They have rounded cores of An_{65-73} and thick euhedral rims of An_{80-82} (Figure 3.8B, D). Some plagioclase antecryst cores are coarsely sieved (Figure 3.8B), whereas others are not (Figure 3.8D). Clinopyroxene antecrysts show similar texture. They are up to 150μm and have rounded cores of $Mg\#_{71}$ and euhedral rims of $Mg\#_{79-81}$ (Figure 3.8D).

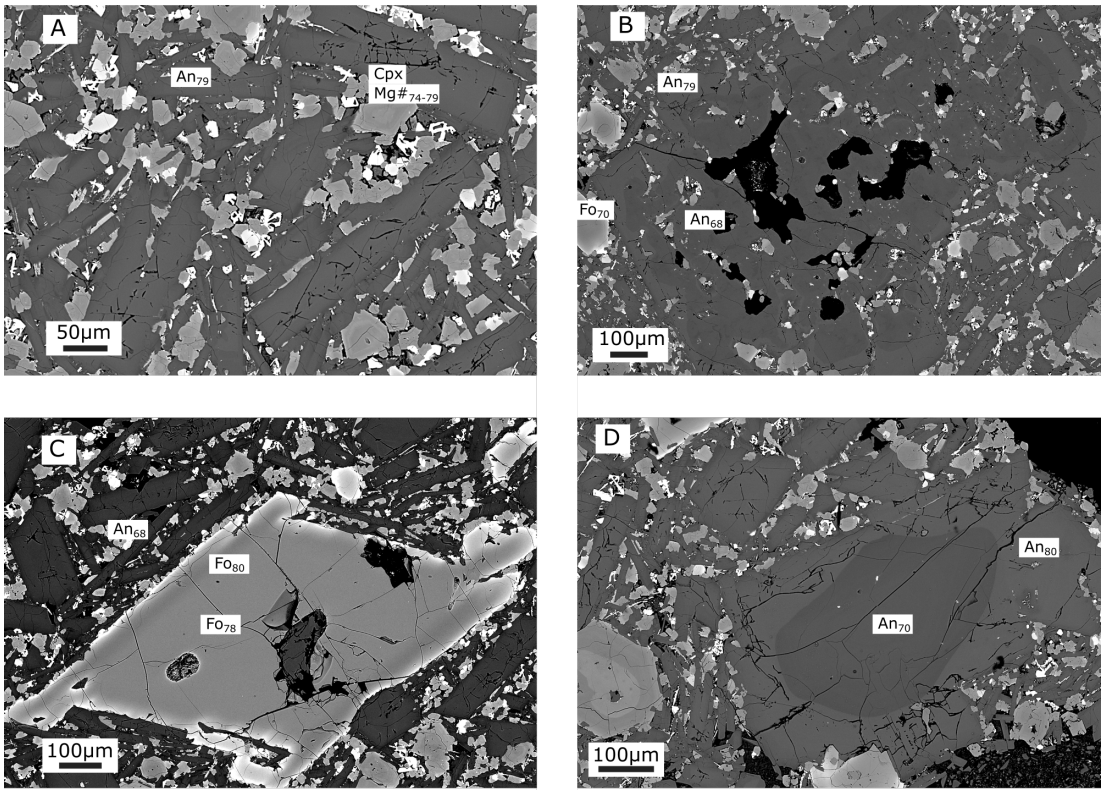

Figure 3.8: Backscatter Electron (BSE) images of representative textures in Orakeikorako basalt. A) Phenocrystic glomerocryst comprised of olivine and plagioclase. B) olivine phenocryst. C) Olivine phenocryst with weak zoning. D) Rare coarsely sieved reverse zoned plagioclase, with rim of same composition as groundmass plagioclase.

3.3 South TVZ

3.3.1 Waimarino (HMB)

Waimarino scoria are dark black-brown in thin section with large visible olivine crystals and crystal clots. They have relatively low vesicularity, with about 10-20% small bubbles. It is porphyritic, comprising approximately 30% crystals and 70% groundmass. Groundmass is composed of approximately 60% plagioclase, which is 10-100μm and lath-shaped, 25% clinopyroxene, which is euhedral-subhedral and 10-40μm and 5% olivine, which is subhedral and <20μm (Figure 3.9D).

Most large (>100μm) crystals in Waimarino are antecrystic. Olivine occurs as single crystals 200μm to 2.5mm in length (Figure 3.9C). They are euhedral to subhedral, and have core compositions of Fo_{90-93} (Figure 3.9A, C, F). Cores often contain inclusions of Cr-spinel. Kink banding is present in some crystals. Olivine shows normal zoning at the rim, down to Fo_{85}. Some olivine also shows thin reaction rims of microcrystalline orthopyroxene of $Mg\#_{73-76}$ (Figure 3.9F). These olivine also occur in clusters up to 2-3mm across. A second population of olivine occurs in clusters with clinopyroxene (Figure 3.9B). This olivine is sub-anhedral and often in the core of clusters, and has a composition of Fo_{85}, which is homogenous across the crystal. The clinopyroxene is up to 1.5mm across, diopsidic-augitic in composition with $Mg\#_{84-88}$ (Figure 3.12) and oscillatory zoned (Figure 3.9B). This clinopyroxene also occurs as broken fragments without olivine in the centre (Figure 3.9E).

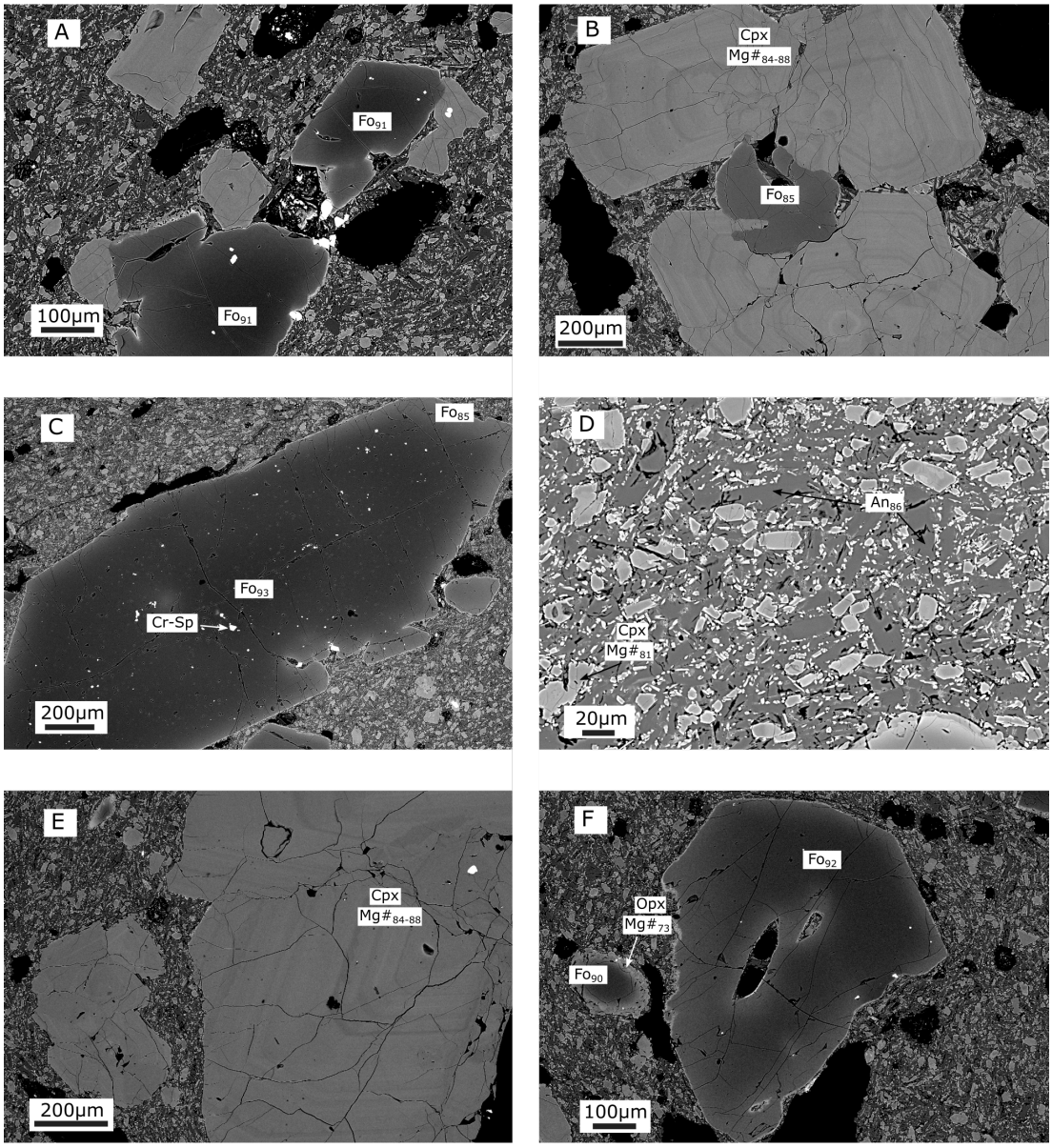

Figure 3.9: Backscatter Electron (BSE) images of representative textures in Waimarino basalt. A) Crystals of high forsterite olivine showing subhedral and euhedral shapes. B) Crystal of lower forsterite olivine surrounded by oscillatory zoned clinopyroxene. C) High forsterite olivine with kinked shape and Cr-spinel inclusions. D) Groundmass texture with plagioclase and clinopyroxene. E) Broken fragment of oscillatory zoned clinopyroxene. F) High forsterite olivine. Small olivine on left has microcrystalline orthopyroxene overgrowth.

3.3.2 Ohakune (HMBA)

Ohakune scoria are dark black-brown in thin section, with large visible crystal clusters of olivine and pyroxene. They are highly vesicular with approximately 40-50% vesicles. The groundmass is approximately 50% glass of andesitic to dacitic composition, with microlites of plagioclase (30%) and clinopyroxene (20%) (Figure 3.10A).

All large (>100μm) crystals in Ohakune are antecrystic, and occur mostly as glomerocrysts up to 5mm across (Figure 3.10B). These are always composed of a combination of clinopyroxene, orthopyroxene and olivine. Most commonly, olivine and orthopyroxene occur together (Figure 3.10E), or orthopyroxene and clinopyroxene (Figure 3.10B, C). Olivine and clinopyroxene do occur together in glomerocrysts, but not alone, always with orthopyroxene (Figure 3.10F). Type one olivine and orthopyroxene glomerocrysts comprise of one or more large, partially resorbed anhedral olivine cores of Fo_{86-88}, overgrown by thick euhedral rims of orthopyroxene of $Mg\#_{80}$ (Figure 3.10E, 3.12). Type 2 two-pyroxene glomerocrysts either comprise of one or more large anhedral clinopyroxenes in the core, with multiple large, oscillatory zoned orthopyroxene overgrowths (Figure3.10B), or as co-grown glomerocrysts, often with matching oscillatory zoning (Figure 3.10E). In the two pyroxene glomerocrysts, orthopyroxene is usually more abundant than clinopyroxene in a ratio of approximately 2:1. Another interesting feature is that oscillatory zoned orthopyroxenes occasionally display thin rims of clinopyroxene (Figure3.10D).

3.4 Mineral compositions

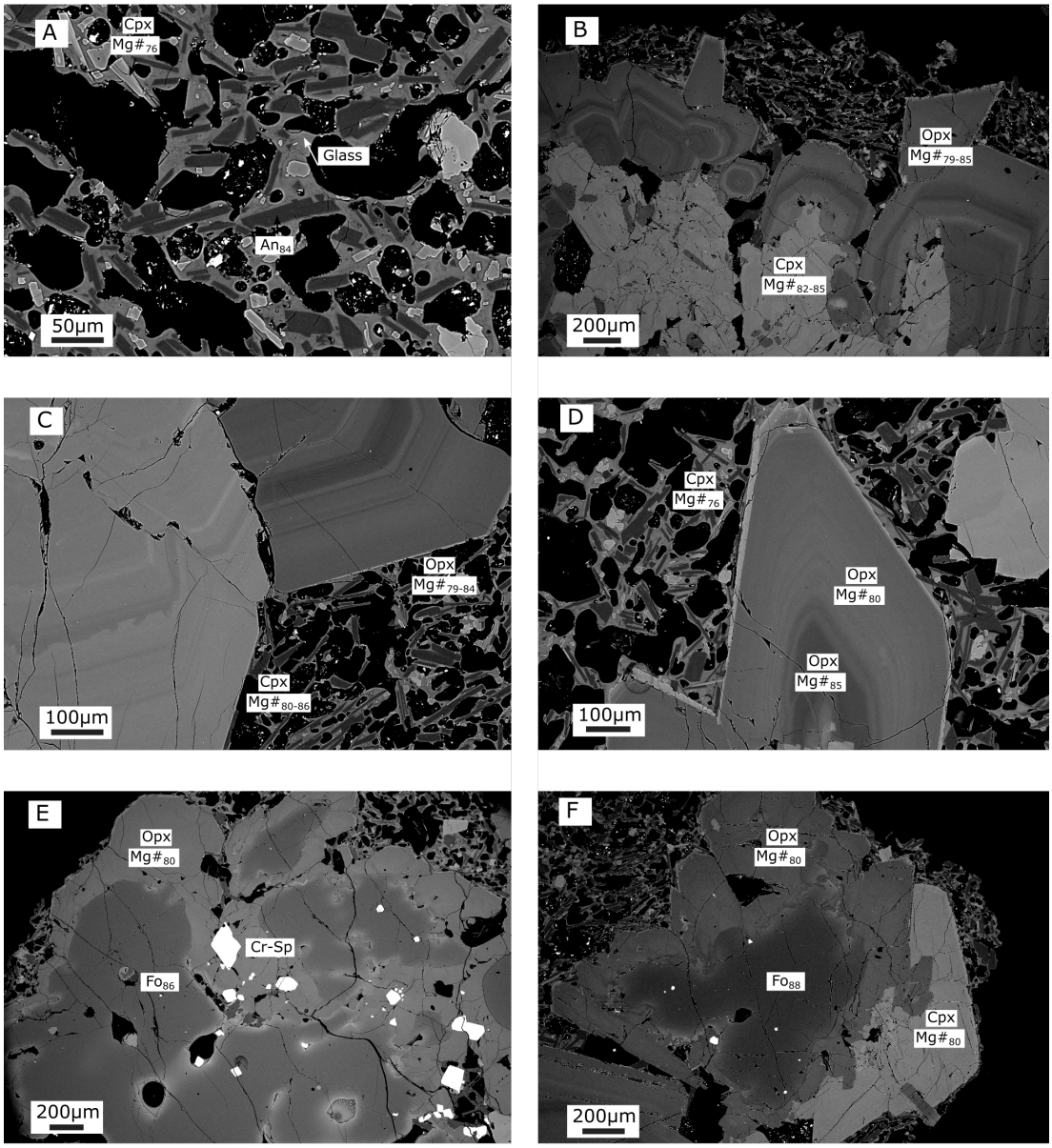

Figure 3.10: Backscatter Electron (BSE) images of representative textures in Ohakune basaltic andesite. A) Groundmass texture with plagioclase and clinopyroxene in andesitic-dacitic glass. B) Glomerocryst of clinopyroxene surrounded by oscillatory zoned orthopyroxene C) Part of two-pyroxene glomerocryst with matching oscillatory zoning. D) Oscillatory zoned orthopyroxene with clinopyroxene core and rim. E) Resorbed anhedral olivine core overgrown by thick rim of orthopyroxene. F) Resorbed anhedral olivine core overgrown by thick rim of orthopyroxene and clinopyroxene.

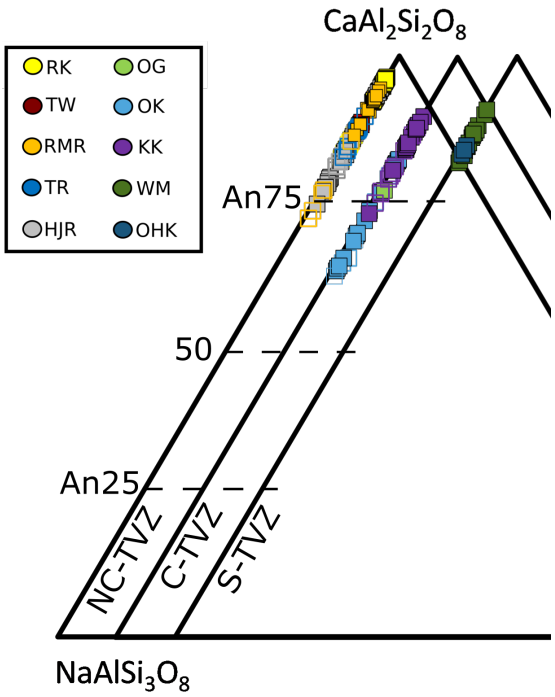

Figure 3.11: Anorthite-Albite-Orthoclase triangular diagram of all analysed plagioclase from mafic TVZ rocks, separated by NC-TVZ (OVC), C-TVZ and S-TVZ. RK - Rotokawau; TW - Tarawera; RMR - Rotomakariri; TR - Terrace Rd; HJR - Harry Johnson Rd; OG - Ongaroto; OK - Orakeikorako; KK - Kakuki; WM - Waimarino; OHK - Ohakune.

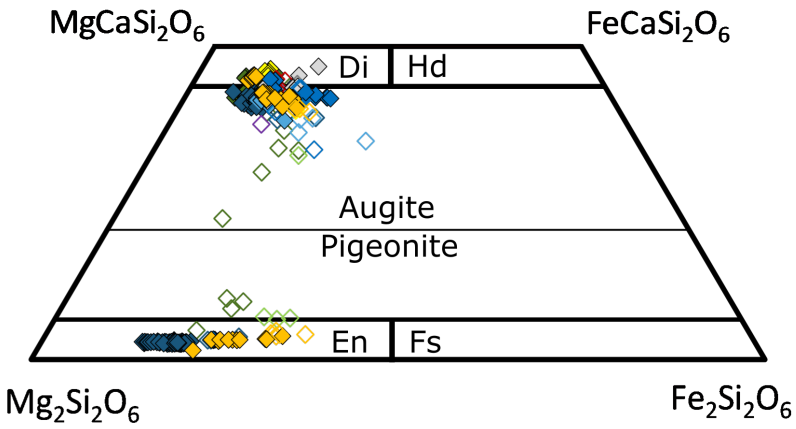

Figure 3.12: Pyroxene quadrilateral diagram of all analysed pyroxenes from mafic TVZ rocks. Symbols the same as in Figure 3.11.

Chapter 4

Complex crystal cargoes from monogenetic magmas

4.1 *Foreword*

Chapter 3 showed that the crystal cargo of the mafic rocks is highly complex and contains multiple populations of crystals. This chapter builds on the textural observations made in Chapter 3 by examining the crystal cargo in more depth through major and minor element compositional variations in crystals and melt. This chapter focuses mostly on plagioclase and clinopyroxene compositions, with compositional variation in the olivine cargo discussed in detail in Chapter 6.

4.2 Introduction

The study of phenocrysts and antecrysts hosted within volcanic products has long been recognised as a powerful tool in understanding sub-volcanic plumbing systems (Davidson et al., 2005). Crystals growing from a magma respond, both chemically and texturally, to changes in the pressure, temperature, volatile content and chemical composition of the magma in which they are growing, and record these changes accordingly in their crystal-growth stratigraphy. Understanding the effects of these changes allows

the reconstruction and evaluation of magma plumbing systems.

In contrast to the direct insight that mineral compositions provide, whole-rock geochemical data tends to obscure many of these geochemical signals, as it represents the final product of crystal fractionation, accompanied by interaction with other magmas, inheritance of crystals from mushes, and assimilation of country rock or cognate cumulates. This means that while whole rock data provides important information on the final composition as an entire entity, it is not possible to accurately reconstruct magmatic histories without detailed petrography and assessment of mineral compositions.

Studies of crystals within rocks erupted from polygenetic volcanoes are common, however this strategy has been relatively under-utilised in investigating monogenetic volcanic centres, as it is often assumed these magmas have a simple source-to-surface pathway. An increasing body of work demonstrates that previously assumed simple monogenetic basaltic centres have surprisingly complex magmatic histories (Brenna et al., 2011; Jankovics et al., 2015, 2019; Re et al., 2017). Complex textures observed in Chapter 3 suggest this may also be true for TVZ basalt. This means that when assessing monogenetic basalt mantle source characteristics, as in Chapter 6, it is vital to first assess the level of processing the magma has undergone in the crust, and the effect this has on the primary mantle-derived signature. This is especially important when the basaltic eruptions in question are used to infer the mantle source characteristics of a much larger volcanic system, such as in the TVZ.

The TVZ is a 150km-long stretch of rifted continental arc stretching from White Island (Whakaari) in the north, to Mt. Ruapehu in the south and is one of the most productive silicic centres worldwide (Wilson and Rowland, 2016). Silicic volcanism is concentrated in the central TVZ, between (and including) Okataina Volcanic Centre in the north, and Taupo Volcanic Centre in the south. The central TVZ exhibits a bimodal style of volcanism, with >98% of erupted products being rhyolitic in composition, and <1% basaltic (Graham et al., 1995). Basalt occurs as monogenetic scoria cones and maars, along faults and caldera rims (Hiess et al., 2007), and is coeval with the

volumetrically dominant rhyolite. For this reason, basaltic compositions are often used as mafic end-member compositions when modelling rhyolite generation (Deering et al., 2010; Price et al., 2005; Rooney and Deering, 2014), as well as for inferring characteristics of the mantle source feeding the region (Rooney and Deering, 2014; Zellmer et al., 2020).

Recent studies (Barker et al., 2020; Zellmer et al., 2020) have identified changes in the composition of primary mantle melt in the TVZ between caldera-forming and non-caldera forming systems, where mafic magmas from caldera-forming centres are formed from larger degrees of mantle melting to those from non-caldera forming centres. In Zellmer et al. (2020), the change in magma flux, tracked through calculated melt F of the mafic rock, is interpreted as the driving force in the maturation of the system from pre-caldera-forming volcanism, to caldera-forming volcanism, to the eventual waning of the magmatic system. Large melt fractions sourced from shallow mantle are associated with caldera-forming volcanism, whereas melt fractions become smaller and melting occurs deeper as the mantle becomes progressively depleted, and this causes caldera-forming volcanism to wane (Zellmer et al., 2020). However, this model has not yet been explored in terms of its implications on magma storage and processing in the crust.

In this chapter we apply thermobarometric models to phenocrysts and melt to estimate storage temperatures and pressures, and use anorthite-melt equilibria to provide constraints on along-arc H_2O variation. Using these parameters we are then able to calculate liquid lines of descent (LLD) for the different crystal populations, to give provenance to phenocrysts and antecrysts, and assess this in terms of the maturation of the magmatic system in the TVZ.

4.3 Petrography and Mineral Chemistry

Back-scatter electron (BSE) images of prepared thin sections were captured for textural analysis according the methods outlined in Chapter 2.3. Quantitative analyses were obtained on a Cameca SX100 electron microprobe according to the methods outlined in Chapter 2.2. A minimum of five EPMA analyses of each phase were taken per population; for example a sample with two populations of plagioclase provided a minimum of five analyses for each population. This approach resulted in much larger datasets for some samples than others, but is considered necessary when tracing the magmatic history of distinct populations of phenocrysts and antecrysts.

4.3.1 Overview

Samples consist of olivine, clinopyroxene, plagioclase and Fe-Ti oxides, with rare orthopyroxene in silica-rich samples and Cr-Spinel as inclusions in some olivines. Samples range in crystallinity from aphyric to highly porphyritic to holocrystalline. Groundmass textures range from microcrystalline, composed of plagioclase + clinopyroxene + Fe-Ti oxides + olivine (in the lowest SiO_2 samples), to hypocrystalline, with up to 40% glass present in basaltic andesite samples. The only aphyric sample is from the 1886 deposit of Tarawera. In Orakeikorako sample, the only holocrystalline sample, there is only a small distinction between macrocryst and groundmass crystal size. Kakuki and Harry Johnson Rd are sparsely porphyritic, comprising approximately 10-15% macrocrysts. All other samples contain between 20 and 40% macrocrysts.

Crystal populations are easily identified from compositional zoning and texture, which is examined in full in Chapter 3. There are multiple populations of crystals for each major phase, and all samples contain a unique combination of these populations, with no two samples containing identical populations of all phases. However, the dominance of some phases and populations over others varies between pre-, syn- and post-caldera setting samples. These form groups that are present within multiple

deposits from a specific segment of the arc, hinting at a common origin. The changes in composition of plagioclase, olivine and clinopyroxene from north to south along the arc is shown in figure 4.1. The most striking feature is the presence of high anorthite plagioclase with low forsterite olivine, and low Mg# clinopyroxene in NC-TVZ samples, versus the presence of high forsterite olivine, high Mg# clinopyroxene and relatively low anorthite plagioclase in S-TVZ samples. BSE images and individual sample descriptions are presented in Chapter 3. Key populations are described in relation to their geographical classification below.

4.3.2 South TVZ

Samples from the S-TVZ contain olivine + clinopyroxene dominated mineral assemblages. The Ohakune sample additionally contains abundant orthopyroxene. Olivine is up to 2mm in diameter, and ranges in composition from Fo_{93-64}. The highest forsterite content olivine (>Fo_{90}) occurs in the cores of 8-10% of olivines in the Waimarino sample (Figure 3.9), suggesting a mantle or mantle-derived origin. This is investigated in Chapter 6. Low Ca contents (<1500ppm) across a range of forsterite contents in S-TVZ olivines is suggestive of a deep origin. Clinopyroxene is up to 2mm in length and is oscillatory zoned (Figure 3.9). Waimarino clinopyroxenes are the most primitive found in all samples, ranging in composition up to $Mg\#_{88}$ and Cr_2O_3 up to 0.96 wt.%. Ohakune clinopyroxenes have similar Mg# but lower Cr_2O_3. Both populations of clinopyroxene show a limited net change in Mg# until the rims, which are much more Mg poor. Orthopyroxene occurs in Ohakune as overgrowths of $Mg\#_{85-75}$ on Fo_{87-82} olivine. It also forms overgrowths on clinopyroxene (Figure 3.10), in addition to forming oscillatory zoned glomerocrysts with clinopyroxene, where compositional zones match between phases. An interesting feature of orthopyroxene in Ohakune is the presence of overgrowths on clinopyroxene, which itself is subsequently overgrown by a clinopyroxene rim, forming assemblages of clinopyroxene cores, large orthopy-

roxene mid regions, and thin clinopyroxene rims. In Waimarino, orthopyroxene only forms thin microcrystalline overgrowths of $Mg\#_{75-78}$ on olivine (Figure 3.9) of Fo_{74-84}. Plagioclase is only present as groundmass microlites and ranges in composition from An_{90-77}.

4.3.3 Central TVZ

Samples from the C-TVZ contain plagioclase and olivine dominated mineral assemblages. The Ongaroto sample is the most primitive and hosts only olivine as a macrocryst phase. Like the Waimarino sample from the S-TVZ, the highest forsterite content olivine (Fo_{91}) occurs in the cores of 8-10% of olivines in the Ongaroto sample (Figure 3.6), and has NiO and CaO contents suggestive of a mantle origin. Plagioclase is only present in the groundmass, showing similarity with the S-TVZ samples. Both Kakuki and Orakeikorako samples have plagioclase dominated mineral assemblages. The dominant plagioclase population is unzoned laths of An_{85-65} up to 250μm. Reverse zoned plagioclase crystals are less abundant and in the Orakeikorako sample range from An_{63-69} in crystal cores, and An_{75-82} in rims. In the Kakuki sample, reverse zoned plagioclase crystals have coarsely sieved spongy cores of An_{74-84} and rims of An_{80-87} (Figure 3.7). Olivine crystals range in composition from Fo_{85-42} and always show normal zoning. The most forsteritic of these compositions occurs as glomerocrysts with plagioclase in Kakuki (Figure 3.7), whereas the most fayalitic of these compositions only occurs as inclusions within plagioclase crystals in Orakeikorako.

4.3.4 Northern Central TVZ

Samples from the NC-TVZ have the most complex crystal cargoes and contain abundant plagioclase, clinopyroxene and olivine. Orthopyroxene occurs in two basaltic andesite samples (Terrace Rd and Rotomakariri). Plagioclase is the most common phase in NC-TVZ eruptions, and ranges in composition from An_{96-72} (Figure 4.1).

The dominant plagioclase population is unzoned laths of An_{88-71} up to 250μm. There is no correlation between the whole rock composition of samples and the anorthite content of the plagioclase. It is common for very different whole rock compositions to have very similar plagioclase phenocryst compositions. e.g. Harry Johnson Rd = SiO_2 = 50.5 wt.% MgO = 5.8 wt.%, An_{81-84}. Terrace Rd = SiO_2 = 55.5 wt.% MgO = 2.7wt.% An_{82-87}, implying that magma composition is not the primary factor controlling plagioclase composition. All NC-TVZ samples, with the exception of the Tarawera sample, contain a population of highly anorthitic plagioclase with groundmass composition rims (Figure 3.1, 3.3, 3.4 3.5). Cores of this population range from An_{92-96}, are 250-500μm in length and are compositionally homogenous. Olivine crystals are <200μm and mostly unzoned, but in some samples have a thin bright Fe-rich zone close to the rim before a reversely zoned Mg-rich rim. Compositions range from Fo_{85-42} and are consistent with a magmatic origin. Significantly larger olivine is present in Rotomakariri and is overgrown by orthopyroxene, clinopyroxene and high-anorthite plagioclase (Figure 3.3). These olivines have Fo_{82-75} and low CaO (<0.15 wt.%) indicative of a plutonic origin. Clinopyroxene ranges from $Mg\#_{87-65}$ (Figures 4.2, 4.1), and includes normal and reverse zoned populations (Figure 3.3, 3.4). Normal zoned clinopyroxene is <400μm in length, of $Mg\#_{80-85}$ with rims of $Mg\#_{70-75}$ (Figure4.2a). Reverse zoned clinopyroxene has cores of $Mg\#_{65-75}$, and outer zones of $Mg\#_{80-85}$ (Figure 4.2c, d). Sometimes clinopyroxene remains at elevated Mg# until the rim (Figure 4.2d), or returns to an intermediate Mg# (Figure 4.2c). A rare additional population is only present in Rotomakariri, and is similar to the primitive normal zoned population, but contains significantly elevated Cr_2O_3 concentrations (Figure 4.2b). Orthopyroxene is present in the basaltic andesite samples Terrace Rd and Rotomakariri. In Rotomakariri, orthopyroxene is present as thick overgrowths of $Mg\#_{78-66}$ on olivine of Fo_{85-74} (Figure 3.3). Orthopyroxene in the Terrace Rd sample is overgrown by thin rims of clinopyroxene (Figure 3.4).

4.3.5 Glomerocrysts and cumulates

Glomerocrysts and crystal clots are a common feature of all the porphyritic rocks. In NC-TVZ eruptions, the high anorthite plagioclase often occurs in clusters with lower-Fo olivine (<Fo_{85}). Lath-shaped phenocrystic plagioclase occurs with small unzoned phenocrystic clinopyroxene. In reversely zoned clinopyroxene, there is an absence of co-grown phases in the lower-Mg# cores, but the higher-Mg# mid and outer zones appear to be co-grown with high-anorthite plagioclase. Rotomakariri contains exceptional antecrystic clots containing all 4 main phases. Olivines form at the core, and are overgrown first by orthopyroxene, and finally high-Mg# clinopyroxene and high-anorthite plagioclase (>An_{90}). (Figure 3.3). Glomerocrysts of phenocrystic plagioclase and olivine, similar to the phenocrystic clots in the NC-TVZ, are found in Kakuki. In the S-TVZ samples, glomerocrysts similar to the Rotomakariri antecrystic clots are found, in which olivine is overgrown by clinopyroxene (Waimarino), or clinopyroxene and orthopyroxene (Ohakune). These overgrowths form the oscillatory zoned clino- and orthopyroxenes described above.

4.4 Mineral-Melt equilibria

All mafic samples clearly show a diverse range of textures and mineral compositions, indicating that there are multiple magmas assembling and contributing to the final eruption of each, consistent with the interpretation of oxygen isotope data in Chapter 5. Consequently, there is a poor correlation between crystal composition and whole rock composition (Gamble et al., 1993; Hiess et al., 2007). This, combined with a lack of quenched glass from most deposits makes assessing mineral-melt equilibria difficult, although this is necessary in order to identify phenocrysts from antecrysts.

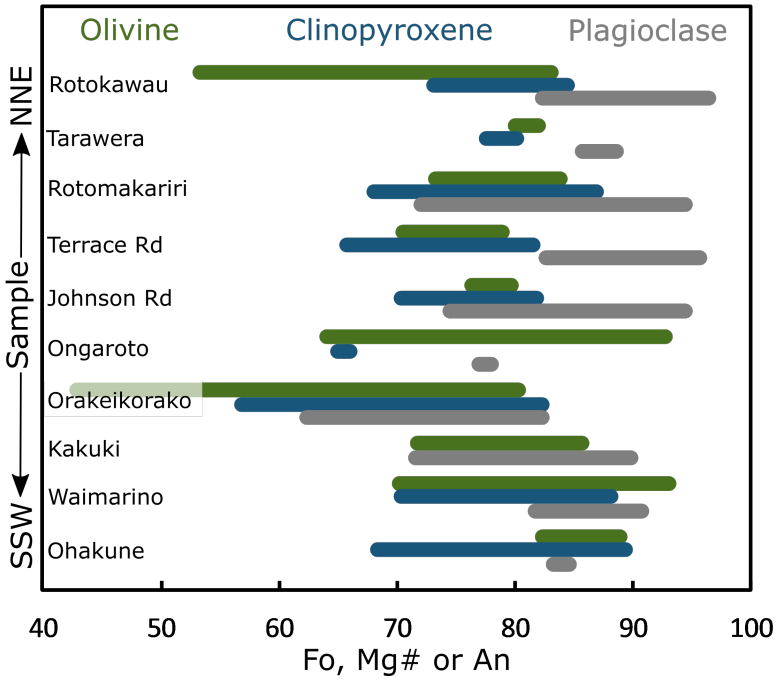

Figure 4.1: Total range of compositions (cores and rims) of olivine, clinopyroxene and plagioclase analysed, arranged by eruption from NNE to SSW.

.

4.4.1 Pyroxene-melt equilibria

Equilibrium between clinopyroxene and whole rock was assessed using a Fe-Mg exchange coefficient of 0.27 +/- 0.07 (Sisson and Grove, 1993b) (Figure 4.3a). In the absence of glass for most samples, whole rock data is the best approximation for groundmass composition. The clinopyroxene cargo for each sample is very diverse, with most samples displaying a range of 20 mol.% Mg#. Clinopyroxene Mg# does not correlate with the Mg# of the whole rock, and somewhat flatlines across the entire range of whole rock Mg#s (Figure 4.3a), with an approximate average of $Mg\#_{79}$.

However, the WR Mg# is susceptible to change proportionally with the amount of Fe-Mg bearing antecrysts it has inherited. Waimarino, Ohakune and Ongaroto contain antecrystic olivine, resulting in high WR Mg#s for these samples. Inheriting 15% olivine of Fo_{90} results in a 20 mol.% shift towards higher Mg#, explaining the apparent disequilibrium between clinopyroxenes and WR in HMB and HMBA samples. These

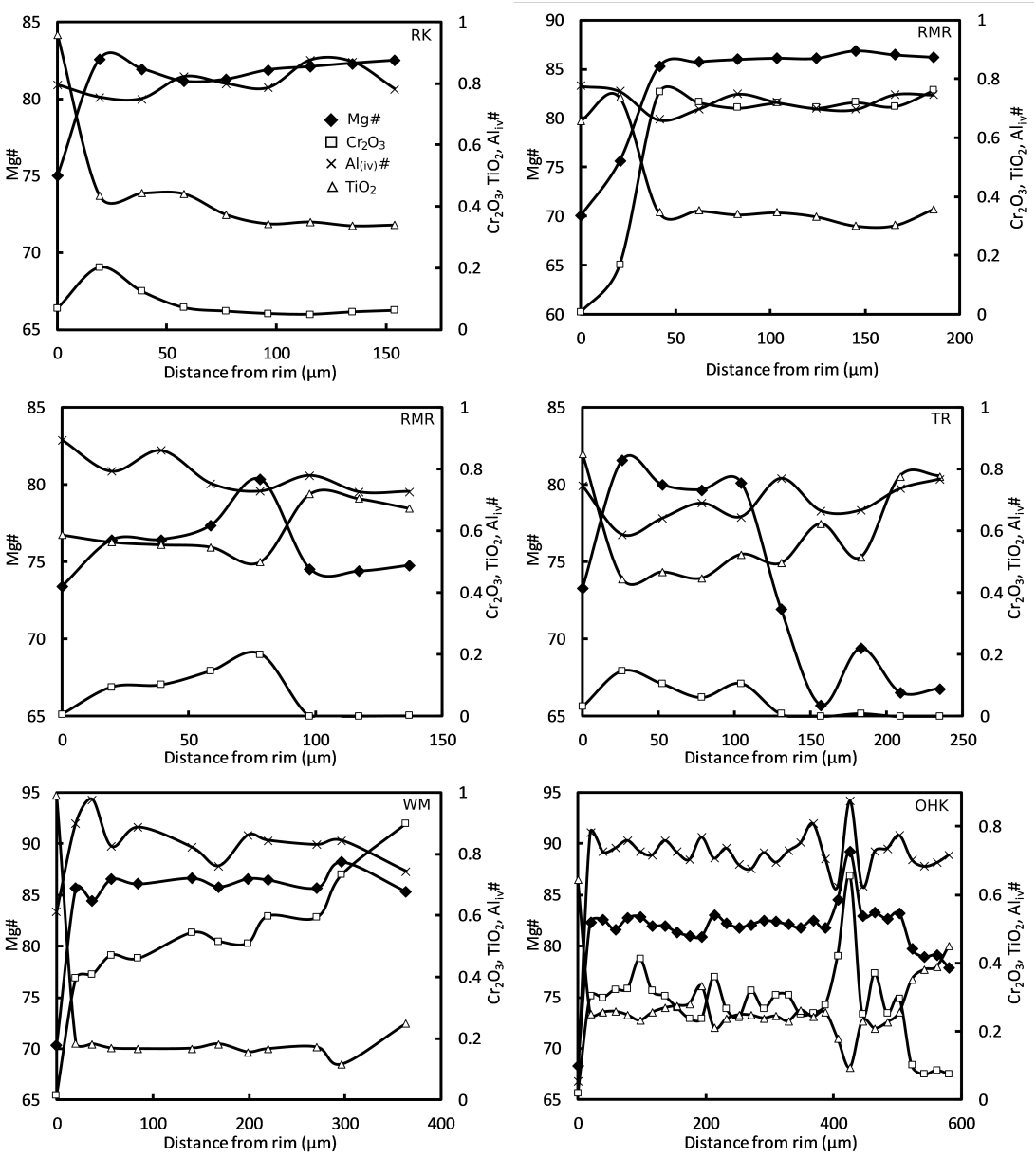

Figure 4.2: Compositional profiles of selected clinopyroxenes. RK = Rotokawau; RMR = Rotomakariri; TR = Terrace Road; WM = Waimarino; OHK = Ohakune. Errors are smaller than symbols. Mg# = Mg/(Mg+Fe)*100. $Al_{(iv)}$# = $Al_{(iv)}/(Al_{(iv)} + Al_{(vi)})$*100.

.

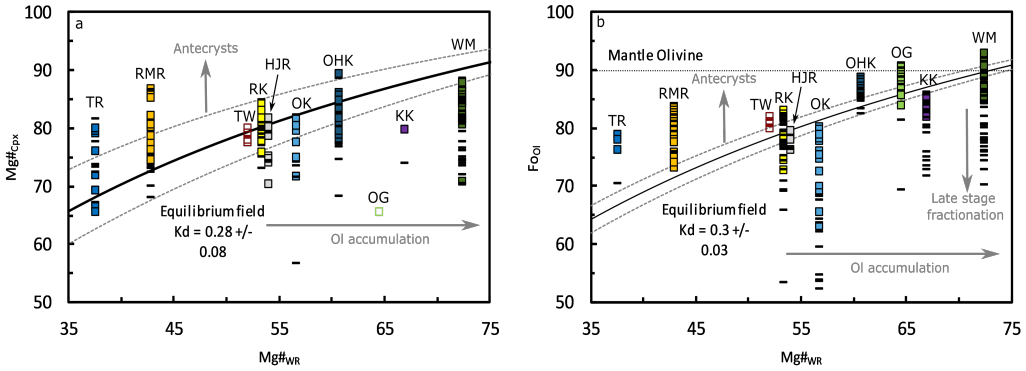

Figure 4.3: A) Predicted equilibria between olivine and melt, K_D=0.3 +/- 0.03 (Roeder and Emslie, 1970). B) Predicted equilibria between clinopyroxene and melt, K_D=0.28 +/- 0.08 (Putirka, 2008; Sisson and Grove, 1993a). Dashed lines represent upper and lower bounds for K_D values.

clinopyroxenes from Waimarino and Ohakune are often oscillatory zoned, possibly recording influxes of high Mg# material shifting the WR composition towards higher Mg#. This possibility is explored in section 4.5.1. Although other samples show evidence of inheriting mafic antecrysts (e.g. reverse zoned clinopyroxenes, clinopyroxenes with significantly higher Mg#), they are not common enough to cause a significant shift in WR Mg#. Tarawera is the only sample that spans a narrow range of clinopyroxene composition, and is entirely in equilibrium with the whole rock (Figure 4.3a).

Samples at lower whole rock Mg#, i.e. those on the left side of figure 4.3a, are only in equilibrium with the lowest Mg# clinopyroxene population. Terrace Rd, at the lowest WR Mg# only has crystal cores in equilibrium with the WR Mg#, all crystal rims would be in equilibrium with melt with significantly higher Mg#. Additionally, a significant proportion of clinopyroxene is too high Mg# to have crystallised from a melt with such low Mg#, suggesting that the crystal cores of the reversely zoned crystals are most similar to the bulk composition, yet a large proportion of the crystal cargo reflects growth from a more primitive magma (Figure 4.3a). Rotomakariri contains both normal and reverse zoned clinopyroxene and is similar to Terrace Rd, with the addition of the 3rd, highest Mg (high Cr) population, and a higher WR Mg# (Figure 4.2). All of the high Mg#, low Cr population have similar compositions to Rotokawau

and Harry Johnson Rd clinopyroxenes, and most would be in equilibrium with the WR Mg# of Rotokawau or Harry Johnson Rd (Figure 4.3a). This, and the presence of only high Mg# clinopyroxene with normal zoning in Rotokawau, suggests that a magma similar in composition to Rotokawau or Harry Johnson Rd could produce the high Mg# populations from other NC-TVZ samples (Rotomakariri and Terrace Rd), and potentially represents a mafic end member for this group of eruptions.

4.4.2 Olivine-melt equilibria

Like the plagioclase and clinopyroxene cargo, the olivine cargo of the TVZ is exceptionally diverse. Using an Fe-Mg exchange coefficient of 0.3 ± 0.03 (Roeder and Emslie, 1970; Sisson and Grove, 1993b), most olivines are not in equilibrium with the WR composition (Figure 4.3b). Using the whole rock composition for assessing olivine equilibria is affected in the same way as for clinopyroxene equilibria described above. Hence, the diversity in Ongaroto and Waimarino is explained by addition of xenocrysts and accumulation of phenocrysts, whilst other eruptions (Rotomakariri, Terrace Rd) require inheritance of forsteritic magmatic antecrysts to explain their most primitive olivines. These populations of olivine would be in equilibrium with melts of $Mg\#_{61}$ and $Mg\#_{54}$, respectively. The remaining samples with olivines too forsteritic for the host rock are likely early formed, and have become out of equilibrium as the magma has evolved. The only eruption that requires mixing of another melt that contains olivine is in low-forsterite plagioclase-hosted olivine inclusions in Orakeikorako. All other crystals are normally zoned, where Fe rich rims are likely a result of evolving melt compositions during ascent and eruption.

4.5 Discussion

It is clear from observing the textures recorded in crystals, and examining mineral-melt equilibria, that the crystal cargo of the monogenetic deposits studied is diverse. Magmatic processes occurring in the crust, such as crystal fractionation, magma mixing, and intrinsic variables, such as the pressure and temperature at which these processes occur, are recorded by the crystal cargo. Fe-Mg diffusion in olivine is rapid, and so many of these compositional signals become blurred during later magmatic processes. However, in clinopyroxenes and plagioclase, diffusion occurs at a much slower rate, and so the preservation potential of these minerals for recording magmatic history is much greater. Clinopyroxene is ubiquitous in the samples studied, and so here, clinopyroxene compositions are used to assess crystal fractionation and magma mixing processes.

Additionally, clinopyroxene-melt equilibria and clinopyroxene-orthopyroxene equilibria are sensitive to the pressure of crystallisation. The equilibrium portion of the clinopyroxene cargo is used to provide constraints on the depths and temperature of crystallisation for each sample. Estimation of H_2O content using plagioclase-liquid equilibria requires accurate estimates of temperature (Lange et al., 2009). By generating independent estimates of temperature and pressure from clinopyroxenes, this is inputted into models estimating H_2O content (Waters and Lange, 2015) from plagioclase-liquid equilibria. This allows comparison between changes in P, T and H_2O conditions of basaltic magma storage in the context of their spatial and temporal position in the arc.

4.5.1 Magmatic processes recorded in clinopyroxene

Crystal Fractionation and Magma Mixing

Clinopyroxenes display a strong positive correlation between Mg# and Cr_2O_3 (Figure 4.4). Composition varies both between deposits and within single eruptions and crystals. To test whether clinopyroxene compositions between samples or populations could

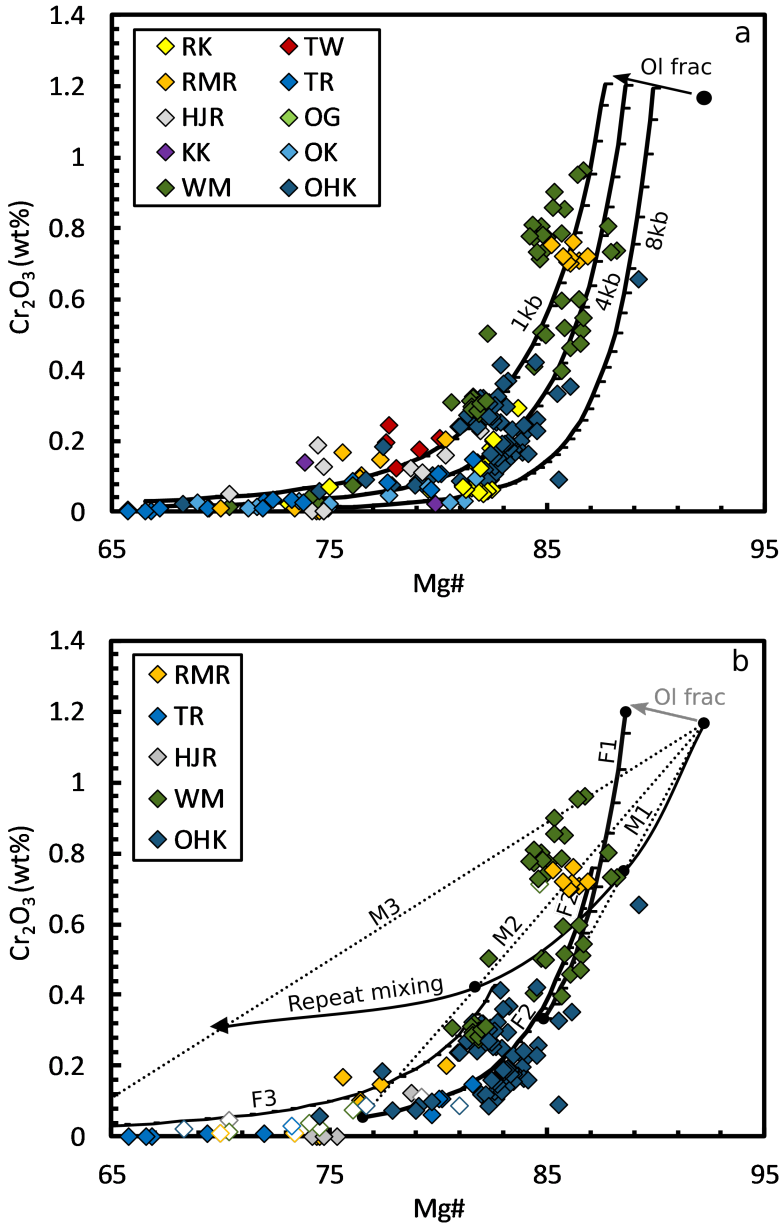

Figure 4.4: Mg# of clinopyroxenes vs Cr_2O_3 (wt.%). A) All clinopyroxene data. Trajectories are fractionation lines modelled at 1, 4 and 8kbar in *Petrolog* (Danyushevsky and Plechov, 2011). B) Only clinopyroxenes containing reverse zoning are plotted. Trajectories show the effect of repeated alternate episodes of pyroxene fractionation and magma mixing. F1, F2, F3 = Fractionation episode 1, 2, 3, respectively. M1, M2, M3 = Mixing epsiode 1, 2, 3, respectively. Repeated mixing line is constructed from point of the primary magma composition, 50% mixing along M1, 33% mixing along M2, 25% mixing along M3 etc. to represent decreasing effect of magma recharge on a fractionating magma chamber.

be explained by crystal fractionation, we conducted forward models of crystallisation using *Petrolog* software (Danyushevsky and Plechov, 2011).

Models were run using a starting composition of a 1:1 ratio mix of a natural near-primary HMB (Elthon and Scarfe, 1984), and a modelled composition based on 5% melting (Asimow et al., 2001; Hirschmann et al., 1998) of DMM (Workman and Hart, 2005), and is listed in Table 4.1 (PMM). Mineral-melt partition coefficients of 0.83 and 10 were used, for Cr in olivine and clinopyroxene, respectively. These were calculated from an average of published partition coefficients in basalt compositions from the GERM K_D database. Fractionation models were run at 1, 4, and 8kbar (Figure 4.4a), to incorporate the effect of pressure on clinopyroxene chemistry. Olivine co-crystallises in the model, as the starting composition is olivine normative, and so will always fractionate some olivine prior to clinopyroxene. This is consistent with petrological observations of olivine followed by clinopyroxene fractionation (Gamble et al., 1990). Lowering the pressure of fractionation increases the proportion of olivine fractionation prior to crystallisation of clinopyroxene, resulting in lower Mg# clinopyroxene at lower pressure (Figure 4.4a). Since Cr is moderately incompatible in olivine, initial Cr concentrations in clinopyroxene increase slightly with decreasing pressure and increasing proportion of prior olivine crystallisation. Fractionation at variable pressure somewhat explains the variation in clinopyroxene chemistry observed in the samples suite studied, and this is explored further in section 4.5.1. However, as some eruptions contain reverse and oscillatory zoned clinopyroxene that cross cut these trajectories multiple times, simple crystal fractionation, even at variable pressure, cannot explain this.

Reverse zoned (NC-TVZ - Rotomakariri, Terrace Rd, Harry Johnson Rd), and oscillatory zoned (S-TVZ - Waimarino, Ohakune), clinopyroxene compositions cannot be explained by crystal fractionation alone. Figure 4.4b shows these clinopyroxenes. To explore the idea that the reverse zoning is caused by variation in magma composition we ran models of repeating alternate episodes of crystal fractionation and magma mixing. All models were run at 4kbar, however it is worth noting that increasing or decreasing

Table 4.1: **Input compositions for *Petrolog* models**

	HMB [a]	**5% Melt** [b]	**PMM** [c]
SiO_2	48.03	44.05	47.21
TiO_2	0.59	1.02	0.59
Al_2O_3	13.01	14.89	13.69
Fe_2O_3	2.44	1.64	1.99
FeO	6.68	7.90	7.17
MnO	0.16	0.19	0.17
MgO	16.74	14.57	15.38
CaO	9.77	13.41	11.38
Na_2O	1.47	1.59	1.50
K_2O	0.54	0.20	0.37
P_2O_5	0.21	0.21	0.20
Cr_2O_3	0.35	0.35	0.34
Total	99.99	100.00	99.99

[a] Elthon and Scarfe (1984)
[b] Workman and Hart (2005), Asimow and Ghiorso (1998), Ghiorso and Sack (1995)
[c] Calculated from a 1:1 ratio of HMB : 5% melt.

the pressure would result in similar trends at higher and lower Mg#s, respectively. The initial fractionation model is the same as the 4kbar model in figure 4.4a. At 200°C intervals during fractionation runs, a fresh batch of magma of the initial composition was added. The volume of the fresh batch of magma is assumed to be the same as the initial volume, and so is mixed in a 1:1 ratio, to produce a mixed magma composition. This mixed composition is fractionated and subsequently mixed. For each subsequent recharge event, the ratio of fresh magma to frationated magma decreases (i.e. 1:2, 1:3, 1:4), and so the influence of the recharge event decreases with each iteration. The alternate episodes of fractionation (F) and mixng (M) are numbered in order in figure 4.4b). In F1 and F2, the mixed magma first produces olivine before clinopyroxene, resulting in the offset of the fractionation line from the mixing line (Figure 4.4). This model is not a unique solution to all clinopyroxene compositional variation, where magma recharge volumes and fractionation rates likely vary between episodes and between samples. However, this model does effectively reproduce the reverse

zoning patterns observed in clinopyroxenes, with individual crystals of clinopyroxene plotting along up to all 3 of the fractionation lines, and shows that influx of multiple batches of primary magma into fractionating basaltic magma in the crust produced the compositional zoning observed in the clinopyroxenes. Clinopyroxene from the S-TVZ (Waimarino and Ohakune) is more primitive and generally plots at higher Mg# and Cr than NC-TVZ clinopyroxene, reflecting crystallisation from a more primitive magma than clinopyroxenes from Harry Johnson Rd and Terrace Rd samples. S-TVZ clinopyroxene also records multiple episodes of magma recharge, as seen in oscillatory zoning patterns (Figure 3.9 3.10), whereas only one magma recharge event is recorded in the reverse zoned clinopyroxene from the NC-TVZ (Figure 4.2). Highly primitive and normally zoned clinopyroxene such as those found in Rotomakariri sample may represent crystals formed in equilibrium with the primitive recharging melt.

Pyroxene thermobarometry

Fractionating mineral assemblages change systematically between S-TVZ, C-TVZ and NC-TVZ basalt, and this likely reflects systematic changes in magma storage conditions in the crust. Clinopyroxene dominates assemblages from the S-TVZ, whereas plagioclase dominates both C-TVZ and NC-TVZ assemblages, suggesting deeper storage of S-TVZ magma. Geophysical observations infer thickening of the lithosphere in the south TVZ towards Ruapehu and Ohakune (Stern et al., 2006), and thinning of the lithosphere associated with rifting in the central TVZ (Hurst et al., 2016; Stern et al., 2006, 2010). Fractional crystallisation and magma mixing modelling has also revealed that multiple populations of clinopyroxene are present in the samples, suggesting polybaric storage of magma.

Although mineral assemblages vary, clinopyroxene is nearly ubiquitous, allowing for clinopyroxene-melt and two pyroxene thermobarometry to investigate relative changes in magma storage between the three segments. The barometer of Neave and

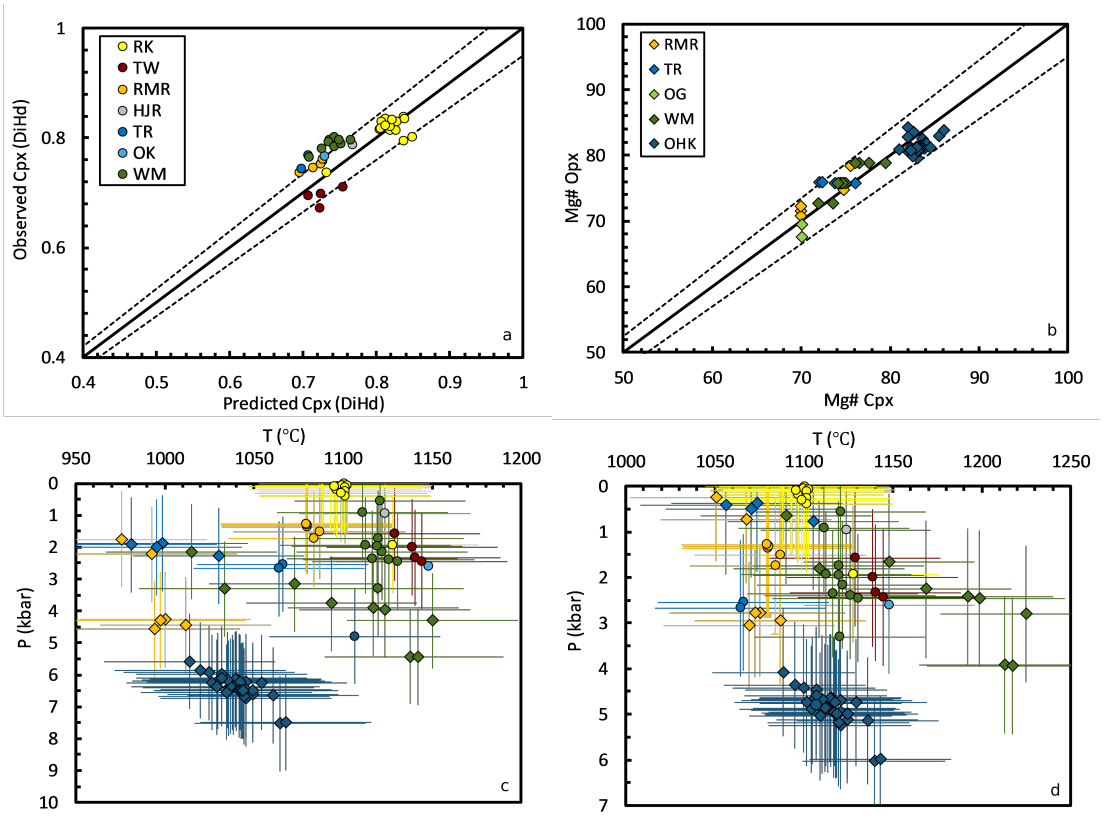

Figure 4.5: Thermobarometry results from selected clinopyroxene melt pairs and clinopyroxene orthopyroxene pairs. Only pairs in equilibrium were selected. A) Predicted clinopyroxene DiHd from melt composition vs. observed clinopyroxene DiHd component. B) Mg# clinopyroxene vs. Mg# orthopyroxene. C) Pressure vs. temperature of selected pairs. Errors are from the accuracy of thermometer/barometer used. D) Pressure vs. temperature of selected pairs, with two pyroxene pairs corrected for systematic offset between models - See text for details.

.

Putirka (2017), which is calibrated between 1 atm and 20 kbar, was used for clinopyroxene melt pairs, using an input temperature from Putirka (2008) (equation 33). Equation 39 from Putirka (2008) was used for orthopyroxene-clinopyroxene pairs, using an input T from equations 36 or 37 dependent on the Mg# of the clinopyroxene (Putirka, 2008). In all cases, only equilibrium pairs were used to assess temperature and pressure. Equilibrium was assessed by Fe-Mg exchange coefficients for two pyroxenes, and by predicted vs observed clinopyroxene components between clinopyroxene and melt, where only those within 95% confidence intervals were used (Figure 4.5a, b). In samples where both orthopyroxene and glass is absent (Rotokawau, Tarawera, Harry Johnson Rd, Orakeikorako), whole rock compositions (Gamble et al., 1993) were used for clinopyroxene-melt models. This was considered appropriate for these samples as their whole rock compositions reflect equilibrium with a significant proportion of the clinopyroxene crystal cargo (Figure 4.3b), and are not skewed by large proportions of olivine or pyroxene accumulation such as Ongaroto, Waimarino and Ohakune. In the cases of Ongaroto, Waimarino and Ohakune, the two-pyroxene thermobarometer of Putirka (2008) was used. This thermobarometer is based on Enstatite-Ferrosilite partitioning between the clino- and orthopyroxene. In Ohakune, co-grown oscillatory zoned ortho-clinopyroxene glomerocrysts allowed for detailed assessment of temperature and pressure of crystallisation across the grain stratigraphy.

The clinopyroxene-melt barometer (eq.39) of Putirka (2008) has an accuracy of +/- 2.8kbar, whereas the newer calibration of Neave and Putirka (2017) increases accuracy to +/- 1.3kbar. Neave and Putirka (2017) also highlight that previous barometers tend to overestimate pressure by up to 1.5kbar. This is evident in our barometry results, showing a systematic offset between the predicted pressure of clinopyroxene-liquid models and two-pyroxene models of consistently approximately 1.5kbar (Figure 4.5c & d). Therefore, we corrected the two-pyroxene results from Putirka (2008) to be consistent with pyroxene-liquid results. This was achieved by measuring the offset between the results from the same sample predicted by both methods, as an internal standard. The

samples that had pressures calculated by both methods were Rotomakariri, Terrace Rd, Ohakune and Waimarino. Pressures were consistently overestimated by 1.5kbar and approximately 70°C using the two-pyroxene method, and so corrected accordingly (Figure 4.5d).

Despite the inherent error involved in this approach, some comparative conclusions can be drawn from pyroxene thermobarometry. Ohakune consistently plots as the deepest stored magma, at approximately 5-6 kbar, which is consistent with barometry results from Kósik et al. (2016). Temperatures are cool in comparison to the broad positive trend displayed by the other magmas (Figure 4.5d). Deeper storage in the crust for the Ohakune magma is consistent with the presence of low Ca contents of olivine in the sample, also suggestive of a plutonic origin. Waimarino, despite having texturally similar clinopyroxene to Ohakune, plots at shallower depths and hotter temperature. This hotter temperature may suggest that the Waimarino magma was erupted at a more primitive stage in the overall inferred magmatic evolution, consistent with the high Cr_2O_3 content of pyroxenes (Figure 4.4), and previous suggestions that Waimarino could be a parental composition to south TVZ magmas (Graham and Hackett, 1987). Shallower crystallisation depths explain the dominance of olivine over orthopyroxene fractionation in comparison to Ohakune. Waimarino also displays a wide range in predicted temperature and depth of fractionation, possibly associated with the timing of orthopyroxene crystallisation. This is a groundmass phase or on olivine rims, indicating it was late stage and, therefore, likely associated with cooling and/or decompression.

Samples from the NC-TVZ display a range of conditions, from 0-4kbar and 1000-1200°C. Rotomakariri and Terrace Rd, which overall host very similar crystal cargoes show two populations: a deeper (4kbar) population and a shallower (<2kbar) population. This is unlikely to be an artefact as two depths are recorded using a single method, corresponding with the two populations observed in clinopyroxenes from these samples. Lower Mg# ($<Mg\#_{70}$) clinopyroxene and orthopyroxene show crystallisation at greater depths, followed by higher Mg# compositions ($>Mg\#_{75}$) at approximately 2 kbar.

Rotokawau and Harry Johnson Rd both show only 1 population of clinopyroxene, and plot at similar depths to the higher Mg# population of clinopyroxene from Rotomakariri and Terrace Rd, consistent with similarities in their composition. Tarawera is within error of the other NC-TVZ eruptions, but suggests slightly hotter and deeper conditions, consistent with other estimates of a slightly deeper source for Tarawera magma than other OVC basalt (Cole et al., 2014).

4.5.2 Origin of high-anorthite plagioclase

High anorthite plagioclase is unique to NC-TVZ samples and is absent from C-TVZ and S-TVZ samples. Within NC-TVZ samples, high-anorthite plagioclase occurs over a wide range of whole rock composition, suggesting that melt composition is not the primary control on the anorthite content of plagioclase. NC-TVZ basalt has a strong subduction signature in trace element compositions, leading to the suggestion that NC-TVZ magma is more hydrous (Barker et al., 2020; Rooney and Deering, 2014) in comparison to C-TVZ or S-TVZ magma (Bégué et al., 2015; Kilgour et al., 2013). It is possible that high H_2O content in the melt may be the cause of high-anorthite plagioclase. Melt H_2O can be estimated from anorthite content and melt or whole rock composition, at a given pressure and temperature (Waters and Lange, 2015). As high-anorthite plagioclase and clinopyroxene commonly occur together in glomerocrysts in HAB samples, temperatures calculated from clinopyroxene thermometry are applicable also to plagioclase. Calculated temperatures and H_2O contents are reported in table 4.2. Two-pyroxene thermometry was used for HMB and HMBA samples. Orthopyroxene crystallisation occurs late on in HMB magmas, at a similar stage to plagioclase. As two-pyroxene thermometry under-predicts temperature and the predicted H_2O content is inversely proportional to temperature, the calculated water contents will therefore provide a maximum estimate for these samples. Results show that NC-TVZ plagioclase requires significantly higher melt H_2O than C-TVZ and S-TVZ plagioclase (table 4.2.

H2O shows a broad positive correlation with WR SiO_2, but with considerable scatter, implying that at least some of the variation in H_2O reflects primary magma variation, in agreement with Barker et al. (2020) and Rooney and Deering (2014).

Table 4.2: **Sample locations and ages, and parameters used for modelling plagioclase equilibrium in figure 4.6.** Error in the temperature calculations was propagated through to water content calculations to give upper and lower limits of H_2O content. L.P = Late Pleistocene.

Eruption	H_2O [a]	(U) [a]	(L) [a]	T (°C) [b]	T (U) [b]	T (L) [b]	Segment	Age [c]
Rotokawau	2.9	3.5	2.3	1097	1139	1055	NC-TVZ	3.4ka
Tarawera	2.3	2.9	1.9	1138	1180	1096	NC-TVZ	1886AD
Rotomakariri	3.3	4	2.7	1050	1092	1008	NC-TVZ	22-28ka
Terrace Rd	3.9	4.6	3.3	1062	1104	1020	NC-TVZ	L.P
Johnson Rd	2	2.6	1.4	1145	1187	1103	NC-TVZ	L.P
Ongaroto	0.2	0.8	-0.3	1144	1187	1103	C-TVZ	80ka
Orakeikorako	1.8	2.4	1.2	1152	1194	1110	C-TVZ	L.P
Kakuki	0.1	0.9	-0.5	1150	1200	1100	C-TVZ	L.P
Waimarino	1.2	1.9	0.6	1114	1159	1069	S-TVZ	17.5ka
Ohakune	1.8	2.5	1.1	1033	1075	991	S-TVZ	31.5ka

[a] Calculated using plagioclase-melt hygrometer of Waters and Lange (2015).
[b] Calculated using the Cpx-melt thermometer of Putirka (2008) for all samples, except Ongaroto where the Cpx-Opx thermometer was used.
[c] Hiess et al. (2007) and references therein

As the Ca/Na ratio between plagioclase and glass is a function of H_2O (Sisson and Grove, 1993a), estimating H_2O allows us to assess whether all plagioclase in a population is in equilibrium with the groundmass Ca/Na ratio. H_2O contents were used to calculate a Ca/Na exchange coefficient for each melt, based on a linear relationship between the 2, 4 and 6 wt. % H_2O K_D values from Sisson and Grove (1993a), along with upper and lower limits for these values, propagated from the uncertainty in temperature calibrations. The K_Ds calculated from this are shown in figure 4.6, and show the upper and lower limits of equilibrium plagioclase compositions at the maximum and minimum H_2O. For aphyric samples, we can assume that whole rock composition is a reasonable analogue for the groundmass composition. However, for samples containing abundant macrocrysts, whole rock composition requires a correction for Ca/Na due to presence of highly calcic plagioclase. Groundmass values, plotted in figure 4.6, were

calculated by taking whole rock Ca/Na ratios of the same samples from Gamble et al. (1993), and applying a mass balance correction for incorporation of antecrystic high Ca/Na plagioclase. The exception to this was in Rotomakariri (BA) and Ohakune (HMBA), where groundmass glass was directly analysed. These samples allow for comparison between using the whole rock vs. the glass composition, and show that whole rock data gives a wider range of possible equilibrium values than glass, and gives a maximum limit for predicting crystals that are in equilibrium. Therefore any plagioclase crystals with Ca/Na higher than predicted by whole rock Ca/Na must be antecrystic. We acknowledge inherent uncertainty in the approach taken, arising from the uncertainty in temperature calculation, and in the absence of analysable glass from the samples. However, figure 4.6 clearly shows a distinction between equilibrium plagioclase, and plagioclase that and either requires much higher H_2O concentrations in the melt, or a much higher Ca/Na of the melt, i.e. a much more primitive magma.

Most plagioclase rims are in equilibrium with the inferred range of groundmass values (Figure 4.6). Some groundmass values extend to lower Ca/Na than predicted, but fall within the expected range if the H_2O content is reduced towards zero, indicating that crystallisation of these rims could have simply occurred during degassing of the magma, i.e. during magma ascent. The only eruption where plagioclase is entirely out of equilibrium with the groundmass is Ongaroto. A possible explanation for this is that the groundmass in this deposit is coarsely crystalline (plagioclase laths 50-200μm), and a large proportion of plagioclase in the groundmass would increase the whole rock Ca/Na. Cores from Waimarino, Ohakune, Orakeikorako and most cores in Kakuki are also in equilibrium with the groundmass for the given H_2O, consistent with textural features such as relatively homogenous plagioclase crystal cargoes.

All eruptions from the NC-TVZ, with the exception of Tarawera, contain a population of highly calcic plagioclase with Ca/Na 12-25, which cannot be in equilibrium with either the whole rock or calculated groundmass composition (Figure 4.6). These plagioclases have compositions implying crystallisation from a melt with considerably

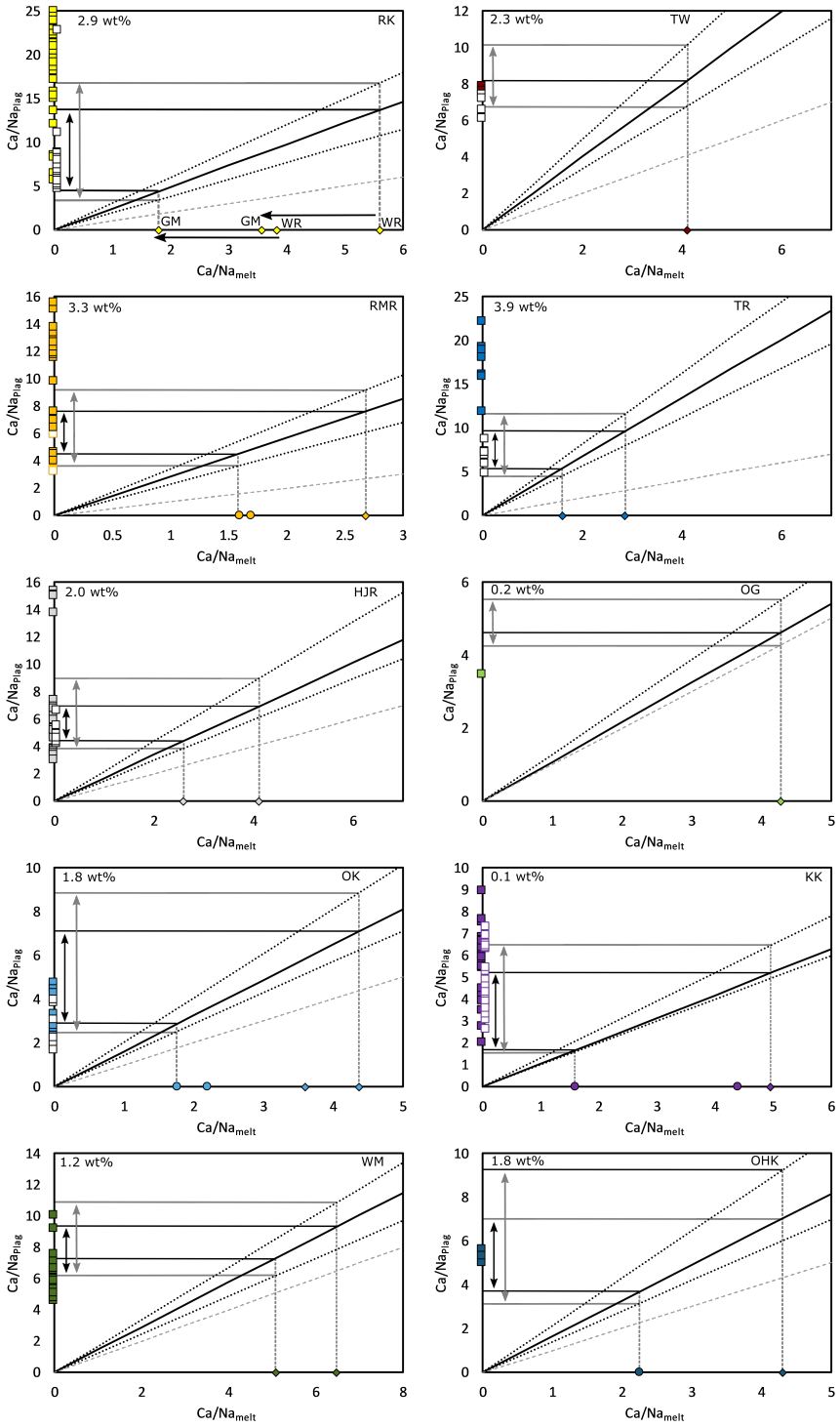

Figure 4.6: Ca/Na melt vs. Ca/Na plagioclase. Plagioclase = squares. Cores = filled, rims = white. Circles = Ca/Na from groundmass glass. Diamond = Whole rock Ca/Na from Gamble et al. (1993). Where more than one diamond is present, the lower Ca/Na value has been corrected for inheritance of high Ca/Na antecrystic plagioclase in the whole rock analysis. Solid black lines are constant K_D Ca/Na for the calculated wt.% of melt H_2O from Waters and Lange (2015). Stippled lines are the maximum and minimum constant K_D Ca/Na calculated from the maximum and minimum melt H_2O. Dashed line is a 1:1 line representing dry conditions (Sisson and Grove, 1993a).

higher H_2O content for the given groundmass composition, and/or a more primitive, higher Ca/Na melt for a constant H_2O content.

If the highly calcic cores are the result of previously higher melt H_2O, and not from a more calcic melt, the H_2O content would need to have exceeded 5wt.% for Rotokawau and Harry Johnson Rd. Predicted H_2O for Rotomakariri and Terrace Rd lies outside of the Sisson and Grove (1993a) calibrations, but can be extrapolated to be approximately 8-9 wt.%. H_2O >6 wt.% for primitive basaltic magma would be amongst the highest H_2O contents reported globally, and considering that H_2O from melt inclusions in cognate rhyolites in the TVZ are <5.5 wt.% (Bégué et al., 2015), this seems improbable. Instead, if plagioclase cores are from a more primitive melt, their composition requires crystallisation from a melt with a Ca/Na ratio of 5-8. A primary arc-type high-Mg basalt has Ca/Na of 7.5 (Elthon and Scarfe, 1984) meaning that the highest Ca/Na cores (Rotokawau), may additionally require at least a small increase in melt H_2O. However high degrees of fractional melt are able to increase the Ca/Na of a primary melt (Neave et al., 2019) and a 5% batch melt of DMM (Workman and Hart, 2005; Hirschmann et al., 1998) has a Ca/Na of 9.4 (Table 4.1). Considering the TVZ sources magma from both an arc and decompression component of melting, it is possible that the primary magma had a higher Ca/Na than a typical primary arc high-Mg basalt, negating the requirement for a higher than predicted melt H_2O. This model is preferred, as large increases in H_2O suppress the saturation point of plagioclase, implying that H_2O of the magma cannot be significantly higher than the concentrations predicted. Higher than predicted magma H_2O contents would also increase the stability of clinopyroxene relative to plagioclase, in turn lowering the Ca/Na of the melt and also promoting HAB compositions by concentrating Al_2O_3 in the melt. Additionally, the anorthite content of plagioclase is known to decrease by approximately 1 mol.% for every 1kbar increase in pressure (Fram and Longhi, 1992), suggesting the highest anorthite plagioclase must form at shallow depths.

Therefore it is most likely high anorthite plagioclase cores crystallised from hydrous,

but water undersaturated, near-primary melts, with limited or no prior clinopyroxene crystallisation (<10%) in the shallow crust (<5kbar). Scenarios in which this is possible have been constrained by phase relations and fractional crystallisation experiments of near-primary high-Mg basalts (Elthon and Scarfe, 1984; Feig et al., 2010; Gust and Perfit, 1987; Hamada and Fujii, 2008). Olivine followed by plagioclase before clinopyroxene crystallisation occurs at shallow (2-4kbar), moderately hydrous (1-4 wt.% H_2O) conditions. We suggest that this is the most likely scenario for the crystallisation of the NC-TVZ high-anorthite plagioclase.

4.5.3 Modelling P-T-H_2O conditions of primitive crystal clots

Rotokawau, Harry Johnson Rd, Terrace Rd, Rotomakariri and Kakuki all contain glomerocrysts of co-grown primitive plagioclase with olivine and/or clinopyroxene, indicating they formed simultaneously from the same magma. This allows calculation of the Mg# and Ca/Na of the magma at a given point of crystallisation. This section attempts to reproduce the compositions of these glomerocrysts by modelling the liquid line of descent (LLD) of a primary magma, which changes as a function of pressure of crystallisation, and H_2O content of the primary magma. Models were run using *Petrolog* software, using the model of Putirka (2005) (olivine), Plechov and Gerya (1998) (plagioclase), and Danyushevsky (2001) (clinopyroxene), all of which are suitable for modelling hydrous systems.

The Mg# and Ca/Na at any given point of the melt is sensitive to pressure, and H_2O content, as both these factors exert a major control on the assemblage fractionating from the melt. As both Ca and Na are incompatible in olivine, olivine crystallisation has the effect of reducing the Mg# of the melt without affecting the ratio of Ca/Na in the melt. Plagioclase crystallisation has little effect on the Mg# of the melt, but alters the Ca/Na ratio of the melt, proportional to the anorthite content of the crystallising plagioclase. Clinopyroxene has the ability to simultaneously alter the Mg# and Ca/Na

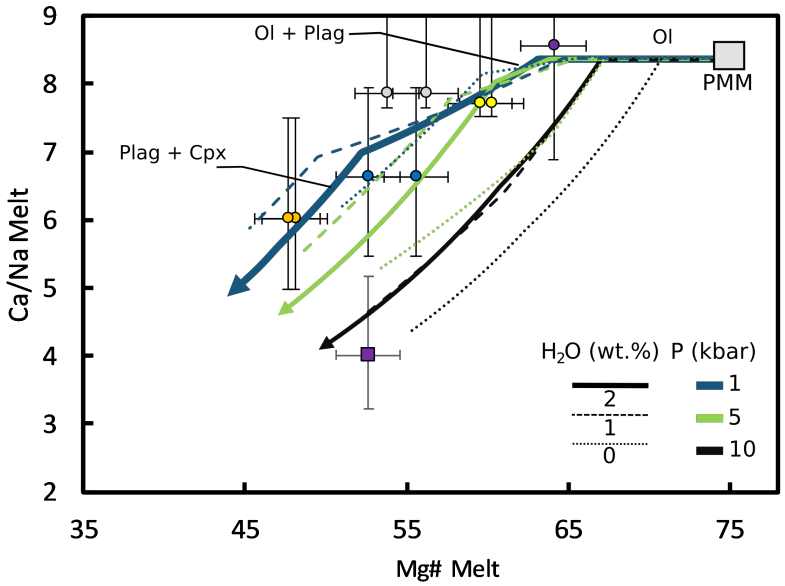

Figure 4.7: Predicted Mg# of melt based on highest Fo and Mg# olivine and pyroxene, respectively, Vs. the predicted Ca/Na ratio of the melt based on the highest anorthite plagioclase and models from figure 4.6. PMM = Primitive Mantle Melt and is a 1:1 mixture of a primitive high-Mg basalt typical of an arc setting (Elthon and Scarfe, 1984) and a 5% batch melt from the depleted MORB mantle (Workman and Hart, 2005) modelled using MELTS software (Asimow and Ghiorso, 1998; Ghiorso and Sack, 1995), to represent a likely rifted arc starting magma composition. Starting compositions are listed in Table 4.1. Fractionation lines are modelled using *Petrolog* software (Danyushevsky and Plechov, 2011), and represent the liquid line of descent at different pressures and H_2O concentration. Errors bars are propagated from uncertainty in H_2O content (Ca/Na) and uncertainty in K_D on Fe-Mg exchange (Roeder and Emslie, 1970; Putirka, 2008). Lower Ca/Na limit estimates are used for Harry Johnson Rd and Rotokawau, as standard estimates result in Ca/Na ratios higher than the PMM composition can produce. sample colours are the same as figure 4.6.

ratio of the melt, and hence altering the stability of clinopyroxene relative to olivine and plagioclase will result in significant changes in the LLD. Adding H_2O to the system has the effect of destabilising plagioclase relative to clinopyroxene and olivine, whilst reducing the pressure of a system has the effect of destabilising clinopyroxene relative to olivine and plagioclase.

Crystallisation of a dry magma at high pressure (10kbar) produces a LLD that promotes early crystallisation of clinopyroxene and plagioclase, relative to shallower or more hydrous models (Figure 4.7a). This LLD does not produce the observed assemblages or mineral compositions, and crystallises a maximum of An_{84} plagioclase, implying that either lower pressure or higher H_2O contents are required to explain the full range of observed compositions. The melt compositions required by the coarsely sieved plagioclase antecryst with clinopyroxene inclusions from Kakuki, is closely matched by a similarly high pressure LLD with 2 wt.% starting melt H_2O. Mineral compositions are most closely matched by a 7kbar LLD, giving An_{80} plagioclase and $Mg\#_{79}$ clinopyroxene. For all other glomerocrysts, only shallow (<5kbar) and or hydrous (>1 wt.%) LLD match melt compositions required. Kakuki represents the most primitive point of all predicted melt compositions. Of the models run, the best fit is at 2 wt.% H_2O and 5kbar, which produces An_{88} plagioclase and Fo_{87} olivine at plagioclase saturation. This estimate of H_2O is higher than estimates based on Waters and Lange (2015), but is most likely due to poor temperature constraints for this sample, as highlighted in section 4.5.2. Higher anorthite contents at lower forsterite contents can be achieved by reducing the pressure of the model. For Kakuki, 1kbar produces far too anorthite-rich compositions, so it is likely that the true pressure of crystallisation is >1 and <5kbar. The melt compositions required by NC-TVZ glomerocrysts are reproduced well by low pressure (<1kbar) and hydrous (2 wt.% H_2O in primary melt) conditions. At plagioclase saturation, this model produces An_{92} plagioclase, and Fo_{86} olivine. However, continued crystallisation to clinopyroxene saturation, which is the final phase on the liquidus at these conditions, produces an

assemblage of An_{94} plagioclase, Fo_{81} olivine, and $Mg\#_{81}$ clinopyroxene, which closely matches the most primitive end member compositions from all of Rotokawau, Terrace Rd, Harry Johnson Rd and Rotomakariri samples. This is a good fit for these samples and shows that crystallisation of the melt that produced the high-An plagioclase must have been hydrous, but water-undersaturated, and stored at very shallow depths in the crust. Notably, continued fractionation of olivine and plagioclase increase the H_2O content of the melt, whilst simultaneously decreasing the Ca/Na ratio. This has the effect of buffering the anorthite content of the plagioclase, and is a possible explanation for the observed compositional homogeneity in the high-anorthite cores of the NC-TVZ eruptions.

4.5.4 Mantle source characteristics

A significant trend is that crystal cargoes of NC-TVZ magmas require higher water contents than those from the central and south TVZ. Evidence for higher magmatic water contents at Okataina Volcanic Centre vs Taupo Volcanic centre has attracted considerable attention (Barker et al., 2020; Bégué et al., 2015; Deering et al., 2012; Rooney and Deering, 2014; Zellmer et al., 2020). Increases in melt water content may arise from increased fluid fluxing from the slab beneath the area of the NC-TVZ (Barker et al., 2020; Rooney and Deering, 2014). This may be due to compositional variation in the slab itself (Barker et al., 2020; Rooney and Deering, 2014), or due to the depletion of fluids after extensive volcanism in the area of the Taupo Volcanic Centre (Zellmer et al., 2020). Alternatively a constant fluid flux across the TVZ but an uneven base of the lithosphere may promote migration of fluids along arc, and pooling in areas of most rifting. Shallowing of fluid-induced seismicity at the base of the crust from Ruapehu northwards to Taupo supports this idea (Reyners et al., 2007). Currently it is not possible to directly constrain the cause of the increased fluids in the mafic eruptions of the NC-TVZ. However, observed mineral assemblages in our primitive

samples support the hypothesis that the NC-TVZ is more hydrous than elsewhere in the TVZ, and that an increase in water is from primary magmas sourced from the mantle, as opposed to any crustal processes such as assimilation of hydrous crust.

4.5.5 Pre, syn and post-caldera variations in magma storage

Some arc systems transition from typical andesitic volcanism during the early stages of magmatism, to silicic volcanism as the system matures (Bachmann et al., 2007; de Silva et al., 2006; de Silva and Gregg, 2014). This is especially apparent in the TVZ, where andesitic volcanism is considered precursory to rhyolitic volcanism (Price et al., 2005) and the transition is associated with rifting of the lithosphere (Deering et al., 2011a). Large-scale silicic systems take time to thermally mature, and are dependent on episodic magma emplacement rates (Annen, 2009, 2011), where rates of magma intrusion into the crust need to be sufficiently high to sustain silicic magma generation (Annen et al., 2015).

Zellmer et al. (2020) calculated mantle fertility and depth of melt segregation for a similar suite of samples to those in this study. Results suggested that the depth of mantle melting increases with time, whereby large melt fractions in the shallow mantle contribute towards feeding caldera forming eruptions. With progressive melting the mantle source region becomes more depleted and melting occurs deeper, so that eruptions that are currently situated in inter-caldera locations tap mantle that has already experienced extensive depletion and arise from small, relatively deep batches of mantle melt. This has important implications on the storage conditions of mafic magma in the TVZ, in terms of both the thermal maturation of the system in response to the waxing and waning of magma fluxes from the mantle, and the complexity of the magma plumbing system the mafic magmas are intruded into at any point during the maturation process.

The south TVZ represents pre-caldera system magma storage, the NC-TVZ samples

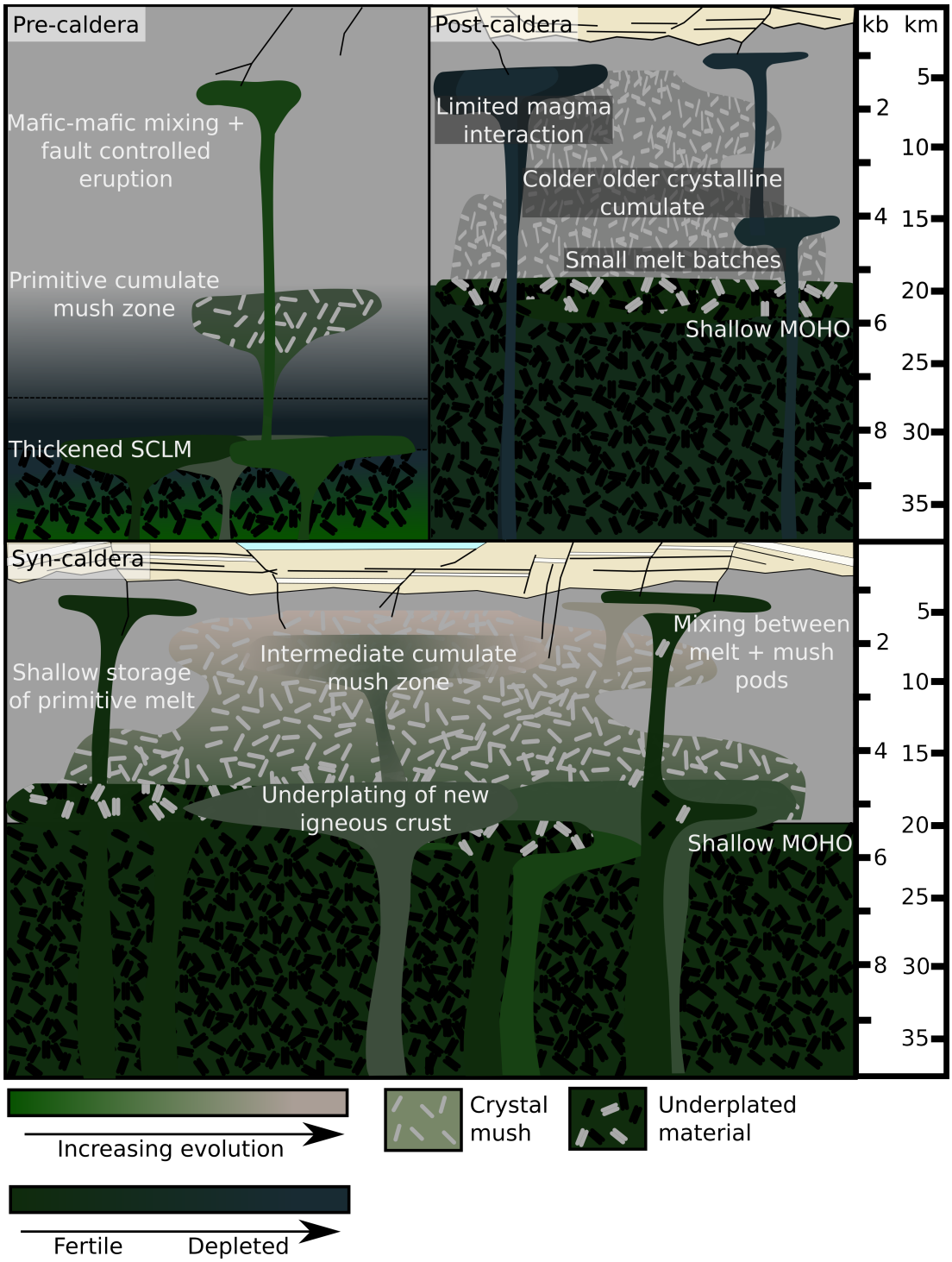

Figure 4.8: Cartoon illustrating lifespan of TVZ caldera systems and influences on basalt magma storage. Model of transcrustal magma system adapted from Cashman et al. (2017), depth of mush zones for syn-caldera setting from Cole et al. (2014), depth of MOHO and thickened SCLM for pre-caldera setting from (Stern et al., 2006).

represent mantle melts from a currently active, well developed caldera system (syn-caldera), and the central TVZ samples represent magma storage in a post-caldera system (Figure 4.8). This makes it possible to review the crystal cargoes of these samples in terms of their spatial and temporal context within the TVZ. For clarity it is worth noting that post-caldera samples here are referred to as inter-caldera basalts in Barker et al. (2020), and that basalts erupted synchronously with the development of the Taupo volcanic centre would also be representative of a syn-caldera system, but in this instance, all central TVZ samples are representative of a post-caldera setting (Zellmer et al., 2020).

The south TVZ is dominated by HMB and HMBA mafic rocks. Waimarino and Ohakune samples have contrasting whole rock compositions, but are related through elevated MgO content at a given SiO_2 (Gamble et al., 1993; Graham and Hackett, 1987). Their clinopyroxene cargoes are texturally similar, although the Waimarino cargo records substantially more primitive compositions (Figure 4.4). Both record multiple episodes of magma recharge prior to eruption (Figure 4.4b). This explains elevated MgO contents of the samples, which arises due to mixing with primitive or primary magmas, and in the case of Waimarino, also due to inheritance of highly forsteritic olivine xenocrysts (Figure 3.9). Waimarino records hot and shallow fractionation (Figure 4.5), similar to Ongaroto in the central TVZ, implying similarities between the two distal HMB samples. Ohakune, at the southern tip of the TVZ, records much deeper fractionation than any other deposit (Figure 4.5) (Kósik et al., 2016). Volcanism ceases south of Ruapehu and Ohakune, it's most southern satellite vent, where the crust thickens and subduction shifts towards a transpressional regime, which inhibits mantle flow (Reyners et al., 2007). As the arc is propagating southwards Ohakune coincides with the thickest and non-rifted portion of crust (Hurst et al., 2016; Reyners et al., 2007; Stern et al., 2006), promoting deeper storage of magma (Figure4.5.5). This is also reflected in the presence of low-Ca olivine in the crystal cargo (Chapter 6), and the dominance of two-pyroxene crystallisation over olivine, indicative of deeper

plutonic storage within the crust. There is no apparent link between deeper storage of magma and proposed depths of melt segregation in the mantle (Zellmer et al., 2020). However, crystals appear to be sourced from deep primitive mush regions within the crust, and ascended rapidly with little interaction with evolved melts or shallow crust. Eruptions are products of multiple batches of primary magma (Figure 4.4), evidenced by oscillatory zoned clinopyroxene, but importantly this is not overprinted inheritance of antecrysts or mixing with more evolved melts in the shallow crust. We suggest that this is linked to the relative immaturity of the plumbing system in the south TVZ, where rhyolitic volcanism has not yet developed (Price et al., 2005), meaning there are less evolved magma mush bodies to interact with on transit through the crust.

The NC-TVZ samples have the most complex crystal cargoes of all the mafic rocks. All eruptions from the NC-TVZ require shallow fractionation for their most primitive end-member glomerocrysts, which are connected through similar storage conditions and magmatic histories. Estimations of 1kbar crystallisation for the high anorthite antecrysts correspond to depths of <5km. Despite the similarities in some crystal populations, all the NC-TVZ samples come from different eruptions, at different vents and at different times. This indicates that an external factor controls fractionation for these eruptions. This control may be structural or tectonic, and is unique to Okataina caldera and the surrounding area, as this population of plagioclase is not found elsewhere in the TVZ. The estimations made on fractionation depths for NC-TVZ basalts are consistent with estimations of fractionation depths for Okataina Volcanic Centre (OVC) rhyolites (Cole et al., 2014). Overall, storage of magma at OVC is considered to be shallow (Cole et al., 2014), whereby crystal fractionation forms mush zones at 8-12km depth (Deering et al., 2010, 2011b). Melt is periodically extracted and stored at higher levels (3-8km) as laccolith or sill-like pods prior to eruption. The only eruption in the NC-TVZ that does not show any evidence of such shallow storage is the 1886 Tarawera basalt, which requires pressures of 3kbar, corresponding to depths of approximately 9km. This is consistent with direct extraction from this intermediate level mush zone,

and fits with previous estimations of melt storage and transport for the 1886 Tarawera eruption (Cole et al., 2014). The estimations of magma storage based on plagiclase and olivine glomerocrysts are also consistent with studies of electrical resistivity. Heise et al. (2010) show that at OVC, beneath Mt. Tarawera, electrical conductivity increases at approximately 10km depth. Their study also shows a zone of high conductivity at very shallow depths of <3km below lake Rotokawau, consistent with the differing depths of fractionation calculated from their crystal cargoes.

Both Terrace Rd and Rotomakariri eruptions require an element of deeper fractionation, from clinopyroxene - orthopyroxene pairs in Terrace Rd, and the low-Ca olivine with orthopyroxene overgrowths in Rotomakariri antecrysts (Figure 3.3, 3.4). These are overgrown by the same population of high An plagioclase as the other eruptions, suggesting that the final stages of growth occurred in similar conditions as the other NC-TVZ eruptions. These deeper stored phases may originate from the intermediate level mush zone (Cole et al., 2014), as discussed above. However, differences in chemistry, notably the high Cr population of clinopyroxene in Rotomakariri implies that these eruptions sample antecrysts derived from variably primitive mushes deeper in the complex plumbing system.

Overall, the complexity within NC-TVZ samples makes each eruption unique, inheriting one or more discrete populations of antecrystic material from a variety of depths, and making the compositions of end-member magmas contributing to the final erupted composition almost impossible to identify. Barker et al. (2020) analysed melt inclusions from 3 samples from Okataina Volcanic Centre, which fall within our category of NC-TVZ eruptions, to show that intra-caldera eruptions are sourced from large degrees (10-30%) of flux and decompression driven mantle melting. This corroborates the suggestion from Zellmer et al. (2020) that eruptions associated with active caldera-forming volcanism are sourced from larger melt fractions than those in post-caldera settings. Our observations from examining antecrysts in the NC-TVZ is that large volumes of magma promote transition from the early style volcanic system as

seen in the south TVZ, into a mature trans-crustal magmatic system (Cashman et al., 2017), where magma bodies are stored as mushes and distinct but variably connected 'pods' in the crust (Figure 4.8). Repeated intrusion of hot mafic magma into this system may promote remelting of these pods and drive eruption of more evolved magma (Cole et al., 2014). Therefore, although monogenetic eruptions of the NC-TVZ are most closely associated with primary magmas feeding the caldera-forming systems, they also have the most complex plumbing framework en-route to the surface, and are much more likely to have these primary signatures obscured by crustal processes. This is consistent with the interpretation of oxygen isotope data in Chapter 5.

Crystal cargoes from the central TVZ show the least diversity of all the samples studied. However, there is still compelling evidence for multiple batches of magma contributing to the final erupted product. The late Pleistocene Ongaroto deposit is the most primitive collected in this study, and perhaps in the TVZ, fractionating only olivine. It is indicative of high temperatures and low pressures of fractionation (Figure 4.5), and less hydrous conditions than those of the NC-TVZ (Figure 4.7). Chapter 6 show that olivines within monogenetic mafic eruptions record multiple magma recharge events, demonstrating that even the most primitive magmas have complicated plumbing histories. Basalt-basalt mixing retains the primitive nature of the magma, and as in the south TVZ, these signatures are preserved in erupted products due to an absence of the type of mixing with cognate mushes noted in the NC-TVZ. The Kakuki sample contains only olivine and plagioclase, which we have determined to have fractionated in the upper portions of the crust, with addition of evolved, sieved and reversely zoned plagioclase and clinopyroxene originating from >15km depth. Plutonic crystals must have been transferred along with a similarly primitive melt, or transferred with minimal magma, given the primitive whole rock composition of Kakuki (48 wt.% SiO_2) (Gamble et al., 1990). In addition, the nearby deposit of Orakeikorako has very similar whole rock major element composition, and yet contains reversely zoned crystal populations spanning a much larger compositional range. However, overall, these eruptions are the

simplest in terms of their crystal cargo. We suggest this is associated with smaller and deeper fractions of melt, resulting from melting of the mantle in a post-caldera system (Figure 4.8). Contrary to eruptions from the NC-TVZ, these are the easiest to trace back to their primary magma compositions, but are associated with primary melts related to a post caldera setting, contrasting the mantle melting regime that drives rhyolitic volcanism (Barker et al., 2020).

Although there is no direct link between melt segregation depths in the mantle and depth of crystallisation in the crust, we find that magma storage depth broadly correlates with thickness of the overlying lithosphere (Chapter 1.3). This in turn is proportional to the amount of rifting that has occurred at any individual point along the arc, which controls mantle productivity and, therefore, maturation of the system into a fully developed transcrustal magma system, capable of forming large-volume silicic eruptions (Cashman et al., 2017).

4.6 Conclusions

Monogenetic vents from along the TVZ have erupted high-Mg basalts, high-Al basalts and high-Mg basaltic andesites, with high-Al basalts prevalent in the NC-TVZ and high-Mg basalts and high-Mg basaltic andesites prevalent in the south TVZ. Monogenetic deposits almost ubiquitously contain a range of glomeroporphyritic textures, with mineral assemblages also systematically varying from NNE to SSW. Textural and compositional complexities within minerals suggests that inheritance of crystals and cognate crystal mush is a significant process operating to form and assemble the erupted magmas. HABs contain plagioclase dominated mineral assemblages, whereas HMBs and HMBAs contain olivine and clinopyroxene dominated mineral assemblages. Orthopyroxene is present in basaltic andesites regardless of whether they are high-Mg or high-Al. Evidence for disequilibria, such as abrupt zonation, sieve textures and overgrowth or corona textures are abundant in all crystal cargoes. Samples from the

south TVZ require relatively dry crystallisation conditions, consistent with measured volatile contents from melt inclusions (Kilgour et al., 2013). The two samples measured however require different storage conditions, whereby Waimarino requires hotter and shallower conditions than Ohakune, which is located at the very southern end of the zone. The deep storage conditions required at Ohakune likely reflect the local tectonic regime, where thickened lithosphere inhibits ascent of primitive magmas to the shallow crust (Stern et al., 2010). These samples are representative of primitive magma compositions in a pre-caldera forming setting. Samples from the central TVZ also require relatively dry conditions of crystallisation, but record different fractionation patterns to south TVZ magmas. Ongaroto, which is the only HMB present in the central TVZ records conditions of crystallisation more similar to Waimarino, and is reflective of it's primitive nature. Overall these are the simplest basalts sampled in terms of their crystal cargo, and reflect small volumes of melt erupted from a largely drained magmatic system. NC-TVZ samples contain the most complex crystal cargoes from the whole arc, and are the only samples studied here that represent the primitive portions of a magma system driving caldera-forming volcanism. The presence of $>An_{90}$ plagioclase crystals requires higher concentrations of H_2O, and very shallow storage in the crust. Multiple populations of clinopyroxenes, sourced from variable depth is consistent with each deposit being formed from multiple batches of magma within the crust. Ultimately NC-TVZ mafic eruptions reflect the shallowing of the magmatic system with ongoing rifting, in addition to the thermal maturation of the NC-TVZ into a well-developed trans-crustal magma system (Cashman et al., 2017).

Chapter 5

Oxygen isotope variability in relation to the waxing and waning of the silicic magma system

5.1 *Foreword*

The following chapter has been submitted to *Journal of Petrology* for publication. The submission is titled: **Along-arc variation in monogenetic mafic magmas from the Taupo Volcanic Zone, New Zealand: Insights from the crystal cargo and oxygen isotopes**. For this reason, there is some unavoidable repetition between the *Methods* section in this chapter, and Chapter 2. Figures referring to petrological observations included in the submitted manuscript are omitted, and refer to the more in-depth petrology in Chapter 3. The text has remained the same as the submitted manuscript.

Chapter 4 showed that the petrogenesis of the mafic rocks is more complex than initially assumed. This chapter builds on the work in Chapter 4 and uses δ^{18}O to examine variations in crustal assimilation and crystal remobilisation between the mafic rocks from different eruptive centres.

5.2 Introduction

A key question in volcanology is understanding how and why some magmatic systems evolve to produce large volumes of eruptible silicic magma, and others do not. One of the main controls is the flux rate of magma over time (Annen, 2009; Annen et al., 2006, 2015). This must be sufficiently high in order to accumulate large bodies of partially molten material, as opposed to forming fully solidified plutons. The Taupo Volcanic Zone (TVZ) New Zealand, is dominated by high-silica magmatism, often resulting in large-volume explosive eruptions, and is one of the most volcanically productive silicic systems worldwide (Wilson et al., 1995b). It is unique in its tectonic setting as an actively rifting continental arc (Wilson and Rowland, 2016), where magma generation is driven by the addition of fluid fluxed from the subducted slab, and by decompression from rifting. The TVZ is one of the clearest examples of maturation of a magmatic system, where the shift from andesitic continental arc-type volcanism to rhyolitic volcanism is both spatial and temporal (Deering et al., 2011a). The arc is propagating southwards with time, and is split into north, central and southern segments (Figure 1.2). Andesitic volcanism is precursory to rhyolitic volcanism in the TVZ (Price et al., 2005) and dominates the south TVZ (S-TVZ), where the onset of volcanism is more recent in comparison with the central TVZ (C-TVZ). The thermally mature central TVZ is dominated by voluminous eruptions of rhyolite magma (>98% total erupted volume) alongside volumetrically minor eruptions (<1% total erupted volume) of basalt (Graham et al., 1995). Primitive mafic rocks from monogenetic scoria cones and maars are often used to infer characteristics of the mantle source region (Barker et al., 2020; Rooney and Deering, 2014; Zellmer et al., 2020).

Recent studies (Barker et al., 2020; Zellmer et al., 2020) have identified changes in the composition of primary mantle melt in the TVZ between caldera-forming and non-caldera forming systems. Specifically, mafic magmas from caldera-forming centres are formed from larger degrees of mantle melting than are those from non-caldera forming

centres. Zellmer et al. (2020), interpreted the change in magma flux, tracked through calculated melt fraction represented by the mafic rocks, as the driving force in the maturation of the system from pre-caldera-forming volcanism, to caldera-forming volcanism, to the eventual waning of the magmatic system. Large melt fractions sourced from shallow mantle are associated with caldera-forming volcanism, whereas melt fractions become smaller and melting occurs deeper as the mantle becomes progressively depleted, eventually causing caldera-forming volcanism to cease (Zellmer et al., 2020). The implications of this model on magma storage and processing in the crust have not yet been explored. Isotopic variation between basalt and andesite in the TVZ requires assimilation of basement Torlesse Terrane (Price et al., 2015) metagreywackes (Blattner et al., 1996; McCulloch et al., 1994; Price et al., 2005). However, the isotopic variation between andesite and rhyolite requires either closed system fractionation (Blattner et al., 1996; McCulloch et al., 1994) or partial melting of andesite composition plutonic material (Price et al., 2005) to generate rhyolite compositions. These trends in whole-rock data lead to a broad model explaining the compositional differences between basalt, andesite and rhyolite. However, where new models imply that flux of magma into the TVZ varies through the lifespan of a caldera-forming system (Zellmer et al., 2020), it is important to consider the effect this has on open vs. closed system processes and magmatic evolution. As the magmatic system matures, the relative importance of fractional crystallisation and crustal melting should vary, as the basement crust is modified by repeated intrusion of magma (Hutchison et al., 2018). This maturation of the system can be evaluated through measuring compositional changes that arise from addition of crust, such as the oxygen isotopic composition (δ^{18}O).

This study aims to examine crustal assimilation through measuring the δ^{18}O of crystals and groundmass in mafic rocks from pre-, syn- and post caldera settings in the TVZ. Oxygen isotopes are a powerful tool for assessing assimilation of continental crust, because they are largely unaffected by the small volumes of contamination that occurs in the mantle wedge in arc environments. However, the insensitivity of δ^{18}O

and the susceptibility of $^{143}Nd/^{144}Nd$ and $^{87}Sr/^{86}Sr$ to mantle source contamination from the subducted slab, makes the combination of these isotope systems a powerful tool in assessing source contamination. Here, we evaluate source contamination by integrating our new oxygen isotope dataset with published whole rock $^{143}Nd/^{144}Nd$ and $^{87}Sr/^{86}Sr$ (Gamble et al., 1993). We then use mineral-melt equilibria to assess the extent of crustal assimilation, magma mixing and crystal remobilisation, and draw comparisons between the different magmatic segments of the arc.

5.3 Sampling Strategy and Methods

Samples of mafic rocks were taken from lava flows and pyroclastic deposits along the length of the arc. Sample locations are shown in Figure 1.2, and coordinates are listed in Table 2.1. The sample sites are divided into categories based on their geographic location along the arc. The sites from the northern portion of the central TVZ (NC-TVZ) are associated with the currently active Okataina Volcanic Complex (OVC). The exception to this is from Harry Johnson Road, located south west of OVC, but this shows most similarity with other NC-TVZ samples. The NC-TVZ deposits sampled are: Rotokawau (RK), Tarawera (TW), Rotomakariri (RMR), Terrace Road (TR), and Harry Johnson Road (HJR). Mafic rocks from the central portion of the central TVZ (C-TVZ) and are not associated with a currently active caldera complex, but were erupted after and through older Whakamaru (350ka) ignimbrites. These are Ongaroto (OG), Kakuki (KK) and Orakeikorako (OK). Rocks sampled from the south TVZ (S-TVZ) are associated with andesitic volcanism, which is considered precursory to rhyolitic volcanism in the maturation of the TVZ volcanic system (Browne et al., 1992; Price et al., 2005). These are Waimarino (WM) and Ohakune (OHK). Previous studies provide a whole-rock geochemical database for the samples including major element, trace element and isotopic data (Blattner and Reid, 1982; Gamble et al., 1990, 1993; Hiess et al., 2007; Kósik et al., 2016). The present study provides a

significantly expanded oxygen isotope dataset on the mafic rocks, and a brief textural and compositional summary of the crystal cargo, linking the isotopic data to crystal populations within the rocks.

For textural analysis back-scatter electron (BSE) images of prepared thin sections were captured on a Zeiss Sigma field-emission gun (FEG) scanning electron microscope (SEM), using an accelerating voltage of 20 kV. Semi-quantitative analyses were recorded using an energy dispersive spectrometer (EDS) to define crystal populations by composition as well as visual characteristics. The instrument was calibrated using a cobalt standard, and a constant working distance of 7 mm was used. Quantitative analyses of mineral phases were obtained on a Cameca SX100 electron microprobe. Analysing conditions are reported in Chapter 2 and secondary standards are reported in appendix A.1.

For oxygen isotope analysis, bulk samples were lightly crushed to separate crystals from groundmass, and sieved into size fractions (125-250μm, 250-500μm and 500μm-1mm) to separate out populations of crystals with contrasting size. Aliquots (1-2mg) of phases were hand-picked to select unaltered and unbroken crystals. δ^{18}O analysis of microcrystalline to glassy groundmass and mineral separates was carried out at the Scottish Universities Environmental Research Centre (SUERC) by laser fluorination following the method of Sharp (1990) modified for ClF_3 (Macaulay et al., 2000). Mineral separates were pre-fluorinated overnight to remove any clay alteration on minerals and environmental adsorbed water from the sample chamber and line. As glass is more reactive in ClF_3, groundmasses were pre-fluorinated for 1 hour. Standards were run at the beginning, end and mid point of each block of 12 analyses, and reproducibility was typically better than 0.14‰ reported in standard notation as permil variations relative to VSMOW. A full description of the laser fluorination technique is included in Chapter 2, alongside standard values.

5.4 Results

5.4.1 Sample Characterisation

Samples range in composition from high-Al basalt (HAB) to high-Mg basalt (HMB) to high-Mg basaltic andesite (HMBA) (Gamble et al., 1990, 1993; Hiess et al., 2007; Kósik et al., 2016). HAB is prevalent in the NC-TVZ and C-TVZ in syn-caldera and post-caldera settings, whereas HMB and HMBA are prevalent in the S-TVZ where caldera-forming volcanism is yet to develop. Samples have variable crystal content, ranging from aphyric to porphyritic (>30% crystals). Macrocryst assemblages, and their crystal compositions, are highly variable between samples (Table 5.1). Olivine and clinopyroxene dominate HMB macrocryst assemblages, with the addition of orthopyroxene in HMBA, whereas plagioclase is the dominant phase, with minor pyroxene and olivine in HAB (Table 5.1) in agreement with observations of Gamble et al. (1990). Samples contain many xenoliths and xenocrysts. These are ultramafic and plutonic in origin in the S-TVZ, comprising coarse-grained olivine + clinopyroxene +/- orthopyroxene (Figure 3.9, 3.10). In OHK, the crystal clots comprising the xenoliths are the only macrocrysts present, whereas HMB sample WM appears to contain ultramafic clots alongside phenocrystic olivine. These populations of crystals have been previously described in detail by Graham and Hackett (1987) and more recently by Kósik et al. (2016). Thermobarometry on clinopyroxene-orthopyroxene pairs in ultramafic clots from OHK indicate crystallisation pressures of 4.8-5.4 kbar, equivalent to a depth of 16-18 km (Kósik et al., 2016). Mafic to ultramafic xenoliths are absent from C-TVZ rocks, which only contain smaller phenocrystic glomerocrysts (Figure 3.7), and rare in NC-TVZ rocks, but are present in RMR and TR basaltic andesites (Figure 3.3, 3.4). NC-TVZ rocks also contain xenoliths of rhyolite composition, that are likely co-genetic and have been entrained within the mafic magmas on ascent. These xenoliths have notably different vesicularity to the mafic rock they are found in (Figure 3.4), implying

that they had erupted and solidified before being entrained into the magma. These xenoliths also have crenulated edges and show partial resorption around crystal and glass edges. Details of xenolith types found in each sample are listed in Table 5.1. Detailed petrological descriptions of samples are written in Chapter 3.

Table 5.1: **Summary of key characteristics of samples.**

Sample	Seg.[a]	Age [b]	SiO_2 [c]	Mg# [c]	Comp. [d]	Ol [e]	Mg# $_{Cpx}$ [e]	An [e]	Xenoliths [e]
Rotokawau	NC	3.4ka	51.1	56	HAB	83-53	84-73	96-82	Rhy
Tarawera	NC	1886AD	50.6	53	HAB	82-80	80-77	88-85	Rhy
Rotomakariri	NC	22-28ka	57.4	43	BA	83-73	86-68	94-72	UM
Terrace Rd	NC	L.P	55.3	38	BA	78-70	81-65	95-82	Rhy & M
Johnson Rd	N/A	L.P	51.7	54	HAB	79-76	81-70	94-74	N/A
Ongaroto	C	80ka	51.0	64	HMB	92-64	66-65	78-77	N/A
Kakuki	C	L.P	48.5	66	HAB	85-71		89-71	N/A
Orakeikorako	C	L.P	50.1	53	HAB	80-42	82-56	82-62	N/A
Waimarino	S	17.5ka	52.2	72	HMB	93-70	88-70	90-81	UM
Ohakune	S	31.5ka	56.8	61	HMBA	88-82	89-68	84-83	UM

[a]Segment (Seg.): NC- North-central, C - Central, S - South. See text for definition of arc segments.
[b]Ages are from Hiess et al. (2007) and references therein; L.P is Late Pleistocene.
[c] Whole-rock data is from Gamble et al. (1990); Hiess et al. (2007).
[d]Composition (Comp.) is from Gamble et al. (1990) & Chapter3.
[e]Mineral composition (Fo, Mg#Cpx, An) and xenolith informations are from this study. Rhy - xenoliths comprising albitic plagioclase, quartz, +/- K-feldspar and biotite. UM/M - Ultramafic/mafic xenoliths comprising olivine + clinopyroxene +/- orthopyroxene +/-plagioclase (mafic (M) only).

5.4.2 Oxygen isotopes

Oxygen isotope results are reported in Table 5.2, expressed in standard delta notation, relative to Vienna Standard Mean Ocean Water (VSMOW).

Olivine

δ^{18}O in olivine varied from 4.8 to 6.4‰. The lower values fall within the range of mantle values (4.8-5.5‰) (Mattey et al., 1994) and those from primitive oceanic basalts of the Havre Trough and the offshore TVZ (Macpherson et al., 1998) (4.8-5.1‰). Offshore TVZ values (inclusive of Havre Trough values (Figures 5.1, 5.2)) provide a useful comparison to TVZ values, as they represent magmas from a similar mantle source to

Table 5.2: **Oxygen isotope data (per mil) relative to VSMOW.** Numbers in brackets denote number of duplicate analyses of the same value.

Sample	Ol	Cpx	Plag	GM
Rotokawau	5.6	5.8 (2), 5.7	6.0, 6.6, 6.7, 7.2, 7.7	6.0, 6.3
Tarawera		7.2	7.2, 7.4, 7.9, 8.7	6.5(2)
Rotomakariri	6.3, 6.4	6.2, 6.3(2), 6.6	6.9, 7.1, 7.2	6.7
Terrace Rd			6.8, 7.0 (2), 7.4, 7.5, 8.4	6.9, 7.2
Johnson Rd	4.8		5.8	6.3
Ongaroto	5.0, 5.1, 5.5 (2), 5.8			5.7, 5.8, 5.9
Kakuki	5.2 (2) 6.0		5.4, 6.5	5.2, 6.2
Orakeikorako	4.9, 5.0, 5.2, 5.3, 5.4	5.9, 6.1,	5.2, 5.3 (2), 5.5	5.4, 6.3
Waimarino	4.9, 5.4 (2), 5.5, 5.9, 6.0	5.6, 5.8, 5.9		5.7, 6.4, 6.5
Ohakune	5.7, 5.9	5.6, 5.7, 6.0, 6.6	11.0, 11.6	5.1 (2)

TVZ magmas that have undergone little to no crustal assimilation (Macpherson et al., 1998). The values are up to +1.3‰ higher than expected for primitive mantle-derived olivine (Figure 5.1a). In samples with multiple populations of olivine (Ongaroto, Waimarino), δ^{18}O varies by 0.8-1.1‰. Kakuki also shows a 0.8‰ variation, but only has one visually identifiable population of olivine crystals.

Clinopyroxene

δ^{18}O in clinopyroxene varied from 5.6 to 7.2‰, although most analyses are within the range of 5.6 to 6.6. As with olivine, the lower end of this range overlaps with mantle values (Mattey et al., 1994) and offshore TVZ values (Macpherson et al., 1998), but the upper end of the range is up to 1.4‰ higher (Figure 5.1b). Most samples show a limited range of δ^{18}O (<0.3‰), although OHK sample shows a 1‰ range in δ^{18}O in clinopyroxene.

Plagioclase

δ^{18}O in plagioclase varies from 5.2 to 8.7, except in plagioclase crystals from Ohakune (OHK) which vary from 11.0 to 11.6 and overlap with values of Torlesse metasediment (McCulloch et al., 1994). Due to the lack of plagioclase phenocrysts in OHK samples, the crystals are most likely crustal xenocrysts and will not be considered as part of

the range of magmatic δ^{18}O values for plagioclase. However, the presence of these xenocrysts confirms Torlesse metasediment is present in the crustal column, and is assimilated into OHK, and possibly other mafic TVZ magmas. The lowest plagioclase values are 0.63‰ lower than predicted values of plagioclase δ^{18}O from offshore TVZ glass values, based on a 0 to 0.5‰ fractionation between glass and plagioclase at magmatic temperatures (1000-1300°C) (Kalamarides, 1986). The highest plagioclase values are 3.05‰ higher than offshore TVZ glass values, based on the same fractionations (Figure 5.1c). Only plagioclase analyses from RK and HJR overlap with predicted mantle-derived values.

Groundmass

δ^{18}O of microcrystalline to glassy groundmass varied from 5.1 to 7.2‰. As with the plagioclase crystals, this ranges from below to significantly higher than mantle-derived values for volcanic glass (Mattey et al., 1994; Macpherson et al., 1998). The only samples that have groundmass analyses below mantle derived values are KK, OK and OHK. Both KK and OK also have groundmass analyses that are significantly heavier and in line with mantle-derived glasses, whereas OHK groundmass shows consistently low δ^{18}O. The large variation of δ^{18}O in the groundmass of samples from KK and OK is reflected in the plagioclase cargo, which also shows heavy and light δ^{18}O values, but this is not seen in the olivine or clinopyroxene cargo of these samples.

Overall, there is a broad positive correlation between the lowest δ^{18}O groundmass and crystal values in each sample. However, each crystal cargo (Ol, Pl, Cpx) shows a wide range of δ^{18}O values. The olivine cargo shows both higher and lower values of δ^{18}O than the range of groundmass δ^{18}O values (Figure 5.1a), whereas plagioclase and clinopyroxene δ^{18}O values extend almost exclusively to higher δ^{18}O than groundmass values (Figure 5.1b, c).

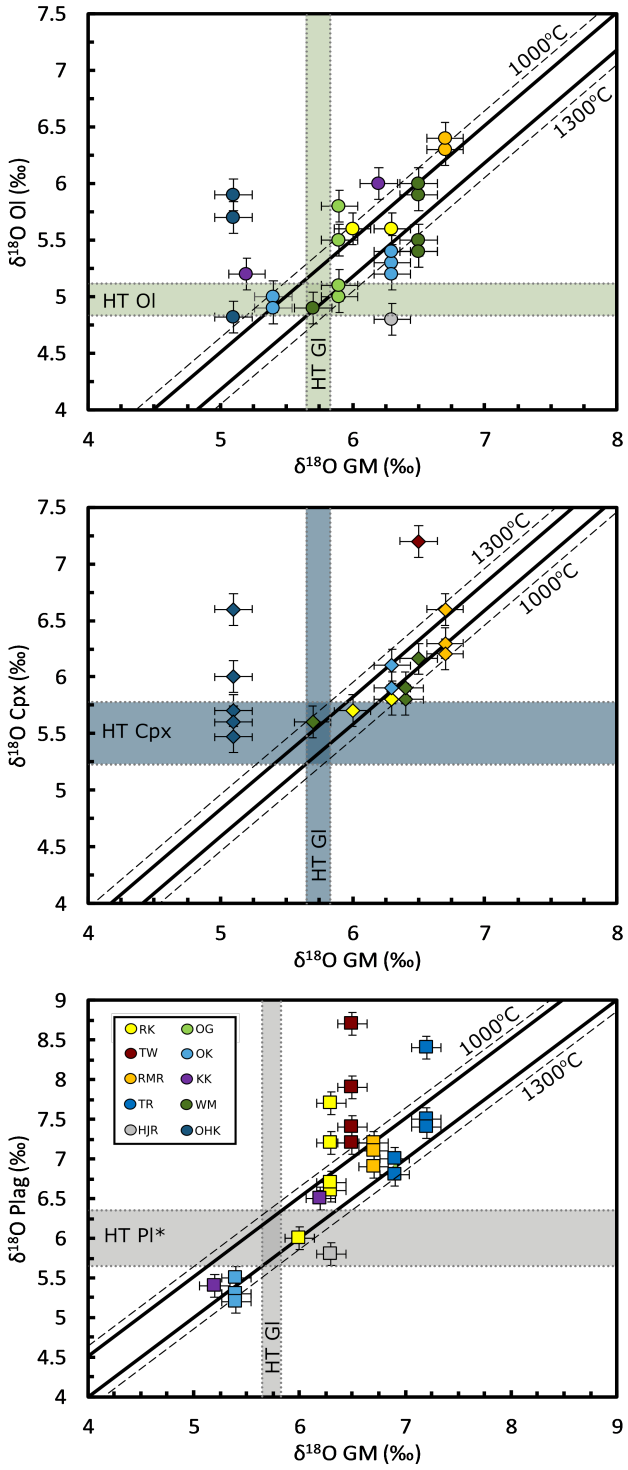

Figure 5.1: δ^{18}O of microcrystalline groundmass, against δ^{18}O of crystal phases. Circles = olivine; Diamonds = clinopyroxene; Squares = plagioclase. Thick black lines show predicted fractionations at 1000°C and 1300°C, as minimum and maximum temperature bounds respectively, (Kalamarides, 1986). Dashed lines are the error on δ^{18}O of this calculation. The bands labelled HT Ol, HT Cpx and HT Pl show the δ^{18}O values of Havre Trough olivine, clinopyroxene and plagioclase, respectively. *HT Pl is calculated from HT Glass at 0‰ fractionation. HT Gl is representative δ^{18}O of mantle melts without crustal addition. Error is propagated from 0.14‰ analytical uncertainty across all phases.

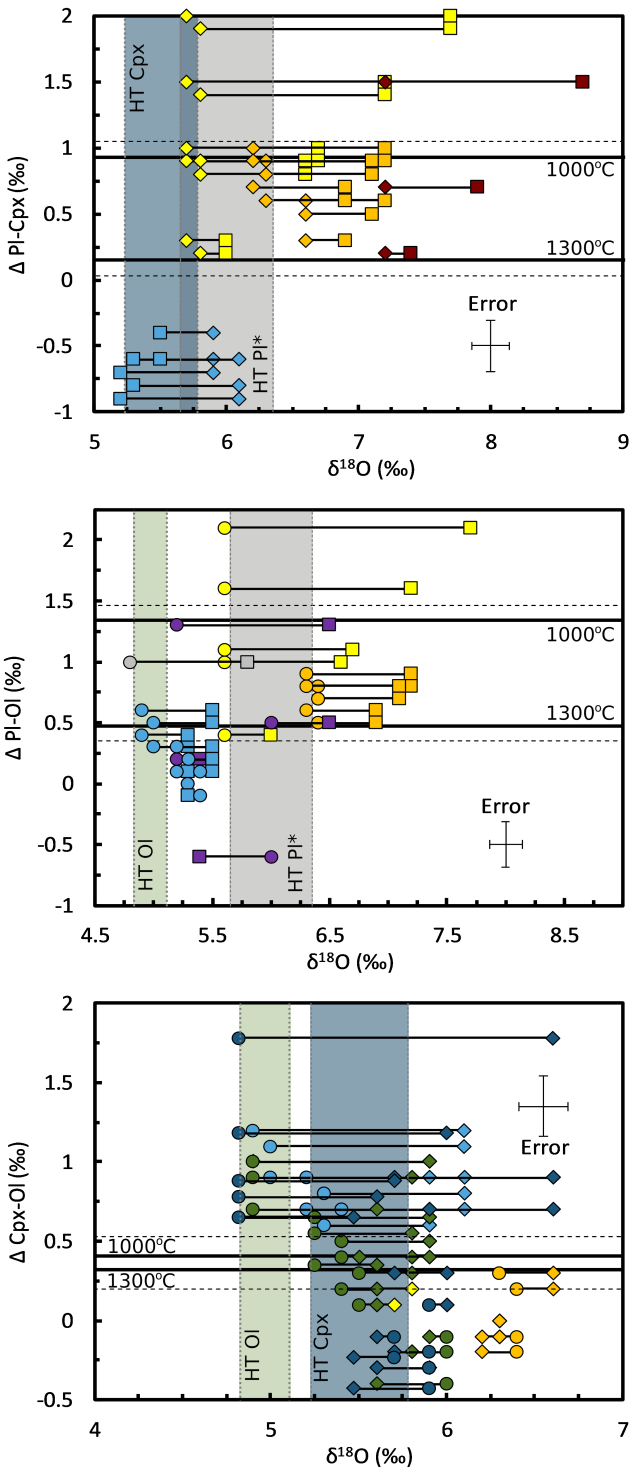

Figure 5.2: δ^{18}O of crystal phases, plotted against the difference in δ^{18}O between the two crystal phases (e.g. δ^{18}O Plag - δ^{18}O Cpx). Circles = olivine; Diamonds = clinopyroxene; Squares = plagioclase. Thick black lines show fractionations at 1000°C and 1300°C, as minimum and maximum temperature bounds respectively, (Kalamarides, 1986). HT Ol, HT Cpx and HT Pl show the δ^{18}O values of Havre Trough olivine, clinopyroxene and plagioclase, respectively. *HT Pl is calculated from HT Glass at 0‰ fractionation. HT Gl is representative δ^{18}O of mantle melts without crustal addition. Error is propagated from 0.14‰ analytical uncertainty across all phases.

5.4.3 Mineral-Melt Equilibria

Crystallisation of mineral phases fractionates oxygen isotopes by fractionation factors that have been calibrated in both experimental (Chiba et al., 1989) and natural (Kalamarides, 1986) systems. Fractionations between olivine and clinopyroxene are small, as are fractionations between plagioclase and melt. In all cases, isotopic fractionation increases with decreasing temperature, resulting in the greatest potential for fractionation between olivine and plagioclase at relatively cool (1000°C) magmatic temperatures. By setting a maximum range of magmatic temperatures (1000-1300°C), it is possible to assess whether or not mineral-mineral, or mineral-melt pairs could be in isotopic equilibrium, and therefore which phases could have crystallised at similar times in similar magmatic environments.

Mineral-mineral equilibria was assessed by plotting the δ^{18}O values of two phases (e.g. plagioclase (min_1) and clinopyroxene (min_2)) against the difference in δ^{18}O between the two values (the Δ Pl-Cpx), and comparing this to the defined magmatic fractionation factors (Kalamarides, 1986). For samples with multiple analyses of an individual phase, each δ^{18}O value of phase one (e.g. plagioclase) was compared to each δ^{18}O value of phase two (e.g. clinopyroxene), to give the maximum number of combinations. This gives a maximum range of possible pairings, and reduces bias towards picking individual pairs that result in an equilibrium range of Δ min_1-min_2.

Isotopically light olivine with values overlapping the offshore TVZ (Macpherson et al., 1998) (4.83 to 5.11‰) (Figure 5.2a, b) is out of isotopic equilibrium with both clinopyroxene and plagioclase in all samples except HJR, where olivine and plagioclase are in equilibrium. This indicates that for all other samples with isotopically light olivine (WM, OHK, OK, KK), olivine crystallised prior to addition of higher δ^{18}O material into the magma, whereas clinopyroxenes extend to higher values that require addition of continental crust to the magma. This fits with the observation that olivine is the first phase to crystallise most TVZ mafic samples (Gamble et al., 1990). Of the

isotopically light population of olivine, only those from WM and OG, the two HMB samples, are also in equilibrium with the groundmass (Figure 5.1a). All other samples have isotopically heavier groundmass δ^{18}O values, suggesting that assimilation of isotopically heavier continental crust occurred after initial crystallisation of isotopically light olivine. However, a significant proportion of olivines are isotopically heavy compared with offshore TVZ values. Olivines with isotopically heavy oxygen from RK and RMR in the NC-TVZ are in isotopic equilibrium with clinopyroxene and with plagioclase at the lighter end of the range in their respective samples, indicating that some phases co-crystallised, but with assimilation of high δ^{18}O material occurring before crystallisation of these phases. However, in RMR, OHK and WM, some clinopyroxenes have lower δ^{18}O than in the isotopically heavy end of the olivine spectrum, indicating either that clinopyroxene crystallised prior to olivine, or that they have originated from melts with different δ^{18}O. Oxygen in high δ^{18}O olivines from OHK, KK and OG is too heavy to be in equilibrium with the groundmass, and this points toward an antecrystic origin, whereas high δ^{18}O olivines from RK and RMR are in equilibrium with the groundmass, pointing to an overall higher δ^{18}O of the magma. Repeat analyses of WM sample show large variation δ^{18}O in both olivines and groundmass, and could indicate mixing of two distinct magmas.

In almost all samples, clinopyroxene spans a narrow range of δ^{18}O, and is largely in isotopic equilibrium with the groundmass (Figure 5.1b). The exceptions are from OHK and TW. δ^{18}O in clinopyroxene is significantly higher than in the groundmass in TW samples, and is in equilibrium with plagioclase that is also isotopically too heavy for the groundmass (Figure 5.2c), suggesting both are antecrystic. δ^{18}O in clinopyroxene in OHK samples extends from mantle values overlapping with offshore TVZ values, to significantly (>1‰) heavier. None of these values is in equilibrium with the groundmass, which is significantly isotopically lighter than offshore TVZ glasses (Figure 5.1b), and also show a similar range in δ^{18}O to olivines from the same sample (Figure 5.1a). The highest of the OHK clinopyroxene values is too high to

be in equilibrium with any olivine from the same sample. Therefore the high δ^{18}O clinopyroxenes from OHK are also most likely antecrysts.

The δ^{18}O values measured in plagioclase crystals in OK and KK samples is too low for the plagioclase to be in equilibrium with olivine or clinopyroxene. However, plagioclase is in equilibrium with the groundmass, and both are isotopically lighter than the baseline of offshore TVZ samples and the mantle. These groundmass and plagioclase values require the addition of δ^{18}O light material. For other samples, many plagioclase-olivine and plagioclase-clinopyroxene pairs could reasonably be in isotopic equilibrium; however most mineral pairs plot significantly above the offshore TVZ baseline. This indicates co-crystallisation of these phases, from a magma with elevated δ^{18}O. The only plagioclase-clinopyroxene pair in equilibrium, which also matches baseline values is from RK (Figure 5.2c). Isotopically heavier plagioclase has δ^{18}O extending up to 8.7‰, is out of equilibrium with all other phases and groundmass, and therefore requires an antecrystic origin. These plagioclases are unique to the NC-TVZ and occur in RK, TW and TR (Figure 5.1c).

5.5 Discussion

5.5.1 Low δ^{18}O alteration

Assimilation of hydrothermally altered crust, alteration of rock through interaction with hydrothermal fluids, and interaction of magma with external fluids can all have the ability to overprint magmatic δ^{18}O signatures. The effect of these processes must be evaluated in order to establish true signatures of source contamination and crustal assimilation in the TVZ mafic rocks.

OK, KK and OHK samples all have δ^{18}O values that are lower than mantle values (Macpherson et al., 1998; Mattey et al., 1994). Since the basement crust in the TVZ has δ^{18}O of 9-12.8‰ (Price et al., 2015), these samples require an alternative, isotopically

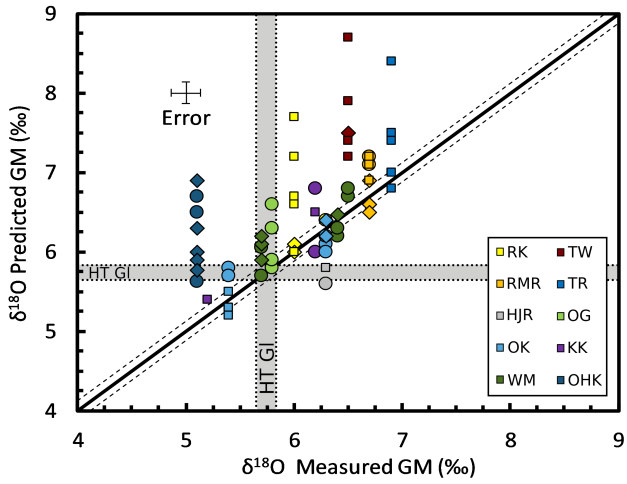

Figure 5.3: δ^{18}O of microcrystalline groundmass plotted against δ^{18}O of glass composition predicted from equilibrium at 1200°C with co-existing mineral phases (Kalamarides, 1986). Different mineral phases are marked by circles (olivine), diamonds (clinopyroxene), and squares (plagioclase). Thick black line is a 1:1 correspondance, thin dashed lines are error estimates from Kalamarides (1986). HT Gl is the δ^{18}O of Havre Trough glass, as a representative mantle baseline without crustal addition. Error on data points is from analytical uncertainty across all phases.

.

light source of contamination.

A total of 25 hydrothermal systems have been noted in the TVZ, with all but two of these concentrated within the central TVZ (Wilson and Rowland, 2016). Both KK and OK are within the bounds of one of these hydrothermal systems (Orakeikorako) (Bibby et al., 1995; Wilson and Rowland, 2016), whereas OHK, at the extreme southern end of the TVZ, is not in proximity to any hydrothermal system. Both OK and KK samples have plagioclase and groundmass δ^{18}O that is lower than mantle values, but clinopyroxene and olivine δ^{18}O that is higher than mantle values (Figure 5.3, 5.4). The differences between groundmass and plagioclase, and olivine and clinopyroxene demonstrate that the process affecting δ^{18}O is preferential to groundmass and plagioclase. Clinopyroxene and olivine are relatively robust indicators of magmatic δ^{18}O, due to the long timescales required for oxygen to re-equilibrate in their crystal structure (Reddy et al., 1980; Ryerson and McKeegan, 1994). The δ^{18}O of plagioclase however, is much more susceptible to late-stage changes, due to the comparatively short timescales required

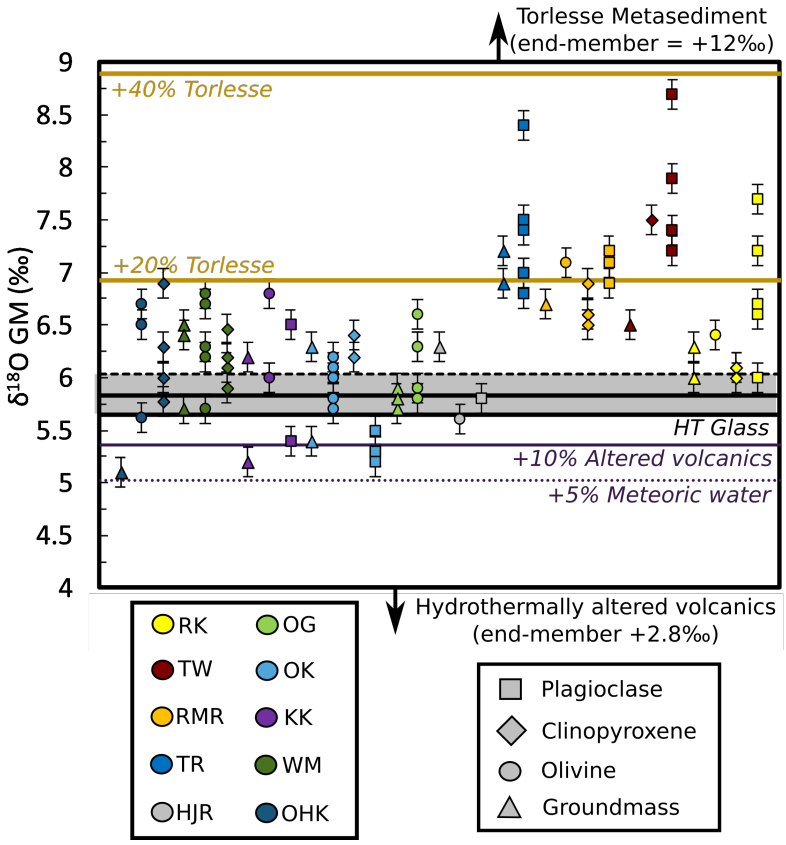

Figure 5.4: δ^{18}O of analysed groundmass, and equilibrium melt composition predicted from crystal δ^{18}O using Δmin-melt values of Kalamarides (1986) and a T of 1200°C. A temperature variation of 100°C produces a difference in Δmin-melt of <0.1, less than analytical uncertainty. Samples are arranged SSW-NNE from left to right. Grey shaded area represents the range of melt values that do not require any crustal input, using the δ^{18}O of Havre Trough (HT) glass (Macpherson et al., 1998) (thick black lines) and maximum deviation from this with closed system fractionation (Bindeman et al., 2004) (Thick black dashed line). Yellow lines represent addition of Torlesse metasedimentary crust to HT glass. Dashed purple line represents 5% addition of meteoric water (Blattner et al., 1996). Thick purple line represents 10% addition of hydrothermally altered volcanic rock of δ^{18}O +2.8‰.

.

for re-equilibration (Giletti et al., 1978). Therefore it seems most likely that a late-stage contaminant is responsible for the low δ^{18}O in the plagioclase and groundmass of these samples.

Hydrothermal fluids at Orakeikorako geothermal field have highly variable δ^{18}O from -1.0 to -7.1‰ (Sheppard and Lyon, 1984). However, direct alteration of magma by percolating hydrothermal fluid is unlikely, as geothermal fluid circulation is generally limited to the upper few kilometres of the crust (Bibby et al., 1995), and probably too shallow to come into direct contact with the magma. Additionally, direct influx of water into the mafic magmas would affect phase relations and cause dissolution or reverse zoning in plagioclase, which is not observed. A more likely scenario is that the magmas assimilated a small amount of hydrothermally altered crust. Both OK and KK were erupted in a post-caldera setting (Zellmer et al., 2020), and as such have erupted through a thick sequence of previously erupted lavas and ignimbrites (Figure 1.2), which were subsequently variably altered (Bignall et al., 1996). There are no δ^{18}O values for these altered volcanics at Orakeikorako, but δ^{18}O values of altered rock from nearby Wairakei geothermal area are as low as 2.2‰, (Clayton and Steiner, 1975), and have similar δ^{18}O fluid compositions to those at Orakeikorako (Sheppard and Lyon, 1984). Addition of 10% of altered rock with δ^{18}O of 2.2‰ to a basalt of mantle composition (5.65‰) results in a shift in magma δ^{18}O to 5.3‰, which explains the low δ^{18}O groundmass and plagioclase values in OK and KK samples (Figure 5.4).

Although there is uncertainty in the δ^{18}O in the original melt and the altered rock, this shows that addition of a small amount of hydrothermally altered rock is sufficient to explain the negative δ^{18}O shift in these samples. If the incorporation of low δ^{18}O material happened in the late stages of magma evolution, this could explain the offset in groundmass and plagioclase δ^{18}O relative to the more robust olivine and clinopyroxene values in these samples, and would suggest that the magmas stalled in the shallow crust in contact with older erupted sequences for a short period of time prior to eruption.

Addition of hydrothermally altered crust is not a likely explanation for the low

δ^{18}O groundmass values in OHK, because the erupted magma did not pass through thick older eruptive sequences on ascent (Figure 1.2). The groundmass is glassy and shows no sign of post-eruptive alteration, indicating that this is not the cause of the low δ^{18}O. Estimates of crystallisation depth from the phenocryst composition indicate storage at pressures of 0.5 MPa (Kósik et al., 2016), at which depth the country rock is most probably Torlesse supergroup greywackes (Price et al., 2015) or meta-igneous granulites (Graham et al., 1990), both with higher δ^{18}O than mantle values. As only the groundmass is affected (there is no phenocrystic plagioclase in OHK) and δ^{18}O of olivine and pyroxenes are at or above mantle values, the process affecting the groundmass must also be late stage, as in OK and KK samples. The most plausible explanation for this is through pre-eruptive interaction with meteoric water, with δ^{18}O of -7‰ (Blattner et al., 1996), as only very small amounts of water are required to produce the negative shift in δ^{18}O (Figure 5.4). Although the mechanism for this remains unclear, diffusion of water through glass at near-magmatic temperature could occur in the order of hours to tens of days (Doremus, 2004; Zhang and Stolper, 1991), and is within the timescales expected by pre-eruptive transport. All other samples have groundmass and crystal δ^{18}O values that reflect crystallisation from mantle-derived melts (5.65‰) with addition of a crustal component, and are representative of the magma they have crystallised from without any late-stage hydrothermal interactions.

5.5.2 Source vs. Crustal contamination

Combining radiogenic isotopes (^{87}Sr/^{86}Sr, ^{143}Nd/^{144}Nd) with δ^{18}O is a useful tool in identifying the source of contamination in magmas. Contamination of the mantle source produces a shift to more radiogenic ^{87}Sr/^{86}Sr and less radiogenic ^{143}Nd/^{144}Nd, without producing a significant shift in δ^{18}O, unless large (and unrealistic) proportions of source contamination is involved (a 1‰ increase requires 20% addition of crustal contaminant in the mantle source region (Figure 5.5)). However, where the crustal

assimilant has significantly different $\delta^{18}O$ to the mantle derived magma, as in the TVZ (Torlesse Terrane = $\delta^{18}O$ 9.5 to 12.8) (Price et al., 2015), the $\delta^{18}O$ of the magma will increase alongside increases in $^{87}Sr/^{86}Sr$, and decreases in $^{143}Nd/^{144}Nd$.

Melt $\delta^{18}O$ values were calculated from mineral $\delta^{18}O$ values and fractionation factors at 1200°C (Kalamarides, 1986). To identify whether source contamination is significant in primitive TVZ magmas, we selected only the lowest calculated $\delta^{18}O$ melt compositions from each sample for use in source contamination models. This does not guarantee that the calculated melt $\delta^{18}O$ reflects a primary melt $\delta^{18}O$ value. However, it is a best estimate of a primitive melt $\delta^{18}O$, prior to assimilation of crust. Isotopic mixing lines were calculated (Langmuir et al., 1978) between depleted mantle (DM), slab-derived fluid and slab sediment end-member compositions (Macpherson et al., 1998) to test whether source contamination affected the isotopic composition of basalt samples. End-member compositions are listed in Table 5.3. Isotopic mixing lines were calculated between offshore TVZ basalt VUW158/4 (OTVZ) (Gamble et al., 1994; Macpherson et al., 1998) with low $^{87}Sr/^{86}Sr$ and high $^{143}Nd/^{144}Nd$, and crustal contaminant end-members Waipapa, Pahau and Kaweka Terranes (Price et al., 2015), to test whether crustal assimilation affected the isotopic composition of basalt samples. Kaweka and Pahau are shallower and deeper members of the Torlesse supergroup underlying the TVZ, respectively (Price et al., 2015). Torlesse crustal end-member is an average composition of the Torlesse supergroup from Graham (1985) and Macpherson et al. (1998). The selected lowest melt $\delta^{18}O$ values were then plotted against $^{87}Sr/^{86}Sr$ and $^{143}Nd/^{144}Nd$ whole rock values from Gamble et al. (1993) (Figure 5.5).

Most samples lie on crustal contamination curves, and have initial $\delta^{18}O$ higher than mantle values (Figure 5.5). This suggests that isotopic compositions of these samples are a result of assimilation in the crust, and not contamination in the mantle wedge. However, HJR, OHK and WM samples have initial melt $\delta^{18}O$ close to mantle values, at relatively radiogenic $^{87}Sr/^{86}Sr$ and unradiogenic $^{143}Nd/^{144}Nd$, plotting close to the source contamination curves. This suggests the isotopic composition of these

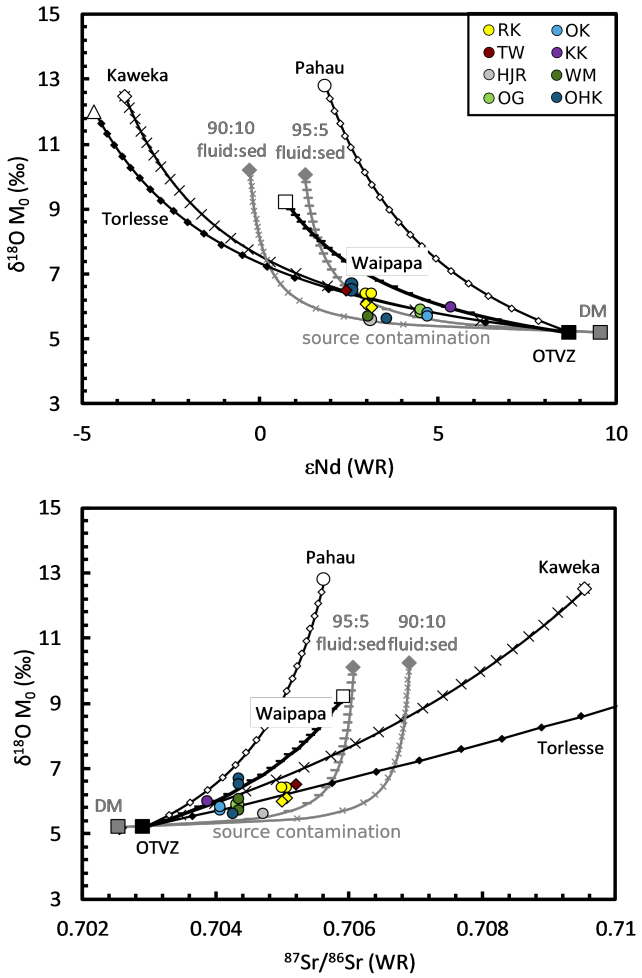

Figure 5.5: Whole rock $^{143}Nd/^{144}Nd$ and $^{87}Sr/^{86}Sr$ plotted against predicted initial melt $\delta^{18}O$ (M_0), using the method of Kalamarides (1986) at 1200°C, from the most primitive $\delta^{18}O$ olivine and clinopyroxene from each sample. Melt predicted from different mineral phases are marked by circles (olivine) and diamonds (clinopyroxene). Grey lines show mixing between depleted mantle (DM) (Macpherson et al., 1998) and source contaminants calculated from 95% slab-derived fluid and 5% slab-derived sediment, and a 90:10 ratio of the same contaminants (Macpherson et al., 1998). Black lines show mixing between offshore TVZ sample VUW158/4 (Gamble et al., 1994; Macpherson et al., 1998) and potential end-member metasedimentary terranes. Pahau and Kaweka are subgroups of the Torlesse Terrane. Waipapa outcrops to the west of the TVZ. Data are from (Price et al., 2015). Torlesse is average Torlesse composition from (Macpherson et al., 1998).

.

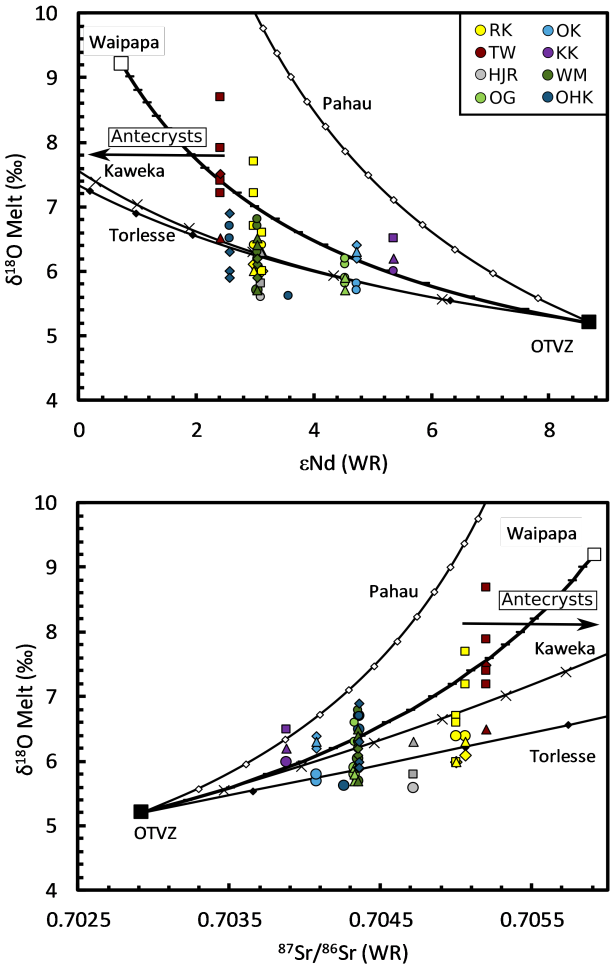

Figure 5.6: Whole rock $^{143}Nd/^{144}Nd$ and $^{87}Sr/^{86}Sr$ plotted against predicted melt $\delta^{18}O$, calculated using the method of Kalamarides (1986) at 1200°C, from $\delta^{18}O$ for all mineral and groundmass analyses. Melt composition predicted by different mineral phases are marked by circles (olivine), diamonds (clinopyroxene), squares (plagioclase). Triangles are direct analyses of groundmass. Black lines show mixing between offshore TVZ sample VUW158/4 (Gamble et al., 1994; Macpherson et al., 1998) and potential end-member metasedimentary terranes. Pahau and Kaweka are subgroups of the Torlesse Terrane. Waipapa outcrops to the west of the TVZ. Data is from (Price et al., 2015). Torlesse is average Torlesse composition from Graham (1985); Macpherson et al. (1998).

.

Table 5.3: **Isotope ratios and composition of mantle, primitive mantle melt, and contaminants used in mixing calculations.**

	δ^{18}O	Sr (ppm)	^{87}Sr/^{86}Sr	Nd (ppm)	^{143}Nd/^{144}Nd	ϵ Nd
DM [a]	5.2	2	0.702556	0.14	0.513129	9.57
Fluid [a]	9.96	34	0.704575	0.73	0.513077	8.56
Sed [a]	12.6	296	0.709325	27.78	0.512515	-2.39
OTVZ [a b]	5.2	172	0.702922	7.3	0.513084	8.7
Waipapa [c]	9.2	379	0.705916	22.4	0.512676	0.74
Pahau [c]	12.8	529	0.705628	20.8	0.512732	1.83
Kaweka [c]	12.5	295	0.709539	35.1	0.512443	-3.8
Torlesse [a d]	12	217	0.71469	30	0.5124	-4.64

[a] Macpherson et al. (1998)
[b] Gamble et al. (1994)
[c] Price et al. (2015)
[d] Graham (1985)

samples are a result of mantle source contamination. However, the δ^{18}O isotopic is calculated from olivine, an early-forming mineral phase, whereas the ^{87}Sr/^{86}Sr and ^{143}Nd/^{144}Nd values are whole-rock compositions. If crustal assimilation has occurred then whole rock data may be shifted toward radiogenic ^{87}Sr/^{86}Sr and unradiogenic ^{143}Nd/^{144}Nd, whilst the early-formed mineral phase will record a δ^{18}O that reflects the melt composition prior to assimilation of crust. Therefore, HJR, OHK and WM samples may indicate source contamination, although it cannot be discounted that this is an artefact of using whole-rock data against early-formed mineral phases. In the case of HJR, the groundmass of the sample has significantly higher δ^{18}O (6.3), than the olivine (4.8‰ with a predicted melt of 5.6‰), indicating that the olivine is an early-formed crystal in a melt that has assimilated crustal material, and that it cannot be used to positively determine whether source contamination has occurred or not. Likewise, groundmass values from OHK are extremely low and have probably been subject to hydrothermal alteration, and so it is not possible to tell whether these values indicate source contamination. However, groundmass δ^{18}O in WM matches the initial melt δ^{18}O calculated from olivine, indicating that the whole rock ^{87}Sr/^{86}Sr and

$^{143}Nd/^{144}Nd$ isotopic compositions are not subject to crustal assimilation. Therefore, we cannot rule out mantle source contamination for WM, or OHK. This means there is the potential for additional source contamination in the south TVZ, although results are inconclusive. We can, however, confidently assume that, based on the lowest $\delta^{18}O$ of all other samples, that all subsequent $\delta^{18}O$ variation is due to crustal assimilation.

TVZ basement lithologies have sufficient contrast in isotopic compositions to impart significant shifts in the isotopic composition of mafic magmas from relatively small amounts of assimilation. Underlying the TVZ, are the roughly westward-dipping Waipapa and Torlesse metasedimentary supergroups. The Waipapa terrane underlies the TVZ at shallowest depths, and outcrops to the west of the TVZ. The Torlesse terrane lies beneath the Waipapa terrane and crops out to the east of the TVZ (Price et al., 2015).

Assessment of mineral-melt equilibria (section 5.4.3) demonstrates that many crystal separates are significantly enriched in $\delta^{18}O$ with respect to their groundmass values (Figure 5.3). These crystal separates must be antecrystic in origin, and derived from a melt with contrasting $^{87}Sr/^{86}Sr$ and $^{143}Nd/^{144}Nd$, to the mafic magma in which they were erupted. Figure 5.6 shows the melt $\delta^{18}O$ required by crystal phases, which was calculated based on isotopic fractionation between crystal phases and melt (Kalamarides, 1986) at 1200°C, in addition to direct $\delta^{18}O$ measurements of groundmass, against whole rock $^{87}Sr/^{86}Sr$ and $^{143}Nd/^{144}Nd$ values. Direct groundmass analyses (triangles) are the best approximation of the final melt composition prior to eruption, and therefore used to assess crustal assimilation. Isotopic mixing lines between a primitive offshore TVZ composition (VUW158/4 (Gamble et al., 1994) (OTVZ)) and the various crustal end-member contaminants help assess the nature of the crustal contaminant.

Most mafic TVZ samples have whole rock radiogenic isotope data that are inconsistent with assimilation of Waipapa rocks (Gamble et al., 1993). This is based on the assumption that KK is the most primitive TVZ sample, due to its low SiO_2, high MgO, unradiogenic $^{87}Sr/^{86}Sr$ and radiogenic $^{143}Nd/^{144}Nd$. However, $\delta^{18}O$ from KK olivine

predicts melt of 6.0‰, whilst unaltered groundmass has δ^{18}O of 6.2‰, requiring significant addition of crust, contrary to interpretations made solely from radiogenic isotope data (Gamble et al., 1993). Whilst assimilation of Waipapa rocks is unlikely for rocks with more radiogenic isotopic compositions (RK, TW) (Gamble et al., 1993), they are a potential assimilant to mafic TVZ magmas with less radiogenic isotopic compositions.

Other crustal end-members considered are all from the Torlesse supergroup (Graham, 1985; Price et al., 2015). The Pahau subgroup is older and deeper than the overlying Kaweka subgroup. From Figure 5.6, it is clear that although these rocks have relatively high δ^{18}O, their ^{87}Sr/^{86}Sr is too low, and ^{143}Nd/^{144}Nd is too high to produce a mixing line that cross mafic TVZ data. Isotopic mixing between OTVZ and the Kaweka rocks subgroup produces a mixing line that overlaps some of the data. However, this creates a mass balance problem, where 5-7% more material is required to produce the ^{87}Sr/^{86}Sr than the ^{143}Nd/^{144}Nd. The higher ^{87}Sr/^{86}Sr value from Graham (1985) at a similar ^{143}Nd/^{144}Nd reconciles this issue. Groundmass δ^{18}O from the S-TVZ, NC-TVZ and OG plot close to the Torlesse mixing line, and shows that 10-20% crustal assimilation of Torlesse rocks is the most likely cause of the increase in δ^{18}O of these samples. This is in broad agreement with interpretations of other isotopic datasets (Blattner and Reid, 1982; Gamble et al., 1993; McCulloch et al., 1994; Waight et al., 2017). OK and KK samples from the central TVZ both have groundmass values that lie significantly above the Torlesse mixing line (Figure 5.6). Waipapa rocks have more-radiogenic ^{143}Nd/^{144}Nd and less-radiogenic ^{87}Sr/^{86}Sr than Torlesse rocks for a similar increase in δ^{18}O. Additionally, the major element composition (63 wt.% SiO_2) is less evolved than Torlesse (70 wt.% SiO_2 (Price et al., 2015), meaning that assimilation of Waipapa rocks is able to alter δ^{18}O while producing smaller changes in other aspects of the magma composition. The addition of 15% of Waipapa rock to a primitive basalt with 48 wt.% SiO_2 results in a 2wt.% increase in SiO_2 in the magma, making the change in composition due to bulk addition of sediment impossible to distinguish from the effects of fractional crystallisation. Therefore, both KK and OK samples have

compositions that are more readily explained by assimilation of Waipapa rocks than by Torlesse rocks.

5.5.3 Evidence for crystal recycling

Each sample contains a diverse $\delta^{18}O$ crystal population, with analyses of crystal separates ranging up to 2.2‰ heavier than their respective groundmass analysis. In NC-TVZ samples (RK, TW, RMR, TR), this variation is largely limited to plagioclase separates, whereas in south TVZ samples (WM, OHK) and OG, the variation in $\delta^{18}O$ is apparent in mafic separates. In each sample, alongside crystal separates that are in equilibrium with the groundmass, other batches of crystals require crystallisation from magma that is 0.8-2.2‰ higher in $\delta^{18}O$ than the magma in which they have been erupted.

The possibility that disequilbrium between crystals and melt was caused by late-stage low alteration of melt by contamination with low $\delta^{18}O$ hydrothermally altered rock or hydrothermal fluids was explored in section 5.5.1. Only the groundmass from OHK, plus groundmass and plagioclase from OK and KK is lower than the Havre Trough baseline, and shows evidence alteration through interaction with a low $\delta^{18}O$ contaminant. Additionally, all other samples have a mixture of equilibrium and disequilibrium mineral-groundmass pairs (Figure 5.3), showing that a proportion of the crystal cargo has crystallised from and is in equilibrium with the groundmass. Therefore, it is most likely that the crystals out of equilibrium with their respective groundmasses are antecrystic, and crystallised from a melt with higher $\delta^{18}O$ than the one in which they are erupted.

It is possible to incorporate antecrystic material through mixing of magmas, or through remobilisation of crystal mush regions. Involvement of melt, as well as crystal entrainment, is key to magma mixing, whereas remobilisation of crystals from a mush does not require mixing of a second magma. Most samples show a narrow range in $\delta^{18}O$ of the groundmass, suggestive of a relatively homogenous melt composition. This

implies that either incorporation of antecrystic material was through remobilisation or plucking of crystals from isotopically distinct mushes, rather than mixing of magmas, or that the melts were mixed for sufficient periods of time to re-equilibrate. The latter scenario is only feasible at timescales greater than the time to re-equilibrate melt, but less than those required to re-equilibrate crystals. A scenario where earlier intrusions of magma that have partially crystallised and assimilated basement crust to form a mush provides a source of the antecrysts. Later intrusions of basaltic melt with near-mantle isotopic composition could then inherit antecrysts from this mush. Multiple analyses of the WM sample show a range of groundmass δ^{18}O values (5.7 - 6.5‰), and could be suggestive of magma mixing shortly before eruption. If this is the case, then mixing would have to be between highly primitive melts, in order to maintain the high Mg# and primitive nature of the sample.

It is also important to note the prevalence of mafic antecrysts within south TVZ samples, plus OG from the central TVZ, compared with the prevalence of plagioclase antecrysts in NC-TVZ samples. Plagioclase antecrysts in the NC-TVZ have δ^{18}O that match δ^{18}O of plagioclase from rhyolites (Blattner et al., 1996). Incorporation of rhyolitic material into mafic NC-TVZ samples is also seen in hand specimen and thin section (Figure 3.1, 3.2, 3.4). Additionally, the only aphyric sample (TW), is also the only sample where all crystal separate analyses have significantly higher δ^{18}O than the groundmass (Figure 5.3), and the only large identifiable crystals in thin section are either in rhyolitic xenoliths or are separated xenocrysts with compositions matching those in the xenoliths. It therefore is reasonable to assume that high δ^{18}O values from plagioclase separates in the NC-TVZ are a result of incorporation of rhyolitic material into mafic magma.

Antecrysts of clinopyroxene and olivine from the S-TVZ and OG cannot be inherited from rhyolitic volcanism. Mafic antecrysts have δ^{18}O of up to 7‰, requiring approximately 20% assimilation of Torlesse basement rock. These mafic antecrysts probably crystallised in a mafic magma mush that assimilated basement crust. Assim-

ilation of basement crust by mafic magma is most likely to occur in the early stages of magmatism, when the crust is less heavily intruded and modified by mantle melts (Hutchison et al., 2018), such as in the south TVZ. Mush remobilisation by melts with mantle δ^{18}O will then entrain crystals with higher δ^{18}O.

5.5.4 Mafic magmas and the maturation of the TVZ

It has long been recognised that some arc systems transition from typical andesitic volcanism during the early stages of magmatism, to silicic volcanism as the system matures (Bachmann et al., 2007; de Silva et al., 2006; de Silva and Gregg, 2014). This is especially apparent in the TVZ, where andesitic volcanism is considered precursory to rhyolitic volcanism (Price et al., 2005) and the transition is associated with rifting (Deering et al., 2011a). This is because large-scale silicic systems take time to thermally mature, and are dependent on episodic magma emplacement (Annen, 2009, 2011), and rates of magma intrusion into the crust need to be sufficiently high to sustain silicic magma generation (Annen et al., 2015). Priming of the crust by repeated injection of mantle-derived magma into the crust modifies the composition of the crust itself, where the first intrusions come into contact with basement rock. With ongoing magmatism, later injections of mantle-derived magma are separated from the crust by solidified or partially crystallised older intrusive bodies. Early isotopic studies on the evolution of rhyolite in the TVZ (Blattner et al., 1996) showed a decreasing trend in whole rock δ^{18}O through time, with the interpretation that access to basement crust is progressively restricted in areas of magma intrusion.

More recent work (Zellmer et al., 2020) has linked the primary major and trace element composition of mafic magma in the TVZ to discrete changes in the evolution of the system. The variation in δ^{18}O observed in the mafic TVZ samples can therefore be assessed in terms of their position in the lifespan and maturation of the rifted arc. The rocks sampled are representative of the three stages of volcanic maturation

described by Zellmer et al. (2020). The south TVZ samples represent pre-caldera system magma storage, the NC-TVZ samples represent mafic magma from a currently active, well developed caldera system (syn-caldera), and the central TVZ deposits represent magma storage in a post-caldera system. These post-caldera deposits are also referred to as inter-caldera basalt, and syn-caldera basalt as intra-caldera basalt (Barker et al., 2020). Basalts erupted within the currently active Taupo volcanic centre are also representative of melt from a syn-caldera system, however in this study, no central TVZ samples are from Taupo Volcanic centre, and are all representative of a post-caldera setting (Zellmer et al., 2020).

The S-TVZ is representative of the earliest stages of magmatism in the TVZ. South TVZ rocks are dominated by mafic crystal phases, crystallised relatively deep in the crust (Kósik et al., 2016). These mafic crystals have high δ^{18}O in comparison to mantle δ^{18}O. The depth of crystallisation coincides with seismic observations of increasing p wave velocity at depths deeper than 15km, commonly interpreted as a transition from felsic (Torlesse Greywackes) to mafic (crystalline intrusive) lithology (Hurst et al., 2016; Stern et al., 2010). Therefore these high δ^{18}O phases are most likely sourced from this deeper crustal crystal mush zone. The high δ^{18}O signature of the crystal separates results from assimilation of Torlesse basement (Figure 5.6) and is in agreement with previous models of assimilation of crust in the TVZ (Blattner and Reid, 1982; Blattner et al., 1996; Charlier et al., 2005; McCulloch et al., 1994; Price et al., 2005), where basalt and andesite magmas are responsible for most of the crustal assimilation. Fractionation accompanied by crustal assimilation is expected in the early stages of magmatism, where the crust is less heavily intruded by prior injections of magma (Hutchison et al., 2018). The mantle δ^{18}O of the groundmass is strong evidence for remobilisation of crystal mush by subsequent intrusion of fresh batches of mantle-derived melt.

NC-TVZ rocks have by far the widest range of δ^{18}O, and contain antecrysts from both the plutonic regions of the plumbing system (Figure 3.3, 3.4), and from previously erupted rhyolites (Figure 3.1, 3.2, 3.4) in addition to phenocrystic phases. The magmatic

system at OVC is complex (Cole et al., 2014), and the diversity in the crystal cargo reflects this. The presence of a large, but compositionally variable and long-lived mush zone (Deering et al., 2011a,b), along with small pod or laccolith-like intrusions in the shallow crust (Cole et al., 2014) provides ample sources for antecrystic material to be incorporated into new intrusions of mantle-derived melt. The range of antecrysts from both plutonic and shallow portions of the crust are evidence for a heavily intruded crust, with distinct batches of partially to wholly crystalline magma that have fractionated different mineral assemblages and incorporated different amounts of Torlesse crust, building a typical transcrustal magma system (Cashman et al., 2017). High δ^{18}O values for groundmasses and phenocrysts indicates that crustal assimilation is an important process in mafic magma evolution (McCulloch et al., 1994; Price et al., 2005), in addition to mixing of magma. The range of δ^{18}O values in the NC-TVZ rocks highlights the complexity in a fully developed caldera-forming system.

In contrast, C-TVZ rocks have the least diverse crystal populations. In mature post-caldera forming settings the crust is likely to be heavily intruded and modified by magmatic intrusion (Annen et al., 2015; Cashman et al., 2017), altering the ratio of fusible crustal material to refractory crystalline material in the crust (Hutchison et al., 2018). Barker et al. (2020) and Zellmer et al. (2020) show that the C-TVZ eruptions derived from low-volume melts in the mantle in comparison to NC-TVZ and S-TVZ magmas. Smaller volumes of melt intrusion further compound the lack of assimilation into these magmas. The lack of diversity in the crystal cargo of C-TVZ rocks is strong evidence in favour of this. This has implications for previous interpretations of TVZ basalt. Commonly KK, has been used as a primitive end-member composition for modelling the evolution of magma in the TVZ (Gamble et al., 1990, 1993). The evidence presented here shows that although KK and other post-caldera basalt may retain primitive isotopic signatures, through lack of fusibility of the country rock, this lack of assimilation and preservation of the mantle signature is inherently linked to the waning of the magma system. The primitive mantle signature it preserves is of a

depleted, post-caldera feeding mantle, rather than of the mantle feeding caldera forming systems (Barker et al., 2020; Zellmer et al., 2020). Assimilation of older hydrothermally altered ignimbrites and lavas is unique to the post-caldera setting in the TVZ, but is observed in other post-caldera settings such as the Snake River Plain, Idaho, (Bindeman et al., 2007; Watts et al., 2011) and Yellowstone (Bindeman et al., 2001).

Overall, the isotopic evidence reported in this study is in broad agreement with models of evolution of the TVZ. The isotopic evidence supports the interpretation that andesitic volcanism is precursory to rhyolitic volcanism in the TVZ (Price et al., 2005), and that the composition of mafic magma is inherently linked to these changes (Barker et al., 2020; Zellmer et al., 2020). Additionally, S-TVZ magmas host primitive composition mafic antecrysts, with δ^{18}O values that imply assimilation of up to 20% basement, consistent with the prevalence of open system processes occurring in mafic magma (Blattner et al., 1996; McCulloch et al., 1994; Price et al., 2005). We see evidence for underplating and remobilisation of mafic mushes in the south TVZ, where the magmatic system is relatively immature. As the magmatic system becomes more complex, recycling of components also becomes more complex and this is seen in the diverse crystal population in the NC-TVZ. Eventually when a caldera is exhausted, mafic magmas erupted through the waning magma system are insulated from the basement rocks by refractory crystalline intrusives, and retain relatively primitive compositions and crystal cargoes (Figure 4.8).

5.6 Conclusions

This study highlights the importance of using mineral-specific data in conjunction with whole-rock data to investigate open-system processes. Advances in spatially resolved techniques for measuring δ^{18}O in individual crystal phases will further expand the application of this technique. We have presented a much expanded dataset for δ^{18}O in mafic TVZ rocks, the results of which can be integrated with andesite and rhyolite

datasets for the TVZ (Blattner and Reid, 1982; Blattner et al., 1996; McCulloch et al., 1994).

Our results show that the interpretation of δ^{18}O in mafic rocks in of TVZ is far from straight forward, and individual samples can show a significant range in δ^{18}O. Physically separating out larger crystals from the groundmass and analysing them provides a useful way of assessing mineral-melt equilibria and has led to the successful identification of multiple populations of crystals in an individual sample. We interpret this as strong evidence for open-system processes occurring in mafic magma in the TVZ, highlighting the importance of crustal assimilation at an early stage in magma evolution. The relative contribution of continental crust appears to lessen through the maturation of the system, in broad agreement with previous work (Blattner et al., 1996; Price et al., 2005). We propose that the variation in crustal contribution to mafic TVZ magmas is primarily controlled by two factors. Firstly, how heavily intruded the crust is, controlling how much continental crust new pulses of magma come into contact with and can therefore assimilate; and secondly, the heat flow of the region, controlled by flux of hot mantle melt into the crust. i.e. the heat from the flux must be enough to induce partial melting of the crust.

Variation of these two factors in mafic rocks erupted in pre-, syn-, and post-caldera settings accounts for the observed textural and oxygen isotopic variability. Mafic rocks from the TVZ record the magmatic maturation of one of the most productive silicic systems on Earth. However, the least contaminated rocks in the TVZ were emplaced in post-caldera environments where conditions do not favour assimilation of crust (Hutchison et al., 2018). Basalt from this setting is most likely to retain primitive mantle-derived compositions, but is not representative of the composition that is supplying caldera-forming systems (Barker et al., 2020; Zellmer et al., 2020). Likewise, the primitive magma supplying caldera-forming volcanism ascends through a complex transcrustal magma system (Cashman et al., 2017), where open-system processes obscure its primitive mantle composition. Syn-caldera basalt is of most

use as a primitive magma end-member, providing its mantle-derived signature can be separated from that which arises due to magma processing in the crust.

Chapter 6

Tracing mantle variation through xenocrystic olivine

6.1 *Foreword*

The following chapter has been accepted in *Lithos* for publication. The paper is titled: **Tracing mantle source variation through xenocrystic olivine in the Taupo Volcanic Zone, New Zealand: A role for lithospheric mantle in the shift from andesite to rhyolite compositions**.

This chapter provides an in-depth evaluation of the olivine crystal cargo from TVZ mafic rocks. Olivine compositions provide an opportunity to see-through most crustal processing. As a result, this chapter moves away from the crustal contamination and plumbing system theme of the previous two chapters, and begins to explore mantle contributions and variations in the sample suite.

6.2 Introduction

Arc volcanism is responsible for some of the most explosive and hazardous eruptions on Earth (Self, 2015). However, the origin of the magmas that ultimately result in large-scale silicic eruptions is of intense debate. Dominant erupted products are

rhyolitic and as such, the result of large amounts of magmatic processing (fractional crystallisation, assimilation of basement, magma mixing etc.) (Annen et al., 2006; Hildreth and Moorbath, 1988; Wolff et al., 2015). This obscures mantle-derived features of parental melts, making it challenging to determine the nature of magmatic processes that ultimately feed and drive large-scale silicic eruptions. Despite this, constraining the spatial and temporal variation in the composition of the mantle source regions for parental melts is key to understanding how silicic magma systems evolve. Eruptions of basalt that are coeval to rhyolite can be used to "see through" most of this crustal processing. However, even the most primitive basaltic magmas can still be subject to deceptively large amounts of magmatic processing, due to storage in the complex MASH (melting, assimilation, storage, homogenisation) zone (Hildreth and Moorbath, 1988; Lynn et al., 2017; Waight et al., 2017; Zellmer et al., 2016), as highlighted in Chapters 5 and 4. Fortunately, some basalts contain xenocrystic material from the mantle, which, when combined with incompatible trace elements from whole rock data can allow us to better evaluate the nature of the mantle source.

The Taupo Volcanic Zone (TVZ), New Zealand, is well known for its frequent, and often explosive silicic eruptions. It is one of the most productive silicic centres worldwide (Wilson and Rowland, 2016). However, we still know comparatively little about the mantle that is melting beneath the TVZ, which ultimately drives volcanism. As a rifted continental arc (Wilson et al., 1995b), mantle melting is induced by thinning and rifting of the lithosphere, in addition to flux melting due to slab-derived fluids (Gamble et al., 1993; Rooney and Deering, 2014; Waight et al., 2017). The arc is propagating southward, with the south TVZ being characterised by predominantly andesitic volcanism, considered precursory to rhyolitic volcanism in the TVZ (Browne et al., 1992; Chambefort et al., 2014, 2016; Price et al., 2005). Both rifting and the prevalence of rhyolitic volcanism are concentrated in the central TVZ (Rowland et al., 2010; Wilson and Rowland, 2016), suggesting a tectonic control on the shift from andesitic to rhyolitic volcanism.

Monogenetic basalt eruptions occur along the length of the arc as small scoria cones and maars (Hiess et al., 2007; Wilson et al., 1995b) (Figure 1.2). They often ascend along normal faults, parallel to the main rift axis (Cole, 1973; Hiess et al., 2007), and reflect the primitive stages of magma evolution in the TVZ (Gamble et al., 1990). These co-genetic basalts have compositional variations along arc, from plagioclase-dominant high-alumina basalts (HABs) in the central TVZ, to plagioclase poor high-magnesia basalts and basaltic andesites (HMBs and HMBAs, respectively) (Gamble et al., 1990; Graham and Hackett, 1987) in the south TVZ, although HMB still occurs sporadically in the central TVZ. HMBs are the most primitive eruptions in the TVZ and contain abundant primitive olivine and clinopyroxene (Cameron et al., 2010; Gamble et al., 1990; Graham and Hackett, 1987).

A compositional continuum between cold-wet-oxidising magmas in the northern parts of the central TVZ, to hot-dry-reducing magmas in the southern part of the central TVZ has been described by Deering et al. (2008, 2010). This change in compositions has been attributed to variation in flux of slab-derived fluids, whereby the northern central TVZ requires greater amounts of fluid flux from the subducting slab (Rooney and Deering, 2014). More recently, these changes in basalt composition have been attributed to changes in the temporal evolution of individual caldera-forming areas of the central TVZ. Basalt from intra- (Barker et al., 2020), or syn- (Zellmer et al., 2020), -caldera regions are thought to be sourced from large, hydrous melt fractions in the shallow mantle, and contribute to driving caldera-forming volcanism. Examples of this are at Okataina Volcanic Centre (OVC) in the northern portion of the central TVZ, and correspond to the cold-wet-oxidising trends observed in Rooney and Deering (2014). Basalt from intra- (Barker et al., 2020), or post- (Zellmer et al., 2020), -caldera regions are thought to be sourced from smaller, drier melt fractions deeper in the mantle, and do not contribute to caldera-forming volcanism. Basalt such as this occurs in inter-caldera regions in the central portion of the central TVZ, between the currently active Taupo and Okataina volcanic centres, and correspond to the hot, dry reducing trends

observed in Rooney and Deering (2014). Whilst only trends within the central TVZ are considered in Barker et al. (2020) and Rooney and Deering (2014), comparison with basalt from the south TVZ is included in Zellmer et al. (2020). It is suggested basalt from the south TVZ is also sourced from large, hydrous melt fractions in the shallow mantle, similar to the intra-caldera basalt of the central TVZ. As the south TVZ is in the waxing stages of magmatism, the south TVZ can therefore be considered as a pre-caldera forming setting. Accordingly, the mantle becomes more depleted through the three stages of pre-, syn-, and post-caldera volcanism (Zellmer et al., 2020). Hf isotopic evidence also requires greater slab contributions in the the south TVZ (Waight et al., 2017), hinting at a rift-related transition from arc-like andesitic volcanism in the south, to a rifted arc in the north, with less contribution from the slab.

In this contribution, we use the composition of xenocrystic olivine, combined with whole rock trace element models, from basalts from the central and south TVZ to constrain the nature of the mantle source region beneath the TVZ. Olivine is a unique petrogenetic indicator, comprising (40-90%) of the Earth's upper mantle, and is the first mineral to crystallise from almost all primary mantle melts (Foley et al., 2013). For these reasons, it has been widely used to provide insights into the composition (Lynn et al., 2017; Sobolev et al., 2005) and melting regimes (e.g. extent of melting, pressure), (Matzen et al., 2017b; Prelevic and Foley, 2007; Sobolev and Shimizu, 1993) of the mantle. However, magmatic processing in the crust can also have a major influence on olivine composition (Herzberg et al., 2016; Lynn et al., 2017; Gleeson and Gibson, 2019), meaning careful examination of olivine textures and olivine minor element chemistry is essential before making inferences on mantle compositions and or melting regimes. Here, we use minor element chemistry of TVZ basalt-hosted olivine xenocrysts to identify overprinting due to fractionation and magma mixing. By modelling the effects of these crustal processes, we can use olivine core compositions to infer the nature of the mantle source region for TVZ basalts.

6.3 Analytical Techniques

We examined seven HABs, two HMBs, one HMBA and one BA (basaltic andesite) with abundant mafic glomerocrysts similar to HMBs, from the length of the TVZ (Figure 1.2). Back-scatter electron (BSE) images were taken on a Zeiss SIGMA field-emission scanning electron microscope (SEM) to identify the largest and most primitive olivines. Approximately 50 olivine crystals were selected and analysed on a Cameca SX100 EPMA in the Department of Earth Sciences, University of Edinburgh, with a sum of approximately 300 point analyses. Profiles across olivines were mostly concentrated into the four samples containing group two and three olivine, which were Rotomakariri, Ongaroto, Waimarino and Ohakune. This decision was based on available preliminary olivine data from Allen (2011) (Appendix A.1), and detailed petrography of the samples (Chapter 3). Inclusions of Cr-spinel occur in olivines from Ongaroto, Waimarino and Ohakune, and were analysed alongside olivine compositions for use with the Al in olivine thermometer of Wan et al. (2008) and Coogan et al. (2014). Analysing conditions are listed in Chapter 2. Secondary standards are reported in Appendix A.1, alongside the full olivine and spinel dataset. Ratios of FeO to Fe_2O_3 in spinel were calculated stoichiometrically. Temperatures from olivine-spinel pairs were calculated using the equations of Wan et al. (2008) and Coogan et al. (2014), and fO_2 in olivine-spinel pairs was calculated using the equation of Ballhaus et al. (1991).

6.4 Sample Characterisation

Key sample characteristics are listed in Table 6.1. Geochemical classification is based on whole rock compositions and petrology (Gamble et al., 1990; Hiess et al., 2007; Kósik et al., 2016) and petrology (Chapter 3). HAB is prevalent in the NC-TVZ and C-TVZ, whereas HMB and HMBA is prevalent in the S-TVZ. Samples have variable crystal content, ranging from aphyric to porphyritic (>30% crystals). Crystallising as-

semblages, along with crystal compositions, are highly variable. Olivine plus clinopyroxene dominate HMB assemblages, with the addition of orthopyroxene in HMBA, whereas plagioclase is the dominant phase, with minor pyroxene and olivine in HAB (Gamble et al., 1990).

Samples contain texturally diverse olivine crystals that can be divided into three groups. Group 1 olivines are euhedral phenocrysts <500μm and are present in all basalt (HMB + HAB) samples, but absent from BA and HMBA (Figure 3.1, 3.2, 3.5, 3.7). Group 2 are large (>500μm) subhedral olivine crystals co-grown with oscillatory zoned clinopyroxene and are present in BA and HMBA (Figure 3.3, 3.10). In Ohakune, this same texture of subhedral olivine is also co-grown with orthopyroxene. Group 3 olivine, present in Waimarino and Ongaroto, is subhedral to euhedral, contains highly forsteritic cores, and a thin (<30μm) overgrowth of microcrystalline orthopyroxene (Figures 3.6,3.9).

Table 6.1: **Table summarising key characteristics of samples**

Location	Segment	Name	Class	Crystal content	Crystal ass.	Pops.	Max. NiO
CTVZ-N	Syn	Rotokawau	HAB	25%	Pl>Cpx>Ol	1	0.14
CTVZ-N	Syn	Tarawera	HAB	<5%	Pl>Cpx>Ol	1	<0.1
CTVZ-N	Syn	Rotomakariri	BA	20%	Pl>Cpx>Ol	2	<0.1
CTVZ-N	Syn	Terrace Rd	HAB	25%	Pl>Cpx>Ol	1	<0.1
CTVZ	Post	Johnson Rd	HAB	10%	Pl>Ol>Cpx	1	<0.1
CTVZ	Post	Ongaroto	HMB	25%	Ol»Cpx=Pl	1 & 3	0.37
CTVZ	Post	Kakuki	HAB	10%	Pl>Ol»Cpx	1	0.14
CTVZ	Post	Orakeikorako	HAB	25%	Pl>Cpx=Ol	1	<0.1
STVZ	Pre	Waimarino	HMB	25%	Ol>Cpx»Pl	1, 2, 3	0.56
STVZ	Pre	Ohakune	HMBA	15%	Cpx=Opx>Ol	2	0.23

6.5 Olivine and spinel chemistry

Olivines from all samples show normal zoning from core to rim (Figure 6.1) but can be grouped into three categories based on compositional and textural differences. All

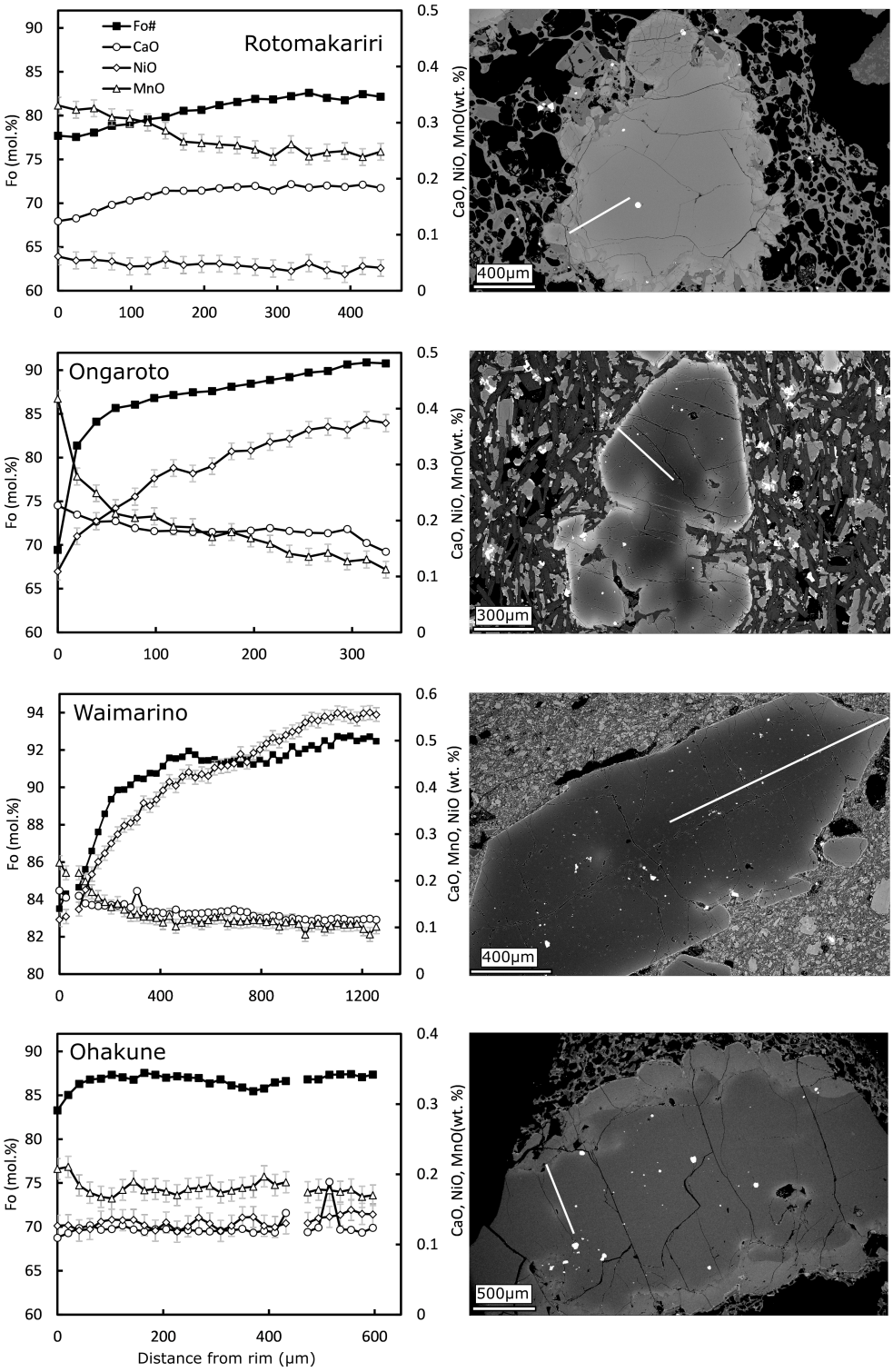

Figure 6.1: BSE images and compositional profiles of TVZ olivines. Group 2 olivines are shown in Rotomakariri and Ohakune images; Group 3 olivines are shown in Ongaroto and Waimarino images. White lines indicate location of tracks. Error is smaller than symbols, except where shown.

HABs contain only phenocrystic group 1 olivine. Compositions range up to Fo_{86} in the most primitive cores, with minor element concentrations consistent with magmatic olivines (De Hoog et al., 2010). NiO is <0.2 wt.% and CaO is >0.18 wt.%. Group 1 olivines show normal zoning, down to Fo_{65}, with some outliers in Orakeikorako and Rotokawau as low as Fo_{53} (Figure 6.2). Rim compositions are in equilibrium with groundmass olivine, where present (See Appendix A for olivine chemistry). Both HMBs also contain group 1 olivine compositions. Group 1 compositions are present as microphenocrysts and in the rim zones of larger crystals with cores of higher forsterite content.

Group 2 olivines, are present in Rotomakariri (BA), Ohakune (HMBA) and Waimarino (HMB). Group 2 olivines are weakly zoned in forsterite content and minor element concentrations. Compositions range from Fo_{72-88} but are homogeneous within individual crystals. Ohakune and Waimarino contain only olivines at the upper end of this range, Fo_{85-88}, whereas olivines in Rotomakariri span the whole range of compositions. CaO contents are low, at <0.15 wt.% (Figure 6.2). This is consistently lower for a given forsterite content compared to group 1 olivines. NiO is 0.1 - 0.15 wt.% in Waimarino and Ohakune, whereas in Rotomakariri NiO is <0.07 wt.% (Figure 6.2). P is below detection in all group 2 olivines from Waimarino and Ohakune and is approximately 100±50 ppm in the lower-forsterite olivines in Rotomakariri. This is very close to the detection limit (<70 ppm) (see Chapter 2.2 for analysing conditions) and is deemed insignificant. More-forsteritic olivines in Rotomakariri also have P concentrations below detection.

Group 3 olivine compositions are defined by forsterite content $Fo_{>90}$, NiO >0.3 wt.% and CaO <0.15 wt.%. Group 3 compositions are present in Waimarino and Ongaroto. In these samples, approximately 8% of olivine macrocrysts have cores of group 3 composition. The core compositions are up to $Fo_{92.5}$ and $Fo_{90.6}$ for Waimarino and Ongaroto, respectively, primitive enough ($Fo_{>90}$) to be mantle-derived (De Hoog et al., 2010). The proportion of group 3 olivines was calculated by calibrating greyscale BSE

maps of polished thin sections to measured forsterite content from EPMA data. All macrocrystic olivines in a section were then traced using imageJ software and thresholded to reveal the proportion of olivines with cores Fo>90. Analysis encompassed an average 400 olivines measured per section, with 30-40 olivines containing high-forsterite ($Fo_{>90}$) cores. NiO in the high-forsterite cores is up to 0.56 wt.% (4411 ppm Ni) and 0.37 wt.% (2904 ppm Ni) in Waimarino and Ongaroto, respectively (Fig.3). CaO in group 3 composition olivine cores for both samples is consistently between 0.1 and 0.15 wt.% (830-1100 ppm Ca) (Figure 6.2), while P is below the detection limit (<70 ppm). Group 3 compositions are only present in crystal cores. The rims of olivines with group 3 composition cores do not have the composition of mantle-derived olivine and are normally zoned down to Fo_{64} in Ongaroto and Fo_{85} in Waimarino, correlating with decreases in NiO and increases in CaO (Figure 6.1). The rim composition falls into the group 1 category; however neither sample contains groundmass glass or groundmass olivine, so it is not possible to assess whether rim compositions were in equilibrium with the melt. Often, rims are overgrown by microcrystalline orthopyroxene, suggesting disequilibrium with the final melt. Phosphorus remains below detection in the rims of olivines with group 3 composition cores in Waimarino, but in Ongaroto up to 400ppm P is detected in the outermost rim zones, indicative of rapid growth (Milman-Barris et al., 2008).

HMB samples contain olivine compositions from both groups 1 and 3. Olivines with group 3 core compositions have group 1 composition rims, producing normal zoning from core to rim. HAB samples only contain group 1 olivine compositions. However, there is a systematic offset in NiO between group 1 compositions in HMBs and HABs, where the former show relative enrichment in NiO for a given forsterite content when compared to the latter (Figure 6.2). All single-crystal olivines in HMB samples exhibit this trend, indicating that the process controlling the rim zonation in these crystals is the same.

Spinel occurs as inclusions in olivine from Ongaroto (HMB), Ohakune (HMBA)

and Waimarino (HMB), and forms two distinct chemical trends: a Cr-Al trend and a Fe-Ti trend (Fig. 4). All three samples contain spinel inclusions that fit a Cr-Al trend, whereas only Ongaroto contains additional spinel that fits a Fe-Ti trend (Figure 6.3). The Cr-Al group from Waimarino and Ohakune have Mg# of 40-70 (atomic Mg/(Mg+Fe) *100), Cr# of 70-80 (atomic Cr/(Cr+Al) *100), and TiO_2 of <0.7 wt.%. Some spinel from Ongaroto also follows a Cr-Al trend, but with Cr# of 50-65. These are restricted to the high-forsterite cores of group 1 Ongaroto olivines. Seven of the 14 spinels in Ongaroto olivines define the Fe-Ti trend (Figure 6.3), with increasing Fe^{3+} and TiO_2, towards the rims of the host olivine. Spinel from the Fe-Ti group overlap magmatic fractionation trends, with Mg# and Cr# decreasing with forsterite content of the host olivine, and Fe^{3+} and TiO_2 increasing, pushing compositions towards a Fe-Ti oxide.

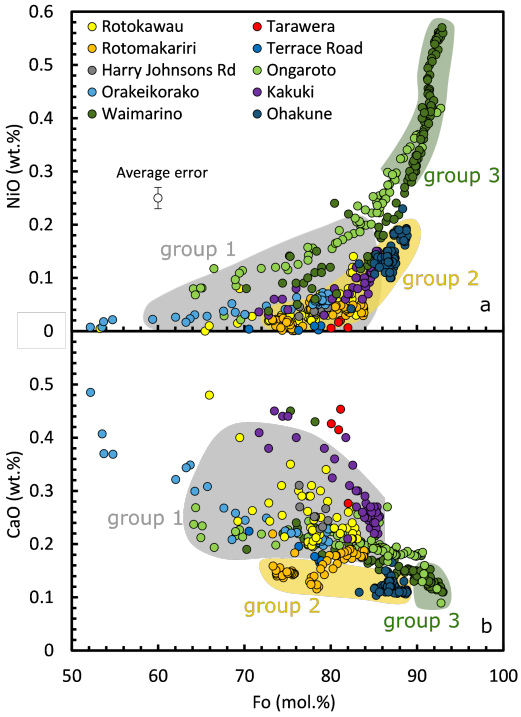

Figure 6.2: a) Fo vs. NiO in olivine. Note the higher concentrations of NiO at lower Fo in Ongaroto and Waimarino olivine. b) Fo vs. CaO in olivine. CaO concentrations are higher in group 1 olivine than in group 2 and 3 olivine at a given forsterite content.

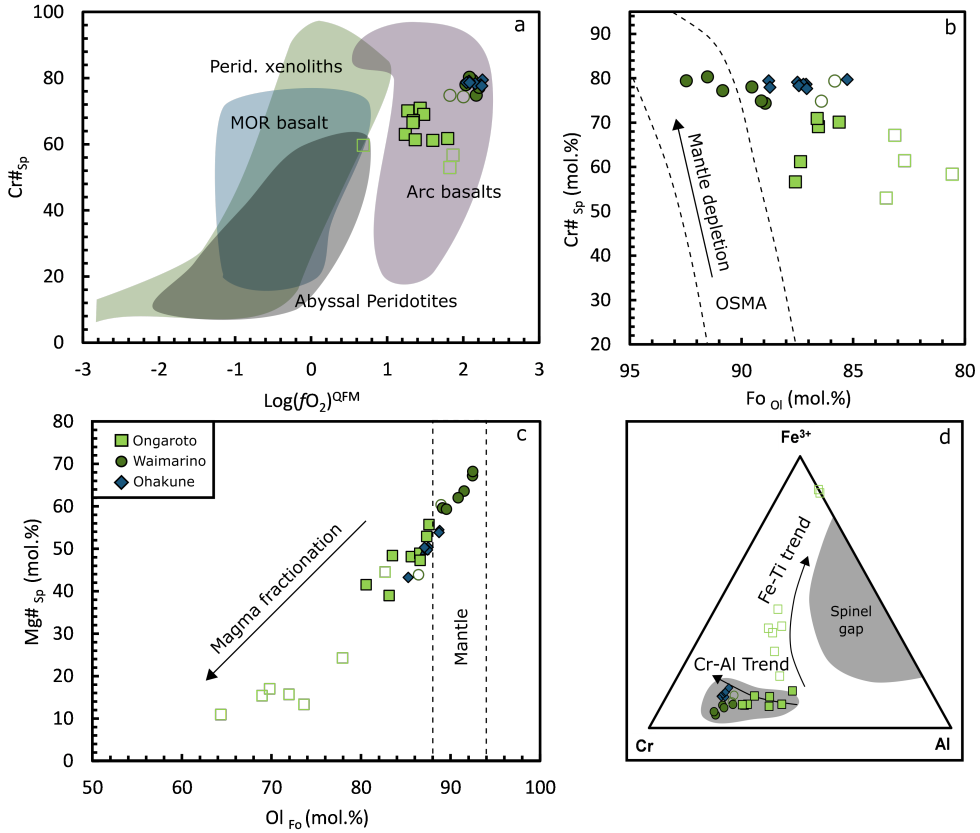

Figure 6.3: a) log FO_2 vs the Cr# of spinels. fO_2 calculated from Ballhaus et al. (1991). Compositional fields also Ballhaus et al. (1991). b)Forsterite content of host olivine vs. Cr# of spinel inclusion. OSMA and direction of mantle depletion from Arai (1994). c) Forsterite content of host olivine vs. Mg# of spinel inclusion. Mantle and magmatic fields also from Arai (1994). d) Proportions of $^{3+}$ ions in spinels. Compositional trends from Barnes and Roeder (2001). Filled colour symbols represent spinel inclusions from cores of olivines. Empty symbols with coloured rims represent spinel inclusions near the rims of olivines.

6.5.1 Al in olivine thermometry

Spinel inclusions in Ongaroto and Waimarino olivine cores are appropriate compositions for use in Al in olivine thermometry (Wan et al., 2008; Coogan et al., 2014). Using the equations of Wan et al. (2008), Ongaroto olivine-spinel pairs yield temperatures of 1200°C +/- 40°C (n=8 st.dev = 28°C). Waimarino olivine-spinel pairs yield temperatures of 1168°C +/- 40°C (n=8, st.dev = 24°C). The error on the calculation (+/- 40°C) is larger than the error calculated in Wan et al. (2008) (+/- 20°C) and is propagated from the error on the measurement of Al in olivine. Using the updated calibrations of Coogan et al. (2014) temperatures are within 3°C of those calculated using Wan et al. (2008). The calculated temperatures are within error of one another, however increasing precision on the measurement of Al in olivine would reduce the error on Al and could potentially reveal more information on temperatures shifts between samples.

6.6 Discussion

Magmatic processes occurring in the crust, such as fractional crystallisation, assimilation and magma mixing have the ability to overprint and obscure primary mantle-derived signatures in olivine (Gleeson and Gibson, 2019; Herzberg et al., 2016; Lynn et al., 2017). We need to circumvent the effects of these processes in order to assess any mantle-derived signatures they may hold. Therefore, we have modelled the effects of fractional crystallisation and magma mixing on the olivine cargo to filter out magmatic processes. The remaining olivines are then assessed for their potential as mantle-derived xenocrysts, and discussed in light of alternative models for producing high-Fo, high-Ni olivines (Matzen et al., 2017a, 2013; Sobolev et al., 2005).

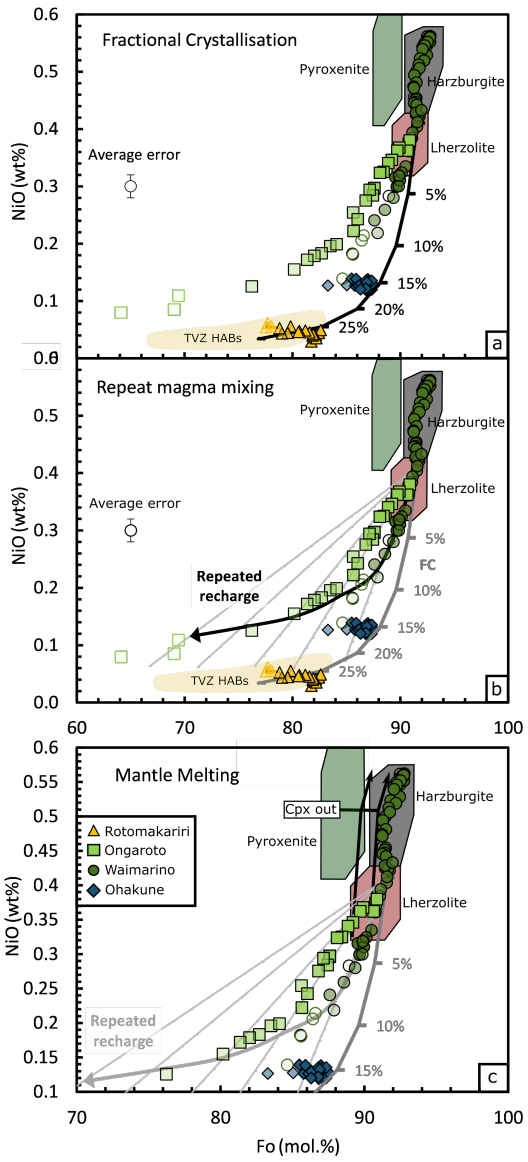

Figure 6.4: Modelling of olivine compositions in Fo vs. NiO space. a) Trajectory of fractional crystallisation model using Petrolog (Danyushevsky and Plechov, 2011) and the model of Beattie (1993). b) Trajectory of repeated magma mixing events, adapted from Gleeson and Gibson (2019) and Straub et al. (2011). c) Trajectory of mantle olivine composition at increasing fractions of melt extraction modelled using MELTS (Asimow and Ghiorso, 1998; Ghiorso and Sack, 1995). Mantle compositional fields from Straub et al. (2011) and Workman and Hart (2005). Opaque symbols represent crystal cores, translucency increases towards rims.

6.6.1 Crustal processing

To test the effect of fractional crystallisation on olivine chemistry we conducted forward models of crystallisation using *Petrolog* software (Danyushevsky and Plechov, 2011). Model details and parameters are presented in Appendix A.7. We simulate crystallisation of olivine only from the melt as this is the only macrocryst phase in Ongaroto, and the first phase to form in all other magmas (Gamble et al., 1990). This simplifies the model by allowing $D_{bulk} = D^{Ni}_{Ol}$. $D^{Ni}_{Ol} = 8$ was calculated from equation 2b in Putirka et al. (2011). The melt composition is a natural near-primary HMB composition from Gust and Perfit (1987) adapted to be in Fe-Mg equilibrium (Roeder and Emslie, 1970) with the most primitive non-mantle olivines from the TVZ (Fo_{90}) (Table 4.1 (HMB)). The model was run at 5kbar as a representative depth for the mid crust in the TVZ; However the model was also run at 10kbar and 1kbar and was shown to be insensitive to changes in pressure. The model was run until 30% fractionation had occurred, at which point it intersected the lowest forsterite compositions. Olivine compositions from HABs are consistent with fractional crystallisation (Figure 6.4). Olivine compositions from HABs have lower maximum forsterite content than primary magma ($< Fo_{90}$) and therefore represent melts that have experienced earlier fractionation and removal of more primitive olivine, consistent with the notion that HABs are not primary basalt (Gust and Perfit, 1987; Sisson and Grove, 1993b).

Group 2 olivines in Rotomakariri and Ohakune are also consistent with prior fractionation of olivine, despite their large size and low CaO contents. However, NiO contents are constant from core to rim, which is inconsistent with fractionation and suggests equilibration of NiO across the grain. Therefore, group 2 olivines are derived from primitive but non-primary melts that have experienced variable degrees of fractionation, with a period of re-equilibration to produce flat forsterite and NiO trends from core to rim.

Group 1 and 3 olivine compositions in Waimarino and Ongaroto have forsterite vs.

NiO trends that are offset to higher NiO at lower forsterite, and cannot be explained by simple crystal fractionation. This trend occurs in the mid to rim zones of all group 1 and 3 olivine (indicated by translucent (mid zones) and hollow (rims) symbols in Figure 6.4), and overprints the primary magma fractionation trend. The lowest forsterite zones show the greatest enrichment in NiO when compared to the modelled fractional crystallisation trend (Figure 6.4), suggestive of a magmatic control. Alternate episodes of fractionation and magma recharge can produce elevated NiO contents in olivines at lower forsterite content. Gleeson and Gibson (2019) produced a mathematical model showing NiO enrichment in fractionated ocean-island olivines can arise as a result of multiple episodes of magma recharge. Here we have adapted the model to reflect crystallisation of olivine in conditions appropriate for the TVZ.

Using the same primary magma composition and D value as above, we ran models of fractional crystallisation (Appendix A for model parameters). At 200°C intervals a batch of fresh magma of the initial composition was added. Each recharge event was assumed to be equal to the initial volume of melt input, meaning that for each subsequent recharge event, the ratio of fresh melt to fractionated melt would decrease, and hence the influence of the recharge event on the melt would also decrease with time. After each recharge event the composition of the mixed magma composition was used to start the next iteration of fractionation. This model effectively reproduces the trend observed in mid-rim zones of group 1 and 3 Ongaroto and Waimarino olivine (Figure 6.4), and indicates that injection of multiple batches of mantle-derived magma contributed to the final eruption of these basalts, and have overprinted the chemistry of the mid to rim zones of the olivines.

6.6.2 Mantle origin of olivine cores and Cr-spinel inclusions

Fo and NiO contents in group 3 olivine cores from Ongaroto and Waimarino (Fo_{90-93}; 0.33-0.56 wt.%) are too high to have crystallised from a fractionated mantle-derived

melt. Group 3 compositions have forsterite contents (>Fo_{90}) that reflect either crystallisation of olivine from a primitive or primary mantle melt, or residual olivine from a mantle lithology. Group 3 Olivine cores from Ongaroto have compositions that overlap with mantle lherzolite (Figure 6.4). However, their compositions could also be in equilibrium wih a primary mantle melt derived from partial melting of lherzolite. Group 3 Ongaroto olivine cores contain numerous small inclusions of Mg-chromite composition spinel, with Cr#'s of 56-70, typical of mantle lherzolite (Arai, 1994; Ballhaus et al., 1991; Workman and Hart, 2005). However, Barker et al. (2020) report olivines in Ongaroto with compositions matching group 3, hosting primitive melt inclusions, suggesting a magmatic origin for these olivines. Like conposition, crystal habit is not a definitive discriminant between magmatic and mantle-derived olivine. Subhedral xenocrystic olivine cores overgrown by magmatic olivine rims produce euhedral crystals (Boudier, 1991). Olivine rims which have a magmatic, not mantle-derived composition, record periods of basaltic fractionation and repeated episodes of magma recharge. This could explain the euhedral shape of olivines with group 3 composition cores, if the cores were mantle-derived (Boudier, 1991). However, the presence of melt inclusions in Fo_{90} composition olivine reported by Barker et al. (2020) strongly suggests a magmatic origin of the group 3 composition cores in Ongaroto. The melt that these olivines crystallised from must have been derived from a lherzolite source rock, with minimal fractionation prior to crystallisation of the group 3 cores, in order to remain in equilibrium with the lherzolite mantle and retain such high NiO contents.

Waimarino olivine cores with Fo and NiO contents that are too high for them to be xenocrysts entrained in the melt from mantle lherzolite (Figure 6.4) also contain highly refractory Cr-spinel ($Cr\#_{70-80}$) (Figure 6.3a). It has been suggested that olivine phenocrysts with similar compositions (Fo_{91-93}; NiO > 0.45 wt.%) in basalt from plume settings crystallised from magma derived from pyroxenite lithologies in the mantle, because lower bulk D_{Ni} in the olivine-free pyroxenite leads to enrichment of Ni in the partial melt (Sobolev et al., 2005). Pyroxenite xenoliths are found in a range of

tectonic settings, so it is possible the sub-arc mantle beneath the TVZ is not composed solely of peridotite but contains veins of pyroxenite. It then follows that the high NiO content of the olivine could be due to a higher NiO content in the primary magma resulting from melting an olivine-free source (Straub et al., 2008, 2011, 2014).

The solidi of pyroxenite and peridotite are similar in the presence of water, but melt productivity is higher for pyroxenite than peridotite at a given temperature and pressure (Sorbadere et al., 2013). Therefore a relatively small proportion of pyroxenite in the source can have a large effect on the relative proportion of melt supplied by pyroxenite and peridotite and hence on the aggregate melt composition. We modelled a hypothetical melting scenario of a mixed pyroxenite-peridotite source for south TVZ samples to test whether a pyroxenite contribution to south TVZ magma would be consistent with observed trace element compositions. The pyroxenite:peridotite ratio was assumed to be 1:9. Melt fractions were assumed to be 0.6 and 0.1 for pyroxenite and peridotite, respectively. The modelled pyroxenite-peridotite mixed composition is shown as the thick black line on Waimarino and Ohakune multi-element plots in Figure 6.6. Given these assumptions the model shows that a pyroxenite contribution from pyroxenite can reasonably explain the whole rock composition of the south TVZ samples. Increasing the proportion of pyroxenite in the source produces overall lower concentrations of trace elements in the melt, due to the higher productivity of pyroxenite, and also has the effect of decreasing concentrations of REE to a greater extent than LILE, due to the overall increased compatibility of REE in pyroxenite over an olivine-dominated mantle source. The maximum proportion of pyroxenite in the source that satisfies the trace element profiles of south TVZ samples is approximately 40% pyroxenite to 60% peridotite. Therefore, a wide range of pyroxenite in the source could satisfy the trace element budget of south TVZ samples. However, south TVZ samples have high MgO content at high SiO_2, and low CaO/Al_2O_3 ratios (Gamble et al., 1993; Graham and Hackett, 1987). Experiments show that pyroxenite-derived melts have similar major element compositions to MORB, but cannot produce melts that have both high SiO_2

and high MgO, with low CaO/Al_2O_3 ratios (Lambart et al., 2009, 2013). Additionally, involvement of pyroxenite does not provide a way of producing high forsterite content in olivine, which is a key criteria in group 3 Waimarino olivine. Whilst we cannot rule out involvement of pyroxenite in the mantle based on the available data, it does not sufficiently explain the data.

Alternatively, the higher nickel content in Waimarino olivine could be associated with the dependence of D_{Ol}^{Ni} on temperature. Matzen et al. (2013, 2017a) showed that D_{Ol}^{Ni} decreases with increasing temperature, emphasising the importance of ΔT between the source and storage region on the compatibility of Ni. For example, a decrease of 100°C results in a 0.05 wt.% increase in NiO in crystallising olivine. If the high-Ni olivines were magmatic, D_{Ol}^{Ni}=8 (Putirka et al., 2011) would require that the Ongaroto olivines crystallised from a magma with approximately 400ppm Ni. Although whole-rock concentrations of Ni are 140ppm for Ongaroto, a value of 400ppm Ni in the magma would approximate a typical primary mantle melt, in line with the highly primitive nature of the Ongaroto olivine cores. For Waimarino, a melt with 700ppm Ni would be required to produce olivines containing 0.56 wt.% NiO. This is significantly higher than a typical primary mantle melt, and the whole-rock Ni content of 340ppm for Waimarino, and constitutes a predicted difference in the Ni content of the magma of 300ppm between the two samples. Assuming no significant variation in primary melt MgO, which also controls D_{Ol}^{Ni}, this variation in melt composition could be produced by a reduction in D_{Ol}^{Ni} from 8 to approximately 3.7. This corresponds to a temperature difference between the source of Ongaroto olivine and the source of Waimarino olivine of approximately 540°C (Matzen et al., 2017a). Such a large difference in temperature between Ongaroto and Waimarino mantle sources is not feasible. Additionally, Al in olivine thermometry (Wan et al., 2008) yields core temperatures of 1200°C +/- 40°C for Ongaroto and 1168°C +/- 40°C for Waimarino. Therefore, it seems unlikely the variation in NiO in the Ongaroto vs. Waimarino olivine is due to temperature alone.

It is more likely that Ni-rich forsteritic cores from Waimarino olivines represent

xenocrysts derived from strongly depleted mantle. To test this, we took the composition of the depleted MORB mantle (DMM) (Workman and Hart, 2005) and ran a melting model using MELTS (Asimow and Ghiorso, 1998; Ghiorso and Sack, 1995), similar in method to Hirschmann et al. (1998). The model was set at 1 GPa, a pressure corresponding to the base of the crust beneath the TVZ (Harrison and White, 2006; Stratford and Stern, 2006), and fO_2 of QFM+1, corresponding to fO_2 values using the spinel oxygen barometer of Ballhaus et al. (1991) (Figure 6.3b). T was increased at 1°C intervals until 20% melting had occurred. At 15% melt, all clinopyroxene had melted out (Figure 6.4), resulting in a harzburgitic residue. A detailed description of using MELTS to calculate peridotite melting can be found in Hirschmann et al. (1998). The model simultaneously reproduces the observed increase in Ni and forsterite content between lherzolite-derived olivine cores from Ongaroto and the high-Fo, high-Ni cores from Waimarino, suggesting that the Waimarino cores are most likely harzburgite-derived xenocrysts. Decreasing the availability of Fe^{2+}, and therefore the total Fe that ca be incorporated into olivine, by increasing fO_2 to QFM+2 (Rowe and Tepley, 2016), exaggerates this trend and produces similar increases in Fo and Ni at 1 mol.% higher Fo for a given melt fraction. Therefore, the high NiO cores from Waimarino more likely reflect previous high volumes of melt extraction on residual mantle olivine, rather than any chemical heterogeneities in the source region for TVZ basalts. This result suggests that high-Ni, high-Fo cores from Waimarino olivines may be harzburgite-derived mantle xenocrysts.

Datasets of xenocrystic and phenocrystic olivine have been compiled to further investigate the source of the Waimarino xenocryst cores (Figure 6.5). Xenocrystic olivine from the lithospheric mantle beneath New Zealand (Brenna et al., 2018; McCoy-West et al., 2014; Scott et al., 2014) has forsterite, NiO and CaO concentrations similar to the Waimarino olivine cores. CaO in NZ lithospheric mantle olivines is concentrated around 0.05-0.11 wt.%, however many olivines have CaO concentrations up to 0.17 wt.%. The CaO content of Waimarino olivine cores is 0.10-0.14 and therefore elevated

in comparison to the main cluster of lithospheric xenocrysts, but well within the total range of observed values (Figure 6.5). NiO concentrations of Waimarino olivine cores also show significant overlap with NZ SCLM olivines, but extend 0.03 wt.% higher than the highest NiO from the SCLM olivines. The SCLM beneath New Zealand is believed to be depleted, but has also undergone variable amounts of refertilisation, potentially by carbonatite melts (McCoy-West et al., 2014; Scott et al., 2014). The varied nature of the NZ SCLM could explain the small offsets in minor element composition of the olivines. The composition of NZ SCLM olivine is similar to other xenocrysts interpreted as originating from the depleted mantle wedge (asthenospheric or lithospheric) in arc settings (Rohrbach et al., 2005), again at moderately higher CaO contents (Figure 6.5).

The alternative is that Waimarino olivine cores are magmatic and either pheno- or antecrystic. Magmatic olivines with simultaneously high forsterite (>Fo_{90}) and NiO contents are uncommon as most magmatic high-NiO olivines are crystallised from a magma derived from a pyroxenite source, resulting in an inherently lower Mg# of the magma. However, Elburg et al. (2006) report high-forsterite and low CaO magmatic olivines from South Sulawesi, Indonesia. These olivines have high NiO contents, up to 0.44 wt.% NiO, which is significantly higher than typical magmatic olivine, and 0.1-0.3 wt.% CaO. These olivines are interpreted as crystallising from a magma with high MgO and low CaO contents. Whilst there is some overlap with the Waimarino olivine compositions, the majority of the South Sulawesi olivines have significantly higher forsterite (up to Fo_{95}, higher CaO (0.16-0.2 wt.% CaO) and lower NiO (0.37-0.44 wt.% NiO) than the Waimarino population. Additionally, the South Sulawesi olivines contain melt inclusions, indicative of a magmatic origin, whereas Waimarino olivines are melt inclusion free. Therefore, despite minor variations in composition, Waimarino olivine compositions most closely resemble compositions of SCLM-derived olivines from New Zealand, and this remains the best explanation for their origin.

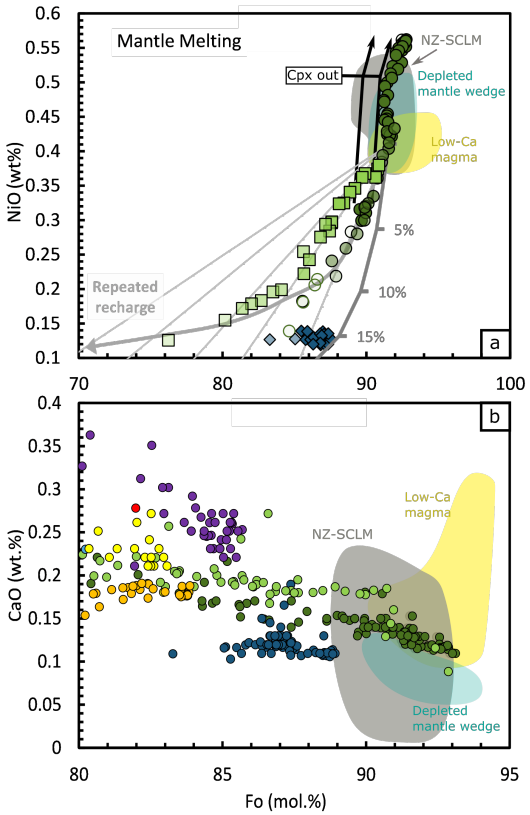

Figure 6.5: Comparison of the forsterite, NiO and CaO contents of TVZ olivine to various magmatic and mantle-derived olivine compositions. NZ SCLM compositions are from Brenna et al. (2018)(Auckland Volcanic Field xenocryst cores), McCoy-West et al. (2014) and Scott et al. (2014). Low Ca magmatic olivines are high forsterite, low CaO and high NiO olivines from Elburg et al. (2006), interpreted as olivines crystallised from a CaO depleted magma. Depleted mantle wedge olivines are from Rohrbach et al. (2005) interpreted as xenocrysts incorporated from lithospheric or asthenospheric mantle in the mantle wedge.

6.6.3 Low-Ca olivine

Group 2 olivine in Ohakune and Rotomakariri have Fo and NiO consistent with fractionation from a primary mantle melt (Figure 6.4, section 6.6.1). However, they also have CaO concentrations (<0.15 wt.%), lower than expected for magmatic olivine (Foley et al., 2013). Group 2 olivines are largely unzoned, suggesting sufficient time for Fe-Mg diffusion and re-equilibration. CaO concentrations are consistent over a range of forsterite contents (Figure 6.1). Historically, based on the work of Simkin and Smith (1970) all low CaO (<0.1 wt.%) olivines have been assumed to have mantle origin. In Rotomakariri, individual, compositionally homogenous grains of olivine exist within glomerocrysts, but with Fo varying from 82-73 mol.% between glomerocrysts. In all of these glomerocrysts, and in Ohakune individual and glomerocrystic olivines, CaO is constant and <0.15 wt.%. This consistency in CaO across a range of forsterite contents in separate crystals suggests that the factor controlling the low CaO is magmatic, and that these crystals are not overgrown mantle xenocrysts.

The CaO content of magmatic olivine is sensitive to melt composition, crystallisation of coexisting phases (Herzberg, 2011; Kamenetsky et al., 2006; Li et al., 2012), temperature, pressure (Köhler and Brey, 1990) and H_2O content (Gavrilenko et al., 2016) of the melt. Low CaO due to elevated H_2O is unlikely as this does not fit with measurements of relatively low H_2O contents from melt inclusions in the south TVZ (Kilgour et al., 2013), and textural evidence suggests a common cause of low CaO between the Ohakune (south TVZ) and Rotomakariri (northern Central TVZ) olivines. There is also scant evidence for significant variation in magmatic T between samples with low CaO olivine, and those without. Evidence for the origin of the low-Ca olivine is present in the glomerocrysts that they are often found within. These glomerocrysts are antecrystic and consistent with being sourced from deep mafic/ultramafic cumulates. Two-pyroxene thermobarometry on Ohakune glomerocrysts indicates storage pressures of 4.8-5.4 kbar, corresponding to depths of 16-18km in the crust (Kósik et al.,

2016). Clinopyroxene is the dominant co-crystallising phase, which will have depleted the melt in CaO whilst having a lesser effect on the MgO content of the melt. Deep fractionation promotes clinopyroxene stability over plagioclase and is most consistent with producing the plagioclase-poor, pyroxene-rich mineral assemblages observed in the HMBs of the south TVZ. Therefore group 2 Ohakune and Rotomakariri olivines with low CaO are antecrystic and consistent with disaggregation from a deep rooted cumulate or crystal mush by the host magma on ascent through the crust.

6.6.4 Revisiting whole-rock trace elements

Recent studies have inferred a change in primary melt composition between basalt from areas of active caldera forming volcanism and basalt from inter-caldera regions (Barker et al., 2020). A temporal context between these regions is introduced by describing these as syn- (intra-) and post-caldera (inter-) forming settings: Basalt erupted in syn-caldera regions feeds active caldera systems, whereas basalt erupted in post-caldera regions is erupted through old inactive calderas and does not drive larger-scale volcanism. Syn-caldera basalt is sourced from large hydrous melt fractions in the shallow mantle, whereas post-caldera basalt is sourced from smaller drier melt fractions deeper in the mantle (Barker et al., 2020; Zellmer et al., 2020). This implies the mantle beneath the TVZ becomes more depleted through time with the waxing and waning of an individual caldera system (Zellmer et al., 2020).

The olivine xenocrysts discussed in this study are associated with a post-caldera basalt in the central TVZ (Ongaroto) and basalt from the south TVZ (Waimarino) (Table 6.1). The south TVZ is not discussed in Barker et al. (2020) but in Zellmer et al. (2020), it is suggested the south TVZ sources the largest melt fractions of magma from the shallowest depth in mantle of the three TVZ segments, with melt segregation pressures of around 1.1 - 1.5 Gpa. The south TVZ can be thought of as an immature system, in the initial waxing stages of magmatism, when compared to the mature caldera-forming

systems of the central TVZ. Thus, as magmatism progresses and the system waxes and wanes, the mantle source region becomes more depleted and melt fractions are smaller and sourced at greater depth.

A variety of whole rock geochemical datasets are available, with varying degrees of sample overlap, to compare olivine xenocryst compositions to melt chemistry and mantle melting regimes. The studies of Barker et al. (2020) and Rooney and Deering (2014) include samples from the central TVZ, whereas samples inclusive of the south TVZ are considered in Zellmer et al. (2020), Lee (2010) and the older datasets of Gamble et al. (1993) and Graham and Hackett (1987). We have combined these datasets for 6 representative samples; two from the south TVZ (pre-caldera setting), two from the north-central TVZ (syn-caldera setting), and two from the central TVZ (post-caldera setting), to assess whole-rock geochemical trends in comparison to mantle xenocryst data.

Multi-element plots for 6 samples are presented in Figure 6.6. All samples show enrichments in LILE, depletions in HFSE, and relatively flat REE trends, typical of arc volcanism. On the whole, the datasets are in good agreement with each other. However, there are some discrepancies. Data for Y in the (Zellmer et al., 2020) dataset is consistently lower than other datasets. In the Kakuki samples, there is considerable discrepancy between the data of (Rooney and Deering, 2014) and (Gamble et al., 1993), and (Zellmer et al., 2020), where the latter shows up to an order of magnitude higher concentrations of LILEs normalised to primitive mantle, in comparison to the former two sets of data, resulting in the highest La/Sm and Th/Nb ratios of all samples across all datasets. In context, this puts the different Kakuki sample analyses at opposite ends of the TVZ basalt array, with La/Sm the highest of all samples for the Zellmer et al. (2020) data, and amongst the lowest of the array for the Rooney and Deering (2014) and Gamble et al. (1993) data. The slope of REE from light to middle-heavy is also steeper than the other analyses for this sample. In the Ongaroto sample, there are anomalously low concentrations of U from the Gamble et al. (1993) dataset, and also

anomalously low Ta from the Zellmer et al. (2020) dataset. This is the only dataset where melt inclusion trace element data is available from Barker et al. (2020), which is in very good agreement with the data from Rooney and Deering (2014), and the other two datasets, disregarding the anomalous U and Ta. New data from Zellmer et al. (2020) for S-TVZ samples is compared to that of Gamble et al. (1993), with very good agreement for the Waimarino sample. Limited trace element data is available from Graham and Hackett (1987), which is in good agreement with more recent datasets from Lee (2010) and Zellmer et al. (2020).

Pre-caldera and syn-caldera samples show the greatest enrichments in LILE and greater depletions in HFSE in comparison to post-caldera samples. Post-caldera samples show only moderate enrichments in LILE and moderate depletions in HFSE. REE trends across all samples are gently sloping. Light REEs are enriched compared to heavy REEs, whereas middle-heavy REEs do not show great amounts of enrichment to heavy REEs. Absolute concentrations of REEs vary across samples, which are lowest in pre-caldera samples, higher in syn-caldera samples, and higher still in post-caldera samples.

Trace element variations are modelled in grey shading in Figure 6.6. Models were produced from a non-modal batch melting model of DMM (Salters and Stracke, 2004), using both garnet bearing composition representative of a deep mantle source, and spinel bearing composition, representative of a shallow mantle source, and the partition coefficients listed therein. Mineral modes are listed in Table 6.2. These are the same mantle input compositions for the melting models in Barker et al. (2020). Addition of slab-derived fluid was incorporated using the amphibolite-derived fluid composition and element mobilities from Tatsumi and Kogiso (1997) and a subducting sediment composition from Gamble et al. (1996). An average of the two compositions was used for the slab-derived fluid composition. We calculated up to 10% mixing between slab-derived fluid and DMM, and subsequent batch melting of these compositions up to F = 0.3. The best fit models are shaded grey and labelled in bold on each sample.

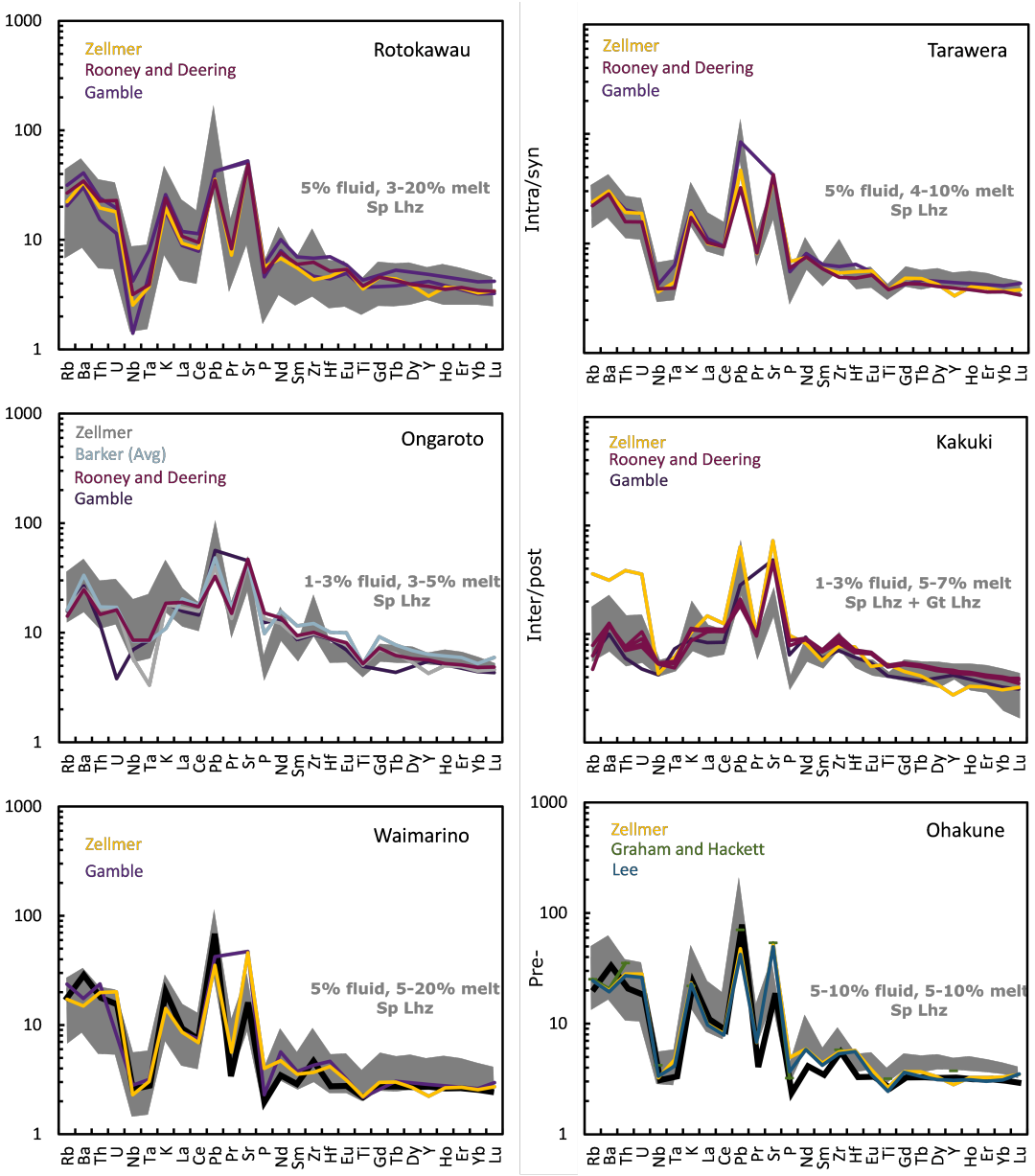

Figure 6.6: Primitive mantle normalised trace element plots of samples from syn-, post- and pre-caldera forming settings. Zellmer = Zellmer et al. (2020), Barker = Barker et al. (2020), Rooney and Deering = Rooney and Deering (2014), Gamble = Gamble et al. (1993), Lee = Lee (2010). Primitive mantle values from Sun et al. (1979). Grey shading shows modelled compositions. Models were created using deep and shallow depleted mantle compositions from Salters and Stracke (2004), fluid composition from Kogiso et al. (1997) and Gamble et al. (1996), element mobility from Tatsumi and Kogiso (1997), and non-modal batch melting. Best fit ranges are in bold grey text for each sample. Solid black line on Waimarino and Ohakune is modelled mantle melting from a hybrid pyroxenite-peridotite source.

Table 6.2: **Mineral modes from Salters and Stracke (2004) used in batch melting models.**

	Ol	Opx	Cpx	Gt
Deep (3Gpa)	0.53	0.08	0.34	0.05
Shallow (2Gpa)	0.53	0.29	0.18	

Syn-caldera samples require approximately 5% slab-derived fluid to produce the observed enrichments in LILE and depletions in HFSE. Smaller melt fractions cannot produce the enrichments in LILE, but also produce REE trends at significantly higher concentrations than observed. All REE trends are gently sloping and consistent with melting of a shallow mantle source. Overall, these samples are consistent with large melt fractions from a shallow mantle source with a 5% slab derived fluid contribution. Post-caldera samples have smaller enrichments in LILE and less pronounced depletion in HFSE than syn-caldera samples. These samples require a smaller slab-derived fluid contribution of 1-3% to produce these trace element variations. These samples also have overall greater concentrations of REE, and possibly suggest smaller melt fractions than syn-caldera samples, although models overlap considerably in this respect (Figure 6.6). The HREE patterns in the Ongaroto samples do not require a garnet-bearing source. However, HREE in the Kakuki sample are steeper, and may require a small amount of garnet in the source, although they are not consistent with either purely a spinel lherzolite or garnet lherzolite melting pattern.

The results of the models for syn- and post-caldera samples are largely consistent with both Zellmer et al. (2020) and Barker et al. (2020). Syn-caldera samples require greater slab-derived fluid contributions to post-caldera samples. However the evidence for larger melt fractions and the depth of melting is equivocal. Zr concentrations have been used to infer the fraction of melting in Barker et al. (2020), which are also highly susceptible to fractionation. A much more reliable test of melt fraction is a moderately incompatible to highly incompatible element ratio, such as La/Sm or Zr/Nb (Figure 6.7). There is no systematic difference between syn- and post-caldera samples with

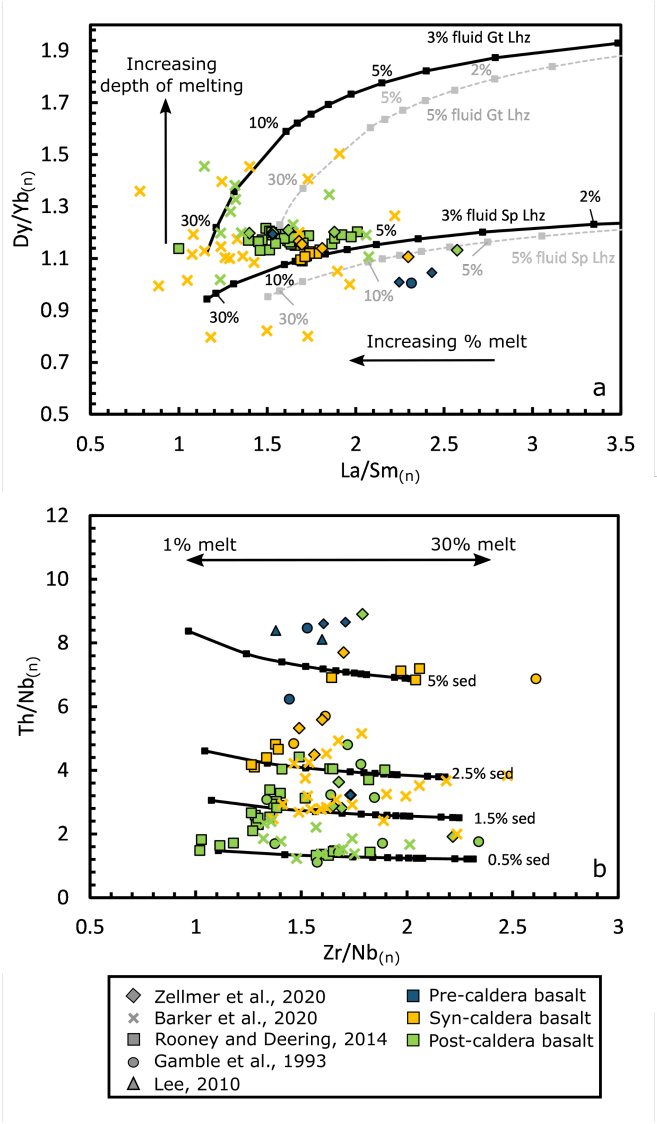

Figure 6.7: Primitive mantle normalised trace element ratio plots of samples from intra- or syn-caldera, inter- or post-caldera and pre-caldera forming settings. Zellmer = Zellmer et al. (2020), Barker = Barker et al. (2020), Rooney and Deering = Rooney and Deering (2014), Gamble = Gamble et al. (1993), Lee = Lee (2010). Primitive mantle values from Sun et al. (1979). A) Models were created using deep (Gt Lhz) and shallow (Sp Lhz) depleted mantle compositions from Salters and Stracke (2004). Grey dashed line shows the effect of additional fluid contribution to models. Fluid composition from Kogiso et al. (1997) and Gamble et al. (1996), element mobility from Tatsumi and Kogiso (1997), and non-modal batch melting. B) All models produced from spinel lherzolite compositions and a 50:50 mix of fluid (Kogiso et al., 1997) and sediment (Gamble et al., 1996). (Salters and Stracke, 2004), using garnet lherzolite has no effect on the model. Sediment compositions from Gamble et al. (1996).

respect to these ratios, showing that the variation in Zr co-varies with Nb concentration in the magmas, and La with Sm, a sign of degree of fractionation, rather than percentage of mantle melting. Additionally, there is no difference between Dy/Yb between the syn- and post-caldera samples, and both sets of samples are consistent with melting of spinel lherzolite, and do not require garnet in the source. Scatter around this is mostly within the melt inclusion dataset (Figure 6.7), but without any clear trends, whereas whole rock data closely follows the spinel lherzolite melting curve. However, it is clear that syn-caldera samples require a greater slab-derived contribution than post-caldera samples, in agreement with previous studies (Barker et al., 2020; Rooney and Deering, 2014; Zellmer et al., 2020). We therefore agree that in the central TVZ, melts with higher fluid contributions are sourced in areas of active caldera-forming volcanism, and melt fractions with lower fluid contributions are sourced in areas of waning volcanism, but see little evidence for association with melt fractions and depth of melting.

Pre-caldera samples show greater similarity to syn-caldera samples than post-caldera samples. These samples require the greatest slab-derived fluid contribution, between 5 and 10% to explain their enrichments in LILE and depletions in HFSE in contrast to their extremely low REE concentrations. Both Waimarino and Ohakune samples have overall very low and flat REE patterns, consistent with large melt fractions. These samples are indicative of shallow melting of a fertile lherzolite source with 5-10% slab-derived fluid. A significant difference between pre-caldera and syn-caldera samples is that pre-caldera samples have increased concentrations of Th, which is fluid immobile, in contrast to syn-caldera samples, which contain comparatively more Ba and Rb, typically fluid mobile elements. Th normalised to Nb indicates the degree of Th enrichment, where pre-caldera samples have the highest ratios of all TVZ basalts (Figure 6.7). Th enrichments are most easily explained by a slab sediment contribution, as opposed to a purely fluid contribution, which preferentially transports fluid mobile elements into the mantle wedge. Addition of 5% slab sediment component which is modelled from Gamble et al. (1996) subducted sediment composition explains the

Th enrichment in pre-caldera samples, indicating that pre-caldera samples require a slab sediment contribution in comparison to a purely fluid composition required for syn-caldera samples. This is consistent with Hf isotope evidence (Waight et al., 2017), which requires a greater sediment contribution for south TVZ basalt.

6.6.5 Implications on the lithosphere and mantle melting

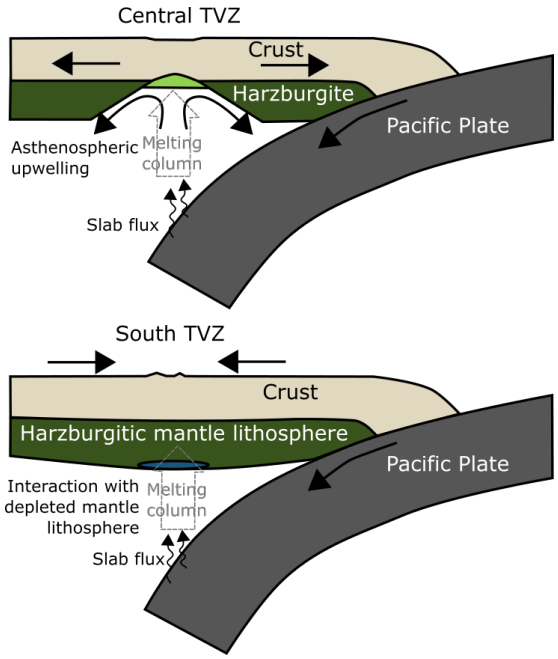

Figure 6.8: Schematic cartoon illustrating the effect of rifting on the depleted lithospheric mantle, adapted from Stern et al. (2006). South TVZ magmas are generated in mantle wedge but interact with depleted SCLM (McCoy-West et al., 2014; Scott et al., 2014) on ascent, promoting inheritance of harzburgitic olivine xenocrysts (Waimarino) and deeper stalling of magma (e.g. Ohakune - dark blue). Central TVZ magmas are still generated in the mantle wedge but rifting pulls apart SCLM leading to inheritance of lherzolitic olivine xenocrysts and promoting shallower stalling and underplating of magma (e.g Ongaroto - pale green).

Basalt-hosted olivines from the TVZ provide evidence for both lherzolite and harzburgite within the mantle source region. The presence of olivine xenocrysts of harzburgitic origin implies that basalt in the south TVZ has sampled regions of mantle already depleted by melting processes. In contrast, lherzolite-derived olivine cores imply that regions of the mantle sampled by the central TVZ are relatively undepleted

and have not been previously affected by large-scale melting (Figure 6.8). The olivine compositions appear to conflict with whole-rock and melt inclusion data, which suggest that the mantle became more depleted with ongoing magmatism at each volcanic centre (Zellmer et al., 2020). Accordingly, the south TVZ, a pre-caldera centre, should inherit olivine xenocrysts from fertile mantle, whereas Ongaroto, a post-caldera basalt, should inherit olivine xenocrysts from depleted mantle.

The sub-continental lithospheric mantle (SCLM) beneath New Zealand is harzburgitic in composition (Scott et al., 2014; McCoy-West et al., 2014), whilst the deeper asthenospheric mantle in the mantle wedge is most likely lherzolitic in composition. Crust in the south TVZ is up to 35km thick, in contrast to the extensively thinned crust (15km thickness) of the central TVZ (Stern et al., 2010; Stratford and Stern, 2006). During the initial stages of magma generation, as is currently occurring in the south TVZ, slab-derived fluids initially promote melt production in the mantle wedge. As magma ascends towards the crust, melts in the south TVZ interact with depleted, harzburgitic mantle and inherit xenocrysts. Interaction of hydrous basalt magma with refractory harzburgite promotes absorption of orthopyroxene into the magma, whilst stabilising residual olivine (Kelemen, 1990; Mitchell and Grove, 2016), resulting in magma enriched in MgO relative to CaO and Al_2O_3, as is observed in HMB and HMBA from the south TVZ. The potential for deeper storage due to the presence of thicker lithosphere promotes clinopyroxene stability over plagioclase,resulting in the olivine + clinopyroxene +/- orthopyroxene assemblages observed in HMBs and HMBA in the south TVZ (Cameron et al., 2010; Graham and Hackett, 1987).

In contrast, as rifting progresses, as is the case in the central TVZ, the lithosphere is thinned, promoting upwelling of asthenospheric mantle (Figure 6.8). As such, a spatial and temporal shift occurs from a subduction-flux-dominated mantle melting regime in the initial stages of magmatism, as in the south TVZ, to one that is controlled by both subduction-flux and decompression melting in the mature central TVZ. With ongoing rifting, the SCLM is thinned and replaced by asthenospheric lherzolite, and central TVZ

melts inherit olivine with this lherzolitic heritage. Lherzolite melting leads to relatively enriched magma with higher concentrations of CaO and Al_2O_3, producing magma similar in composition to TVZ HABs, which are concentrated in the central TVZ. Shallow storage of magma resulting from thinning fo the crust promotes plagioclase over clinopyroxene stablity, producing plagioclase-dominated mineral assemblages, similar to HABs (Gamble et al., 1990). Similar models have been proposed for other continental rifts, such as the Rio Grande rift. Without a slab fluid inducing melting in the mantle wedge, initial magma compositions reflect melting of SCLM. With progressive rifting, compositions are derived from melting of asthenospheric mantle (Fitton et al., 1991; McMillan et al., 2000), with the shift in magma composition associated with the pulling apart of the continental lithosphere. In the TVZ, harzburgite-derived olivine xenocrysts from the south TVZ most likely represent the interaction of basaltic melt with the depleted SCLM, rather than the magma itself arising from a depleted mantle source. Large melt fractions increase the reaction of refractory harzburgite (Mitchell and Grove, 2016), whilst the presence of thick SCLM may also promote deeper storage of magma in addition to inhibiting large melt fractions reaching the surface, consistent with lower erupted volumes in the south TVZ (Wilson et al., 1995b). In the central TVZ, mantle melts may become more depleted with ongoing melt extraction (Zellmer et al., 2020) whilst retaining a lherzolitic source. Basalt from both intra- and inter-caldera settings are expected to have xenocrysts of lherzolitic heritage if they were to inherit any. Additionally it is possible that the complexity of the magma plumbing system at intra-caldera settings (Cole et al., 2014) (Chapters 4, 5) inhibits basalt magma from retaining mantle-derived xenocrysts, whereas in inter-caldera settings where basalt magma has less interaction with the crust, it is more likely to retain its primitive composition and mantle-derived xenocrysts.

6.7 Conclusions

Basalt-hosted xenocrysts provide a useful insight into the mantle source region of one of the most productive magmatic regions on Earth. Variation in olivine composition allows for assessment of mantle source contributions in greater detail than traditional whole-rock methods. Therefore, study of olivines within mafic rocks in other magmatic settings where changes in eruptive style are attributed to changes in mantle source may be a useful tool in assessing source composition. Magmas in the south TVZ interacted with depleted harzburgitic mantle. Whole-rock data suggest that magmas here are sourced from large melt fractions in the shallow mantle, and potentially require a greater slab sediment contribution than elsewhere in the rifted arc. Central TVZ magmas show no evidence for interaction with depleted harzburgitic mantle. Variation in the extent of slab-derived fluid input during melting is required to account for geochemical differences between syn-caldera and post-caldera basalt, with syn-caldera basalt requiring greater input from the slab. All basalt compositions from the TVZ are consisten with a spinel lherzolite mantle source with variable slab contribution. We suggest that thinning of the lithosphere in the central TVZ promotes the transition from continental arc style volcanism to rhyolitic volcanism. This implies a direct link between rifting, magma composition and volcanic productivity. Although subduction promotes mantle melting due to fluid fluc, it is the extent of rifting that determines the mantle lithology with which the magmas interact, and this rifting exerts a control on primitive magma composition and fractionation pathways in the crust.

Chapter 7

Experimental phase relations of HMB and HMBA

7.1 *Foreword*

Chapter 6 showed that basalt from the south TVZ inherits olivine xenocrysts of harzburgitic composition from the mantle lithosphere, and suggested that this also exerts a control on the major element composition, shifting compositions to high SiO_2 and high MgO, at low CaO and Al_2O_3. This chapter is an experimental investigation into the crystallisation of hydrous high-Al basalt similar to mafic rocks in the central TVZ, and hydrous high-Mg basaltic andesite, a product of melt-rock reaction and mixing between high-Mg basalt and harzburgite, similar to primitive rocks in the south TVZ.

7.2 Introduction

The compositions of mafic rocks in the TVZ show a systematic shift, from high-Mg basalt and high-Mg basaltic andesite (collectively referred to as HMBA herein) in the south TVZ (Gamble et al., 1990; Graham and Hackett, 1987), to high-Mg basalt and high-Al basalt (HMB, HAB) in the central TVZ (Gamble et al., 1990). Chapter 6 showed that although all TVZ mafic rocks are ultimately sourced from lherzolitic mantle, there

are distinct geochemical differences between the parental magma compositions of pre-, syn- and post-caldera mafic rocks. This is in line with recent major and trace element studies on TVZ basalt compositions in relation to their mantle source (Barker et al., 2020; Zellmer et al., 2020). Syn-caldera basalt requires a more hydrous parental magma than post-caldera basalt. Mineral assemblages and phase relations of syn-caldera basalt are systematically different to post-caldera basalt (Chapter 4). e.g. the presence of high-anorthite plagioclase in syn-caldera basalt, which suggests high melt H_2O contents. However, enrichments in SiO_2 and MgO, plus the presence of harzburgite-derived xenocrysts in south-TVZ mafic rocks require the addition of a mantle lithosphere component to explain their compositions and crystal cargoes. Additionally, all TVZ mafic rocks show unique mineral assemblages, which cannot be produced by the same crystallisation pathways in the crust, suggesting each basalt crystallised at differing P-T conditions to one another. It is not clear how large a role the suggested differences in parental magma composition, i.e. changes in initial H_2O content, and enrichment in SiO_2 and MgO, play in producing the observed changes in mineral assemblage, or whether these differences are largely due to different crystallisation conditions of the mafic magma.

This chapter uses piston-cylinder apparatus to experimentally simulate production of TVZ basalt and HMBA. Three different synthetic mixes of powders are used as close natural analogues to pre-, syn- and post-caldera mafic compositions. Through a series of equilibrium experiments, we produce mineral-melt phase relations for 3 compositions. These are then compared to one another, before being used to infer characteristics of the parental magmas of TVZ mafic rocks, in addition to differences in mafic magma crystallisation conditions. The experiments reproduce the shift between basalt and HMBA exceptionally well, and this is inferred as strong evidence for lithospheric mantle contamination of south TVZ mafic magmas.

7.3 Methods

7.3.1 Starting Materials

Finding an appropriate composition to represent a parental magma to TVZ basalt is not straight forward. Traditionally, the Kakuki basalt has been used as a mafic end-member for TVZ rocks, due to its relatively aphyric nature, high Mg number, and primitive isotopic composition. However, Chapters 4 and 5 have shown that the Kakuki basalt is not as primitive as previously thought, and even so, is only representative of post-caldera samples. Syn-caldera basalt taps systematically more fertile and hydrous mantle (Barker et al., 2020; Zellmer et al., 2020) (Chapter 6).

Additionally, historical work has shown that high-Al basalt is not a primary basalt composition, and is produced from early fractionation of olivine, depleting MgO and concentrating Al_2O_3 in the melt phase (Gust and Perfit, 1987). This is consistent with modelling of HAB olivine chemistry in Chapter 6. High-Mg basalts in arc settings are more likely parental magma candidates than high-Al basalts (Elthon and Scarfe, 1984; Gust and Perfit, 1987; Sisson and Grove, 1993b). Whilst high-Mg basalts can be primary, the two high-Mg basalts sampled (OG and WM) are not primary. Both are primitive and contain xenocrystic mantle-derived olivine, but both are affected by crystal accumulation and repeated episodes of magma mixing, skewing their whole rock composition towards olivine (OG) and olivine + clinopyroxene compositions (WM). Therefore, no natural sample from the TVZ is a suitable analogue for a primary mantle melt, from which to fractionate the different mineral assemblages.

A closer natural parental magma to TVZ basalt is a high-Mg basalt from Elthon and Scarfe (1984). This is an aphyric high-MgO basalt from the Tortuga ophiolite complex in southern Chile, with a WR Mg# of 75.9, indicating equilibrium with mantle derived melt. This composition was used as a starting point due to it's highly primitive, near-primary composition. The Fe-Mg ratio was adjusted to be in equilibrium with Fo_{90}

olivine, the most primitive magmatic olivines in the central TVZ. Forward modelling removal of olivine demonstrates that this composition is able to successfully match the composition of Kakuki basalt. The original Elthon and Scarfe (1984) composition and the synthetic start composition for experiments is listed in table 7.1.

To simulate the differences between hydrous, syn-caldera basalts and less hydrous post-caldera basalts, two versions of this mix were created, with 5 wt.% and 2 wt.% H_2O, HMB(5) and HMB(2) in table 7.1, respectively. To make the start compositions, high-purity oxides and carbonates were weighed, ground under acetone, then decarbonated in a muffle furnace at 600-900°C over 6 hours, and held at 900°C for a further 9 hours to remove all CO_2. The mixture was then homogenised by melting at 1250°C for 30 minutes and quenching to a glass, before grinding under acetone for a further 30 minutes. H_2O content was controlled by adding some of the required MgO as brucite after glassing, up to 2wt.% H_2O, and 5 wt.% H_2O, with the remainder of the required MgO being added as oxide during the initial mix preparation.

The final starting composition used in experiments here is a HMBA representative of the pre-caldera forming system. High-Mg basaltic andesite magma in the TVZ is primitive, up to $Mg\#_{75}$ (Gamble et al., 1990; Graham and Hackett, 1987; Zellmer et al., 2020), and therefore likely acquires its high-Si, high-Mg composition from the mantle. These rocks therefore require a mantle process which can simultaneously increase SiO_2 and MgO in the melt phase. HMBA cannot form through dry or wet melting of lherzolitic mantle (Gaetani and Grove, 1998; Parman and Grove, 2004; Wood and Turner, 2009). Addition of H_2O to the lherzolitic mantle wedge increases SiO_2 content of the liquid, but not MgO (Gaetani and Grove, 1998; Parman and Grove, 2004; Wood and Turner, 2009). However, both older (Kushiro, 1972; Kelemen et al., 1990) and more recent (Mitchell and Grove, 2016; Wood and Turner, 2009) studies have shown that removal of a diopsidic (Ca-rich) clinopyroxene component in the mantle produces melts that are enriched in SiO_2 and MgO. The presence of harzburgite composition mantle lithosphere beneath the south TVZ can also be inferred from harzburgite-derived olivine

xenocrysts from Waimarino basalt. Parental magmas of the south TVZ therefore likely require a composition that is representative of melt-rock reaction between a hydrous, fertile mantle wedge melt, and a layer of depleted subcontinental lithospheric mantle.

Recent experiments (Mitchell and Grove, 2016) at upper mantle wedge conditions provided a suite of equilibrium melt compositions arising from the reaction of hydrous basalt with harzburgite, at variable melt:harzburgite ratios and temperatures. The melt compositions produced contained 52-57.5 wt.% SiO_2, and 4.7-17 wt.% MgO. However, these experiments had significantly higher H_2O contents (5-8 wt.%) than is expected for the south TVZ (2 wt.% Kilgour et al. (2013)). Therefore, to simulate formation of HMBA parental melts in the south TVZ, a series of melt-rock reaction experiments were performed between the 2 wt.% start composition described above (HMB) and the same harzburgite (Harz) composition from Mitchell and Grove (2016), to attain an equilibrium melt composition. The 2 wt.% HMB was chosen over the 5 wt.% HMB as it more closely resembles the H_2O content of south TVZ magma (Kilgour et al., 2013). The harzburgite composition was synthesised from high purity oxides in the same method as described above. Due to the high liquidus temperature of this mix, the glass and quench step of the process was bypassed, in order to avoid producing crystals which may not reequilibrate during experimental runs. The two starting powders were subsequently mixed as separate batches of powder with 10:90 and 20:80 basalt to harzburgite ratios, respectively. These experiments produced large crystals of olivine with variably interconnected pockets of orthopyroxene saturated melt. The melt compositions of these experiments are shown, along with the Mitchell and Grove (2016) glass compositions in Figure 7.1. Overall, there is good agreement between the compositions from (Mitchell and Grove, 2016) and the melt-rock reaction experiments performed here. The HMBA composition used most closely matches the Mitchell and Grove (2016) experiments using 5% basalt to 95% harzburgite, and our 10% basalt to 90% harzburgite experiment at 1250°C. This composition is listed in Table 7.1.

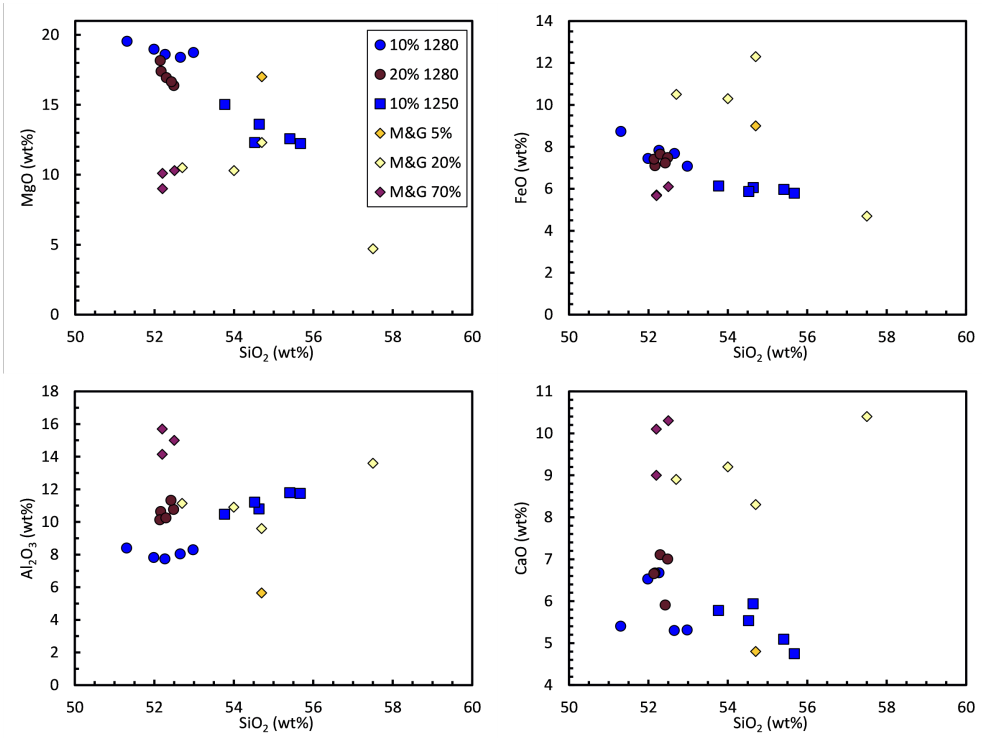

Figure 7.1: Chemical composition of experimental melts produced by mixing experiments between 2 wt.% H_2O basalt (HMB) and harzburgite (Mitchell and Grove, 2016). Experimental melt compositions of Mitchell and Grove (2016) is shown for comparison.

Table 7.1: **Composition of starting materials (wt.%)**

Oxide	NT-23 [a]	Harz [b]	10% [c]	20% [c]	HMB(2)	HMB(5)	HMBA(2)
SiO_2	47.25	44.31	44.53	44.75	49.4	50.1	55.8
TiO_2	0.79	0.04	0.12	0.19	0.72	0.91	0.82
Al_2O_3	13.64	0.3	1.7	3.1	14.9	15.2	9.8
FeO	9.77	7.81	7.87	7.93	6.9	7.1	6.9
MnO	0.14	0.17	0.17	0.16	0.01	0.01	0.01
MgO	17.61	46.9	44.0	41.0	14.7	16.5	16.4
CaO	9.58	0.46	1.30	2.14	9.56	9.48	6.7
Na_2O	0.89	0.02	0.20	0.38	2.1	2.0	2.1
K_2O	0.06	0.00	0.01	0.02	0.2	0.3	0.3
Cr_2O_3		0.61	0.55	0.49	0.1	0.1	0.1
H_2O		0.0	0.2	0.4	2.0	5	2
Total	99.73	100.69	100.63	100.57	98.65	100.75	100.93

[a] Natural high-Mg basalt composition from Elthon and Scarfe (1984)
[b] Harzburgite composition from Mitchell and Grove (2016)
[c] Compositions resulting from 10% & 20% mixing between HMB(2) and Harzburgite compositions

7.3.2 Experimental Techniques

All experiments were conducted using a 0.5 inch end-loaded solid medium piston cylinder apparatus at the University of Edinburgh. Starting materials were loaded into 4mm diameter Pt capsules, required due to high run temperatures. Fe loss is a common problem when using Pt as a capsule material. The Pt capsules were pre-saturated in Fe to minimise Fe loss to from the experimental charge to the capsule during experiments. This was achieved by annealing the Pt crucibles in an anhydrous version of the HMB starting composition, at 950°C in a muffle furnace for between 7-14 days. A lower temperature was chosen so as not to melt the mixture, but a long annealing time to allow Fe to diffuse into the Pt. After annealing, the sintered HMB mixture was mechanically removed from the Pt. Fe loss during high-pressure/temperature experiments is <10% in all runs, and is discussed in further detail in section 7.4.3. <10% loss is low enough to reliably be analogous to experiments that have not experienced Fe loss (Mitchell and Grove, 2016), and to the natural systems replicated.

Mixes were packed into a Pt capsule, which was triple crimped and welded shut. Hammered capsules were inserted into alumina holders. These were loaded into the hot point of a half inch talc-pyrex-graphite assembly. Each piston cylinder run was pressurised first at room temperature, before heating at 100°C /min up to the final temperature to prevent crystallisation whilst heating. The minimum pressure of experimental runs was dictated by the minimum pressure required to stabilise experiments on the piston cylinder apparatus. This minimum pressure was 5 kbar, so no experiments were run at lower pressures than this. It is acknowledged that this pressure is higher than predicted from phase equilibria (Chapter 4), However, this still provides significant overlap with the mid-lower crust in the TVZ (15-35km), but it is recognised that compositions of certain phases (e.g. high-An plagioclase) may not be reproduced using this setup. Runs were held at temperature for 23-26 hours, before isobarically quenching by switching off the power to the heating circuit whilst maintaining pressure, to prevent

growth of quench crystals. During quenching, temperature dropped to below 100°C in approximately 10 seconds. Once the experiment was cooled, pressure was slowly bled to avoid decompression cracking. Temperature was monitored and maintained throughout using an R-type thermocouple accurate to +/- 10°C, and a 12% pressure correction was used to correct for friction. For more detail on the piston cylinder technique, see Chapter 5.3.

7.3.3 Analytical Techniques

Capsules were ground, polished to 1μm using diamond solutions and examined under reflected light, before analysis on a Zeiss Sigma FEG SEM at the University of Edinburgh. BSE images were obtained using an accelerating voltage of 20 kV. Semi-quantitative analyses were recorded using an energy dispersive spectrometer (EDS) to identify phases. Modal proportions of minerals were estimated by thresholding BSE images to separate different phases based on greyscale values using *ImageJ* software.

Quantitative analyses of minerals and melt were obtained by calibrating the SEM electron beam against a cobalt standard, and using a fixed working distance of 7mm. Secondary standards of St. Johns Island olivine (SJI olivine), plus internal lab clinopyroxene, jadeite, andradite and wollastonite standards were run at approximately 1-2hr intervals, to check for drift. These are reported in Appendix A.1. Overall, secondary standard totals are 0-1 wt.% higher than reported electron microprobe values, but are internally consistent and show no drift through sessions. EDS spectra were not corrected for elevated totals. An advantage of acquiring EDS spectra is the increased speed of an individual analysis. Over 1200 data points were collected over 2 analysis sessions, providing much better statistics on variation within phases than with traditional EPMA quantitative analysis. Nevertheless, some experiments were also analysed using the electron microprobe, using the same SJI olivine and clinopyroxene secondary standards, which showed no significant shift between EDS and EPMA data. Analysing

conditions and secondary standards are reported in Supplement 1 for both EDS and EPMA data.

7.4 Experimental Results

A total of 39 equilibrium experiments were carried out across the three compositions. 12 using the 2 wt.% basalt, 12 using the 5 wt.% basalt, and 15 using the HMBA. Representative BSE images of experimental run products are shown in Figure 7.2. Experimental run conditions and phase proportions are presented in tables 7.2, 7.3, 7.4, and phase relations of the 3 compositions are presented in Figure 7.3.

7.4.1 Phase Equilibria

2 wt.% H_2O basalt composition

Of the 12 experiments run using the 2 wt.% H_2O starting composition (2 wt.% experiments), 11 produced hydrous silicate melt in equilibrium with their respective mineral assemblages. One experiment, H-1100-10 did not produce silicate melt. No experiments reached 100% melt. Olivine is the first phase on the liquidus at all pressures investigated (Figure 7.3), at approximately 1250-1300°C. At 10kbar, clinopyroxene, orthopyroxene and plagioclase replace olivine at 1225°C. At all pressures less than 10kbar at 1225°C, olivine remains in equilibrium and is joined at lower temperature and pressure by plagioclase, producing troctolite assemblages. At 5kbar, clinopyroxene is the third phase on the liquidus without orthopyroxene. At 7-10kbar, two pyroxenes are stabilised together, producing gabbro assemblages. Spinel is only stable in 10kbar runs, at temperatures <1200°C and low melt fractions.

5 wt.% H_2O basalt composition

All experiments run using the 5 wt.% H_2O starting composition (5 wt.% experiments) produced hydrous silicate melt in equilibrium with their respective mineral assemblages. Like the 2 wt.% experiments, olivine is the first phase on the liquidus (Figure 7.3) at approximately 1250-1300°C. At high pressure, the stability field of olivine is greater than in the 2 wt.% experiments, and is present, alongside clinopyroxene and orthopyroxene until 1200°C. Orthopyroxene is more abundant than clinopyroxene at high temperature and pressure (1225°C, 10kbar), whereas clinopyroxene abundance increases with decreasing temperature at a constant pressure. At pressures of 5 and 7kbar, plagioclase is the first phase to join olivine on the liquidus, similar to the 2 wt.% H_2O experiments. At 5kbar, the next phase to crystallise after plagioclase is clinopyroxene, whereas at 7kbar, two pyroxenes appear near-on simultaneously. Orthopyroxene stability is greater at higher pressure, and less at lower pressure, whereas clinopyroxene stability shows a greater dependence on temperature and possibly melt fraction/composition. Spinel is only stable in 10kbar runs, but appears at higher temperature than in 2 wt.% experiments.

2 wt.% High-Mg basaltic andesite composition

All experiments run using the 2 wt.% High-Mg basaltic andesite composition (HMBA) produced hydrous silicate melt in equilibrium with orthopyroxene, ± clinopyroxene, ± plagioclase, ± spinel. Orthopyroxene is the first phase on the liquidus at all investigated pressures (Figure 7.3). Spinel is the second phase on the liquidus. At pressure >7kbar it is always present, but at lower pressure it is stable only in experiments run at temperatures of 1150°C or less. Clinopyroxene is the third phase on the liquidus and joins at 1200°C at pressures of 10kbar, at 1175°C at 7kbar and at 1150°C at 5kbar, producing a two-pyroxene websterite crystallising assemblage (Figure 7.3). The point of clinopyroxene crystallisation correlates to a roughly 50-60% remaining melt fraction.

Plagioclase is the last phase to crystallise. Plagioclase is more stable at higher temperature at higher pressure (1175°C at 10kbar, 1065°C at 5kbar). This is due to smaller remaining melt fractions at 10kbar relative to 5kbar for a given temperature, therefore concentrating plagioclase components in the silicate melt. Plagioclase saturation is only achieved at <50% remaining melt fraction.

Table 7.2: **Experimental conditions and summary of results from hydrous (2 wt.% H_2O) experimental runs.** Phases: *Cpx* clinopyroxene; *Opx* orthopyroxene; *Pl* plagioclase; *Sp* spinel; *Gl* glass/melt; *Ol* olivine.H_2O melt calculated as average water by difference in glass analyses.

Run	T (°C)	P (kbar)	*t* (h)	H_2O (wt.%)	H_2O_{melt} [a] (wt.%)	Phase (modal proportions)	Calc. $fO2$ [b] (ΔQFM)	Fe loss (wt.%)
H-1100-10	1100	10	24	2		Cpx(27), Opx(28), Pl(43), Sp(3)		
H-1200-10	1200	10	18	2	1.74	Gl(4), Cpx(22), Opx(37), Pl(36), Sp(2)	4.67	5.9
H-1225-10	1225	10	24	2	1.02	Gl(40), Cpx(12), Opx(23), Pl(25)	4.48	9.1
H-1250-10	1250	10	18	2	2.51	Gl(84), Ol(16)		-7.7
H-1225-08	1225	8	22	2	1.39	Gl(82), Ol(18)		-2.9
H-1175-07	1175	7	26	2	2.58	Gl(30), Cpx(21), Opx(29), Pl(20)	4.76	10.4
H-1200-07	1200	7	24	2	1.12	Gl(44), Ol(8), Cpx(13) Opx(15), Pl(20)	4.43	-0.11
H-1225-07	1225	7	22	2	2.09	Gl(80), Ol(20)		-4.6
H-1250-07	1250	7	20	2	1.3	Gl(89), Ol(11)		0
H-1125-05	1125	5	25	2	1.3	Gl(52), Ol(18), Cpx(14), Pl(16)	4.04	25.4
H-1175-05	1175	5	22	2	1.9	Gl(58), Ol(21), Pl(23)		0.69
H-1225-05	1225	5	26	2	0.99	Gl(85), Ol(15)		5.58

[a] H_2O melt calculated as average water by difference in glass analyses.
[b] Calculated using France et al. (2010)

7.4.2 Glass and mineral compositions

2 wt.% H_2O glass and mineral compositions

Glass was analysed in the 11 experiments containing analysable melt pockets. SiO_2 varied from 49-53 wt.%, whereas Mg# ranges from $Mg\#_{74-56}$. MgO decreases with decreasing temperature, whereas SiO_2, FeO, CaO and Al_2O_3 do not show significant variation, and Na_2O and K_2O show broad increases (Figure 7.4). As decreases in temperature are linked with decreasing melt fractions, similar trends are observed with decreasing melt fraction. Trends in melt compositions are best observed using Mg# bivariate plots (Figure 7.5), as mafic phases are the dominant fractionating phases, and have only a small effect on SiO_2. MgO decreases linearly with Mg#, as FeO increases.

Table 7.3: **Experimental conditions and summary of results from wet (5 wt.% H_2O) experimental runs.** Phases: *Cpx* clinopyroxene; *Opx* orthopyroxene; *Pl* plagioclase; *Sp* spinel; *Gl* glass/melt; *Ol* olivine.H_2O melt calculated as average water by difference in glass analyses.

Run	T (°C)	P (kbar)	*t* (h)	H_2O (wt.%)	H_2O_{melt} [a] (wt.%)	Phase (modal proportions)	Calc. $fO2$ [b] (ΔQFM)	Fe loss (wt.%)
W-1175-10	1175	10	24	5	3.46	Gl(2), Cpx(28), Opx(26), Pl(44), Sp(2)	4.54	9.19
W-1200-10	1200	10	24	5	2.11	Gl(19), Ol(5), Cpx(14), Opx(28), Pl(32), Sp(2)	4.59	5.3
W-1225-10	1225	10	25	5		Gl(71), Ol(3), Cpx(4), Opx(20), Sp(1)		-5.9
W-1250-10	1250	10	26	5		Gl(81), Ol(19)		2.9
W-1150-07	1150	7	25	5	2.6	Gl(17), Ol(9), Cpx(15), Opx(15), Pl(45)	5.59	13.2
W-1175-07	1175	7	26	5	2.27	Gl(51), Ol(15), Cpx(2), Opx(2), Pl(30)	4.34	10.3
W-1200-07	1200	7	24	5	1.65	Gl(60), Ol(13), Pl(27)		7.9
W-1225-07	1225	7	24	5	2.8	Gl(85), Ol(15)		15.7
W-1150-05	1150	5	24	5		Gl(50), Ol(18), Cpx(6), Pl(26)	5.42	10.4
W-1175-05	1175	5	23	5		Gl(50), Ol(20), Pl(30)		
W-1200-05	1200	5	24	5		Gl(65), Ol(16), Pl(18)		-0.02
W-1225-05	1225	5	26	5		Gl(86), Ol(14)		0

[a] H_2O melt calculated as average water by difference in glass analyses.
[b] Calculated using France et al. (2010)

Table 7.4: **Experimental conditions and summary of results from high-Mg basaltic andesite (2 wt.% H_2O) experimental runs.** Phases: *Cpx* clinopyroxene; *Opx* orthopyroxene; *Pl* plagioclase; *Sp* spinel; *Gl* glass/melt; *Ol* olivine.H_2O melt calculated as average water by difference in glass analyses.

Run	T (°C)	P (kbar)	*t* (h)	H_2O (wt.%)	H_2O_{melt} [a] (wt.%)	Phase (modal proportions)	Calc. $fO2$ [b] (ΔQFM)	Fe loss (%)
BA-1090-10	1090	10	23	2	4.5	Gl(21), Opx(27), Sp(2), Cpx(19), Pl(32)	4.2	-2.7
BA-1175-10	1175	10	27	2	2.8	Gl(39), Opx(44), Sp(1), Cpx(13), Pl(3)		-2.5
BA-1200-10	1200	10	24	2	3.1	Gl(54), Opx(38), Sp(1), Cpx(8)		-3.3
BA-1225-10	1225	10	24	2	2.5	Gl(59), Opx(36), Cpx(4)		-1.7
BA-1250-10	1250	10	26	2	1.4	Gl(69), Opx(31)		5.6
BA-1150-07	1150	7	24	2	2.8	Gl(45), Opx(33), Sp(2), Cpx(14), Pl(5)	5.6	3.1
BA-1175-07	1175	7	24	2	2.1	Gl(46), Opx(42), Sp(1), Cpx(10)	5.5	1.8
BA-1200-07	1200	7	25	2	2.3	Gl(68), Opx(31), Sp(1)		5.2
BA-1225-07	1225	7	25	2	1.2	Gl(70), Opx(30)		4.4
BA-1250-07	1250	7	26	2	1.6	Gl(70), Opx(30)		2.8
BA-1065-05	1065	5	26	2	3.8	Gl(29), Opx(39), Cpx(18), Pl(14)	4.2	-9.6
BA-1110-05	1110	5	24	2	3.9	Gl(54), Opx(32), Cpx(13)	2.8	-35.1
BA-1150-05	1150	5	24	2	2.1	Gl(53), Opx(38), Cpx(7)		-8.5
BA-1225-05	1225	5	24	2	6.5	Gl(79), Opx(21)		-27.8
BA-1300-05	1300	5	26	2	2	Gl(79), Opx(21)		0

[a] H_2O melt calculated as average water by difference in glass analyses.
[b] Calculated using France et al. (2010)

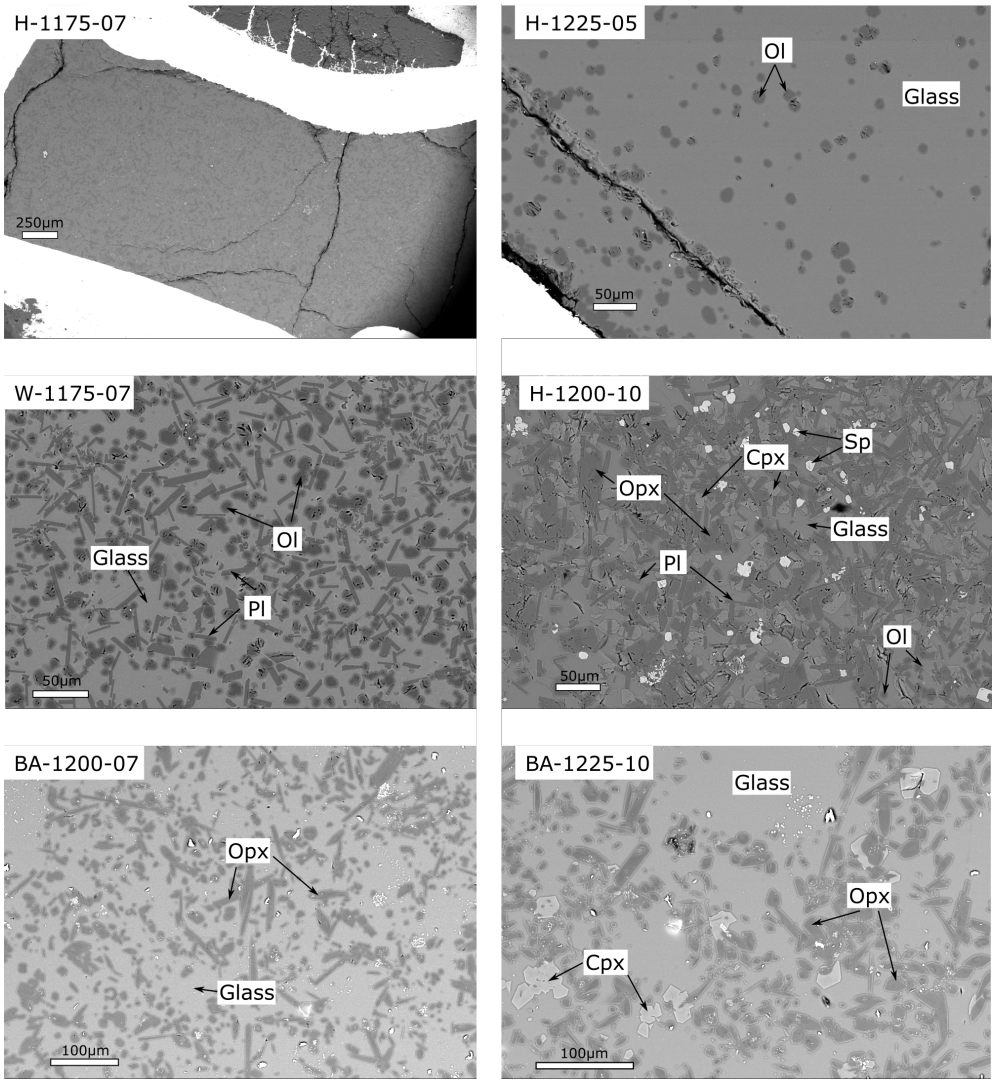

Figure 7.2: BSE SEM images from experimental runs. Mineral abbreviations as in table 7.2.

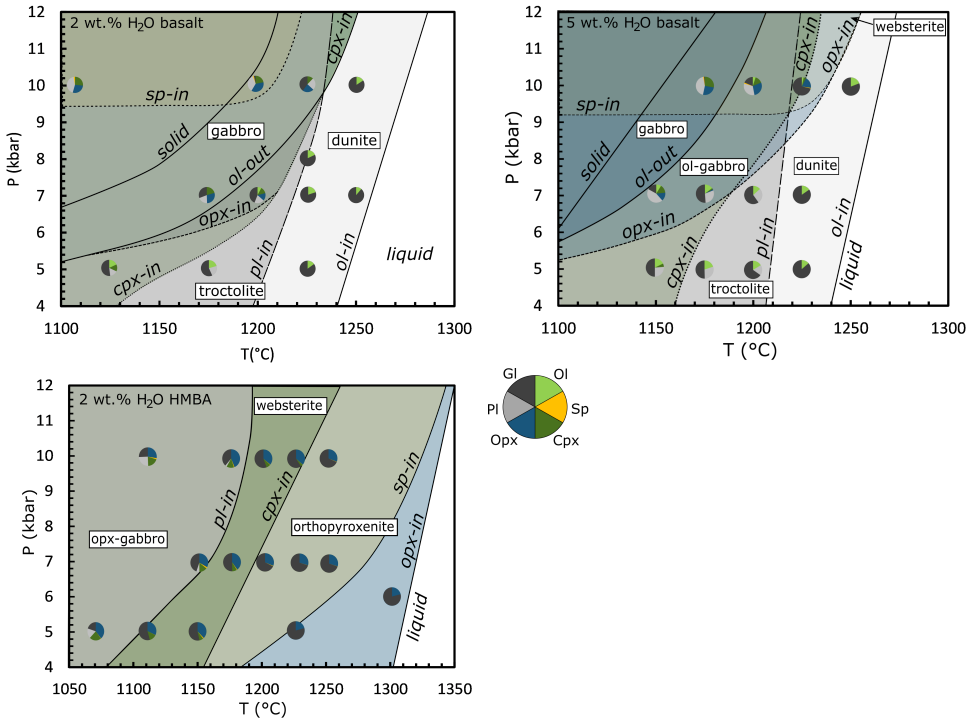

Figure 7.3: Phase relations for the 3 experimental series HMB(2), HMB(5) and HMBA. Mineral abbreviations are as in Table 7.2. Pie charts show proportions of phases in each experiment. Different coloured fields represent different crystallised mineral assemblages.

The exception to this is in H-1125-05, which shows an offset from both trends (Figure 7.5), and suggests the experiment has lost significant FeO, shifting Mg# to the right. Al_2O_3 first increases with decreasing Mg#, consistent with crystallisation of olivine ± clinopyroxene, then decreases, consistent with crystallisation of plagioclase. CaO also first increases with decreasing Mg#, consistent with fractionation of olivine, then decreases, consistent with crystallisation of clinopyroxene and plagioclase. Both Na_2O and K_2O increase with decreasing Mg# and show broadly incompatible behaviour, as plagioclase compositions are Ca rich (An_{80-90}).

Olivine is Fo_{90-95} and does not show significant variation in composition with decreasing Mg# of the melt (Figure 7.6). Clinopyroxene is augite in composition and $Mg\#_{75-90}$. Mg# in clinopyroxene is broadly correlated to Mg# in the melt (Figure 7.6). Orthopyroxene is $Mg\#_{87-91}$, and does not show significant variation with Mg# of the melt (Figure 7.6). Plagioclase shows a limited range in composition from An_{81-85}, with the exception of H-1125-05 which has highly variable plagioclase from An_{85-91} (Figure 7.6).

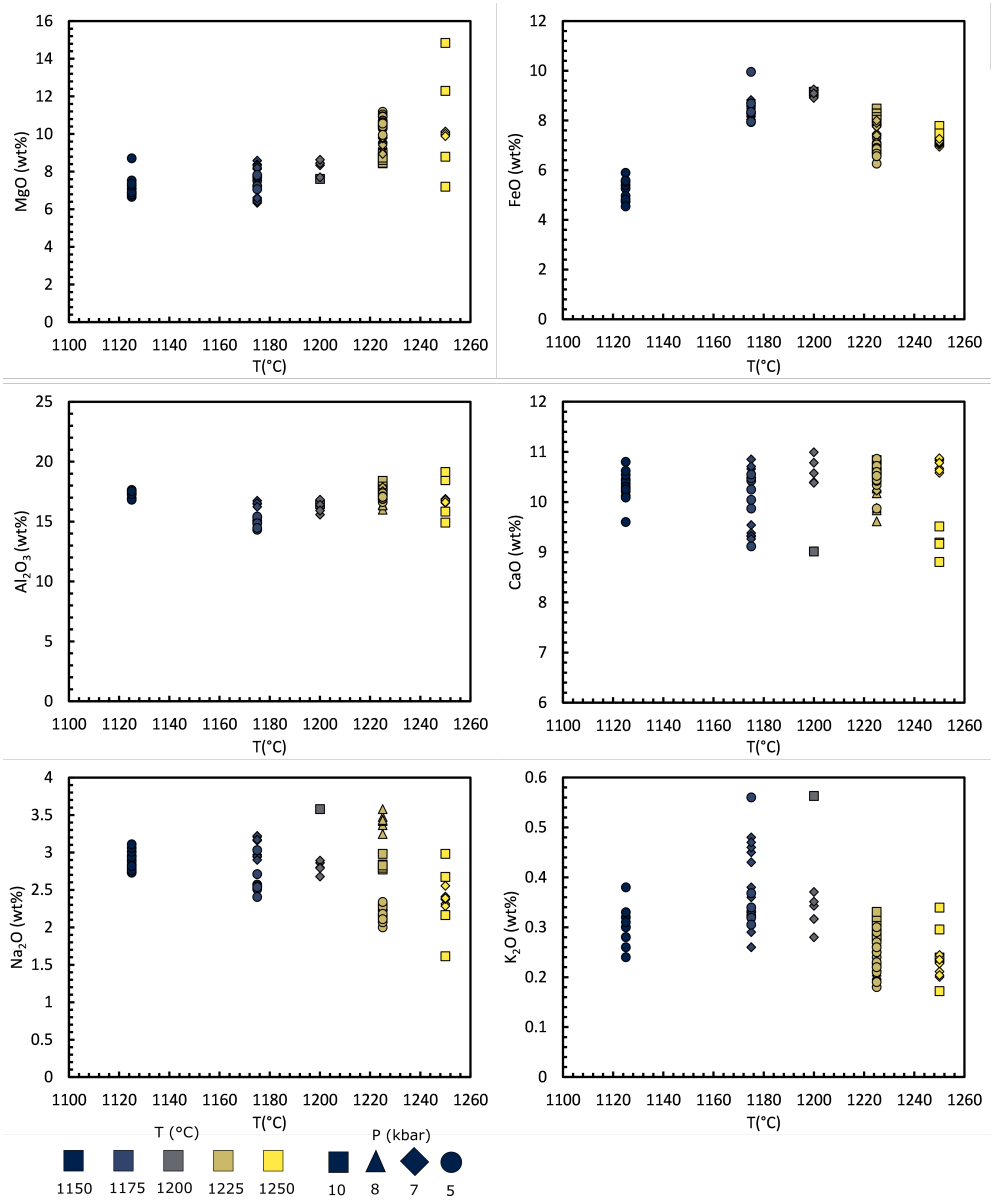

Figure 7.4: Compositional variation of glass in 2 wt.% H_2O experiments as a function of temperature.

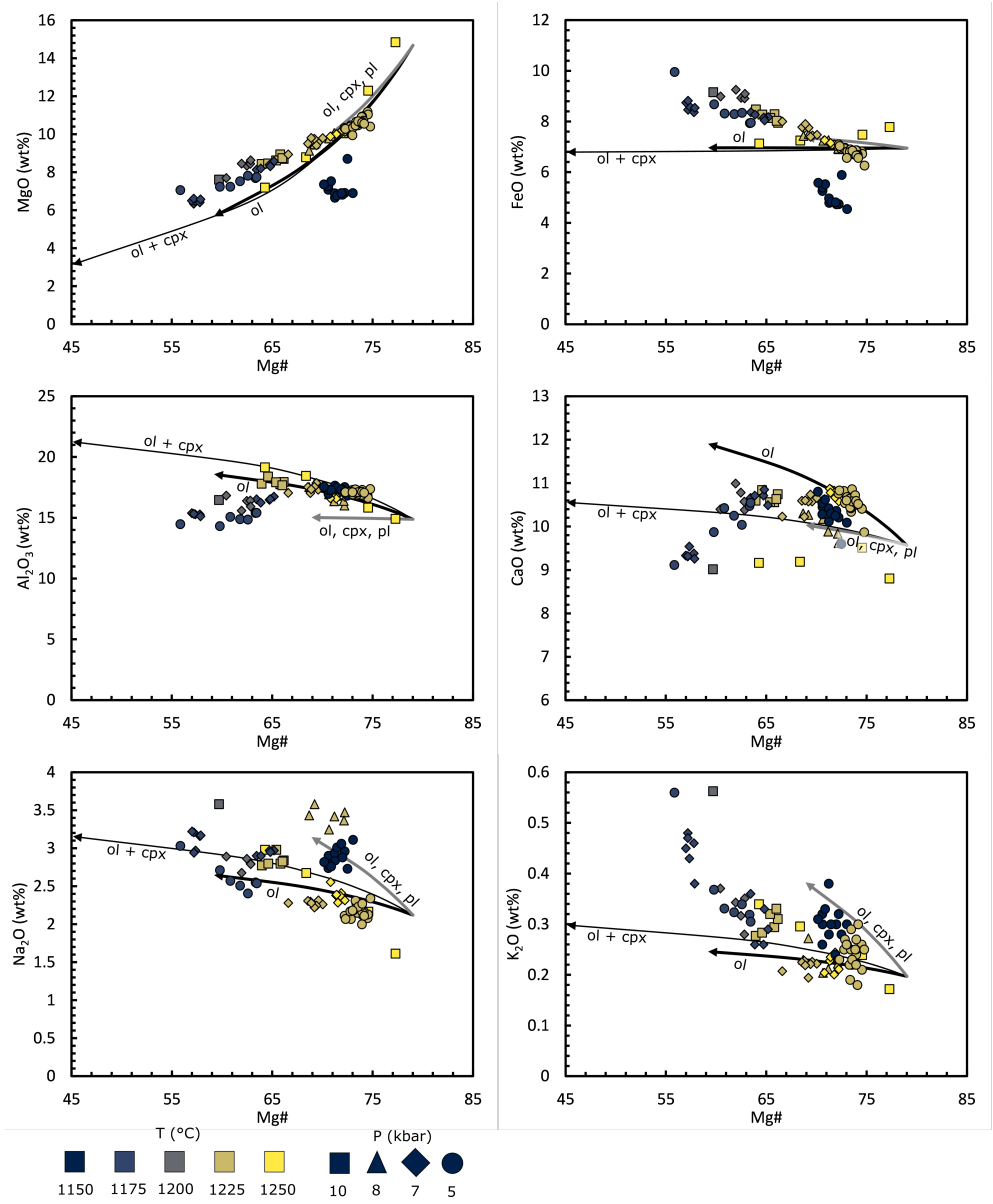

Figure 7.5: Compositional variation of glass in 2 wt.% H_2O experiments as a function of the Mg# of the melt. Fractionation lines show the broad trajectory of melt composition when crystallising out the labelled mineral assemblage. Mineral compositions used for modelling these lines are averages from 2 wt.% mineral data. Mineral abbreviations are as in Table 7.2.

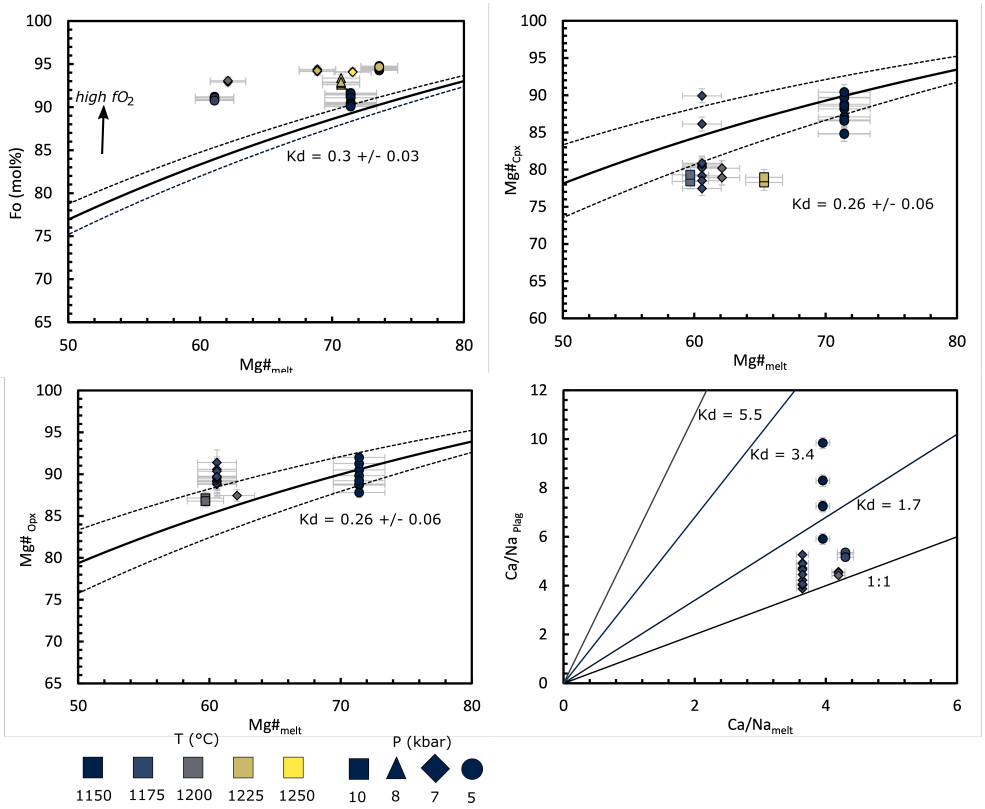

Figure 7.6: Composition of experimental minerals against the Mg# or Ca/Na ratio of the melt. Kd values are from Roeder and Emslie (1970) (olivine) Putirka (2008) (clinopyroxene, orthopyroxene), and Sisson and Grove (1993a) (plagioclase). For plagioclase, a Kd of 1.7 is the expected value for a melt containing 2 wt.% H_2O. For details on the effect of increased fO_2 on olivine, see section 7.4.3.

5 wt.% H_2O glass and mineral compositions

Glass was analysed from all 12 experiments. SiO_2 ranges from 49-54 wt.%, and, like the 2 wt.% experiments, does not show any observable major element trends. MgO decreases with decreasing temperature, whilst FeO increases (Figure 7.7). Al_2O_3 decreases with decreasing temperature (Figure 7.7). This trend is more pronounced in lower pressure experiments, and is associated with greater amounts of plagioclase crystallisation. CaO shows two divergent trends with decreasing temperature (Figure 7.7). In high pressure (10kbar) experiments, CaO rapidly decreases with temperature. 1175°C and 10kbar is very close to the solidus of the 5 wt.% composition, and has experienced more fractionation of clinopyroxene and plagioclase than the same composition at equivalent temperature but lower pressure, resulting in more rapid depletion of CaO with temperature. Na_2O concentrations remain constant with decreasing temperature in lower pressure experiments, but increases in 10kbar runs. This is because melt fractions reduce more rapidly at higher pressure, producing the similar but opposite trend to CaO. K_2O behaves incompatibly and increases with decreasing temperature. All experiments show a good correlation between Mg# and MgO (Figure 7.8), indicating that all experiments retained FeO and Mg#s are a good representation of the amount of crystallisation the experiments have undergone. There is a broad negative correlation between Mg# and FeO, with greatest FeO enrichment occurring in lower temperature and more crystalline runs. Both Al_2O_3 and CaO concentrations first increase with decreasing Mg#, before decreasing (Figure 7.8). The initial increase is associated with crystallisation of mafic phases. In experiments where clinopyroxene crystallises there is a less pronounced enrichment in CaO. The decrease is associated with runs that have crystallised plagioclase, depleting the melt in both Al_2O_3 and CaO. Na_2O and K_2O both show broad increases with decreasing Mg# showing that neither are incorporated in large concentrations into any crystallising phases.

Olivine is Fo_{90-95} and does not show any variation with Mg# of the melt (Figure

7.9). Clinopyroxene is augitic in composition with $Mg\#_{72-87}$. Sector zoning is observed in clinopyroxene from W-1225-10, with zones of low SiO_2 (47 wt.%), high Al_2O_3 (11 wt.%), high CaO (20 wt.%) and lower Mg# ($Mg\#_{75-77}$), and zones of high SiO_2 (52 wt.%), low Al_2O_3 (6.5 wt.%), low CaO (17 wt.%) and higher Mg# ($Mg\#_{83-86}$). Only the high Mg# zones plot in equilibrium with the Mg# of the melt (Figure 7.9). Orthopyroxene is $Mg\#_{85-92}$ and shows good correlation with the Mg# of the melt, in addition to being within the predicted equilibrium range of compositions for the melt Mg# (Figure 7.9). Plagioclase is An_{80-92}. Plagioclase compositions in high pressure runs are homogenous, but in lower pressure runs (7 and 5 kbar) are variable within individual runs.

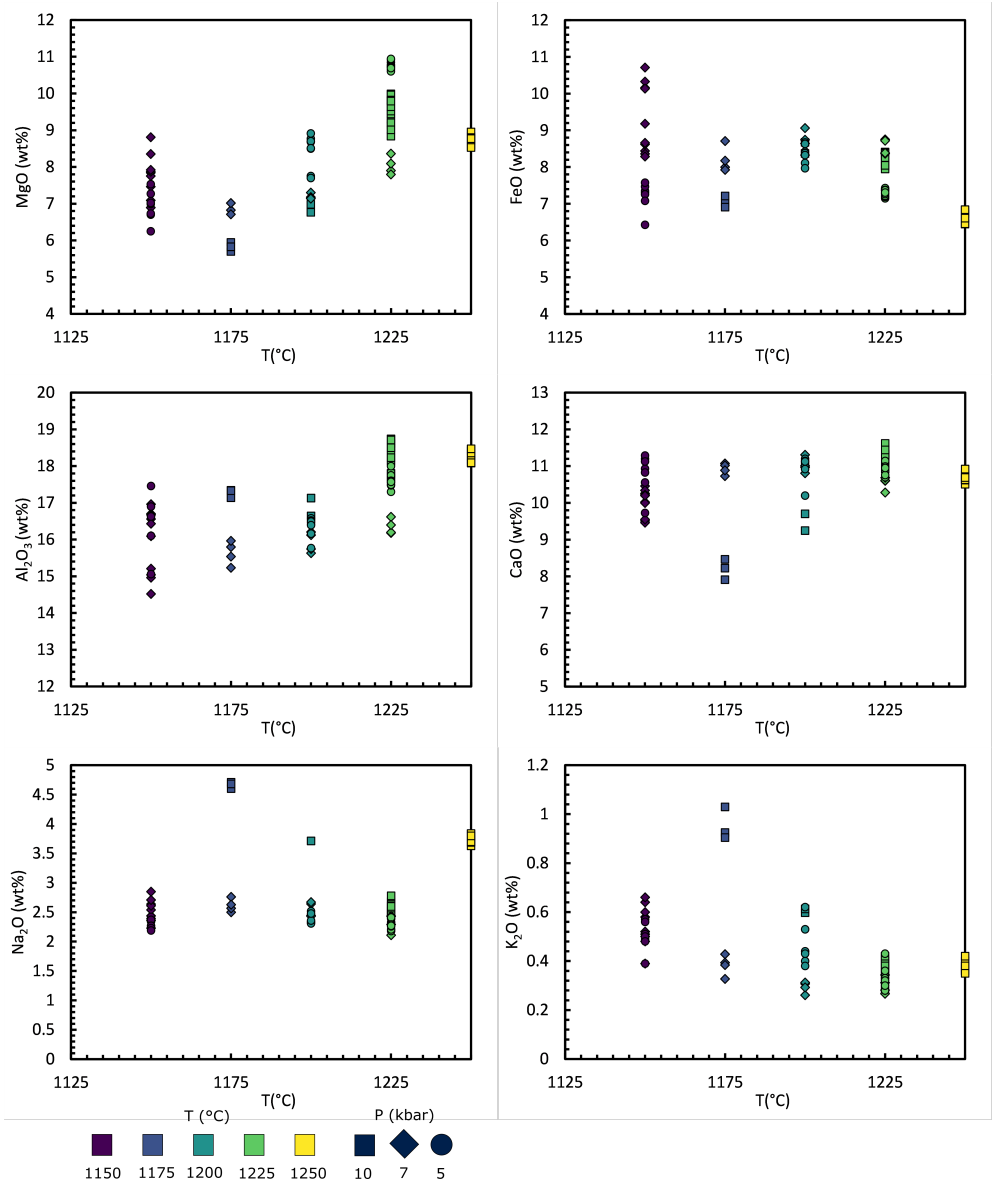

Figure 7.7: Compositional variation of glass in 5 wt.% H_2O experiments as a function of temperature.

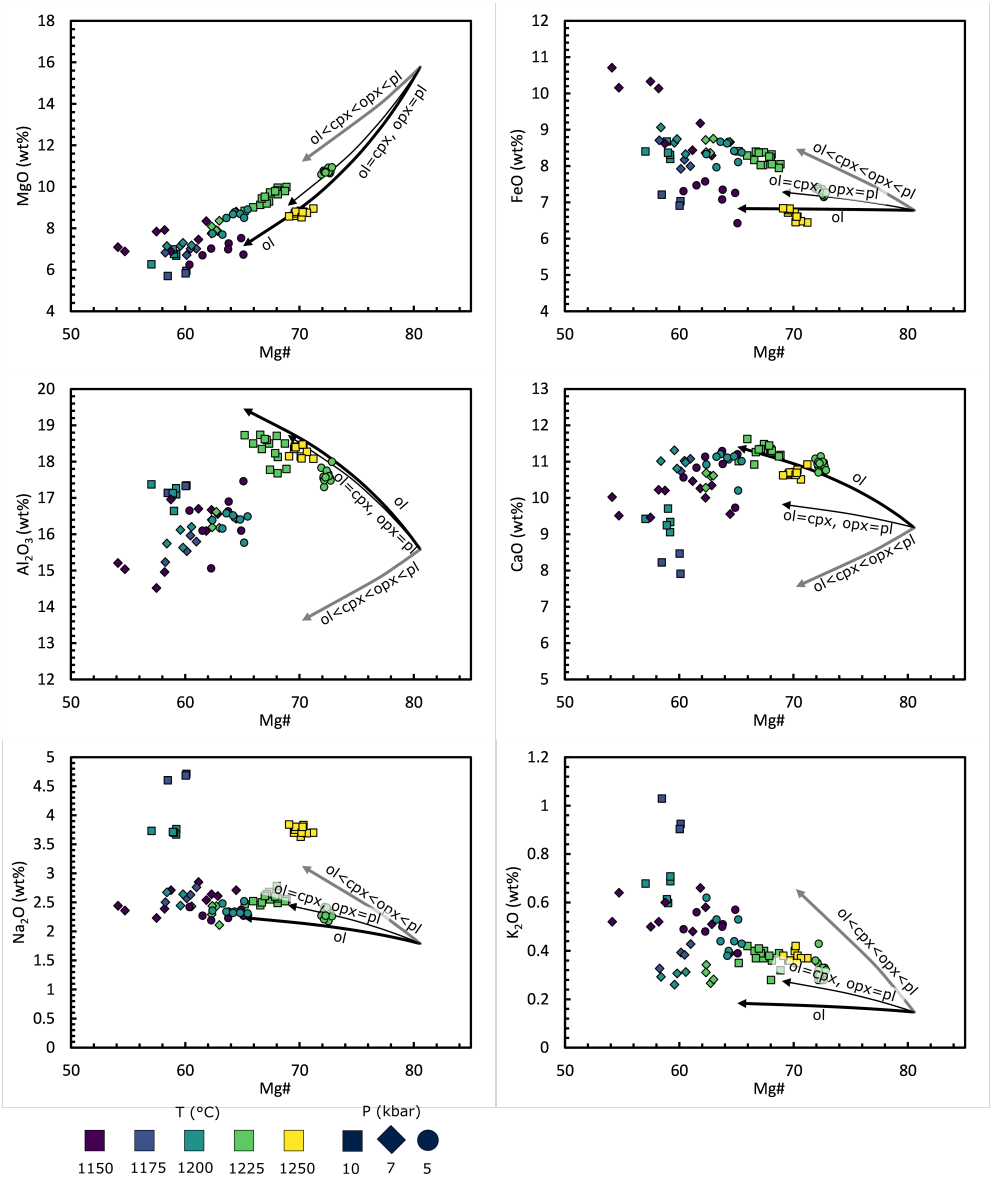

Figure 7.8: Compositional variation of glass in 5 wt.% H_2O experiments as a function of the Mg# of the melt. Fractionation lines show the broad trajectory of melt composition when crystallising out the labelled mineral assemblage. Mineral compositions used for modelling these lines are averages from 5 wt.% mineral data. Mineral abbreviations are as in Table 7.2.

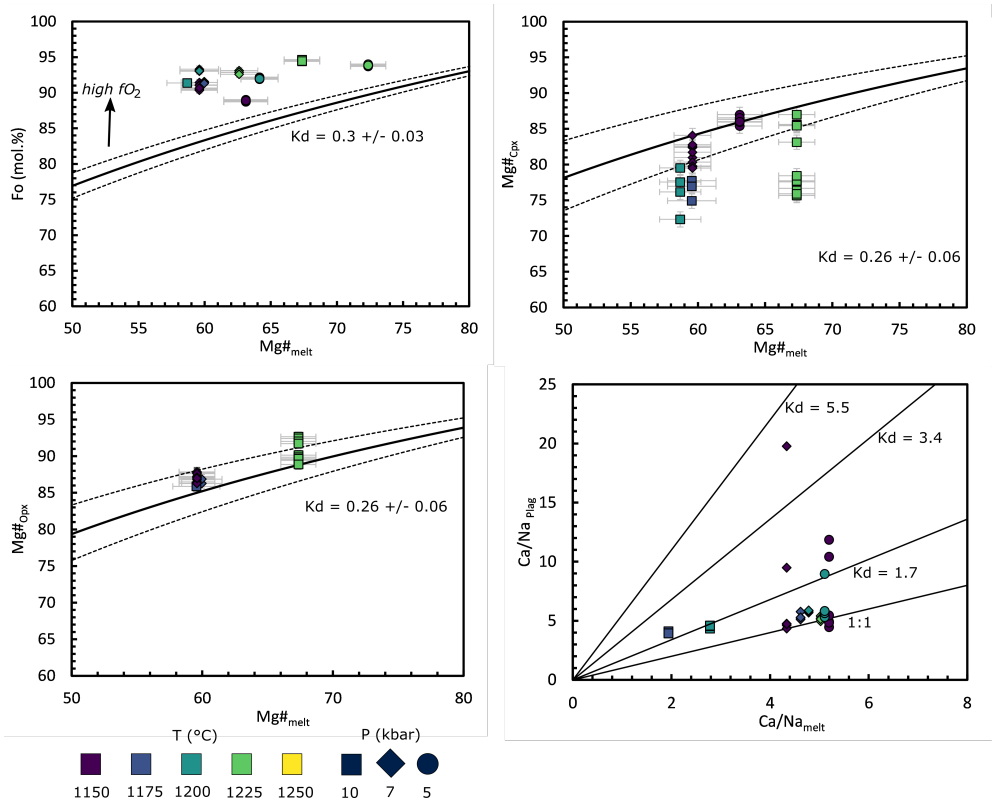

Figure 7.9: Composition of experimental minerals against the Mg# or Ca/Na ratio of the melt. Kd values are from Roeder and Emslie (1970) (olivine) Putirka (2008) (clinopyroxene, orthopyroxene), and Sisson and Grove (1993a) (plagioclase). For plagioclase, a Kd of 3.4 is expected for a melt containing 4 wt.% H_2O. A Kd of 5.5 is expected for a melt containing 6 wt.% H_2O. For details on the effect of increased fO_2 on olivine, see section 7.4.3.

High-Mg basaltic andesite glass and mineral compositions

Glass analyses were obtained from all 15 HMBA experimental runs. SiO_2 ranges from 57-74 wt.% and shows clear trends with all major elements. With decreasing temperature, MgO concentrations decrease, FeO, Al_2O_3 and CaO all show an initial increase and subsequent decrease, and SiO_2, Na_2O and K_2O all increase (Figure 7.10). The same major element trends are observed with decreasing melt fraction. With the exception of BA-1225-05, all experiments show a good correlation between Mg# and MgO, and Mg# and FeO (Figure 7.11), indicating that experiments have not experienced significant FeO loss. BA-1225-05 has clearly experienced FeO loss, and plots significantly away from the trend of the other experiments. BA-1225-05 also shows significantly higher SiO_2 and Al_2O_3 for a given melt fraction in comparison to other experiments. For these reasons it is shown greyed out as the capsule shows clear compositional signs of contamination. With decreasing melt fraction, both Al_2O_3 and CaO initially increase before decreasing in concentration. CaO begins to decrease first at higher Mg# than Al_2O_3. This is consistent with fractionation of orthopyroxene first, followed by clinopyroxene and lastly plagioclase. Both Na_2O and K_2O increase with decreasing melt fraction, showing incompatible behaviour throughout the crystallisation sequence. The same trends observed with decreasing Mg# are observed with increasing SiO_2 (Figure 7.12). MgO decreases steeply with little impact on SiO_2 in the hottest and least crystallised experiments. This is consistent with crystallisation of orthopyroxene only, with similar SiO_2 to the starting composition, but significantly higher MgO, depleting the melt of MgO but producing only a small shift in SiO_2. Significant SiO_2 enrichment begins with the addition of clinopyroxene into the equilibrium assemblage.

Orthopyroxene is $Mg\#_{85-95}$ and shows a broad positive correlation with Mg# of the melt. Clinopyroxene is augite in composition and $Mg\#_{77-92}$ and also shows a broad positive correlation with Mg# of the melt. Plagioclase is An_{50-72} and shows good positive correlation with the anorthite content of the melt. Anorthite within individual

experimental runs is much less variable than in both suites of basaltic experiments.

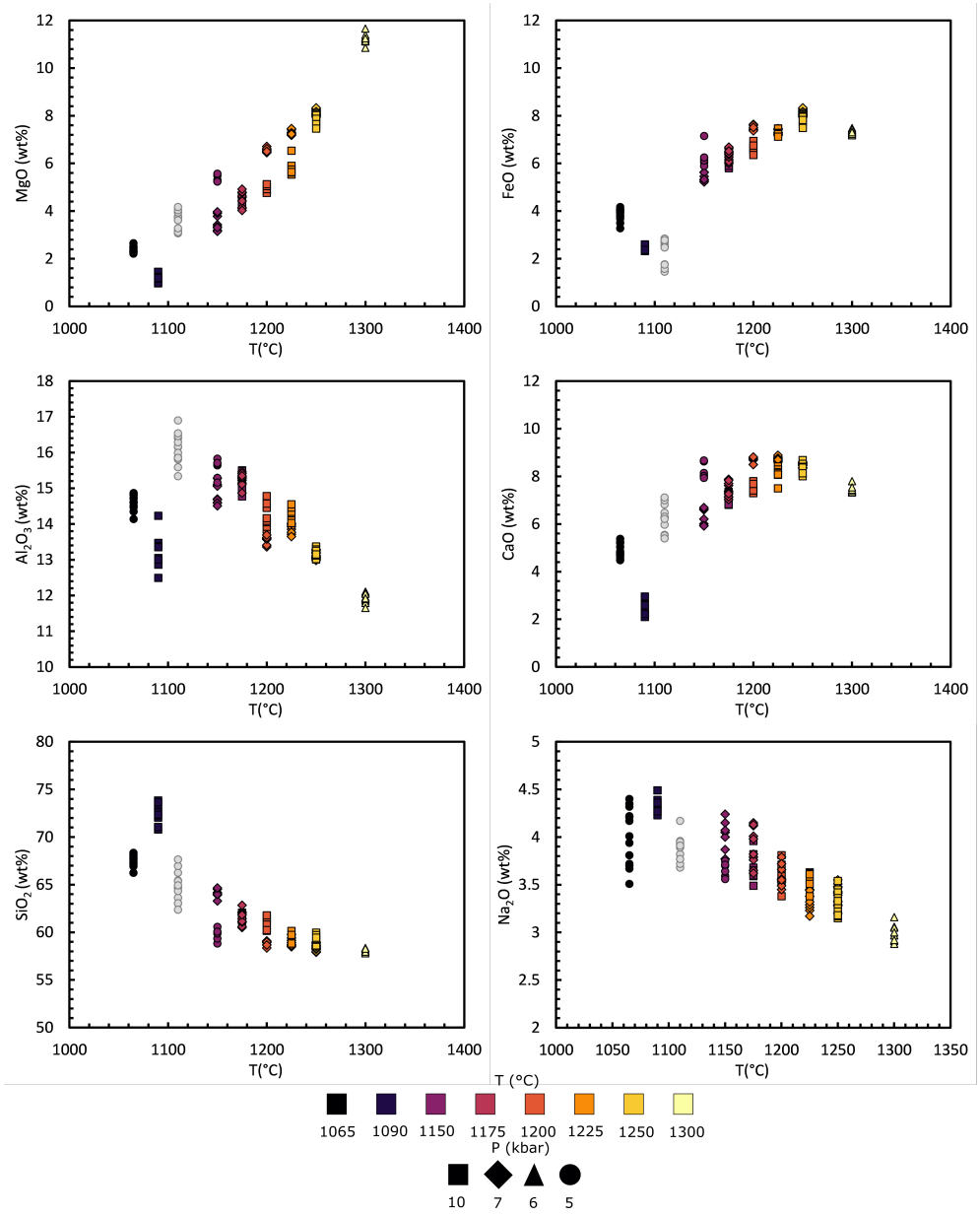

Figure 7.10: Compositional variation of glass in HMBA experiments as a function of temperature. BA-1225-05 is greyed out due to showing signs of partial capsule failure (see section 7.4.2 for details).

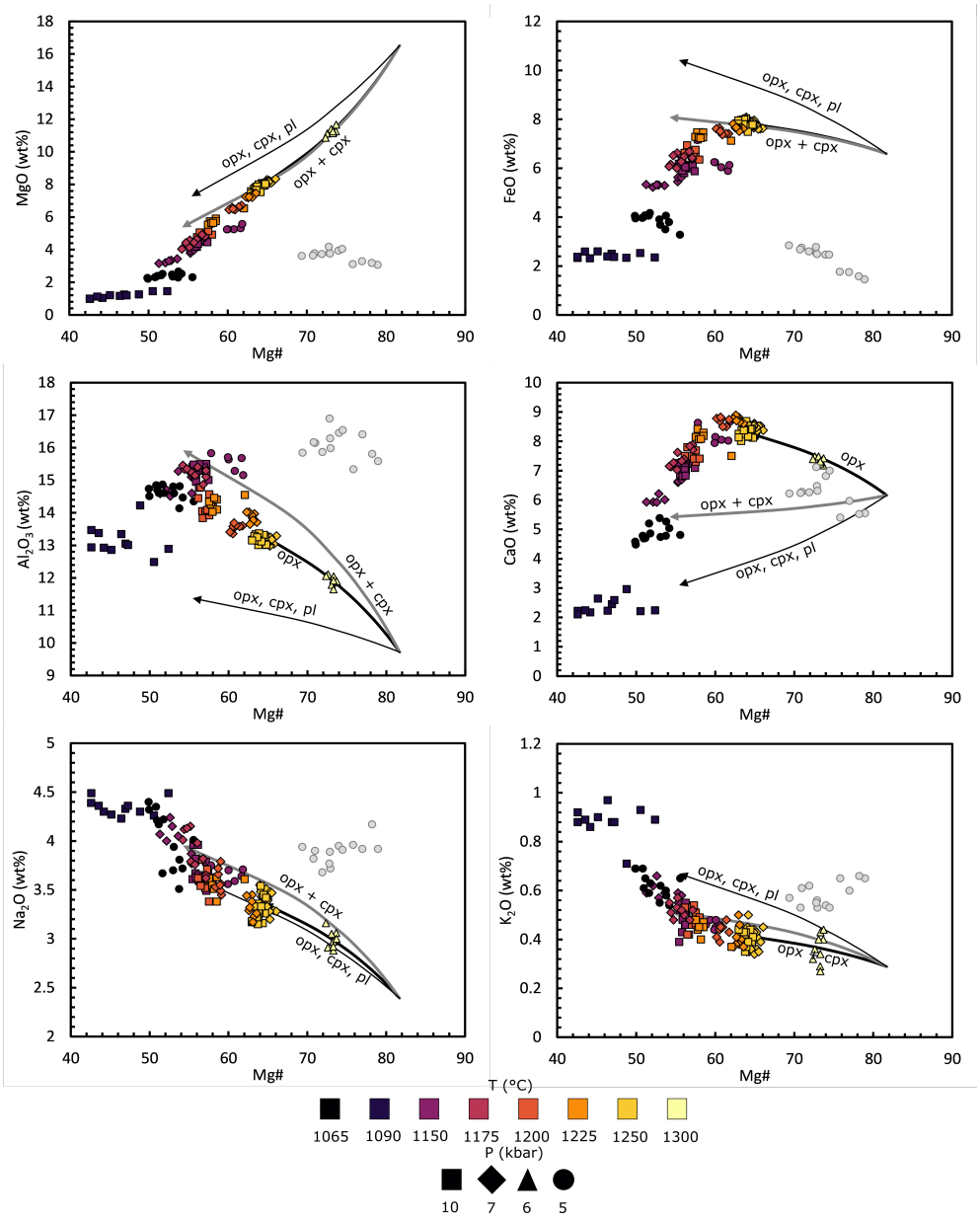

Figure 7.11: Compositional variation of glass in HMBA experiments as a function of the Mg# of the melt. Fractionation lines show the broad trajectory of melt composition when crystallising out the labelled mineral assemblage. Mineral compositions used for modelling these lines are averages from HMBA mineral data. Mineral abbreviations are as in Table 7.2. BA-1225-05 is greyed out due to showing signs of partial capsule failure (see section 7.4.2 for details).

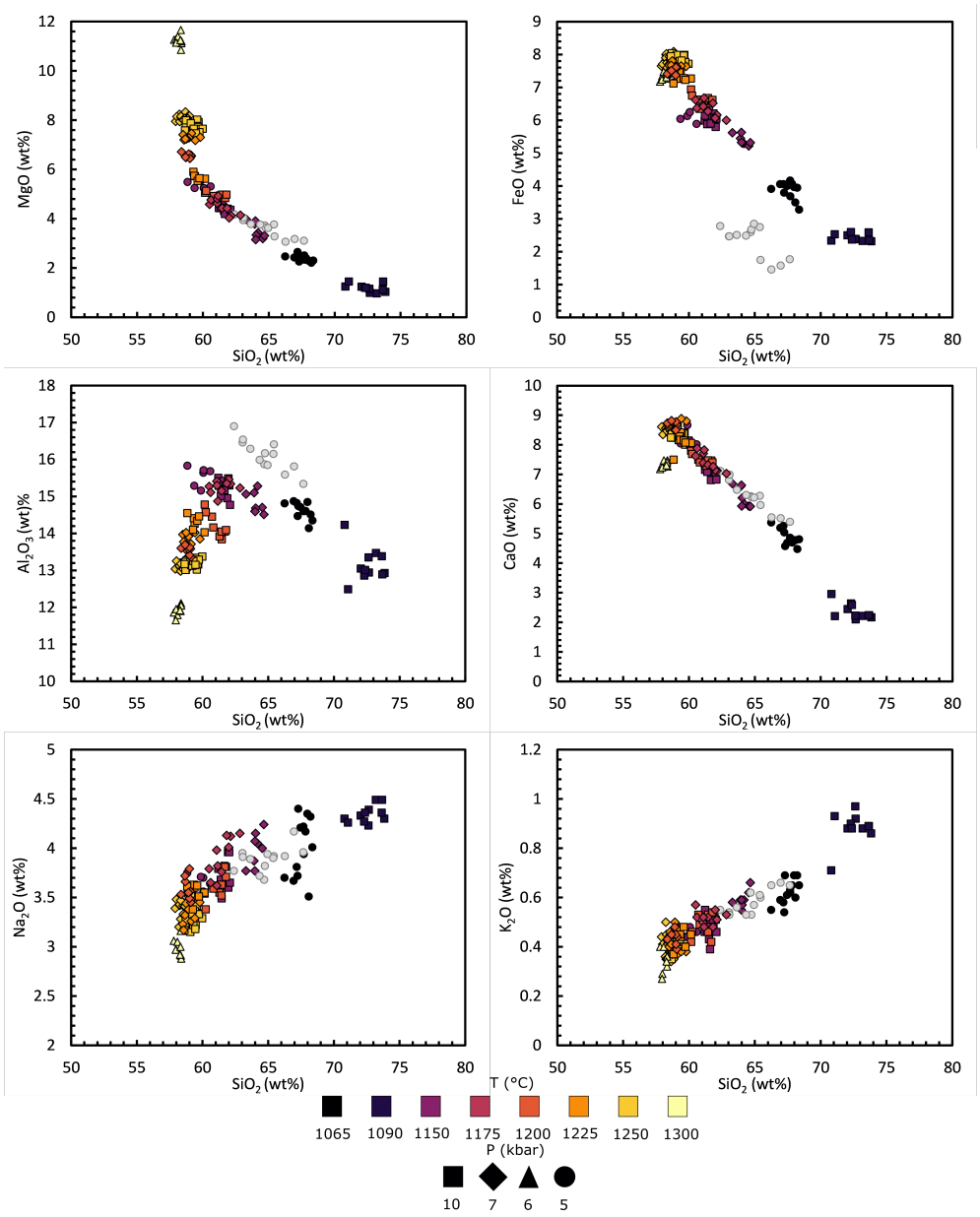

Figure 7.12: Compositional variation of glass in HMBA experiments as a function of the SiO_2 of the melt.BA-1225-05 is greyed out due to showing signs of partial capsule failure (see section 7.4.2 for details).

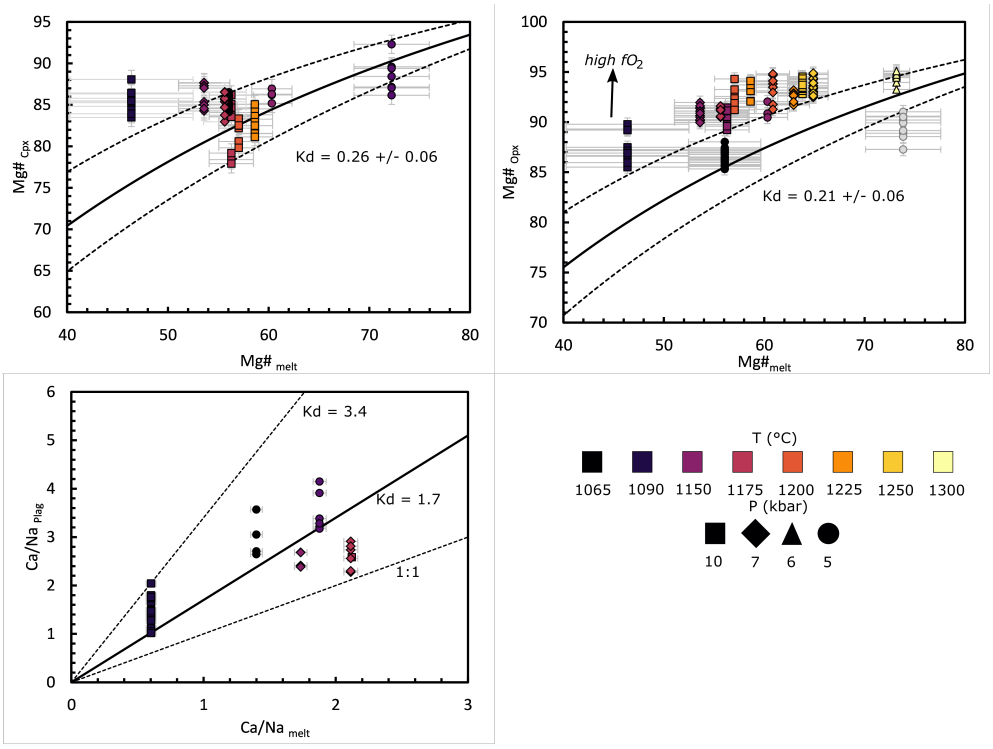

Figure 7.13: Composition of experimental minerals against the Mg# or Ca/Na ratio of the melt. Kd values are from Roeder and Emslie (1970) (olivine) Putirka (2008) (clinopyroxene, orthopyroxene), and Sisson and Grove (1993a) (plagioclase). For plagioclase, a Kd of 1.7 is the expected value for a melt containing 2 wt.% H_2O. BA-1225-05 is greyed out due to showing signs of partial capsule failure (see section 7.4.2 for details).

7.4.3 Assessing equilibrium

Long run durations at high pressure and temperature were used to allow sufficient time for chemical equilibration. Equilibration is facilitated through relatively high melt fractions in most runs, resulting in fully interconnected melt pockets (Figure 7.2). Equilibrium conditions were established first using textural evidence from experimental capsules. Crystals in equilibrium with melt should have homogenous compositions and euhedral crystal shapes, whereas melt should be free of quench crystals or compositional gradients. Representative examples of experimental runs showing clear equilibrium textures are shown in Figure 7.2, where crystals have well-formed equilibrated crystal faces in contact with melt.

Fe loss/gain

Fe loss is a common problem in experimental design. Fe loss occurs when Fe in the melt alloys with the Pt capsule. To avoid this, capsules were pre-annealed in an anhydrous starting composition, containing approximately 8wt.% FeO, as described in section 7.3.2. The extent of any Fe loss from experimental charges was constrained by back calculating the starting composition in each run by mass balance, which gives a total FeO content for the experimental run. Most experimental runs came to within 1 wt.% of the start composition FeO, which corresponds to <10% Fe loss to the Pt capsule. This verges toward 0 when taking into account error in mass balance calculations. Experiments that experience >10% Fe loss cannot reliably be used to predict the phase relations of experiments that did not lose Fe (Mitchell and Grove, 2016). Fe loss/gain values are reported in tables 7.2, 7.3 and 7.4 for 2 wt.%, 5 wt.% and HMBA experiments, respectively. Some experiments show moderate Fe gain using this calculation method. Experiments could have gained Fe from the Fe-saturated Pt, or this could simply be due to inaccuracies arising from mass balance calculations, which requires accurate estimation of phase relations. Small (1-2%) changes in estimation of phase abundances

could produce small (<10%) errors in the calculation of total FeO.

As a whole, the majority of experiments have not lost significant Fe. Experiments that experienced significant Fe loss are anomalous and do not indicate a systematic error in the Pt annealing technique, but rather a partial failure of the capsule. These experiments are: H-1125-05, BA-1110-05 and BA-1225-05. BA-1225-05 is a low-pressure, near liquidus experiment. When an experiment is run near the liquidus at low pressure, the capsule becomes more ductile and is more susceptible to deformation and partial or complete failure. Complete failure results in a flat or empty capsule, with all melt escaped. However partial failures, where volatiles have leaked in or out, or components from the assembly (SiO_2, Al_2O_3, Na_2O, Boron) have leaked in, are sometimes harder to identify. In BA-1225-05, orthopyroxene is concentrated at the bottom of the capsule, in equilibrium with melt. The top of the capsule is 100% glass. There is a compositional gradient in the capsule whereby glass at the top is more silica rich (10 wt.%) than the bottom. This is also evident when shown in a graph of Mg# vs. MgO in the glass (Figure7.11), where BA-1225-05 deviates significantly from the trend, giving high Mg# melt composition, due to the lack of FeO, rather than high MgO content. It is possible this experiment has experienced a partial capsule failure, and has been contaminated with elements present in the pyrex sleeve of the assembly. This could be tested for by analysing for Boron in the glass. An uncontaminated experiment should be B-free or B-poor, but a contaminated experiment may show up to wt.% concentrations of B, as it makes up 4wt.% of the pyrex glass assembly (Brooker, 1998). H-1125-05 and BA-1110-05 do not show the same silica enrichment as BA-1225-05 and so we cannot be sure of the cause of the Fe loss.

H_2O loss/gain

Hydrous piston cylinder experiments are always subject to some H_2O loss due to H diffusion through the Pt capsule walls under high pressure/temperature conditions.

The volatile content of the melt can be assessed by the 'water by difference' method on quantitative analyses of glass, where the remainder of the total analysis to 100% is assumed to be H_2O or other volatiles. Calculated H_2O contents of the glass are presented in tables 7.2, 7.3 and 7.4 for 2 wt.%, 5 wt.% and HMBA experiments, respectively. Water by difference predicts that 2 wt.% experiments contain 1-2.5 wt.% H_2O, 5 wt.% H_2O experiments contain 1.7- 3.5 wt.% H_2O, and HMBA experiments contain 1.4-4.5 wt.% H_2O in the melt. The exception to this is BA-1225-05 which contains 6.5 wt.% H_2O, and has clearly gained volatiles, as discussed in section 7.4.3. H_2O contents correlate with melt fraction, suggesting most water has been retained within the capsules. Additionally, there is no correlation between run duration and H_2O content, showing that if volatile loss has occurred, it must have been early on during the run, and the 24 hours run time is sufficient to reach equilibrium. However, this suggests that although the basalt experiments are still hydrous and water undersaturated, they have not retained consistently sufficient H_2O to facilitate simple comparisons between the two sets of phase relations. Greater H_2O loss from more hydrous melts is not surprising, as a higher geochemical gradient promotes greater H diffusion. However it is not clear whether the difference between H_2O in the experimental glasses is significant, or simply an artefact of scatter on analytical totals. To draw conclusions between the two sets of hydrous experiments requires direct analysis of the H_2O content of the experimental glasses. This could easily be carried out by secondary ion mass spectrometry (SIMS).

Another way of checking volatile content is through plagioclase-melt equilibrium. the Ca/Na of plagioclase is a function of the Ca/Na of the melt it is in equilibrium with, and the H_2O content of the melt. at 2wt.% H_2O in the melt, the Ca/Na of plagioclase should be 1.7 times that of the melt (Sisson and Grove, 1993a). The Ca/Na of plagioclase and melt is shown in Figure 7.6, Figure 7.9 and Figure 7.13 for 2 wt.%, 5 wt.% and HMBA experiments, respectively.

2 wt.% H_2O basalt experiments containing plagioclase show between 0 and 2

wt.% H_2O (Figure 7.6), consistent with calculations of H_2O using water by difference. However, H-1125-05 may have gained volatiles. Plagioclase in this experiment has highly variable Ca/Na ratios of up to 9. When compared with the Ca/Na of the melt this ratio is higher than expected for an experiment with 2 wt.% H_2O (Figure 7.6), suggesting that the experiment has gained H_2O. Ca/Na ratios in plagioclase from 5 wt.% H_2O experiments have highly variable Ca/Na ratios. Higher pressure experiments plot closely along the Kd=1.7 line, suggesting approximately 2 wt.% H_2O in the melt, however some experiments give highly variable Ca/Na ratios, suggesting either H_2O loss from the capsule, or another factor controlling Ca/Na of the plagioclase composition. Plagioclase in 5 wt.% experiments contains up to 2 wt.% FeO, most likely present as Fe^{3+}. This unusually high concentration of Fe_2O_3 is predicted in highly oxidising systems, as Fe^{3+} is compatible in plagioclase (Sugawara, 2001). FeO in plagioclase negatively correlates with CaO, and although the exact cause of this relationship is not clear, it is possible that the high concentrations of FeO affect plagioclase Ca/Na ratios and under-predict melt H_2O, as glass totals clearly suggest higher H_2O than the Ca/Na method. Fe^{3+} substitutes for Al or Si on the tetrahedral site, and this substitution may cause complex defects affecting incorporation of Ca and Na into the plagioclase. However, it is possible that due to the large size of the Fe^{3+} ion, it preferentially substitutes for Ca^{2+} creating a more albitic plagioclase composition. It is not currently clear why Ca/Na ratios in the basaltic experiments are lower than predicted from the predicted water content and Ca/Na of the glass. The uncertainty in the H_2O content, and in the crystal chemistry of plagioclase makes this impossible to conclude, and requires further work. However, fO_2 in 5 wt.% H_2O basalt experiments is higher than in 2 wt.% H_2O basalt experiments and is difficult to explain if the H_2O content is similar between both sets of experiments. Greater H_2O loss could result in additional oxidation of samples during experimental runs, as H diffuses through the Pt capsule and leaves a higher partial pressure of oxygen.

Plagioclase in HMBAs plot closely to the Kd=1.7 line, and correlate well to H_2O

values predicted from water by difference.

Mineral-melt equilibria

Alongside textural evidence for attainment of equilibrium, it is useful to assess whether minerals and melt are in compositional equilibrium. This has been partially discussed above in section 7.4.3 in relation to plagioclase regarding volatile loss or gain to/from experiments. Olivine, clinopyroxene and orthopyroxene should follow set Fe-Mg exchange coefficients (Kd) according to the Fe and Mg content of the melt. For olivine, the Fe-Mg Kd is commonly estimated to be 0.3 ± 0.03 (Roeder and Emslie, 1970). However, olivine in all experiments is significantly more Mg-rich than predicted by this value (Figure 7.6, 7.9). Olivine forsterite content increases with increasing fO_2, as the majority of FeO can only be incorporated into the olivine structure as Fe^{2+}, not Fe^{3+}. fO_2 was calculated using the oxygen barometer of France et al. (2010), which uses FeO partitioning between clinopyroxene, plagioclase and melt to estimate fO_2. Fugacities are reported in tables 7.2, 7.3 and 7.4. On average, fO_2 of all experimental runs is 4.5 log units above the QFM buffer. The high fO_2 of the experiments explains the high forsterite content of the olivine. Additionally Matzen et al. (2011) and Melekhova et al. (2014) report similar difficulties in using a constant Kd value for assessing olivine-melt equilibrium in oxidising systems. Therefore the presence of highly forsteritic olivines in the basaltic melt should not be used as evidence for disequilibrium in the system. The same principle affects orthopyroxene compositions, which also cannot easily accommodate Fe^{3+}. Orthopyroxene Fe-Mg equilibria was based on a Kd of 0.26 ± 0.06 for the basaltic systems (Putirka, 2008). This was adjusted for silica rich systems to give a Kd of 0.21 ± 0.06 for the basaltic andesite system (Putirka, 2008). Orthopyroxenes in the two basaltic systems plot within the equilibrium lines for their given melt Mg#. Orthopyroxenes in the basaltic andesite experiments systematically lie above the predicted equilibrium range for the given Mg# of the melt. This may again

be due to the high fO_2 of the melt, or inaccuracies in the calibration for equilibrium orthopyroxenes in higher silica systems. As crystals and melt are clearly in textural equilibrium (Figure 7.2), the systematic error in predicting crystal-melt equilibrium more likely suggests issues with using constant Kd values to predict equilibrium in experiments with high fO_2 and variable H_2O contents, than disequilibrium within the capsules themselves.

7.5 Discussion

7.5.1 Validity of controlling H_2O content

A key aim of this project was to investigate the impact of different concentrations of H_2O on the crystallisation sequence of high-Mg basalt. This was attempted by adding calculated amounts of brucite ($Mg(OH)_2$) into starting mix compositions to make identical basalts, with 2 wt.% and 5 wt.% H_2O each. This technique has the advantage over traditional micro-pipetting of H_2O into individual capsules, in that H_2O is added to the bulk mixture, before separating into capsules, and so each experiment should be identical. It also improves the accuracy of H_2O concentration, due to the larger volumes being added (each start mix is 5g, as opposed to 0.1-0.2g of sample in each capsule). Although H_2O has not been directly analysed, the H_2O of experiments has been checked through water by difference and plagioclase-melt equilibrium.

Experiments run at high pressure (10kbar) appear to better preserve H_2O concentrations than experiments run at 7kbar and 5kbar, which are more prone to losing, or gaining volatiles (Section 7.4.3). As the compositions are identical within error, other than H_2O content, the preservation of (or lack of) volatiles within runs dictates whether the phase relations differ between the two sets. As a result, high pressure phase relations between the two basaltic sets are significantly different (Figure 7.3), whereas low pressure (5kbar) phase relations are strikingly similar. Most importantly, H_2O plays a vital role in delaying the onset of plagioclase crystallisation in basaltic melts, and produces high-anorthite compositions at lower temperatures (Baker and Eggler, 1987; Sisson and Grove, 1993a). There is very little difference between the onset of plagioclase crystallisation between the two compositions (Figure 7.3), and both sets produce similar composition plagioclase at An_{80-90}, indicating relatively similar H_2O contents. However, as mentioned in section7.4.3, the composition of plagioclase may be affected by the high fO_2 of the melt. This in turn may be controlled not through

the H_2O content itself but the proportion of H loss, with greater H loss causing higher fO_2. Additionally, it may be a combination of partial H_2O loss and a delayed onset of plagioclase crystallisation which is not resolvable at the 25°C temperature intervals of experiments.

Highly variable Ca/Na in some experiments (Figure 7.6, 7.9) suggests that H_2O loss was only partial, and that some areas of the capsule retained H_2O better than others. With this in mind, basalt phase relations will be discussed but in the knowledge that some mineral compositions, i.e. plagioclase, and some phase relations at lower pressure may not represent the precise concentration of H_2O initially desired.

The same brucite addition technique was used for HMBA experiments, where 2 wt.% H_2O was added. However, unlike the basalt experiments, HMBA experiments appear to have retained H_2O relatively well, across all pressure ranges. Analytical totals of glass show good correlation with melt fraction and SiO_2, and plagioclase Ca/Na ratios plot closely to the Kd=1.7 line (Figure 7.13) which represents the Kd at 2 wt.% H_2O. It is strange that HMBA experiments with identical design retain H_2O better than basalt experiments. It is possible that the different melt structure of HMBA allow easier incorporation of -OH into the melt structure than in the basalt melt, and are therefore less likely to lose H_2O.

7.5.2 Comparison of phase assemblages to natural samples

TVZ mafic rocks display a wide range of mineral assemblages. HABs have plagioclase dominated mineral assemblages, ± olivine, ± clinopyroxene. HMBs have olivine dominated assemblages, ± clinopyroxene, and are plagioclase poor, where plagioclase is usually only present in the groundmass. HMBAs have two-pyroxene dominated assemblages, ± disequilibrium or resorbed or overgrown olivine. HABs have the additional complication that mineral assemblages vary between intra- (syn-) caldera, and inter- (post-) caldera settings. Syn-caldera basalt contains higher proportions of

antecrysts, comprising mostly of clinopyroxene, plagioclase and rare orthopyroxene, whereas post-caldera basalt is more crystal-poor, and contains a higher proportion of phenocrystic plagioclase and olivine.

Kakuki basalt has the most primitive mineral assemblage of TVZ HABs, and is a post-caldera basalt (Zellmer et al., 2020). It is often used as the mafic end-member when modelling fractionation of more evolved compositions in the central TVZ (Gamble et al., 1990, 1993; Graham et al., 1995; Rooney and Deering, 2014). Its mineral assemblage is olivine of Fo_{80-85} and plagioclase of An_{80-85}. Clinopyroxene is absent. In experiments, this mineral assemblage was produced in low pressure (5kbar) basalt runs at temperatures of 1175-1200°C. Other HABs contain clinopyroxene in addition to plagioclase and olivine. These are Rotokawau and Tarawera from the syn-caldera samples, and Orakeikorako from the post-caldera samples. This assemblage was also produced in low pressure (5kbar) experiments at temperatures of 1150°C or less. However, a key feature of Rotokawau basalt, and other Okataina Volcanic centre basalt, is the presence of high-anorthite composition plagioclase, which these experiments have not produced, possibly indicating that higher H_2O contents are required to reproduce the natural assemblage, or that the high fO_2 of the experiments has affected plagioclase compositon. This is consistent with Chapters 4 and 6. Terrace Rd and Rotomakariri require the addition of orthopyroxene. Rotomakariri contains glomerocrysts with olivine cores overgrown by clinopyroxene, orthopyroxene and plagioclase. This assemblage can only be produced at pressures of 7kbar or greater. At 10kbar, the maximum temperature limit would be 1200°C, but at 7kbar this is reduced to 1175°C, although at 1175°C, two pyroxenes are only just crystallised, and so 1150°C is potentially a better temperature estimate for the crystallisation of these mineral assemblages. Alternatively, and perhaps a more simple explanation is that olivine in Rotomakariri was crystallised at hotter temperatures, and the two pyroxene plagioclase assemblage overgrew the olivine core as the magma body cooled. This assemblage is produced along a decreasing temperature path at pressures of 7kbar or greater in 2 wt.% and 5 wt.% basalt. However,

Chapter 4 predicts lower crystallisation pressures for the two-pyroxene glomerocrysts in Rotomakariri. In both the 2 wt.% and 5 wt.% experiments, there is a significant melt fraction remaining in the lowest temperature runs at 5 kbar. Temperatures predicted from two-pyroxene thermobarometry for Rotomakariri in Chapter 4 are 1000-1100°C. Therefore it is possible that by extending the temperature range to lower T, orthopyroxene would appear on the liquidus. Ongaroto is the only sample with an olivine-only phenocryst assemblage. It is impossible to constrain a pressure of crystallisation on this sample. However all experiments run at 1200°C or less, contain at least one other phase co-crystallising with olivine. Therefore crystallisation of the Ongaroto mineral assemblage had to occur at temperatures >1200°C. The results of this are consistent with temperature estimates from olivine-spinel thermometry in chapter 6.

The two-pyroxene mineral assemblage of Ohakune HMBA is not produced by either of the basalt crystallisation sequences. Olivine is always the first phase on the liquidus in basalt experiments, and two-pyroxenes are almost always joined by plagioclase. The only conditions to crystallise olivine, clinopyroxene and orthopyroxene without plagioclase is in the 5 wt.% H_2O composition at 1225°C and 10kbar. A key feature of the Ohakune HMBA is that it is plagioclase-poor, and only contains microlites of plagioclase in glassy groundmass. However, south TVZ rocks are typically water-poor (Kilgour et al., 2013), and the same experiment at 2wt.% H_2O produces abundant plagioclase. Additionally, the glass composition produced does not provide a good match to Ohakune HMBA. Ohakune mineral assemblages are better produced by the HMBA (2 wt.% H_2O) composition, which crystallises two pyroxenes at all investigated pressures, at temperatures of 1225-1100°C. Compositions of clinopyroxene and orthopyroxene from Ohakune are most consistent with clinopyroxene and orthopyroxene compositions in experiments run at 5kbar and 1100°C. This is in good agreement with thermobarometry results from Chapter 4 and Kósik et al. (2016). The experimental mineral assemblages also match two-pyroxene assemblages observed in other natural HMBA samples in the south TVZ, such as from Hauhungatahi (Cameron et al., 2010),

Whakapapa and Mangawhero (Conway et al., 2016).

The only natural mineral assemblage not produced by any experiments is the olivine + clinopyroxene assemblage from Waimarino HMB. Like Ohakune HMBA, it is plagioclase poor. It also has a tholeiitic composition (Graham and Hackett, 1987) and is enriched in SiO_2 compared to HABs, and the other HMB sample, Ongaroto. In the basaltic composition experiments, the only conditions where clinopyroxene saturation occurs before plagioclase saturation is at high pressures and temperatures, which is also where olivine is no longer in equilibrium. In the HMBA experiments, clinopyroxene is always the second major phase on the liquidus after orthopyroxene. The starting composition used is silica saturated (55 wt.% SiO_2), and therefore will not crystallise olivine. However, a similarly CaO and Al_2O_3 poor, MgO rich composition, with less SiO_2 would likely crystallise olivine first instead of orthopyroxene. Although the experiments run cannot produce this composition, this seems to be the most logical composition for future reference. This composition could be produced by a process such as magma mixing between the two end-member compositions, or a lesser reaction in the mantle wedge between hydrous basalt and mantle lithosphere (Figure 7.1) (Mitchell and Grove, 2016), only partly enriching the resultant melt in the orthopyroxene component.

7.5.3 Comparison of glass compositions to natural samples

Figure 7.14 shows glass compositions from 2 wt.%, 5 wt.% and HMBA experiments, compared to a compilation of data from TVZ basalt and high-Mg (basaltic) andesite. Basalt compositions are from whole-rock data from the central TVZ (Gamble et al., 1990; Rooney and Deering, 2014; Zellmer et al., 2020), and melt inclusion data also from the central TVZ (Barker et al., 2020). HM(B)A compositions are from whole-rock data from the south TVZ. The localities are; Waimarino basalt, Red Crater basalt, Ruapehu basalt and Ohakune basaltic andesite (Gamble et al., 1990), Ohakune (Kósik

et al., 2016), Hauhungatahi volcano, a partially eroded andesitic edifice west of Ruapehu (Cameron et al., 2010), and the Whakapapa and Mangawhero formations from Ruapehu (Conway et al., 2016). High-Mg andesites from White Island in the north TVZ (Heyworth et al., 2007) are also included in TVZ HMBA data.

TVZ basalt compositions show considerable overlap with both 2wt.% and 5 wt.% basalt glass compositions (Figure 7.14). Only the most evolved natural compositions, which are basaltic andesite (Terrace Road and Rotomakariri) and products of magma mixing between basalt and andesite (Chapter 4), show any significant divergence away from the experimental basaltic glass data. The experimental glasses show striking similarity in SiO_2, total alkali content, CaO, Al_2O_3 and Mg# to natural whole rock basalt samples. Most of the natural basalt data plotted are HAB whole-rock compositions, as opposed to our experimental glasses. HABs are not primary basalts, and require prior fractionation and separation of mafic phases to deplete MgO and enrich Al_2O_3. The experimental glasses therefore reproduce this early fractionation step extremely well, regardless of H_2O content or high fO_2.

TVZ HMBA compositions also show considerable overlap with HMBA experimental glasses. The experimental glasses and natural data show similarity in SiO_2, MgO, total alkali content, Al_2O_3 and CaO. Natural data extends to significantly lower Mg# but this is to be expected when samples become relatively evolved. Additionally, the experiments are relatively oxidised, buffering the FeO content of the melt. If the magmatic system is more reducing, then FeO may concentrate more in the melt, giving a wider range of Mg# with fractional crystallisation. The only samples which show overlap between HMBA experimental glasses and basalt experimental glasses are those from Hauhungatahi (Cameron et al., 2010), which sit at 55 wt.% SiO_2 and 9 wt.% MgO. These are similar to Waimarino basalt, as both have high concentrations of MgO, and SiO_2 concentrations that are intermediate between the basalt and HMBA compositions.

Most importantly, there is a striking compositional gap between HAB samples and

HMBA samples. There does not appear to be a simple way of producing an HMBA composition from the basaltic starting composition, which successfully produces HAB composition glasses.

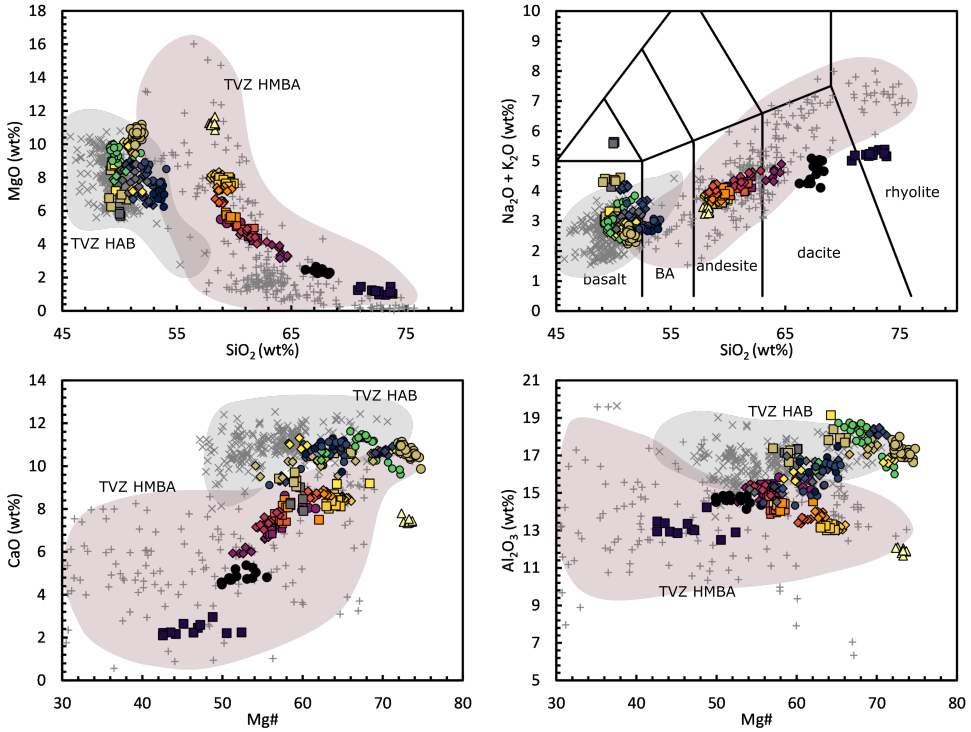

Figure 7.14: Chemical compositions of experimental glasses (symbols as in Figure 7.5 for 2 wt.% glasses, Figure 7.8 for 5 wt.% glasses and Figure 7.11 for HMBA glasses), compared with compositions of TVZ mafic rocks. TVZ basalt data are shown as diagonal crosses (x), TVZ HMBA and HMA data are plus signs (+). TVZ basalt data are whole rock compositions from Gamble et al. (1990), Rooney and Deering (2014), Zellmer et al. (2020), and melt inclusion data from Barker et al. (2020). HMBA and HMA data are from Gamble et al. (1990), Kósik et al. (2016), Cameron et al. (2010), Conway et al. (2016) and Heyworth et al. (2007). See text in section 7.5.3 for localities of data used.

7.5.4 Conclusions, and implications for magma generation and storage in the TVZ

From the experimental data, hydrous basalt compositions do not crystallise and produce HMBA compositions under any of the temperatures or pressures investigated. High-Mg basalt experiments produce HAB composition glasses extremely well, across the

whole P-T space, regardless of the mineral assemblages crystallising. Similarly, HMBA experiments do not produce HAB mineral assemblages, nor HAB glass compositions. However, they do produce two-pyroxene, followed by two-pyroxene and plagioclase assemblages, typical of HMBA in the south TVZ, and glass compositions that span the range of natural HMBA compositions.

The implication is that HMBA from the south TVZ requires a compositionally distinct parental magma to HAB from the central TVZ. Each experimental start composition reproduces natural compositions extremely well, with very little overlap between the two. The basalt start mix represents a close analogue to a primary high-Mg basalt that is produced by hydrous partial melting of the mantle wedge in an arc setting (Elthon and Scarfe, 1984; Gust and Perfit, 1987; Sisson and Grove, 1993a). However, the HMBA start composition is a product of mixing between hydrous basalt and harzburgite in experiments by (Mitchell and Grove, 2015, 2016), and similar experiments conducted as a part of this project. Previous studies have shown that neither dry nor wet melting of lherzolite can produce the high-Si, high-Mg compositions required to produce HMBAs (Gaetani and Grove, 1998; Parman and Grove, 2004; Wood and Turner, 2009), whilst experiments have long shown that removal of the diopsidic (Ca rich) clinopyroxene component from the mantle residue produces simultaneous enrichment in SiO_2 and MgO in the liquid (Kushiro, 1972; Kelemen et al., 1990). Therefore, experimental studies are in good agreement that a harzburgite component in the residue is required to produce the high-Si, high-Mg signature of HMBA.

The presence of harzburgite-derived xenocrysts in south TVZ samples, and the ability of the HMBA composition to reproduce natural HMBA compositions from the south TVZ is strong evidence for a lithospheric mantle control on parental magma composition in the south TVZ. Mitchell and Grove (2016) showed that varying the proportion of basalt to harzburgite and the temperature at which the mixing occurs has a strong influence on the composition of the resultant melt. The HMBA composition used is toward the SiO_2 enriched end of the spectrum of compositions. Therefore, it is

reasonable to assume that other transitional samples which show less pronounced SiO_2 enrichment, such as Hauhungatahi and Waimarino basalt could be produced from less SiO_2 enriched parental compositions that lie along the spectrum of glass compositions produced by Mitchell and Grove (2016).

Finally, high-Mg basaltic andesites are not unique to the TVZ. They also occur at the southern tip of the Coromandel Volcanic Zone (NZ) (Booden et al., 2010), and further afield, such as at Mt Shasta (USA) and the Setouchi Belt (Japan), as examples. The HMBA experiments run show that enrichment of the parental melt in SiO_2 and MgO produces a composition which crystallises two-pyroxene assemblages over a wide P-T range. Melt compositions match a wide range of HMBA compositions from the TVZ (Figure7.14). Consequently, these experiments may also be applicable to other HMBA systems found globally. They also support an argument for the role of lithospheric mantle in controlling continental arc magma composition.

Chapter 8

Synthesis, Conclusions and suggestions for further work

8.1 Conclusions

This thesis has investigated and discussed the nature of basalt in the Taupo Volcanic Zone. Here follows a summary of the work from each chapter, and conclusions that can be drawn when tying these findings together. The final section includes some recommendations for further work that will help to advance our knowledge in some key questions that have arisen out of this PhD.

8.1.1 Chapter 4: Mineral compositions and magma storage

1. Basalt contains a range of glomeroporphyritic textures, with mineral assemblages systematically varying between pre-, syn- and post-caldera basalt.

2. Evidence for disequilibria, such as abrupt zonation, sieve textures and overgrowth or corona textures are abundant in all crystal cargoes. The general lack of phenocrysts and dominance of antecrysts is interpreted to be a sign of relatively aphyric melts inheriting crystals from cognate mushes on ascent.

3. The deep storage conditions required at Ohakune in the south TVZ likely reflect

the local tectonic regime, where thickened lithosphere inhibits ascent of primitive magmas to the shallow crust.

4. The presence of >An_{90} plagioclase crystals in OVC basalt and basaltic andesite requires high concentrations of H_2O, and shallow storage in the crust. The ubiquity of >An_{90} plagioclase throughout OVC samples suggests that an external factor controls crystallisation of >An_{90} plagioclase. This control may be structural or tectonic, and is unique to OVC and the surrounding area, as this population of plagioclase is not found elsewhere in the TVZ.

5. Post-caldera basalts are the simplest in terms of their crystal cargo, and undergo minimal processing in the crust.

8.1.2 Chapter 5: Oxygen isotopes

1. Interpretation of $\delta^{18}O$ in mafic rocks in of TVZ is much more complex than initial assumptions.

2. Individual samples can show a significant range in $\delta^{18}O$, which is unexpected in basalt that is commonly believed to have a simple magmatic history.

3. There are multiple populations of crystals in an individual sample. This is interpreted as evidence for open-system processes occurring in mafic magma, and highlights the importance of crustal assimilation at an early stage in magma evolution.

4. The relative contribution of continental crust appears to lessen through the maturation of the system, in broad agreement with previous work for the TVZ.

5. Variation in crustal contribution to mafic TVZ magmas is primarily controlled by two factors.

- How heavily intruded the crust is, controlling how much continental crust new pulses of magma come into contact with and can therefore assimilate
- The heat flow of the region, controlled by flux of hot mantle melt into the crust. i.e. the heat from the flux must be enough to induce partial melting of the crust.

8.1.3 Chapter 6: Olivine and whole-rock trace element modelling

1. South TVZ magmas interact with depleted harzburgitic mantle. Magma is sourced from large melt fractions in the shallow mantle, and potentially requires a greater slab sediment contribution than elsewhere in the rifted arc.

2. Interaction with depleted harzburgitic mantle may influence the major element composition of south TVZ magma, towards higher MgO and SiO_2, and lower CaO and Al_2O_3.

3. Central TVZ magmas show no evidence for interaction with depleted harzburgitic mantle. Variation in slab-derived fluids is required between syn-caldera basalt and post-caldera basalt, whereby syn-caldera basalt requires greater input from the slab than post-caldera basalt. All basalt compositions from the TVZ are consistent with a spinel lherzolite mantle source, with variable slab contribution.

4. Thinning of the lithosphere, which occurs in the central TVZ, promotes the transition from continental arc style volcanism, to rhyolitic volcanism. This implies a direct link between rifting, magma composition and volcanic productivity.

8.1.4 Chapter 7: High pressure/temperature experiments

1. Hydrous high-Mg basalt (HMB) compositions do not crystallise and produce high-Mg basaltic andesite (HMBA) compositions. HMB experiments produce

HAB composition glasses extremely well, across the whole P-T space, regardless of the mineral assemblages crystallising.

2. HMBA experiments do not produce HAB mineral assemblages, or HAB glass compositions. However, they do produce two-pyroxene, followed by two-pyroxene and plagioclase assemblages, typical of HMBA in the south TVZ, and glass compositions that span the range of natural HMBA compositions.

3. HMBA from the south TVZ requires a compositionally distinct parental magma to HAB from the central TVZ. Each experimental start composition reproduces natural compositions extremely well, with very little overlap between the two.

4. Experiments producing HMB and HMBA strongly support the interpretation that south TVZ magmas inherit part of their major element composition from interaction with harzburgitic mantle lithosphere. Dissolution of the orthopyroxene component in harzburgite shifts basalt compositions to higher silica content, whilst retaining high concentrations of Mg.

5. Comparison of experiments to natural samples is promising. The next step is to compare experiments to current thermodynamic thermobarometers and thermodynamic models e.g. MELTs software.

8.2 Summary

Basalt petrogenesis in the TVZ is much more complex than previously assumed. This has important consequences in terms of other studies that use basalt compositions to infer characteristics of the mantle source. This does not mean that monogenetic basalt compositions do not retain a primitive mantle-derived composition, but it is important to account for the effects of crustal contamination and magma mixing, even from monogenetic deposits. Basalt magma in the TVZ appears relatively primitive and

aphyric, but entrains a range of antecryst compositions from cognate cumulate mushes at variable depth in the crust. This thesis has shown it is possible to trace crystal origins through their chemical and isotopic compositions (Chapters 5, 4), and reveal some of the complexities of the mafic plumbing system. This work has lead to the conclusion that basalt in post-caldera settings is most likely to retain primitive mantle-derived compositions, but is not representative of the composition that is supplying caldera-forming systems. Likewise, open-system processes tend to obscure primitive mantle composition in syn-caldera basalt. This means that syn-caldera basalt is of most use as a primitive magma end-member when modelling the silicic system, but only providing its mantle-derived signature can be separated from that which arises due to magma processing in the crust.

This thesis has shown that by picking apart components of the basalt, it is possible to infer characteristics of various source regions. The multiple populations of mantle-derived olivine from Chapter 6 suggest that basalt magmas interact with different lithologies on ascent. In the south TVZ, basalt inherits xenocrysts sourced from the subcontinental lithospheric mantle. Experiments conducted in Chapter 7 support this by showing that primitive compositions derived from mixing of basalt and harzburgite crystallise similar phase assemblages to south TVZ mafic rocks, and also produce the observed range of natural HMBA compositions in the TVZ. This has important implications on the genesis of HMBA on a global scale, and other settings where hydrous basalts may interact with refractory layers of lithospheric mantle.

8.3 Suggestions for further work

1. Oxygen isotope analysis on crystal separates has revealed that crystals from pre- and syn-caldera basalt have highly variable δ^{18}O. Secondary ion mass spectrometry (SIMS) allows spatially resolved analyses of δ^{18}O in individual crystals. SIMS analysis could reveal the timing of crustal assimilation in the crystal stratigraphy.

2. An attempt at constraining the H_2O content of basalt has been made through modelling of crystal-melt equilibria and high-pressure/temperature experiments. Better constraints on H_2O through analysis of melt inclusions in crystals, and in melt pockets in samples with sufficient glass will greatly help future models.

3. High-anorthite plagioclase crystals are ubiquitous in samples from OVC. This thesis has suggested these result from low-pressure crystallisation of hydrous magma with high CaO content. High-anorthite plagioclase is not unique to the TVZ, and is usually occurs in primitive melts with much higher melt H_2O content. However no experiments to date have constrained the conditions needed to form high-anorthite plagioclase. As there appears to be an external (tectonic or structural) constraint on the formation of high-anorthite plagioclase, this work would greatly benefit from experimental or thermodynamic constraints on its formation.

4. Olivine xenocrysts in Ongaroto and Waimarino samples show strong normal zoning towards the rim. These olivines would lend themselves extremely well to a diffusion study to elicit timescales.

5. This thesis was not exhaustive in its sampling of mafic rocks from the south TVZ. The ideas presented in this thesis, and the requirement of interaction with depleted mantle lithosphere could be greatly expanded in a targeted study of rocks from the south TVZ. This includes, but is not limited to: samples from Hauhungatahi, Pukekaikiore, Red Crater basalt, Ruapehu basalt and the Mangawhero and Whakapapa formations of Ruapehu. On this note, samples from the north TVZ have not been discussed, however olivine andesites occur at White Island. Detailed study of the crystal cargo of these samples would test the conclusions drawn from the olivine cargo and major element compositions of the rocks in this thesis.

6. High-pressure/temperature experiments would greatly benefit through direct analysis of the H_2O content of glass. Whilst the differences between HMB ad HMBA experiments are clear, it it not clear whether the two sets of basalt have retained H_2O and that the H_2O content has a minimal effect on the phase relations of the basalt, or whether both are subject to moderate but variable H_2O loss. Plagioclase in experiments also contains >1 wt.% FeO, and Ca/Na ratios suggest lower H_2O than predicted using water by difference. It is unclear whether the relatively low Ca/Na ratios are associated with H_2O loss in experiments, or are a secondary effect of high fO_2 causing Fe^{3+} incorporation into plagioclase, and potential knock-on structural defects in plagioclase, altering Ca/Na ratios.

Bibliography

Allan, A. S., Morgan, D. J., Wilson, C. J. N., and Millet, M.-A. (2013). From mush to eruption in centuries : assembly of the super-sized Oruanui magma body. *Contributions to Mineralogy and Petrology*, 166:143–164.

Annen, C. (2009). From plutons to magma chambers : Thermal constraints on the accumulation of eruptible silicic magma in the upper crust. *Earth and Planetary Science Letters*, 284(3-4):409–416.

Annen, C. (2011). Implications of incremental emplacement of magma bodies for magma differentiation, thermal aureole dimensions and plutonism-volcanism relationships. *Tectonophysics*, 500(1-4):3–10.

Annen, C., Blundy, J. D., Leuthold, J., and Sparks, R. S. J. (2015). Construction and evolution of igneous bodies : Towards an integrated perspective of crustal magmatism. *Lithos*, 230:206–221.

Annen, C., Blundy, J. D., and Sparks, R. S. J. (2006). The Genesis of Intermediate and Silicic Magmas in Deep Crustal Hot Zones. *Journal of Petrology*, 47(3):505–539.

Arai, S. (1994). Characterization of spinel peridotites by olivine-spinel compositional relationships: Review and interpretation. *Chemical Geology*, 113(3-4):191–204.

Asimow, P. D. and Ghiorso, M. S. (1998). Algorithmic modifications extending MELTS to calculate subsolidus phase relations. *American Mineralogist*, 83(9-10):1127–1132.

Asimow, P. D., Hirschmann, M. M., and Stolper, E. M. (2001). Calculation of Peridotite Partial Melting from Thermodynamic Models of Minerals and Melts, IV. Adiabatic Decompression and the Composition and Mean Properties of Mid-ocean Ridge Basalts. *Journal of Petrology*, 42(5):963–998.

Bachmann, O. and Bergantz, G. W. (2004). On the origin of crystal-poor rhyolites: Extracted from batholithic crystal mushes. *Journal of Petrology*, 45(8):1565–1582.

Bachmann, O., Deering, C. D., Lipman, P. W., and Plummer, C. (2014). Building zoned ignimbrites by recycling silicic cumulates: Insight from the 1,000 km3 Carpenter Ridge Tuff, CO. *Contributions to Mineralogy and Petrology*, 167(6):1–13.

Bachmann, O., Miller, C. F., and de Silva, S. L. (2007). The volcanic-plutonic connection as a stage for understanding crustal magmatism. *Journal of Volcanology and Geothermal Research*, 167(1-4):1–23.

Baker, D. R. and Eggler, D. H. (1987). Compositions of anhydrous and hydrous melts coexisting with plagioclase, augite, and olivine or low-Ca pyroxene from 1 atm to 8 kbar: application to the Aleutian volcanic center of Atka. *American Mineralogist*, 72(1-2):12–28.

Ballhaus, C., Berry, R. F., and Green, D. H. (1991). High pressure experimental calibration of the olivine-orthopyroxene-spinel oxygen geobarometer: implications for the oxidation state of the upper mantle. *Contributions to Mineralogy and Petrology*, 107(1):27–40.

Barboni, M., Annen, C., and Schoene, B. (2015). Evaluating the construction and evolution of upper crustal magma reservoirs with coupled U/Pb zircon geochronology and thermal modeling: A case study from the Mt. Capanne pluton (Elba, Italy). *Earth and Planetary Science Letters*, 432:436–448.

Barker, S., Rowe, M. C., Wilson, C. J. N., Gamble, J. A., Rooyakkers, S. M., Wysoczanski, R. J., Illsley-Kemp, F., and Kenworthy, C. C. (2020). What lies beneath? Reconstructing the primitive magmas fueling voluminous silici volcanism using olivine-hosted melt inclusions. *Geology*, 48(5):1–5.

Barnes, S. J. and Roeder, P. L. (2001). The Range of Spinel Compositions in Terrestrial Mafic and Ultramafic Rocks. *Journal of Petrology*, 42(12):2279–2302.

Beattie, P. (1993). Olivine-melt and orthopyroxene-melt equilibria. *Contributions to Mineralogy and Petrology*, 115(1):103–111.

Bégué, F., Gravley, D. M., Chambefort, I., Deering, C. D., and Kennedy, B. M. (2015). Magmatic volatile distribution as recorded by rhyolitic melt inclusions in the Taupo Volcanic Zone, New Zealand. *Geological Society Special Publication*, 410(1):71–94.

Bibby, H. M., Caldwell, T. G., Davey, F. J., and Webb, T. H. (1995). Geophysical evidence on the structure of the Taupo Volcanic Zone and its hydrothermal circulation. *Journal of Volcanology and Geothermal Research*, 68(1-3):29–58.

Bignall, G., Browne, P. R., and Kyle, P. R. (1996). Geochemical characterisation of hydrothermally altered ignimbrites in active geothermal fields from the central Taupo Volcanic zone, New Zealand. *Journal of Volcanology and Geothermal Research*, 73(1-2):79–97.

Bindeman, I. N., Ponomareva, V. V., Bailey, J. C., and Valley, J. W. (2004). Volcanic arc of Kamchatka: A province with high-δ18O magma sources and large-scale 18O/16O depletion of the upper crust. *Geochimica et Cosmochimica Acta*, 68(4):841–865.

Bindeman, I. N., Valley, J. W., Wooden, J. L., and Persing, H. M. (2001). Post-caldera volcanism: In situ measurement of U-Pb age and oxygen isotope ratio in Pleistocene zircons from Yellowstone caldera. *Earth and Planetary Science Letters*, 189(3-4):197–206.

Bindeman, I. N., Watts, K. E., Schmitt, A. K., Morgan, L. A., and Shanks, P. W. (2007). Voluminous low δ18O magmas in the late Miocene Heise volcanic field, Idaho: Implications for the fate of Yellowstone hotspot calderas. *Geology*, 35(11):1019–1022.

Blattner, P. and Reid, F. (1982). The origin of lavas and ignimbrites of the Taupo Volcanic Zone, New Zealand, in the light of oxygen isotope data. *Geochimica et Cosmochimica Acta*, 46:1417–1429.

Blattner, P., Rui-Zhong, H., Graham, I. J., and Houston-Eleftheriadis, C. (1996). Temperatures and isotopic evolution of silicic magmas, Taupo Volcanic Zone and Coromandel, New Zealand. *New Zealand Journal of Geology and Geophysics*, 39(3):353–362.

Booden, M. A., Smith, I. E., Mauk, J. L., and Black, P. M. (2010). Evolving volcanism at the tip of a propagating arc: The earliest high-Mg andesites in northern New Zealand. *Journal of Volcanology and Geothermal Research*, 195(2-4):83–96.

Boudier, F. (1991). Olivine xenocrysts in picritic magmas. *Contributions to Mineralogy and Petrology*, 109(1):114–123.

Brenna, M., Cronin, S. J., Németh, K., Smith, I. E., and Sohn, Y. K. (2011). The influence of magma plumbing complexity on monogenetic eruptions, Jeju Island, Korea. *Terra Nova*, 23(2):70–75.

Brenna, M., Cronin, S. J., Smith, I. E., Tollan, P. M., Scott, J. M., Prior, D. J., Bambery, K., and Ukstins, I. A. (2018). Olivine xenocryst diffusion reveals rapid monogenetic basaltic magma ascent following complex storage at Pupuke Maar, Auckland Volcanic Field, New Zealand. *Earth and Planetary Science Letters*, 499:13–22.

Brooker, R. (1998). Reduction in piston-cylinder experiments: The detection of carbon infiltration into platinum capsules. *American Mineralogist*, 83(9-10):985–994.

Brown, S. J., Wilson, C. J., Cole, J. W., and Wooden, J. (1998). The Whakamaru group ignimbrites, Taupo Volcanic Zone, New Zealand: Evidence for reverse tapping of a zoned silicic magmatic system. *Journal of Volcanology and Geothermal Research*, 84(1-2):1–37.

Browne, P., Graham, I., Parker, R., and Wood, C. (1992). Subsurface andesite lavas and plutonic rocks in the Rotokawa and Ngatamariki geothermal systems, Taupo Volcanic Zone, New Zealand. *Journal of Volcanology and Geothermal Research*, 51(3):199–215.

Cameron, E., Gamble, J., Price, R., Smith, I., McIntosh, W., and Gardner, M. (2010). The petrology, geochronology and geochemistry of Hauhungatahi volcano, S.W. Taupo Volcanic Zone. *Journal of Volcanology and Geothermal Research*, 190(1-2):179–191.

Carter, L., Shane, P., Alloway, B., Hall, I. R., Harris, S. E., and Westgate, J. A. (2003). Demise of one volcanic zone and birth of another - A 12 m.y. marine record of major rhyolitic eruptions from New Zealand. *Geology*, 31(6):493–496.

Cashman, K. V., Sparks, R. S. J., and Blundy, J. D. (2017). Vertically extensive and unstable magmatic systems: A unified view of igneous processes. *Science*, 355(6331).

Chambefort, I., Buscarlet, E., Wallis, I. C., Sewell, S., and Wilmarth, M. (2016). Ngatamariki Geothermal Field, New Zealand: Geology, geophysics, chemistry and conceptual model. *Geothermics*, 59(2):266–280.

Chambefort, I., Lewis, B., Wilson, C. J., Rae, A. J., Coutts, C., Bignall, G., and Ireland, T. R. (2014). Stratigraphy and structure of the Ngatamariki geothermal system from new zircon U-Pb geochronology: Implications for Taupo Volcanic Zone evolution. *Journal of Volcanology and Geothermal Research*, 274:51–70.

Charlier, B. L. A., Wilson, C. J. N., and Davidson, J. P. (2008). Rapid open-system assembly of a large silicic magma body: Time-resolved evidence from cored plagioclase crystals in the Oruanui eruption deposits, New Zealand. *Contributions to Mineralogy and Petrology*, 156(6):799–813.

Charlier, B. L. A., Wilson, C. J. N., Lowenstern, J. B., Blake, S., van Calsteren, P. W., and Davidson, J. P. (2005). Magma generation at a large, hyperactive silicic volcano (Taupo, New Zealand) revealed by U-Th and U-Pb systematics in zircons. *Journal of Petrology*, 46(1):3–32.

Charlier, B. L. A., Wilson, C. J. N., and Mortimer, N. (2010). Evidence from zircon U-Pb age spectra for crustal structure and felsic magma genesis at Taupo volcano, New Zealand. *Geology*, 38(10):915–918.

Chiba, H., Chacko, T., Clayton, R. N., and Goldsmith, J. R. (1989). Oxygen isotope fractionations involving diopside, forsterite, magnetite, and calcite: Application to geothermometry. *Geochimica et Cosmochimica Acta*, 53(11):2985–2995.

Clayton, R. N. and Steiner, A. (1975). Oxygen isotope studies of the geothermal system at Wairakei, New Zealand. *Geochimica et Cosmochimica Acta*, 39(8):1179–1186.

Cole, J. (1973). High-alumina basalts of Taupo Volcanic Zone, New Zealand. *Lithos*, 6(1):53–64.

Cole, J. W., Deering, C. D., Burt, R. M., Sewell, S., Shane, P. A., and Matthews, N. E. (2014). Okataina Volcanic Centre, Taupo Volcanic Zone, New Zealand: A review of volcanism and synchronous pluton development in an active, dominantly silicic caldera system. *Earth-Science Reviews*, 128:1–17.

Cole, J. W. and Lewis, K. B. (1981). Evolution of the Taupo-Hikurangi subduction system. *Tectonophysics*, 72(1-2):1–21.

Coleman, D. S., Gray, W., and Glazner, A. F. (2004). Rethinking the emplacement and evolution of zoned plutons: Geochronologic evidence for incremental assembly of the Tuolumne Intrusive Suite, California. *Geology*, 32(5):433–436.

Comeau, M. J., Unsworth, M. J., Ticona, F., and Sunagua, M. (2015). Magnetotelluric images of magma distribution beneath Volcán Uturuncu, Bolivia: Implications for magma dynamics. *Geology*, 43(3):243–246.

Conway, C. E., Leonard, G. S., Townsend, D. B., Calvert, A. T., Wilson, C. J., Gamble, J. A., and Eaves, S. R. (2016). A high-resolution 40Ar/39Ar lava chronology and edifice construction history for Ruapehu volcano, New Zealand. *Journal of Volcanology and Geothermal Research*, 327:152–179.

Coogan, L. A., Saunders, A. D., and Wilson, R. N. (2014). Aluminum-in-olivine thermometry of primitive basalts: Evidence of an anomalously hot mantle source for large igneous provinces. *Chemical Geology*, 368:1–10.

Cooper, G. F., Morgan, D. J., and Wilson, C. J. N. (2017). Rapid assembly and rejuvenation of a large silicic magmatic system: Insights from mineral diffusive profiles in the Kidnappers and Rocky Hill deposits, New Zealand. *Earth and Planetary Science Letters*, 473:1–13.

Cooper, G. F. and Wilson, C. J. N. (2014). Development, mobilisation and eruption of a large crystal-rich rhyolite: The Ongatiti ignimbrite, New Zealand. *Lithos*, 198-199(1):38–57.

Cooper, K. M. and Kent, A. J. (2014). Rapid remobilization of magmatic crystals kept in cold storage. *Nature*, 506(7489):480–483.

Danyushevsky, L. V. (2001). The effect of small amounts of H2O on crystallisation of mid-ocean ridge and backarc basin magmas. *Journal of Volcanology and Geothermal Research*, 110(3-4):265–280.

Danyushevsky, L. V. and Plechov, P. (2011). Petrolog3: Integrated software for modeling crystallization processes. *Geochemistry, Geophysics, Geosystems*, 12(7).

Davidson, J. P., Hora, J. M., Garrison, J. M., and Dungan, M. A. (2005). Crustal forensics in arc magmas. *Journal of Volcanology and Geothermal Research*, 140(1-3):157–170.

De Hoog, J. C. M., Gall, L., and Cornell, D. H. (2010). Trace-element geochemistry of mantle olivine and application to mantle petrogenesis and geothermobarometry. *Chemical Geology*, 270(1-4):196–215.

de Silva, S. and Gregg, P. M. (2014). Thermomechanical feedbacks in magmatic systems: Implications for growth, longevity, and evolution of large caldera-forming magma reservoirs and their supereruptions. *Journal of Volcanology and Geothermal Research*, 282:77–91.

de Silva, S., Zandt, G., Trumbull, R., and Viramonte, J. (2006). Large-Scale Silicic Volcanism -The Result of Thermal Maturation of the Crust. *Advances in Geosciences*, 1(June 2014):215–230.

Deering, C. D., Bachmann, O., Dufek, J., and Gravley, D. M. (2011a). Rift-Related Transition from Andesite to Rhyolite Volcanism in the Taupo Volcanic Zone (New Zealand) Controlled by Crystal-melt Dynamics in Mush Zones with Variable Mineral Assemblages. *Journal of Petrology*, 52(11):2243–2263.

Deering, C. D., Cole, J. W., and Vogel, T. A. (2008). A rhyolite compositional continuum governed by lower crustal source conditions in the taupo volcanic zone, New Zealand. *Journal of Petrology*, 49(12):2245–2276.

Deering, C. D., Cole, J. W., and Vogel, T. A. (2011b). Extraction of crystal-poor rhyolite from a hornblende-bearing intermediate mush: A case study of the caldera-forming

Matahina eruption, Okataina volcanic complex. *Contributions to Mineralogy and Petrology*, 161(1):129–151.

Deering, C. D., Gravley, D. M., Vogel, T. A., Cole, J. W., and Leonard, G. S. (2010). Origins of cold-wet-oxidizing to hot-dry-reducing rhyolite magma cycles and distribution in the Taupo Volcanic Zone, New Zealand. *Contributions to Mineralogy and Petrology*, 160(4):609–629.

Deering, C. D., Horton, T. W., Gravley, D. M., and Cole, J. W. (2012). Hornblende, cummingtonite, and biotite hydrogen isotopes: Direct evidence of slab-derived fluid flux in silicic magmas of the Taupo Volcanic Zone, New Zealand. *Journal of Volcanology and Geothermal Research*, 233-234:27–36.

Doremus, R. H. (2004). Transport of oxygen in silicate glasses. *Journal of Non-Crystalline Solids*, 349(1-3):242–247.

Eberhart-Phillips, D., Bannister, S., and Reyners, M. (2020). Attenuation in the mantle wedge beneath super-volcanoes of the Taupo Volcanic Zone, New Zealand. *Geophysical Journal International*, 220(1):703–723.

Eberhart-Phillips, D., Reyners, M., Chadwick, M., and Chiu, J. M. (2005). Crustal heterogeneity and subduction processes: 3-D Vp, Vp/Vs and Q in the southern North Island, New Zealand. *Geophysical Journal International*, 162(1):270–288.

Elburg, M., Kamenetsky, V. S., Nikogosian, I., Foden, J., and Sobolev, A. V. (2006). Coexisting high- and low-calcium melts identified by mineral and melt inclusion studies of a subduction-influenced syn-collisional magma from South Sulawesi, Indonesia. *Journal of Petrology*, 47(12):2433–2462.

Elthon, D. and Scarfe, C. M. (1984). High-pressure phase equilibria of a high-magnesia basalt and the genesis of primary oceanic basalts. *American Mineralogist*, 69(1-2):1–15.

Farrell, J., Smith, B. R., Husen, S., and Diehl, T. (2014). Tomography from 26 years of seismicity revealing that the spatial extent of the Yellowstone crustal magma reservoir extends well beyond the Yellowstone caldera. *Geophysical Research Letters*, 41:3068–3073.

Feig, S. T., Koepke, J., and Snow, J. E. (2010). Effect of oxygen fugacity and water on phase equilibria of a hydrous tholeiitic basalt. *Contributions to Mineralogy and Petrology*, 160(4):551–568.

Fitton, J. G., James, D., and Leeman, W. P. (1991). Basic magmatism associated with late Cenozoic extension in the western United States: compositional variations in space and time. *Journal of Geophysical Research*, 96(B8).

Foley, S., Prelevic, D., Rehfeldt, T., and Jacob, D. (2013). Minor and trace elements in olivines as probes into early igneous and mantle melting processes. *Earth and Planetary Science Letters*, 363:181–191.

Fram, M. S. and Longhi, J. (1992). Phase equilibria of dikes associated with Proterozoic anorthosite complexes. *American Mineralogist*, 77(5-6):605–616.

France, L., Ildefonse, B., Koepke, J., and Bech, F. (2010). A new method to estimate the oxidation state of basaltic series from microprobe analyses. *Journal of Volcanology and Geothermal Research*, 189(3-4):340–346.

Gaetani, G. A. and Grove, T. L. (1998). The influence of water on melting of mantle peridotite. *Contributions to Mineralogy and Petrology*, 131(4):323–346.

Gamble, J., Woodhead, J., Wright, I., and Smith, I. (1996). Basalt and sediment geochemistry and magma petrogenesis in a transect from oceanic island arc to rifted continental margin arc: The Kermadec-Hikurangi Margin, SW Pacific. *Journal of Petrology*, 37(6):1523–1546.

Gamble, J. A., Smith, I. E., McCulloch, M. T., Graham, I. J., and Kokelaar, B. P. (1993). The geochemistry and petrogenesis of basalts from the Taupo Volcanic Zone and Kermadec Island Arc, S.W. Pacific. *Journal of Volcanology and Geothermal Research*, 54(3-4):265–290.

Gamble, J. A., Smith, I. E. M., Graham, I. J., Peter Kokelaar, B., Cole, J. W., Houghton, B. F., and Wilson, C. J. N. (1990). The petrology, phase relations and tectonic setting of basalts from the taupo volcanic zone, New Zealand and the Kermadec Island arc - havre trough, SW Pacific. *Journal of Volcanology and Geothermal Research*, 43(1-4):253–270.

Gamble, J. A., Wright, I. C., Woodhead, J. D., and McCulloch, M. T. (1994). Arc and back-arc geochemistry in the southern Kermadec arc-Ngatoro Basin and offshore Taupo Volcanic Zone, SW Pacific. *Geological Society Special Publication*, 81(81):193–212.

Gavrilenko, M., Herzberg, C., Vidito, C., Carr, M. J., Ozerov, A., and Tenner, T. (2016). A Calcium-in-Olivine Geohygrometer and its Application to Subduction Zone Magmatism. *Journal of Petrology*, 57(9):1811–1832.

Ghiorso, M. S. and Sack, R. O. (1995). Chemical mass transfer in magmatic processes IV. A revised and internally consistent thermodynamic model for the interpolation and extrapolation of liquid-solid equilibria in magmatic systems at elevated temperatures and pressures. *Contributions to Mineralogy and Petrology*, 119(2-3):197–212.

Giletti, B. J., Semet, M. P., and Yund, R. A. (1978). Studies in diffusion-III. Oxygen in feldspars: an ion microprobe determination. *Geochimica et Cosmochimica Acta*, 42(1):45–57.

Gleeson, M. L. and Gibson, S. A. (2019). Crustal controls on apparent mantle pyroxenite signals in ocean-island basalts. *Geology*, 47(4):321–324.

Graham, I. J. (1985). RbSr geochronology and geochemistry of torlesse metasediments from the Central North Island, New Zealand. *Chemical Geology: Isotope Geoscience Section*, 52(3-4):317–331.

Graham, I. J., Blattner, P., and McCulloch, M. T. (1990). Meta-igneous granulite xenoliths from Mount Ruapehu, New Zealand: Fragments of altered oceanic crust? *Contributions to Mineralogy and Petrology*, 105(6):650–661.

Graham, I. J., Cole, J. W., Briggs, R. M., Gamble, J. A., and Smith, I. E. (1995). Petrology and petrogenesis of volcanic rocks from the Taupo Volcanic Zone: a review. *Journal of Volcanology and Geothermal Research*, 68(1-3):59–87.

Graham, I. J. and Hackett, W. R. (1987). Petrology of Calc-alkaline Lavas from Ruapehu Volcano and Related Vents, Taupo Volcanic Zone, New Zealand. *Journal of Petrology*, 28(3):531–567.

Gust, D. A. and Perfit, M. R. (1987). Phase relations of a high-Mg basalt from the Aleutian Island Arc: Implications for primary island arc basalts and high-Al basalts. *Contributions to Mineralogy and Petrology*, 97(1):7–18.

Hackett, W. R. (1985). *Geology and Petrology of Ruapehu and Related Vents*. PhD thesis, Victoria University Wellington.

Hamada, M. and Fujii, T. (2008). Experimental constraints on the effects of pressure and H2O on the fractional crystallization of high-Mg island arc basalt. *Contributions to Mineralogy and Petrology*, 155(6):767–790.

Harrison, A. and White, R. S. (2006). Lithospheric structure of an active backarc basin: The Taupo Volcanic Zone, New Zealand. *Geophysical Journal International*, 167(2):968–990.

Heise, W., Bibby, H. M., Caldwell, T. G., Bannister, S. C., Ogawa, Y., Takakura, S.,

and Uchida, T. (2007). Melt distribution beneath a young continental rift: The Taupo Volcanic Zone, New Zealand. *Geophysical Research Letters*, 34(14):1–6.

Heise, W., Caldwell, T. G., Bibby, H. M., and Bennie, S. L. (2010). Three-dimensional electrical resistivity image of magma beneath an active continental rift, Taupo Volcanic Zone, New Zealand. *Geophysical Research Letters*, 37(10):2–6.

Herzberg, C. (2011). Identification of source lithology in the Hawaiian and Canary Islands: Implications for origins. *Journal of Petrology*, 52(1):113–146.

Herzberg, C., Vidito, C., and Starkey, N. A. (2016). Nickel-cobalt contents of olivine record origins of mantle peridotite and related rocks. *American Mineralogist*, 101(9):1952–1966.

Herzer, R. H. (1995). Seismic stratigraphy of a buried volcanic arc, Northland, New Zealand and implications for Neogene subduction. *Marine and Petroleum Geology*, 12(5):511–531.

Heyworth, Z., Turner, S., Schaefer, B., Wood, B., George, R., Berlo, K., Cunningham, H., Price, R., Cook, C., and Gamble, J. (2007). U – 230 Th – 226 Ra – 210 Pb constraints on the genesis of high-Mg andesites at White Island, New Zealand. *Chemical Geology*, 243:105–121.

Hiess, J., Cole, J. W., and Spinks, K. D. (2007). Influence of the crust and crustal structure on the location and composition of high-alumina basalts of the Taupo Volcanic Zone, New Zealand. *New Zealand Journal of Geology and Geophysics*, 50(4):327–342.

Hildreth, W. and Moorbath, S. (1988). Crustal contributions to arc magmatism in the Andes of Central Chile. *Contributions to Mineralogy and Petrology*, 98(4):455–489.

Hirschmann, M. M., Ghiorso, M. S., Wasylenki, L. E., Asimow, P. D., and Stolper, E. M. (1998). Calculation of Peridotite Partial Melting from Thermodynamic Models

of Minerals and Melts. I. Review of Methods and Comparison with Experiments. *Journal of Petrology*, 39(6):1091–1115.

Houghton, B. F., Wilson, C. J. N., McWilliams, M. O., Lanphere, M. A., Weaver, S. D., Briggs, R. M., and Pringle, M. S. (1995). Chronology and dynamics of a large silicic magmatic system: Central Taupo Volcanic Zone, New Zealand. *Geology*, 23(1):13–16.

Huppert, H. E. and Sparks, R. S. J. (1988). The generation of granitic magmas by intrusion of basalt into continental crust. *Journal of Petrology*, 29(3):599–624.

Hurst, T., Heise, W., Hreinsdottir, S., and Hamling, I. (2016). Geophysics of the Taupo Volcanic Zone: A review of recent developments. *Geothermics*, 59:188–204.

Hutchison, W., Mather, T. A., Pyle, D. M., Boyce, A. J., Gleeson, M. L., Yirgu, G., Blundy, J. D., Ferguson, D. J., Vye-Brown, C., Millar, I. L., Sims, K. W., and Finch, A. A. (2018). The evolution of magma during continental rifting: New constraints from the isotopic and trace element signatures of silicic magmas from Ethiopian volcanoes. *Earth and Planetary Science Letters*, 489:203–218.

Jankovics, M. E., Harangi, S., Nemeth, K., Kiss, B., and Ntaflos, T. (2015). A complex magmatic system beneath the Kissomlyó monogenetic volcano (western Pannonian Basin): Evidence from mineral textures, zoning and chemistry. *Journal of Volcanology and Geothermal Research*, 301:38–55.

Jankovics, M. E., Sagi, T., Astbury, R. L., Petrelli, M., Kiss, B., Ubide, T., Nemeth, K., Ntaflos, T., and Harangi, S. (2019). Olivine major and trace element compositions coupled with spinel chemistry to unravel the magmatic systems feeding monogenetic basaltic volcanoes. *Journal of Volcanology and Geothermal Research*, 369:203–223.

Kalamarides, R. I. (1986). High-temperature oxygen isotope fractionation among the

phases of the kiglapait intrusion, Labrador, Canada. *Chemical Geology: Isotope Geoscience Section*, 58(4):303–310.

Kamenetsky, V. S., Elburg, M., Arculus, R., and Thomas, R. (2006). Magmatic origin of low-Ca olivine in subduction-related magmas: Co-existence of contrasting magmas. *Chemical Geology*, 233(3-4):346–357.

Karakas, O., Degruyter, W., Bachmann, O., and Dufek, J. (2017). Lifetime and size of shallow magma bodies controlled by crustal-scale magmatism. *Nature Geoscience*, 10(6):446–450.

Karakas, O., Wotzlaw, J.-f., Guillong, M., Ulmer, P., Brack, P., Economos, R., Bergantz, G. W., Sinigoi, S., and Bachmann, O. (2019). The pace of crustal-scale magma accretion and differentiation beneath silicic caldera volcanoes. *Geology*, 47(8):1–5.

Kelemen, P. B. (1990). Reaction between ultramafic rock and fractionating basaltic magma I. phase relations, the origin of calc-alkaline magma series, and the formation of discordant dunite. *Journal of Petrology*, 31(1):51–98.

Kelemen, P. B., Joyce, D. B., Webster, J. D., and Holloway, J. R. (1990). Reaction between ultramafic rock and fractionating basaltic magma II. experimental investigation of reaction between olivine tholeiite and harzburgite at 1150-1050°C and 5 kb. *Journal of Petrology*, 31(1):99–134.

Kilgour, G., Blundy, J., Cashman, K., and Mader, H. M. (2013). Small volume andesite magmas and melt–mush interactions at Ruapehu, New Zealand: evidence from melt inclusions. *Contributions to Mineralogy and Petrology*, 166(2):371–392.

Kogiso, T., Tatsumi, Y., and Nakano, S. (1997). Trace element transport during dehydration processes in the subducted oceanic crust: 1. Experiments and implications for the origin of ocean island basalts. *Earth and Planetary Science Letters*, 148(1-2):193–205.

Köhler, T. P. and Brey, G. P. (1990). Calcium exchange between olivine and clinopyroxene calibrated as a geothermobarometer for natural peridotites from 2 to 60 kb with applications. *Geochimica et Cosmochimica Acta*, 54(9):2375–2388.

Kósik, S., Németh, K., Kereszturi, G., Procter, J. N., Zellmer, G. F., and Geshi, N. (2016). Phreatomagmatic and water-influenced Strombolian eruptions of a small-volume parasitic cone complex on the southern ringplain of Mt. Ruapehu, New Zealand: Facies architecture and eruption mechanisms of the Ohakune Volcanic Complex controlled by an unstabl. *Journal of Volcanology and Geothermal Research*, 327:99–115.

Kushiro, I. (1972). Determination of liquidus relations in synthetic silicate systems with electron probe analysis: The system forsterite-diopside-silica at 1 atmosphere. *American Mineralogist*, 57:1260–1271.

Lambart, S., Laporte, D., and Schiano, P. (2009). An experimental study of pyroxenite partial melts at 1 and 1.5 GPa: Implications for the major-element composition of Mid-Ocean Ridge Basalts. *Earth and Planetary Science Letters*, 288(1-2):335–347.

Lambart, S., Laporte, D., and Schiano, P. (2013). Markers of the pyroxenite contribution in the major-element compositions of oceanic basalts: Review of the experimental constraints. *Lithos*, 160-161(1):14–36.

Lange, R. A., Frey, H. M., and Hector, J. (2009). A thermodynamic model for the plagioclase-liquid hygrometer/thermometer. *American Mineralogist*, 94(4):494–506.

Langmuir, C. H., Vocke, R. D., Hanson, G. N., and Hart, S. R. (1978). A general mixing equation with applications to Icelandic basalts. *Earth and Planetary Science Letters*, 37(3):380–392.

Lee, T. R. (2010). *The thermal evolution of subduction zone lithosphere: Evidence from the chemical development of Mt. Ruapehu and surrounding vents, New Zealand.* PhD thesis, Durham University.

Leonard, G. S., Cole, J. W., Nairn, I. A., and Self, S. (2002). Basalt triggering of the c. AD 1305 Kaharoa rhyolite eruption, Tarawera Volcanic Complex, New Zealand. *Journal of Volcanology and Geothermal Research*, 115(3-4):461–486.

Li, C., Thakurta, J., and Ripley, E. M. (2012). Low-Ca contents and kink-banded textures are not unique to mantle olivine : evidence from the Duke Island Complex, Alaska. *Mineralogy and Petrology*, 104:147–153.

Lipman, P. W. (2007). Incremental assembly and prolonged consolidation of Cordilleran magma chambers: Evidence from the Southern Rocky Mountain volcanic field. *Geosphere*, 3(1):42–70.

Lynn, K. J., Shea, T., and Garcia, M. O. (2017). Nickel variability in Hawaiian olivine: Evaluating the relative contributions from mantle and crustal processes. *American Mineralogist*, 102(3):507–518.

Macaulay, C. I., Fallick, A. E., Haszeldine, R. S., and Graham, C. M. (2000). Methods of laser-based stable isotope measurement applied to diagenetic cements and hydrocarbon reservoir quality. *Clay Minerals*, 35(1):313–322.

Macpherson, C. G., Gamble, J. A., and Mattey, D. P. (1998). Oxygen isotope geochemistry of lavas from an oceanic to continental arc transition, Kermadec-Hikurangi margin, SW Pacific. *Earth and Planetary Science Letters*, 160(3-4):609–621.

Mattey, D., Lowry, D., and Macpherson, C. (1994). Oxygen isotope composition of mantle peridotite. *Earth and Planetary Science Letters*, 128(3-4):231–241.

Matzen, A. K., Baker, M. B., Beckett, J. R., and Stolper, E. M. (2011). Fe-Mg

partitioning between olivine and high-magnesian melts and the nature of Hawaiian parental liquids. *Journal of Petrology*, 52(7-8):1243–1263.

Matzen, A. K., Baker, M. B., Beckett, J. R., and Stolper, E. M. (2013). The temperature and pressure dependence of nickel partitioning between olivine and silicate melt. *Journal of Petrology*, 54(12):2521–2545.

Matzen, A. K., Baker, M. B., Beckett, J. R., Wood, B. J., and Stolper, E. M. (2017a). The effect of liquid composition on the partitioning of Ni between olivine and silicate melt. *Contributions to Mineralogy and Petrology*, 172(1):1–18.

Matzen, A. K., Wood, B. J., Baker, M. B., and Stolper, E. M. (2017b). The roles of pyroxenite and peridotite in the mantle sources of oceanic basalts. *Nature Geoscience*, 10(July):530–535.

McCoy-West, A. J., Bennett, V. C., O'Neill, H. S. C., Hermann, J., and Puchtel, I. S. (2014). The interplay between melting, refertilization and carbonatite metasomatism in off-cratonic lithospheric mantle under Zealandia: An integrated major, trace and platinum group element study. *Journal of Petrology*, 56(3):563–604.

McCulloch, M. T., Kyser, T. K., Woodhead, J. D., and Kinsley, L. (1994). Pb-Sr-Nd-O isotopic constraints on the origin of rhyolites from the Taupo Volcanic Zone of New Zealand: evidence for assimilation followed by fractionation from basalt. *Contributions to Mineralogy and Petrology*, 115(3):303–312.

McMillan, N. J., Dickin, A. P., and Haag, D. (2000). Evolution of magma source regions in the Rio Grande rift, Southern New Mexico. *Bulletin of the Geological Society of America*, 112(10):1582–1593.

Melekhova, E., Blundy, J., Robertson, R., and Humphreys, M. C. (2014). Experimental evidence for polybaric differentiation of primitive arc basalt beneath St. Vincent, Lesser Antilles. *Journal of Petrology*, 56(1):161–192.

Miller, C. F., Furbish, D. J., Walker, B. A., Claiborne, L. L., Koteas, G. C., Bleick, H. A., and Miller, J. S. (2011). Growth of plutons by incremental emplacement of sheets in crystal-rich host: Evidence from Miocene intrusions of the Colorado River region, Nevada, USA. *Tectonophysics*, 500(1-4):65–77.

Milman-Barris, M. S., Beckett, J. R., Baker, M. B., Hofmann, A. E., Morgan, Z., Crowley, M. R., Vielzeuf, D., and Stolper, E. (2008). Zoning of phosphorus in igneous olivine. *Contributions to Mineralogy and Petrology*, 155(6):739–765.

Mitchell, A. L. and Grove, T. L. (2015). Melting the hydrous, subarc mantle: the origin of primitive andesites. *Contributions to Mineralogy and Petrology*, 170(2):1–23.

Mitchell, A. L. and Grove, T. L. (2016). Experiments on melt–rock reaction in the shallow mantle wedge. *Contributions to Mineralogy and Petrology*, 171(12):1–21.

Neave, D. A., Namur, O., Shorttle, O., and Holtz, F. (2019). Magmatic evolution biases basaltic records of mantle chemistry towards melts from recycled sources. *Earth and Planetary Science Letters*, 520:199–211.

Neave, D. A. and Putirka, K. D. (2017). A new clinopyroxene-liquid barometer, and implications for magma storage pressures under Icelandic rift zones. *American Mineralogist*, 102(4):777–794.

Parman, S. W. and Grove, T. L. (2004). Harzburgite melting with and without H 2 O: Experimental data and predictive modeling . *Journal of Geophysical Research: Solid Earth*, 109(B2):1–20.

Plechov, P. and Gerya, T. (1998). Effect of H2O on plagioclase-melt equilibrium. *Experiment in Geosciences*, 7(2):7–9.

Prelevic, D. and Foley, S. F. (2007). Accretion of arc-oceanic lithospheric mantle in the Mediterranean : Evidence from extremely high-Mg olivines and Cr-rich spinel inclusions in lamproites. *Earth and Planetary Science Letters*, 256:120–135.

Price, R. C., Gamble, J. A., Smith, I. E., Stewart, R. B., Eggins, S., and Wright, I. C. (2005). An integrated model for the temporal evolution of andesites and rhyolites and crustal development in New Zealand's North Island. *Journal of Volcanology and Geothermal Research*, 140(1-3):1–24.

Price, R. C., Mortimer, N., Smith, I. E., and Maas, R. (2015). Whole-rock geochemical reference data for Torlesse and Waipapa terranes, North Island, New Zealand. *New Zealand Journal of Geology and Geophysics*, 58(3):213–228.

Putirka, K., Ryerson, F. J., Perfit, M., and Ridley, W. I. (2011). Mineralogy and composition of the oceanic mantle. *Journal of Petrology*, 52(2):279–313.

Putirka, K. D. (2005). Mantle potential temperatures at Hawaii, Iceland, and the mid-ocean ridge system, as inferred from olivine phenocrysts: Evidence for thermally driven mantle plumes. *Geochemistry, Geophysics, Geosystems*, 6(5):1–14.

Putirka, K. D. (2008). Thermometers and barometers for volcanic systems. *Reviews in Mineralogy and Geochemistry*, 69(December):61–120.

Re, G., Palin, J. M., White, J. D., and Parolari, M. (2017). Unravelling the magmatic system beneath a monogenetic volcanic complex (Jagged Rocks Complex, Hopi Buttes, AZ, USA). *Contributions to Mineralogy and Petrology*, 172(11-12).

Reddy, K., Oh, S., Major Jr., L., and Cooper, A. (1980). Oxygen diffusion in forsterite. *Journal of Geophysical Research*, 85(B1):322–326.

Reyners, M., Eberhart-Phillips, D., and Bannister, S. (2011). Tracking repeated subduction of the Hikurangi Plateau beneath New Zealand. *Earth and Planetary Science Letters*, 311(1-2):165–171.

Reyners, M., Eberhart-phillips, D., and Stuart, G. (2007). The role of fluids in lower-crustal earthquakes near continental rifts. *Nature*, 446(April):1075–1078.

Roeder, P. L. and Emslie, R. F. (1970). Olivine-liquid equilibrium. *Contributions to Mineralogy and Petrology*, 29(4):275–289.

Rohrbach, A., Schuth, S., Ballhaus, C., Münker, C., Matveev, S., and Qopoto, C. (2005). Petrological constraints on the origin of arc picrites, New Georgia Group, Solomon Islands. *Contributions to Mineralogy and Petrology*, 149(6):685–698.

Rooney, T. O. and Deering, C. D. (2014). Conditions of melt generation beneath the Taupo Volcanic Zone: The influence of heterogeneous mantle inputs on large-volume silicic systems. *Geology*, 42(1):3–6.

Rosenberg, M. D., Wilson, C. J., Bignall, G., Ireland, T. R., Sepulveda, F., and Charlier, B. L. (2020). Structure and evolution of the Wairakei–Tauhara geothermal system (Taupo Volcanic Zone, New Zealand) revisited with a new zircon geochronology. *Journal of Volcanology and Geothermal Research*, 390:106705.

Rowe, M. C. and Tepley, F. J. (2016). Origin and petrogenetic implications of anomalous olivine from a Cascade forearc basalt. *American Mineralogist*, 101(8):1807–1819.

Rowland, J. V., Wilson, C. J., and Gravley, D. M. (2010). Spatial and temporal variations in magma-assisted rifting, Taupo Volcanic Zone, New Zealand. *Journal of Volcanology and Geothermal Research*, 190(1-2):89–108.

Ryerson, F. J. and McKeegan, K. D. (1994). Determination of oxygen self-diffusion in åkermanite, anorthite, diopside, and spinel: Implications for oxygen isotopic anomalies and the thermal histories of Ca-Al-rich inclusions. *Geochimica et Cosmochimica Acta*, 58(17):3713–3734.

Salters, V. J. and Stracke, A. (2004). Composition of the depleted mantle. *Geochemistry, Geophysics, Geosystems*, 5(5).

Scott, J. M., Waight, T. E., van der Meer, Q. H. A., Palin, J. M., Cooper, A. F., and Münker, C. (2014). Metasomatized ancient lithospheric mantle beneath the

young Zealandia microcontinent and its role in HIMU-like intraplate magmatism. *Geochemistry, Geophysics, Geosystems*, 15(9):3477–3501.

Seebeck, H., Nicol, A., Villamor, P., Ristau, J., and Pettinga, J. (2014). Structure and kinematics of the Taupo Rift, New Zealand. *Tectonics*, 33(6):1178–1199.

Self, S. (2015). Explosive Super-Eruptions and Potential Global Impacts. In *Volcanic Hazards, Risks and Disasters*, number M, pages 399–418. Elsevier.

Shane, P., Nairn, I. A., Smith, V. C., Darragh, M., Beggs, K., and Cole, J. W. (2008). Silicic recharge of multiple rhyolite magmas by basaltic intrusion during the 22.6 ka Okareka Eruption Episode, New Zealand. *Lithos*, 103(3-4):527–549.

Sharp, Z. D. (1990). A laser-based microanalytical method for the in situ determination of oxygen isotope ratios of silicates and oxides. *Geochimica et Cosmochimica Acta*, 54(5):1353–1357.

Sheppard, D. S. and Lyon, G. L. (1984). Geothermal fluid chemistry of the Orakeikorako field, New Zealand. *Journal of Volcanology and Geothermal Research*, 22(3-4):329–349.

Simkin, T. and Smith, J. V. (1970). Minor-Element Distribution in Olivine. *The Journal of Geology*, 78(3):304–325.

Sisson, T. W. and Grove, T. L. (1993a). Experimental investigations of the role of H2O in calc-alkaline differentiation and subduction zone magmatism. *Contributions to Mineralogy and Petrology*, 113(2):143–166.

Sisson, T. W. and Grove, T. L. (1993b). Temperatures and H2O contents of low-MgO high-alumina basalts. *Contributions to Mineralogy and Petrology*, 113(2):167–184.

Sobolev, A. V., Hofmann, A. W., Sobolev, S. V., and Nikogosian, I. K. (2005). An olivine-free mantle source of Hawaiian shield basalts. *Nature*, 434(7033):590–597.

Sobolev, A. V. and Shimizu, N. (1993). Ultra-depleted primary melt included in an olivine from the Mid-Atlantic Ridge. *Nature*, 363(6425):151–154.

Sorbadere, F., Médard, E., Laporte, D., and Schiano, P. (2013). Experimental melting of hydrous peridotite-pyroxenite mixed sources: Constraints on the genesis of silica-undersaturated magmas beneath volcanic arcs. *Earth and Planetary Science Letters*, 384:42–56.

Stern, T., Stratford, W., Seward, A., Henderson, M., Savage, M., Smith, E., Benson, A., Greve, S., and Salmon, M. (2010). Crust-mantle structure of the central North Island, New Zealand, based on seismological observations. *Journal of Volcanology and Geothermal Research*, 190(1-2):58–74.

Stern, T. A. (1987). Asymmetric back-arc spreading, heat flux and structure associated with the Central Volcanic Region of New Zealand. *Earth and Planetary Science Letters*, 85(1-3):265–276.

Stern, T. A., Stratford, W. R., and Salmon, M. L. (2006). Subduction evolution and mantle dynamics at a continental margin: Central North Island, New Zealand. *Reviews of Geophysics*, 44(4):RG4002.

Stratford, W. R. and Stern, T. A. (2006). Crust and upper mantle structure of a continental backarc: central North Island, New Zealand. *Geophysical Journal International*, 166(1):469–484.

Straub, S. M., Gomez-Tuena, A., Stuart, F. M., Zellmer, G. F., Espinasa-Perena, R., Cai, Y., and Iizuka, Y. (2011). Formation of hybrid arc andesites beneath thick continental crust. *Earth and Planetary Science Letters*, 303(3-4):337–347.

Straub, S. M., LaGatta, A. B., Martin-Del Pozzo, A. L., and Langmuir, C. H. (2008). Evidence from high-Ni olivines for a hybridized peridotite/pyroxenite source for oro-

genic andesites from the central Mexican Volcanic Belt. *Geochemistry, Geophysics, Geosystems*, 9(3).

Straub, S. M., Zellmer, G. F., Gómez-Tuena, A., Espinasa-Pereñ A., R., Martin-Del Pozzo, A. L., Stuart, F. M., and Langmuir, C. H. (2014). A genetic link between silicic slab components and calc-alkaline arc volcanism in central Mexico. *Geological Society Special Publication*, 385(1):31–64.

Streck, M. J. and Grunder, A. L. (1995). Crystallization and welding variations in a widespread ignimbrite sheet; the Rattlesnake Tuff, eastern Oregon, USA. *Bulletin of Volcanology*, 57(3):151–169.

Sugawara, T. (2001). Ferric iron partitioning between plagioclase and silicate liquid: Thermodynamics and petrological applications. *Contributions to Mineralogy and Petrology*, 141(6):659–686.

Sun, S.-S., Nesbitt, R. W., and Sharaskin, A. Y. (1979). Geochemical characteristics of mid-ocean ridge basalts. *Earth and Planetary Science Letters*, 44(1):119–138.

Tatsumi, Y. and Kogiso, T. (1997). Trace element transport during dehydration processes in the subducted oceanic crust: 2. Origin of chemical and physical characteristics in arc magmatism. *Earth and Planetary Science Letters*, 148(1-2):207–221.

Villamor, P. and Berryman, K. R. (2006). Evolution of the southern termination of the taupo rift, New Zealand. *New Zealand Journal of Geology and Geophysics*, 49(1):23–37.

Waight, T. E., Troll, V. R., Gamble, J. A., Price, R. C., and Chadwick, J. P. (2017). Hf isotope evidence for variable slab input and crustal addition in basalts and andesites of the Taupo Volcanic Zone, New Zealand. *Lithos*, 284-285:222–236.

Wallace, L. M., Beavan, J., Mccaffrey, R., and Daraby, D. (2004). Subduction zone

coupling and tectonic block rotations in the North Island, New Zealand. *Journal of Geophysical Research*, 109:1–21.

Wan, Z., Coogan, L. A., and Canil, D. (2008). Experimental calibration of aluminum partitioning between olivine and spinel as a geothermometer. *American Mineralogist*, 93(July):1142–1147.

Waters, L. E. and Lange, R. A. (2015). An updated calibration of the plagioclase-liquid hygrometer-thermometer applicable to basalts through rhyolites. *American Mineralogist*, 100(10):2172–2184.

Watts, K. E., Bindeman, I. N., and Schmitt, A. K. (2011). Large-volume rhyolite genesis in caldera complexes of the Snake River Plain: Insights from the Kilgore Tuff of the Heise volcanic field, Idaho, with comparison to Yellowstone and Bruneau-Jarbidge rhyolites. *Journal of Petrology*, 52(5):857–890.

Wilson, C. J., Houghton, B. F., Kampt, P. J., and Mc Williams, M. O. (1995a). An exceptionally widespread ignimbrite with implications for pyroclastic flow emplacement. *Nature*, 378(6557):605–607.

Wilson, C. J. and Rowland, J. V. (2016). The volcanic, magmatic and tectonic setting of the Taupo Volcanic Zone, New Zealand, reviewed from a geothermal perspective. *Geothermics*, 59:168–187.

Wilson, C. J. N., Gravely, D. M., Leonard, G. S., and Rowland, J. V. (2009). Volcanism in the Central Taupo Volcanic Zone, New Zealand: tempo, styles and controls. In *Studies in Volcanology: The Legacy of George Walker*, pages 225–247.

Wilson, C. J. N., Houghton, B. F., McWilliams, M. O., Lanphere, M. A., Weaver, S. D., and Briggs, R. M. (1995b). Volcanic and structural evolution of Taupo Volcanic Zone, New-Zealand: a review. *Journal of Volcanology and Geothermal Research*, 68(1-3):1–28.

Wolff, J. A., Ellis, B. S., Ramos, F. C., Starkel, W. A., Boroughs, S., Olin, P. H., and Bachmann, O. (2015). Remelting of cumulates as a process for producing chemical zoning in silicic tuffs: A comparison of cool, wet and hot, dry rhyolitic magma systems. *Lithos*, 236-237:275–286.

Wood, B. J. and Turner, S. P. (2009). Origin of primitive high-Mg andesite: Constraints from natural examples and experiments. *Earth and Planetary Science Letters*, 283(1-4):59–66.

Workman, R. K. and Hart, S. R. (2005). Major and trace element composition of the depleted MORB mantle (DMM). *Earth and Planetary Science Letters*, 231(1-2):53–72.

Zellmer, G. F., Kimura, J.-I., Stirling, C. H., Lube, G., Shane, P. A., and Iizuka, Y. (2020). Genesis of recent mafic magmatism in the Taupo Volcanic Zone, New Zealand: insights into the birth and death of very large volume rhyolitic systems? *Journal of Petrology*.

Zellmer, G. F., Pistone, M., Iizuka, Y., Andrews, B. J., Gomez-Tuena, A., Straub, S. M., and Cottrell, E. (2016). Petrogenesis of antecryst-bearing arc basalts from the Trans-Mexican Volcanic Belt: Insights into along-Arc variations in magma-mush ponding depths, H2O contents, and surface heat flux. *American Mineralogist*, 101(11):2405–2422.

Zhang, Y. and Stolper, E. M. (1991). Water diffusion in a basaltic melt. *Nature*, 351(6324):306–309.

Appendix A

A.1 EPMA Secondary Standard Analyses

Table A.1: **St. John's Island olivine secondary standard analyses**

SiO_2	FeO	MnO	MgO	CaO	NiO	P_2O_5	Total	Date/time	Fo
41.36	**9.48**	**0.14**	**49.60**	**0.01**	**0.39**		**100.98**		90.32
41.03	9.83	0.13	49.53	0.01	0.33	0.02	100.87	18/03/2019 12:20	89.98
41.33	10.01	0.12	49.20	0.01	0.33	0.02	100.99	18/03/2019 12:27	89.75
41.07	9.77	0.12	49.49	0.01	0.35	0.02	100.84	18/03/2019 12:33	90.02
40.95	9.79	0.13	49.54	0.01	0.34	0.01	100.77	19/03/2019 05:22	90.02
41.24	9.49	0.13	49.62	0.01	0.33	0.01	100.83	19/03/2019 05:28	90.31
40.84	9.84	0.12	49.65	0.01	0.33	0.01	100.80	19/03/2019 05:34	89.99
41.29	9.79	0.13	49.52	0.01	0.34	0.02	101.09	19/03/2019 05:41	90.02
41.18	9.74	0.12	49.44	0.01	0.35	0.01	100.85	19/03/2019 05:47	90.05
41.54	9.85	0.11	49.33	0.01	0.35	0.01	101.19	19/03/2019 08:40	89.93
40.35	9.47	0.14	48.37	0.00	0.33	0.02	98.69	19/03/2019 08:46	90.10
40.47	9.93	0.14	48.81	0.01	0.34	0.02	99.70	19/03/2019 08:52	89.76
41.34	9.76	0.12	49.31	0.01	0.33	0.01	100.89	19/03/2019 09:00	90.00
41.44	9.70	0.13	49.04	0.01	0.33	0.01	100.65	19/03/2019 09:06	90.02
41.28	9.78	0.12	49.42	0.01	0.34	0.01	100.97	19/03/2019 09:13	90.00
41.47	9.75	0.12	49.34	0.01	0.35	0.01	101.04	20/03/2019 07:48	90.02
41.65	9.76	0.13	49.08	0.01	0.34	0.01	100.97	20/03/2019 07:54	89.96
40.53	9.82	0.11	48.71	0.01	0.34	0.02	99.53	20/03/2019 08:01	89.84
41.77	9.55	0.13	49.14	0.01	0.34	0.01	100.93	20/03/2019 08:48	90.17
40.58	9.78	0.12	48.07	0.01	0.34	0.01	98.90	20/03/2019 08:54	89.76
41.19	9.74	0.13	48.89	0.01	0.34	0.02	100.30	20/03/2019 09:00	89.95
40.94	9.72	0.13	48.15	0.01	0.34	0.02	99.32	20/03/2019 09:42	89.83

40.67	9.74	0.12	49.24	0.01	0.34	0.02	100.13	22/03/2019 08:48	90.01
40.44	9.64	0.13	49.78	0.01	0.35	0.02	100.36	22/03/2019 08:54	90.20
41.49	9.60	0.12	50.08	0.01	0.33	0.01	101.64	23/03/2019 10:15	90.29
40.52	9.68	0.12	49.22	0.01	0.33	0.02	99.89	23/03/2019 10:21	90.06
41.17	9.65	0.12	50.04	0.01	0.35	0.01	101.35	23/03/2019 10:27	90.24
40.14	9.63	0.12	48.97	0.01	0.34	0.01	99.22	29/04/2019 12:20	90.06
41.03	9.67	0.12	49.32	0.01	0.33	0.02	100.50	29/04/2019 12:26	90.09
40.10	9.54	0.13	48.69	0.01	0.36	0.01	98.84	30/04/2019 04:09	90.09
40.12	9.68	0.14	49.02	0.01	0.34	0.01	99.31	30/04/2019 04:15	90.02
40.39	9.57	0.13	49.00	0.01	0.34	0.01	99.45	30/04/2019 04:21	90.12
40.16	9.90	0.13	48.92	0.01	0.34	0.01	99.46	30/04/2019 04:27	89.80
40.08	9.46	0.12	48.64	0.01	0.33	0.02	98.66	30/04/2019 04:33	90.16
40.05	9.57	0.12	48.99	0.01	0.34	0.01	99.09	30/04/2019 04:39	90.12
40.42	9.63	0.12	48.70	0.01	0.33	0.02	99.21	30/04/2019 10:28	90.02
40.72	9.55	0.12	48.93	0.01	0.34		99.68	30/04/2019 10:37	90.13
40.38	9.69	0.12	48.96	0.01	0.33		99.51	30/04/2019 10:42	90.00
40.49	9.87	0.12	49.04	0.01	0.35		99.89	30/04/2019 10:46	89.86
40.77	9.61	0.14	49.01	0.01	0.34		99.88	30/04/2019 10:50	90.09
40.18	9.75	0.12	49.06	0.01	0.33	0.02	99.48	01/05/2019 03:59	89.97
40.25	9.42	0.13	48.64	0.01	0.35	0.02	98.81	01/05/2019 04:05	90.20
40.49	9.90	0.13	49.00	0.01	0.34	0.01	99.87	01/05/2019 04:12	89.82
40.34	9.73	0.12	48.97	0.01	0.34	0.01	99.51	01/05/2019 04:18	89.97
40.23	9.73	0.11	48.98	0.01	0.35	0.02	99.43	01/05/2019 04:24	89.97
41.16	9.63		49.27				100.06	01/05/2019 17:52	90.12
40.86	9.53		49.61				100.00	01/05/2019 17:53	90.27
41.42	9.65		49.95				101.02	01/05/2019 17:55	90.22
40.95	9.62		49.60				100.16	01/05/2019 17:56	90.19
40.32	9.52	0.13	49.05	0.01	0.35	0.01	99.38	02/05/2019 03:18	90.18
40.56	9.55	0.13	48.98	0.01	0.34	0.02	99.58	02/05/2019 03:24	90.14
40.38	9.43	0.13	48.96	0.01	0.34	0.02	99.26	02/05/2019 03:30	90.25
40.03	9.52	0.13	48.91	0.01	0.33	0.01	98.95	02/05/2019 03:36	90.16
40.96	9.68	0.12	49.90	0.01	0.33	0.02	101.01	07/05/2019 12:11	90.19
41.10	9.92	0.11	49.98	0.01	0.34	0.02	101.48	07/05/2019 12:16	89.98
41.20	9.93	0.12	50.02	0.01	0.32	0.01	101.62	08/05/2019 04:39	89.98
41.08	9.67	0.12	49.77	0.01	0.34	0.01	101.00	08/05/2019 04:45	90.17
41.48	9.64	0.12	49.71	0.01	0.34	0.02	101.32	08/05/2019 04:52	90.19
41.08	9.82	0.12	49.83	0.01	0.34	0.01	101.21	08/05/2019 04:58	90.04
41.10	10.02	0.13	49.75	0.01	0.34	0.01	101.36	08/05/2019 05:04	89.85
41.43	9.59	0.12	49.92	0.01	0.33	0.02	101.42	08/05/2019 08:58	90.28
41.41	9.96	0.12	49.96	0.01	0.32	0.02	101.79	08/05/2019 09:03	89.94
41.09	9.71	0.13	50.23	0.01	0.33	0.02	101.52	08/05/2019 09:45	90.22
41.11	9.67	0.13	50.12	0.01	0.33	0.02	101.37	08/05/2019 09:49	90.23

40.96	10.08	0.13	49.85	0.01	0.34	0.02	101.38	09/05/2019 01:50	89.81
41.15	9.72	0.12	50.12	0.01	0.33	0.02	101.46	09/05/2019 01:55	90.18
40.79	10.00	0.12	49.97	0.01	0.34	0.02	101.25	09/05/2019 01:59	89.91
41.47	9.78	0.12	49.81	0.01	0.33	0.01	101.54	09/05/2019 05:32	90.08
40.91	9.48	0.12	49.90	0.01	0.33	0.01	100.75	09/05/2019 05:38	90.37
41.16	9.95	0.13	50.11	0.01	0.34	0.02	101.72	09/05/2019 05:44	89.97
41.17	10.08	0.12	49.87	0.01	0.34	0.02	101.61	09/05/2019 05:51	89.81
41.18	9.90	0.14	50.05	0.01	0.33	0.01	101.62	09/05/2019 05:57	90.01
41.48	9.68	0.13	50.12	0.01	0.33	0.01	101.76	09/05/2019 08:19	90.22
40.65	9.80	0.12	49.87	0.01	0.33	0.02	100.79	09/05/2019 08:23	90.07
40.94	9.97	0.13	50.28	0.01	0.33	0.00	101.65	09/05/2019 08:28	89.99
40.55	9.93	0.13	49.52	0.01	0.32	0.02	100.48	09/05/2019 17:36	89.89
41.23	10.22	0.12	49.94	0.01	0.32	0.02	101.84	09/05/2019 17:41	89.70
40.79	9.67	0.14	50.02	0.00	0.31	0.02	100.96	09/05/2019 17:45	90.21
41.30	9.87	0.13	49.98	0.01	0.33	0.01	101.63	10/05/2019 07:36	90.03
41.26	9.74	0.11	49.89	0.01	0.32	0.02	101.34	10/05/2019 07:43	90.13
41.24	9.76	0.13	49.85	0.01	0.33	0.03	101.34	10/05/2019 07:49	90.10
41.07	9.63	0.10	49.70	0.01	0.33	0.02	100.85	10/05/2019 07:55	90.20
40.76	9.97		49.11				99.84	02/08/2019 11:35	89.78
40.30	9.99		49.00				99.28	02/08/2019 11:36	89.73
40.51	9.96		49.20				99.67	02/08/2019 11:37	89.80
40.89	9.78		49.12				99.79	02/08/2019 11:39	89.95
40.46	9.84	0.13	47.57	0.01	0.34	0.02	98.36	03/08/2019 01:26	89.60
40.24	9.71	0.12	47.88	0.01	0.33	0.02	98.30	03/08/2019 01:32	89.79
40.70	9.87	0.12	47.53	0.01	0.34	0.01	98.57	03/08/2019 01:38	89.57
40.66	9.78	0.12	47.42	0.01	0.34	0.01	98.34	03/08/2019 01:44	89.63
40.86	9.39	0.12	48.92	0.01	0.33		99.67	31/07/2018 08:29	90.27
40.45	10.15	0.13	49.40	0.01	0.33		100.47	31/07/2018 08:35	89.66
40.54	9.96	0.11	49.53	0.01	0.33		100.48	31/07/2018 08:41	89.86

Table A.2: **BCR2G secondary standard analyses**

SiO_2	**TiO_2**	**Al_2O_3**	**FeO**	**MnO**	**MgO**	**CaO**	**Na_2O**	**K_2O**	**Total**	
54.97	**2.32**	**13.10**	**13.86**	**0.21**	**3.57**	**7.10**	**3.14**	**1.77**	**100.04**	
53.40	2.28	13.43	12.76	0.22	3.72	7.35	3.37	1.76	98.62	18/03/2019 11:39
53.98	2.27	13.26	12.91	0.20	3.66	7.33	3.03	1.73	98.72	18/03/2019 11:44
54.58	2.27	13.32	12.50	0.20	3.72	7.04	3.24	1.79	99.00	18/03/2019 11:49
54.31	2.25	13.55	12.61	0.19	3.69	7.29	3.22	1.79	99.25	19/03/2019 05:53
54.07	2.26	13.20	12.34	0.20	3.75	7.20	3.23	1.71	98.32	19/03/2019 05:58
53.79	2.25	13.68	12.90	0.19	3.60	7.28	2.06	1.88	97.98	19/03/2019 06:03
54.16	2.25	13.68	12.83	0.19	3.58	7.23	3.01	1.75	99.07	19/03/2019 06:08

54.14	2.25	13.79	12.18	0.20	3.75	7.30	2.45	1.83	98.23	19/03/2019 06:13
55.33	2.26	13.31	12.35	0.19	3.61	7.24	3.33	1.78	99.76	19/03/2019 07:58
54.53	2.26	13.68	12.19	0.21	3.47	7.07	3.32	1.73	98.80	19/03/2019 08:04
54.77	2.24	13.58	12.46	0.20	3.58	7.32	3.22	1.81	99.53	19/03/2019 08:09
54.30	2.26	13.27	12.71	0.20	3.63	7.30	2.60	1.72	98.33	20/03/2019 08:07
54.77	2.28	13.59	12.65	0.20	3.71	7.26	3.18	1.85	99.81	20/03/2019 08:12
53.81	2.26	13.50	12.53	0.20	3.67	7.11	3.29	1.75	98.49	20/03/2019 08:17
55.12	2.25	13.44	12.42	0.21	3.71	7.27	3.19	1.80	99.75	30/04/2019 05:40
54.76	2.26	13.71	12.43	0.21	3.59	7.21	3.28	1.69	99.45	30/04/2019 05:45
54.38	2.26	13.51	12.60	0.20	3.70	7.22	3.15	1.78	99.14	30/04/2019 05:50
54.27	2.26	13.65	12.73	0.20	3.55	7.41	3.06	1.82	99.30	30/04/2019 05:55
54.27	2.28	13.49	12.42	0.20	3.82	7.28	3.20	1.78	99.06	01/05/2019 05:15
54.54	2.29	13.80	12.73	0.19	3.61	7.38	3.32	1.76	100.00	01/05/2019 05:20
54.98	2.25	13.29	13.15	0.20	3.51	7.25	3.21	1.81	100.01	01/05/2019 05:25
54.57	2.27	13.90	12.57	0.20	3.70	7.26	3.22	1.82	99.86	01/05/2019 05:30
55.27	2.27	13.31	12.30	0.20	3.54	7.32	3.22	1.82	99.62	01/05/2019 05:36
55.60	2.26	13.09	12.86	0.20	3.50	7.30	2.70	1.78	99.64	02/05/2019 04:40
55.71	2.24	13.60	12.50	0.20	3.62	7.13	3.24	1.77	100.37	02/05/2019 04:45
54.91	2.26	13.67	12.73	0.19	3.47	7.32	3.07	1.85	99.83	02/05/2019 04:50
55.64	2.25	13.58	12.35	0.20	3.56	7.01	3.21	1.87	100.03	02/05/2019 04:55
54.51	2.26	13.18	12.57	0.21	3.55	7.14	3.04	1.79	98.59	02/05/2019 05:01
53.66	2.26	13.32	12.83	0.20	3.67	7.11	3.21	1.71	98.32	08/05/2019 05:11
53.82	2.25	13.41	12.20	0.21	3.58	7.19	3.21	1.77	97.97	08/05/2019 05:16
54.74	2.24	13.53	12.88	0.21	3.60	6.96	2.90	1.76	99.16	08/05/2019 05:21
54.51	2.25	13.59	12.38	0.20	3.60	7.21	3.28	1.86	99.23	08/05/2019 05:26
54.03	2.23	13.59	12.53	0.18	3.57	7.20	3.36	1.93	98.99	08/05/2019 05:31
54.20	2.26	13.62	13.19	0.19	3.62	7.20	3.15	1.79	99.58	08/05/2019 08:11
53.57	2.25	13.56	12.46	0.20	3.69	7.10	3.38	1.83	98.39	08/05/2019 08:16
53.87	2.26	13.40	12.70	0.20	3.63	7.18	3.19	1.93	98.70	08/05/2019 08:21
54.36	2.26	13.24	12.82	0.20	3.64	7.11	3.30	1.71	99.01	09/05/2019 06:04
54.54	2.25	13.35	12.75	0.20	3.60	7.26	2.70	1.81	98.81	09/05/2019 06:09
54.36	2.27	13.19	12.92	0.20	3.56	7.33	3.28	1.81	99.29	09/05/2019 06:14
53.47	2.28	13.29	12.83	0.20	3.52	7.21	3.23	1.80	98.15	09/05/2019 06:19
54.25	2.27	13.30	12.84	0.19	3.68	7.43	3.08	1.74	99.12	09/05/2019 06:24
54.05	2.26	13.48	12.59	0.20	3.64	7.23	3.23	1.77	98.81	09/05/2019 08:03
53.89	2.26	13.73	12.77	0.19	3.77	7.22	3.22	1.75	99.16	09/05/2019 08:08
54.51	2.27	13.54	12.64	0.19	3.53	7.28	3.05	1.69	99.07	09/05/2019 08:14
53.94	2.28	13.66	12.75	0.20	3.55	7.24	3.25	1.78	99.02	10/05/2019 08:08
54.88	2.27	13.17	12.97	0.20	3.65	7.44	3.28	1.82	100.01	10/05/2019 08:13
54.38	2.30	13.33	13.09	0.18	3.61	7.17	3.11	1.77	99.32	10/05/2019 08:18
54.13	2.27	13.51	13.08	0.20	3.68	7.23	3.16	1.68	99.31	10/05/2019 08:23
53.95	2.26	13.69	12.86	0.20	3.56	7.19	3.13	1.76	98.95	10/05/2019 08:29

Table A.3: **In-house clinopyroxene secondary standard analyses**

SiO_2	Al_2O_3	FeO	MnO	MgO	CaO	Na_2O	Total	
51.10	**0.68**	**16.06**	**0.52**	**8.28**	**22.69**	**0.68**	**100.01**	
50.78	0.63	16.78	0.47	8.20	22.99	0.72	100.60	18/03/2019 11:54
50.86	0.60	16.55	0.49	8.08	23.11	0.72	100.43	18/03/2019 12:03
50.77	0.59	16.46	0.49	8.03	22.95	0.72	99.99	18/03/2019 12:12
50.29	0.62	16.95	0.49	8.03	23.01	0.72	100.12	19/03/2019 04:38
50.44	0.64	16.87	0.47	7.96	23.02	0.72	100.12	19/03/2019 04:47
51.01	0.60	16.95	0.49	8.02	23.02	0.71	100.80	19/03/2019 04:56
50.65	0.63	16.79	0.49	7.99	22.91	0.71	100.20	19/03/2019 05:04
50.25	0.61	16.78	0.48	8.04	23.12	0.72	100.00	19/03/2019 05:13
50.81	0.67	16.79	0.47	7.97	22.79	0.71	100.23	19/03/2019 09:19
50.58	0.61	16.69	0.49	8.01	22.94	0.71	100.04	19/03/2019 09:28
49.43	0.60	16.69	0.49	7.76	22.77	0.72	98.47	20/03/2019 07:22
49.63	0.59	16.71	0.49	7.84	22.78	0.71	98.77	20/03/2019 07:31
50.68	0.64	16.58	0.50	8.00	22.82	0.70	99.94	20/03/2019 07:40
50.36	0.62	16.61	0.49	7.92	22.79	0.71	99.49	20/03/2019 09:06
50.96	0.65	16.75	0.50	7.92	22.68	0.71	100.17	20/03/2019 09:15
50.30	0.63	16.95	0.49	8.00	22.95	0.72	100.05	20/03/2019 09:24
49.88	0.61	16.58	0.50	7.85	22.60	0.71	98.74	29/04/2019 12:02
49.67	0.59	16.55	0.48	7.59	22.39	0.71	97.98	29/04/2019 12:11
50.30	0.62	16.64	0.50	7.64	22.64	0.71	99.06	29/04/2019 12:35
50.04	0.58	16.36	0.49	7.78	22.70	0.72	98.69	29/04/2019 12:59
49.79	0.58	16.46	0.49	7.75	22.55	0.72	98.35	30/04/2019 04:45
50.53	0.61	16.13	0.49	22.52	8.01	0.71	98.99	22/03/2019 10:56
50.63	0.67	16.61	0.49	8.16	22.76	0.71	100.02	22/03/2019 11:14
49.75	0.58	16.25	0.50	8.10	22.69	0.70	98.60	22/03/2019 11:22
51.12	0.61	16.59	0.47	8.30	23.06	0.70	100.87	22/03/2019 11:49
50.19	0.63	16.02	0.47	8.20	23.02	0.70	99.22	23/03/2019 09:31
50.72	0.63	16.16	0.47	8.19	23.04	0.70	99.92	23/03/2019 09:39
49.37	0.60	16.26	0.47	7.99	22.37	0.70	97.77	23/03/2019 09:48
50.71	0.62	16.07	0.47	8.17	22.82	0.70	99.57	23/03/2019 09:57
50.55	0.64	16.33	0.47	8.17	22.69	0.69	99.54	23/03/2019 10:06
49.84	0.65	16.57	0.49	7.72	22.59	0.72	98.59	30/04/2019 04:55
50.13	0.62	16.40	0.47	7.76	22.56	0.71	98.67	30/04/2019 05:04
49.99	0.64	16.47	0.49	7.85	22.69	0.72	98.87	30/04/2019 05:13
49.70	0.54	16.51	0.50	7.72	22.81	0.72	98.52	30/04/2019 05:22
49.87	0.65	16.46	0.50	7.70	22.52	0.72	98.44	30/04/2019 05:31

49.95	0.63	16.29	0.48	7.52	22.73	0.75	98.35	30/04/2019 08:21
49.39	0.57	16.37	0.48	7.52	22.65	0.73	97.73	30/04/2019 08:26
49.81	0.61	16.35	0.50	7.51	22.56	0.74	98.07	30/04/2019 08:31
50.37	0.60	16.30	0.47	7.84	22.65	0.00	98.25	30/04/2019 10:13
49.99	0.60	16.61	0.50	7.85	22.71	0.00	98.29	30/04/2019 10:18
49.80	0.64	16.25	0.48	7.76	22.62	0.00	97.56	30/04/2019 10:23
50.26	0.59	16.47	0.48	7.98	22.71	0.00	98.49	30/04/2019 11:14
50.50	0.61	16.39	0.48	7.93	22.61	0.00	98.54	30/04/2019 11:19
50.11	0.54	16.46	0.50	7.84	22.84	0.00	98.31	30/04/2019 11:24
49.86	0.59	16.44	0.51	7.87	22.66	0.00	97.93	30/04/2019 11:29
50.27	0.55	15.98	0.49	8.09	22.65	0.72	98.76	01/05/2019 04:30
50.19	0.53	16.08	0.51	8.15	22.70	0.72	98.88	01/05/2019 04:39
50.59	0.62	16.19	0.49	8.06	22.68	0.71	99.35	01/05/2019 04:48
49.91	0.58	16.22	0.49	8.05	22.65	0.73	98.64	01/05/2019 04:57
50.26	0.59	16.35	0.49	8.08	22.59	0.73	99.08	01/05/2019 05:06
49.79	0.66	16.15	0.46	7.89	22.54	0.71	98.23	01/05/2019 08:56
50.32	0.57	16.15	0.47	8.04	22.45	0.71	98.74	01/05/2019 09:05
49.42	0.52	16.27		7.84	22.78	0.00	96.84	01/05/2019 13:32
49.89	0.64	16.21		7.82	22.64	0.00	97.19	01/05/2019 13:34
50.02	0.58	16.17		7.94	22.78	0.00	97.50	01/05/2019 13:37
49.99	0.56	16.11		7.89	22.55	0.00	97.10	01/05/2019 13:39
49.94	0.62	16.32		7.93	22.59	0.00	97.39	01/05/2019 13:41
49.86	0.59	16.34		7.76	22.37	0.00	96.92	01/05/2019 13:43
50.40	0.62	16.01		7.89	22.55	0.00	97.46	01/05/2019 14:13
50.21	0.62	16.13		7.98	22.48	0.00	97.42	01/05/2019 14:16
50.73	0.59	15.99		8.01	22.70	0.00	98.03	01/05/2019 14:18
50.25	0.57	16.32		7.94	22.83	0.00	97.90	01/05/2019 14:20
50.37	0.64	16.20	0.00	8.04	22.54	0.00	97.77	02/05/2019 03:48
49.61	0.56	16.14	0.00	7.97	22.65	0.00	96.92	02/05/2019 03:50
50.24	0.58	16.14	0.00	8.00	22.60	0.00	97.57	02/05/2019 03:53
49.92	0.55	16.07	0.49	7.94	22.60	0.72	98.30	02/05/2019 03:55
50.38	0.56	16.03	0.48	7.92	22.74	0.72	98.84	02/05/2019 04:04
49.99	0.62	16.31	0.49	7.94	22.52	0.72	98.60	02/05/2019 04:13
50.22	0.57	16.42	0.48	7.90	22.78	0.72	99.10	02/05/2019 04:22
50.27	0.58	15.94	0.49	7.94	22.66	0.72	98.59	02/05/2019 04:31
50.90	0.63	16.79	0.49	7.94	23.00	0.71	100.46	07/05/2019 11:25
50.81	0.63	17.19	0.45	7.81	23.25	0.71	100.85	07/05/2019 11:30
51.18	0.62	16.76	0.49	7.90	23.31	0.72	101.00	07/05/2019 11:35
50.75	0.63	16.52	0.48	7.94	23.05	0.72	100.10	08/05/2019 03:54
50.88	0.61	16.66	0.49	7.98	23.24	0.71	100.58	08/05/2019 04:03
50.50	0.56	16.72	0.48	8.02	23.14	0.72	100.15	08/05/2019 04:12
50.56	0.66	16.78	0.50	8.06	22.59	0.72	99.88	08/05/2019 04:21

50.74	0.63	16.29	0.49	8.05	23.08	0.72	100.03	08/05/2019 04:30
50.35	0.62	16.46	0.47	7.95	23.26	0.72	99.86	08/05/2019 08:43
50.87	0.58	16.70	0.47	7.93	23.06	0.73	100.36	08/05/2019 08:48
50.28	0.65	16.86	0.48	8.01	23.16	0.73	100.16	08/05/2019 08:53
50.89	0.60	17.00	0.49	8.00	23.31	0.72	101.02	09/05/2019 04:54
50.81	0.55	16.58	0.48	7.96	23.03	0.71	100.13	09/05/2019 04:59
51.00	0.61	16.98	0.48	8.03	23.29	0.72	101.11	09/05/2019 05:04
50.60	0.62	16.97	0.47	7.99	23.19	0.73	100.57	09/05/2019 05:13
50.02	0.60	17.01	0.47	7.80	23.28	0.72	99.92	09/05/2019 05:22
50.81	0.59	16.62	0.48	8.11	22.94	0.72	100.29	09/05/2019 08:32
51.33	0.61	16.51	0.46	7.92	23.40	0.72	100.95	09/05/2019 08:37
51.24	0.63	16.52	0.48	7.91	23.18	0.73	100.69	09/05/2019 08:42
51.34	0.63	16.38	0.49	7.98	23.01	0.72	100.56	09/05/2019 17:22
51.48	0.67	16.56	0.49	7.98	23.28	0.72	101.20	09/05/2019 17:27
51.19	0.60	16.55	0.53	8.03	23.21	0.69	100.80	09/05/2019 17:32
50.72	0.61	16.69	0.49	8.13	22.92	0.72	100.28	10/05/2019 02:05
50.56	0.65	17.02	0.48	7.95	23.01	0.73	100.39	10/05/2019 02:10
50.97	0.62	17.17	0.47	7.97	23.16	0.72	101.08	10/05/2019 06:51
51.13	0.58	16.85	0.50	7.85	23.00	0.72	100.61	10/05/2019 07:00
50.67	0.67	17.00	0.47	7.94	23.53	0.72	101.02	10/05/2019 07:09
51.19	0.60	16.89	0.49	7.88	23.08	0.71	100.87	10/05/2019 07:18
51.28	0.61	17.02	0.48	7.99	23.15	0.72	101.26	10/05/2019 07:27
51.30	0.62	16.13	0.48	7.77	23.33	0.75	100.38	31/07/2018 07:10
51.26	0.68	16.27	0.48	7.74	23.11	0.74	100.28	31/07/2018 07:19
51.55	0.66	15.96	0.50	7.86	22.87	0.73	100.14	31/07/2018 07:28
51.20	0.61	16.08	0.51	7.63	22.86	0.75	99.65	01/08/2018 02:06
51.44	0.67	16.18	0.52	7.70	23.23	0.75	100.48	01/08/2018 02:15
51.02	0.73	16.66	0.51	7.57	23.16	0.77	100.43	01/08/2018 02:24
51.29	0.71	16.08	0.51	7.66	23.01	0.75	100.03	01/08/2018 02:33
51.26	0.71	16.42	0.51	7.73	23.20	0.75	100.56	01/08/2018 02:42
51.01	0.68	16.37	0.49	7.74	23.07	0.76	100.13	01/08/2018 02:51
50.97	0.74	16.18	0.49	7.64	23.02	0.74	99.80	01/08/2018 03:00
51.24	0.69	16.18	0.51	7.71	23.11	0.75	100.19	01/08/2018 03:09

A.2 EPMA Olivine data

Table A.4: **Olivine analyses**

Sample	SiO_2	Al_2O_3	FeO	MnO	MgO	CaO	NiO	P_2O_5	Total	Distance from core (μm)	
Rotokawau											
Rotokawau	38.67	0.03	20.43	0.33	41.20	0.25	0.02	0.12	101.08	core	09/05/2019 22:02
Rotokawau	38.64	0.03	20.52	0.32	40.88	0.25	0.03	0.07	100.76	mid	09/05/2019 22:08
Rotokawau	38.52	0.03	21.10	0.34	40.37	0.26	0.04	0.08	100.76	mid	09/05/2019 22:14
Rotokawau	37.57	0.04	24.98	0.37	37.54	0.28	0.02	0.11	100.94	mid	09/05/2019 22:21
Rotokawau	38.46	0.03	21.11	0.33	40.50	0.20	0.03	0.05	100.71	core	10/05/2019 02:20
Rotokawau	38.68	0.02	21.18	0.33	40.62	0.20	0.03	0.04	101.13	core	10/05/2019 02:26
Rotokawau	38.20	0.02	20.78	0.34	40.84	0.20	0.02	0.08	100.49	mid	10/05/2019 02:33
Rotokawau	39.19	0.02	20.06	0.31	41.12	0.21	0.04	0.08	101.07	mid	10/05/2019 02:39
Rotokawau	38.59	0.03	19.93	0.31	41.40	0.22	0.04	0.07	100.60	mid	10/05/2019 02:46
Rotokawau	38.63	0.03	20.31	0.31	41.18	0.22	0.03	0.10	100.84	mid	10/05/2019 02:52
Rotokawau	38.41	0.03	21.09	0.32	41.13	0.23	0.02	0.11	101.37	inner rim	10/05/2019 02:58
Rotokawau	37.69	0.03	23.70	0.36	38.57	0.25	0.03	0.03	100.67	outer rim	10/05/2019 03:05
Rotokawau	38.32	0.02	24.71	0.39	37.93	0.23	0.02	0.02	101.65	0	10/05/2019 06:09
Rotokawau	38.69	0.02	25.10	0.40	37.46	0.22	0.01	0.00	101.93	14.32	10/05/2019 06:16
Rotokawau	38.31	0.02	24.59	0.38	37.64	0.24	0.01	0.07	101.30	28.64	10/05/2019 06:22
Rotokawau	38.83	0.03	20.29	0.32	40.09	0.23	0.03	0.06	99.91	core	30/04/2019 15:45
Rotokawau	38.40	0.03	20.28	0.33	40.25	0.21	0.03	0.12	99.66	mid	30/04/2019 15:51
Rotokawau	38.39	0.02	19.94	0.33	40.31	0.21	0.03	0.05	99.31	mid	30/04/2019 15:57
Rotokawau	37.27	0.06	27.12	0.42	34.21	0.24	0.01	0.03	99.39	rim	30/04/2019 16:03
Rotokawau	38.18	0.02	22.86	0.36	37.72	0.21	0.02	0.04	99.44	core	30/04/2019 17:22
Rotokawau	37.60	0.03	24.23	0.40	36.62	0.24	0.02	0.03	99.19	rim	30/04/2019 17:36
Rotomakariri											
Rotomakariri	38.10	0.02	23.39	0.36	37.76	0.14	0.03	0.03	99.84	0	22/03/2019 20:55
Rotomakariri	37.83	0.02	23.77	0.36	37.49	0.14	0.01	0.03	99.66	24.73	22/03/2019 21:01
Rotomakariri	37.83		23.62	0.37	38.54	0.15	0.02	0.03	100.87	49.46	22/03/2019 21:07
Rotomakariri	38.02	0.02	23.42	0.34	37.50	0.15	0.02	0.02	99.50	74.19	22/03/2019 21:13
Rotomakariri	37.92		23.83	0.36	38.23	0.16	0.01	0.03	101.54	98.92	22/03/2019 21:19
Rotomakariri	38.48	0.02	24.27	0.36	38.16	0.14	0.02	0.01	101.46	123.65	22/03/2019 21:26
Rotomakariri	38.04	0.01	23.79	0.36	37.37	0.15	0.02	0.02	99.77	148.38	22/03/2019 21:32
Rotomakariri	38.68	0.02	24.37	0.37	38.19	0.15	0.01	0.01	101.81	173.11	22/03/2019 21:38
Rotomakariri	38.69	0.02	24.63	0.37	37.97	0.16	0.02	0.01	101.87	197.84	22/03/2019 21:44

Rotomakariri	38.46	0.01	24.65	0.39	37.89	0.22	0.02	0.01	101.66	222.57	22/03/2019 21:50
Rotomakariri	38.75	0.02	23.63	0.34	38.72	0.14	0.02	0.02	101.65	core	22/03/2019 23:05
Rotomakariri	38.00	0.02	22.89	0.32	39.59	0.14	0.02	0.02	101.01	0	23/03/2019 01:03
Rotomakariri	38.37	0.02	22.76	0.35	39.54	0.14	0.01	0.02	101.23	35.86	23/03/2019 01:09
Rotomakariri	38.37	0.02	22.80	0.34	39.40	0.15	0.00	0.02	101.13	71.73	23/03/2019 01:15
Rotomakariri	38.29	0.02	22.33	0.34	39.26	0.14	0.00	0.03	100.45	107.59	23/03/2019 01:21
Rotomakariri	38.53	0.01	22.53	0.33	39.32	0.14	0.00	0.03	100.91	179.32	23/03/2019 01:34
Rotomakariri	38.71	0.04	22.69	0.34	39.91	0.18	0.00	0.03	101.97	215.19	23/03/2019 01:40
Rotomakariri	37.53	0.01	22.46	0.34	38.46	0.15	0.01	0.03	99.00	322.79	23/03/2019 01:59
Rotomakariri	38.12	0.02	22.90	0.35	38.92	0.15	0.02	0.03	100.52	358.65	23/03/2019 02:05
Rotomakariri	37.81	0.02	22.82	0.32	38.46	0.14	0.02	0.04	99.64	394.52	23/03/2019 02:11
Rotomakariri	37.90	0.02	22.78	0.35	38.19	0.15	0.02	0.01	99.42	430.38	23/03/2019 02:17
Rotomakariri	39.27	0.02	16.75	0.25	43.24	0.18	0.04	0.02	99.77	0	02/08/2019 14:19
Rotomakariri	39.57	0.03	16.41	0.24	43.25	0.19	0.04	0.01	99.75	24.52	02/08/2019 14:25
Rotomakariri	39.50	0.02	17.23	0.25	43.31	0.19	0.03	0.01	100.54	49.01	02/08/2019 14:31
Rotomakariri	39.53	0.03	16.94	0.25	43.36	0.19	0.04	0.03	100.34	73.5	02/08/2019 14:37
Rotomakariri	39.04	0.02	16.24	0.24	43.27	0.18	0.05	0.02	99.06	98.02	02/08/2019 14:43
Rotomakariri	39.26	0.03	16.57	0.26	42.99	0.19	0.04	0.02	99.36	122.51	02/08/2019 14:49
Rotomakariri	39.13	0.02	16.99	0.24	42.98	0.18	0.04	0.00	99.59	147.01	02/08/2019 14:55
Rotomakariri	39.30	0.02	16.79	0.25	42.65	0.19	0.04	0.01	99.26	171.51	02/08/2019 15:01
Rotomakariri	39.20	0.03	17.08	0.26	42.38	0.19	0.05	0.00	99.20	196.02	02/08/2019 15:07
Rotomakariri	39.32	0.02	17.41	0.26	42.12	0.18	0.05	0.01	99.37	220.51	02/08/2019 15:14
Rotomakariri	39.15	0.02	17.93	0.26	41.91	0.18	0.05	0.00	99.51	245.01	02/08/2019 15:20
Rotomakariri	38.66	0.02	17.96	0.27	41.70	0.18	0.05	0.01	98.84	269.51	02/08/2019 15:26
Rotomakariri	38.93	0.02	18.66	0.29	41.45	0.18	0.06	0.00	99.58	294.02	02/08/2019 15:32
Rotomakariri	38.86	0.02	18.84	0.30	41.15	0.17	0.04	0.01	99.38	318.51	02/08/2019 15:38
Rotomakariri	39.09	0.02	19.15	0.31	40.52	0.16	0.04	0.01	99.31	343.01	02/08/2019 15:44
Rotomakariri	38.71	0.02	20.01	0.33	39.96	0.14	0.06	0.00	99.22	392.02	02/08/2019 15:56
Rotomakariri	39.11	0.04	20.46	0.32	39.66	0.13	0.05	0.01	99.78	416.51	02/08/2019 16:02
Rotomakariri	38.64	0.02	20.29	0.33	39.65	0.12	0.06	0.00	99.13	441.01	02/08/2019 16:08
Tarawera											
Tarawera	38.75	0.22	17.51	0.23	42.27	0.45	0.02	0.00	100.07	GM	07/05/2019 16:30
Tarawera	38.47	0.08	17.91	0.29	42.61	0.41	0.02	0.00	100.02	GM	07/05/2019 16:39
Tarawera	37.67	0.02	18.75	0.28	42.22	0.43	0.01	0.00	99.43	GM	07/05/2019 16:48
Tarawera	39.23	0.08	17.01	0.26	43.47	0.28	0.01	0.00	100.35	GM	07/05/2019 17:06
Tarawera	39.19	0.08	17.47	0.29	41.98	0.41	0.00	0.15	99.62	GM	01/05/2019 17:09
Tarawera	39.55	0.06	17.70	0.28	42.88	0.32	0.02	0.02	100.84	GM	01/05/2019 17:15

Terrace Rd											
Terrace Rd	38.72	0.02	21.76	0.34	39.30	0.20	0.00	0.04	100.40	core	29/04/2019 17:28
Terrace Rd	38.38	0.02	19.59	0.30	40.64	0.16	0.00	0.02	99.12	core	29/04/2019 20:44
Terrace Rd	38.71	0.02	19.60	0.28	40.36	0.17	0.00	0.02	99.18	mid	29/04/2019 20:50
Terrace Rd	38.47	0.02	19.43	0.30	40.72	0.17	0.01	0.01	99.16	mid	29/04/2019 20:56
Terrace Rd	38.58	0.02	20.11	0.29	40.31	0.18	0.01	0.01	99.51	mid	29/04/2019 21:02
HJR											
HJR	38.81	0.07	19.20	0.29	41.55	0.27	0.05	0.09	100.34	core	07/05/2019 17:59
HJR	38.69	0.04	20.37	0.30	41.12	0.25	0.03	0.05	100.88	mid	07/05/2019 18:06
HJR	38.97	0.03	19.84	0.31	41.20	0.23	0.04	0.05	100.69	core	07/05/2019 22:39
HJR	39.04	0.04	19.60	0.30	41.47	0.23	0.04	0.04	100.80	mid	07/05/2019 22:45
HJR	39.74	0.05	19.00	0.28	41.78	0.24	0.04	0.04	101.21	mid	07/05/2019 22:52
HJR	38.61	0.13	21.12	0.33	38.70	0.33	0.03	0.16	99.47	mid	07/05/2019 23:04
HJR	38.62	0.07	20.62	0.32	41.23	0.25	0.04	0.05	101.23	core	08/05/2019 03:06
HJR	38.00	0.13	21.33	0.31	38.76	0.27	0.05	0.06	98.96	mid	08/05/2019 03:12
HJR	38.78	0.08	21.99	0.36	39.82	0.31	0.03	0.05	101.46	mid	08/05/2019 03:18
Ongaroto											
Ongaroto	39.56	0.03	15.93	0.24	43.71	0.19	0.21	0.02	99.90	core	31/07/2018 09:17
Ongaroto	38.78	0.02	20.52	0.35	39.52	0.24	0.14	0.00	99.60	rim	31/07/2018 09:24
Ongaroto	39.39	0.03	15.81	0.26	44.35	0.20	0.21	0.03	100.29	core	31/07/2018 09:39
Ongaroto	37.07	0.02	30.69	0.47	32.13	0.23	0.08	0.02	100.77	rim	31/07/2018 09:45
Ongaroto	39.48	0.03	13.09	0.20	45.75	0.19	0.26	0.02	99.03	core	31/07/2018 10:01
Ongaroto	39.37	0.03	13.93	0.22	45.62	0.19	0.22	0.05	99.65	mid	31/07/2018 10:07
Ongaroto	39.46	0.03	15.64	0.25	44.15	0.20	0.19	0.04	99.97	mid	31/07/2018 10:14
Ongaroto	38.96	0.02	20.93	0.32	40.17	0.21	0.13	0.02	100.81	mid	31/07/2018 10:20
Ongaroto	39.82	0.03	13.25	0.22	46.27	0.19	0.26	0.01	100.06	core	31/07/2018 11:07
Ongaroto	39.51	0.03	14.57	0.24	45.26	0.21	0.20	0.02	100.05	mid	31/07/2018 11:14
Ongaroto	36.60	0.03	31.07	0.47	32.28	0.21	0.08	0.04	100.81	rim	31/07/2018 11:20
Ongaroto	39.64	0.03	14.02	0.23	45.74	0.19	0.24	0.01	100.14	core	31/07/2018 11:26
Ongaroto	39.64	0.03	16.20	0.25	43.90	0.19	0.21	0.02	100.46	mid	31/07/2018 11:33
Ongaroto	36.92	0.08	29.68	0.43	33.05	0.19	0.12	0.03	100.56	mid	31/07/2018 11:39
Ongaroto	53.06	0.59	18.20	0.50	23.36	3.44	0.02	0.01	99.65	rim	31/07/2018 11:46

Ongaroto	40.08	0.03	12.55	0.19	46.46	0.19	0.26	0.01	99.78	core	31/07/2018 11:52
Ongaroto	39.87	0.03	13.04	0.20	46.48	0.19	0.25	0.01	100.10	core	31/07/2018 11:58
Ongaroto	40.37	0.03	13.46	0.20	46.46	0.19	0.24	0.01	100.97	mid	31/07/2018 12:05
Ongaroto	39.80	0.03	13.92	0.21	45.72	0.19	0.24	0.02	100.14	mid	31/07/2018 12:11
Ongaroto	38.30	0.02	20.90	0.32	40.05	0.20	0.16	0.01	99.98	rim	31/07/2018 12:18
Ongaroto	40.57	0.04	9.27	0.12	50.15	0.13	0.35	0.01	100.66	core	31/07/2018 13:24
Ongaroto	38.86	0.04	15.16	0.23	44.69	0.19	0.23	0.11	99.53	mid	31/07/2018 13:31
Ongaroto	40.40	0.03	12.83	0.20	46.63	0.18	0.27	0.01	100.56	mid	31/07/2018 13:37
Ongaroto	39.38	0.02	17.83	0.28	42.64	0.20	0.19	0.02	100.57	rim	31/07/2018 13:43
Ongaroto	37.32	0.02	23.17	0.38	38.52	0.22	0.12	0.02	99.81	rim	31/07/2018 13:50
Ongaroto	40.59	0.03	11.63	0.19	46.03	0.19	0.30	0.01	98.98	core	20/03/2019 10:27
Ongaroto	40.09	0.03	13.59	0.20	45.41	0.24	0.25	0.01	99.84	core	20/03/2019 10:43
Ongaroto	39.68	0.03	15.42	0.26	43.82	0.20	0.20	0.02	99.66	core	20/03/2019 11:25
Ongaroto	40.30	0.03	12.66	0.19	45.74	0.27	0.26	0.02	99.49	core	20/03/2019 11:40
Ongaroto	39.26	0.03	16.05	0.25	43.02	0.22	0.18	0.01	99.04	core	20/03/2019 11:55
Ongaroto	39.43	0.03	16.53	0.27	42.32	0.22	0.18	0.01	99.00	0	20/03/2019 12:01
Ongaroto	39.01	0.02	18.14	0.31	41.16	0.22	0.15	0.02	99.05	12.5	20/03/2019 12:07
Ongaroto	40.65	0.04	9.41	0.12	48.51	0.18	0.37	0.01	99.32	core	20/03/2019 12:49
Ongaroto	41.11	0.03	12.18	0.18	47.19	0.18	0.29	0.01	101.19	core	20/03/2019 13:04
Ongaroto	40.15	0.03	12.66	0.19	45.93	0.17	0.30	0.00	99.43	mid	20/03/2019 13:19
Ongaroto	37.58	0.02	26.69	0.41	34.59	0.21	0.11	0.01	99.68	rim	20/03/2019 13:33
Ongaroto	38.36	0.02	24.12	0.38	37.75	0.20	0.12	0.02	101.01	rim	20/03/2019 13:46
Ongaroto	40.44	0.04	9.03	0.11	49.88	0.14	0.37	0.02	100.08	0	02/08/2019 12:31
Ongaroto	40.17	0.04	8.77	0.13	49.02	0.16	0.38	0.02	98.73	19.67	02/08/2019 12:37
Ongaroto	40.56	0.05	8.99	0.13	48.85	0.18	0.36	0.01	99.19	39.34	02/08/2019 12:43
Ongaroto	40.58	0.04	9.74	0.14	48.68	0.18	0.37	0.00	99.76	59.01	02/08/2019 12:49
Ongaroto	40.07	0.03	9.82	0.14	48.09	0.18	0.36	0.01	98.72	78.68	02/08/2019 12:55
Ongaroto	40.22	0.04	10.32	0.14	47.85	0.18	0.35	0.00	99.12	98.35	02/08/2019 13:01
Ongaroto	40.21	0.04	10.66	0.16	47.75	0.19	0.34	0.02	99.37	118.02	02/08/2019 13:07
Ongaroto	39.99	0.04	11.13	0.17	47.78	0.18	0.33	0.02	99.65	137.69	02/08/2019 13:13
Ongaroto	40.03	0.04	11.33	0.18	47.09	0.18	0.32	0.01	99.20	157.36	02/08/2019 13:19
Ongaroto	39.56	0.03	11.83	0.17	46.90	0.18	0.30	0.01	98.98	177.03	02/08/2019 13:25
Ongaroto	39.91	0.04	11.93	0.19	46.69	0.18	0.28	0.02	99.25	196.7	02/08/2019 13:31
Ongaroto	39.85	0.03	13.23	0.20	45.78	0.19	0.24	0.02	99.55	255.71	02/08/2019 13:49
Ongaroto	39.88	0.10	13.52	0.21	45.30	0.20	0.22	0.02	99.46	275.39	02/08/2019 13:55
Ongaroto	39.50	0.03	14.87	0.25	44.15	0.20	0.20	0.02	99.21	295.06	02/08/2019 14:01
Ongaroto	38.84	0.03	17.14	0.28	42.04	0.21	0.17	0.02	98.73	314.73	02/08/2019 14:07
Ongaroto	37.09	0.03	27.17	0.42	34.64	0.23	0.11	0.02	99.71	334.4	02/08/2019 14:13

Ongaroto	40.25	0.03	16.09	0.24	44.51	0.26	0.24	0.01	101.63	core	22/03/2019 12:30
Ongaroto	37.32	0.04	20.47	0.34	40.57	0.20	0.16	0.00	99.21	rim	22/03/2019 12:45
Ongaroto	37.49	0.02	27.99	0.45	34.87	0.22	0.10	0.01	101.16	rim	22/03/2019 13:31
Ongaroto	39.45	0.03	18.38	0.29	42.73	0.20	0.16	0.01	101.28	mid	22/03/2019 13:46
Kakuki											
Kakuki	39.67	0.04	14.91	0.23	45.42	0.24	0.10	0.09	100.70	0	09/05/2019 13:37
Kakuki	40.14	0.04	14.79	0.23	45.59	0.25	0.11	0.07	101.24	9.43	09/05/2019 13:44
Kakuki	39.55	0.04	14.80	0.22	45.30	0.24	0.09	0.11	100.37	18.87	09/05/2019 13:50
Kakuki	39.39	0.04	14.94	0.25	45.20	0.25	0.10	0.12	100.31	28.3	09/05/2019 13:56
Kakuki	39.84	0.04	14.67	0.23	45.04	0.26	0.11	0.09	100.31	37.74	09/05/2019 14:03
Kakuki	39.36	0.05	16.45	0.26	43.68	0.35	0.08	0.06	100.33	47.17	09/05/2019 14:09
Kakuki	40.42	0.04	13.84	0.20	46.42	0.25	0.13	0.12	101.46	0	09/05/2019 14:16
Kakuki	39.40	0.04	13.89	0.21	45.33	0.26	0.13	0.15	99.45	10.03	09/05/2019 14:22
Kakuki	39.75	0.04	15.29	0.25	45.23	0.28	0.08	0.08	101.03	20.06	09/05/2019 14:28
Kakuki	37.38	0.05	25.12	0.43	35.72	0.41	0.04	0.18	99.39	30.08	09/05/2019 14:35
Orakei Korako											
Orakei Korako	38.63	0.02	19.23	0.31	42.48	0.20	0.03	0.00	100.90	core	31/01/2018 00:01
Orakei Korako	36.60	0.03	28.30	0.49	34.64	0.29	0.03	0.00	100.39	rim	31/01/2018 00:05
Orakei Korako	38.49	0.03	20.71	0.33	41.03	0.22	0.05	0.00	100.89	core	31/01/2018 00:18
Orakei Korako	36.35	0.01	31.88	0.56	31.40	0.35	0.02	0.00	100.61	rim	31/01/2018 00:22
Orakei Korako	38.19	0.02	20.50	0.33	41.25	0.21	0.06	0.00	100.53	core	31/01/2018 00:26
Orakei Korako	33.40	0.13	40.06	0.72	26.06	0.37	0.02	0.00	100.90	rim	31/01/2018 00:30
Orakei Korako	37.96	0.02	22.87	0.37	39.38	0.22	0.04	0.00	100.87	core	31/01/2018 01:19
Orakei Korako	38.36	0.03	19.81	0.32	41.90	0.21	0.06	0.00	100.70	core	31/01/2018 01:27
Orakei Korako	36.15	0.72	33.50	0.60	27.49	0.66	0.02	0.00	99.29	rim	31/01/2018 01:31
Orakei Korako	35.87	0.03	32.21	0.55	31.10	0.34	0.02	0.00	100.17	core	31/01/2018 02:00
Orakei Korako	34.66	0.08	39.79	0.74	24.35	0.49	0.01	0.00	100.18	rim	31/01/2018 02:04
Orakei Korako	38.65	0.01	20.33	0.34	41.45	0.21	0.06	0.00	101.08	core	31/01/2018 02:08
Orakei Korako	39.10	0.05	20.58	0.30	40.95	0.22	0.05	0.00	101.39	0	08/05/2019 18:11
Orakei Korako	39.35	0.06	19.63	0.29	41.69	0.23	0.07	0.00	101.49	11.05	08/05/2019 18:17
Orakei Korako	38.67	0.04	19.46	0.30	42.33	0.22	0.05	0.00	101.20	22.09	08/05/2019 18:23

Orakei Korako	38.94	0.04	20.21	0.30	41.51	0.22	0.05	0.00	101.34	33.14	08/05/2019 18:30
Orakei Korako	38.54	0.05	23.39	0.36	38.82	0.22	0.04	0.00	101.51	44.18	08/05/2019 18:36
Orakei Korako	36.72	0.05	31.38	0.51	31.65	0.30	0.03	0.00	100.81	55.23	08/05/2019 18:42
Orakei Korako	38.90	0.04	20.08	0.32	41.14	0.21	0.06	0.00	100.79	0	09/05/2019 02:04
Orakei Korako	38.60	0.04	20.32	0.32	41.61	0.21	0.06	0.00	101.20	10.15	09/05/2019 02:10
Orakei Korako	38.97	0.04	19.44	0.30	41.98	0.21	0.05	0.00	101.03	20.29	09/05/2019 02:17
Orakei Korako	39.06	0.04	18.52	0.29	42.28	0.23	0.06	0.00	100.55	30.44	09/05/2019 02:23
Orakei Korako	39.17	0.04	19.28	0.31	42.49	0.23	0.07	0.00	101.62	40.59	09/05/2019 02:29
Orakei Korako	38.81	0.05	20.31	0.33	41.26	0.22	0.06	0.00	101.09	50.74	09/05/2019 02:36
Orakei Korako	37.91	0.03	24.98	0.42	37.02	0.25	0.05	0.00	100.72	60.88	09/05/2019 02:42
Orakei Korako	34.58	0.09	39.03	0.64	25.21	0.41	0.01	0.00	100.18	71.03	09/05/2019 02:48
Orakei Korako	38.90	0.04	19.77	0.31	41.68	0.21	0.06	0.00	101.02	0	09/05/2019 02:55
Orakei Korako	38.57	0.05	20.10	0.30	40.83	0.21	0.05	0.00	100.15	14.98	09/05/2019 03:01
Orakei Korako	38.80	0.04	20.31	0.31	41.69	0.20	0.06	0.00	101.44	29.96	09/05/2019 03:07
Orakei Korako	39.08	0.04	19.82	0.32	41.42	0.21	0.06	0.00	100.97	44.95	09/05/2019 03:14
Orakei Korako	39.18	0.03	19.50	0.31	41.49	0.20	0.06	0.00	100.79	59.93	09/05/2019 03:20
Orakei Korako	39.07	0.03	19.86	0.31	41.81	0.21	0.07	0.00	101.37	74.91	09/05/2019 03:26
Orakei Korako	39.20	0.04	19.93	0.31	41.54	0.21	0.06	0.00	101.32	89.89	09/05/2019 03:33
Orakei Korako	38.66	0.03	22.14	0.33	39.49	0.22	0.06	0.00	100.98	104.87	09/05/2019 03:39
Orakei Korako	37.21	0.03	29.28	0.46	34.28	0.27	0.04	0.00	101.63	119.85	09/05/2019 03:45
Orakei Korako	37.87	0.03	27.23	0.41	35.76	0.24	0.03	0.00	101.64	core	09/05/2019 03:52
Orakei Korako	37.92	0.03	28.08	0.45	34.98	0.26	0.04	0.00	101.81	mid	09/05/2019 03:58
Orakei Korako	37.14	0.04	30.36	0.52	32.63	0.31	0.03	0.00	101.12	mid	09/05/2019 04:04
Orakei Korako	35.48	0.04	38.32	0.63	26.01	0.37	0.02	0.00	101.02	rim	09/05/2019 04:11
Orakei Korako	38.48	0.04	19.43	0.32	40.65	0.20	0.06	0.02	99.21	0	02/05/2019 00:18
Orakei Korako	38.68	0.04	19.15	0.31	40.48	0.21	0.05	0.02	98.95	9.9	02/05/2019 00:24
Orakei Korako	39.19	0.04	18.66	0.30	41.38	0.21	0.06	0.02	99.87	19.8	02/05/2019 00:30
Orakei Korako	39.14	0.04	17.66	0.30	41.56	0.23	0.07	0.06	99.07	29.7	02/05/2019 00:36
Orakei Korako	39.13	0.04	17.89	0.31	41.61	0.23	0.06	0.02	99.32	39.6	02/05/2019 00:42
Orakei Korako	38.96	0.04	19.31	0.33	40.66	0.23	0.05	0.01	99.60	49.5	02/05/2019 00:48
Orakei Korako	38.41	0.05	22.81	0.37	37.77	0.24	0.05	0.01	99.75	59.4	02/05/2019 00:54
Orakei Korako	36.53	0.04	31.07	0.52	30.35	0.32	0.03	0.03	98.95	69.3	02/05/2019 01:00
										0	02/05/2019 01:06
Orakei Korako	38.47	0.05	19.25	0.32	40.80	0.21	0.05	0.02	99.20	14.98	02/05/2019 01:12
Orakei Korako	38.64	0.04	19.50	0.31	40.81	0.21	0.06	0.03	99.61	29.96	02/05/2019 01:18
Orakei Korako	38.57	0.04	19.14	0.32	40.64	0.21	0.05	0.02	98.99	44.94	02/05/2019 01:25
Orakei Korako	38.71	0.03	19.38	0.31	40.84	0.21	0.05	0.01	99.55	59.91	02/05/2019 01:31
Orakei Korako	38.57	0.04	19.06	0.30	40.59	0.21	0.06	0.01	98.84	74.89	02/05/2019 01:37

Orakei Korako	38.58	0.04	19.22	0.32	40.63	0.20	0.06	0.01	99.07	89.87	02/05/2019 01:43
Orakei Korako	38.77	0.04	18.92	0.30	40.75	0.21	0.05	0.01	99.07	104.85	02/05/2019 01:49
Waimarino											
Waimarino	40.45	0.02	14.19	0.21	45.66	0.22	0.14	0.01	100.90	core	18/03/2019 14:32
Waimarino	40.75	0.02	13.68	0.19	46.48	0.17	0.18	0.01	101.48	core	18/03/2019 16:39
Waimarino	41.79	0.02	7.33	0.12	50.43	0.13	0.53	0.00	100.34	core	18/03/2019 16:58
Waimarino	42.02	0.02	7.44	0.11	51.24	0.12	0.56	0.00	101.52	core	18/03/2019 17:59
Waimarino	41.55	0.02	7.42	0.10	51.01	0.12	0.55	0.00	100.78	core	18/03/2019 18:19
Waimarino	41.71	0.02	8.55	0.12	50.26	0.13	0.46	0.00	101.26	core	18/03/2019 18:32
Waimarino	41.46	0.02	8.74	0.12	50.03	0.14	0.38	0.00	100.89	core	18/03/2019 18:45
Waimarino	40.64	0.02	10.77	0.15	48.55	0.15	0.28	0.00	100.56	mid	18/03/2019 18:51
Waimarino	40.58	0.02	13.06	0.21	46.62	0.15	0.21	0.00	100.84	rim	18/03/2019 19:12
Waimarino	40.56	0.02	13.81	0.20	45.89	0.17	0.18	0.00	100.84	rim	18/03/2019 19:25
Waimarino	41.62	0.02	8.28	0.12	50.14	0.15	0.44	0.00	100.77	mid	18/03/2019 19:31
Waimarino	40.54	0.03	7.14	0.10	51.40	0.12	0.56	0.00	99.89		02/08/2019 20:22
Waimarino	40.71	0.02	7.43	0.10	51.19	0.12	0.56	0.00	100.13	0	02/08/2019 20:28
Waimarino	40.76	0.02	7.17	0.09	51.21	0.12	0.56	0.00	99.93	25.63	02/08/2019 20:34
Waimarino	40.52	0.02	7.30	0.10	51.30	0.12	0.56	0.01	99.92	51.25	02/08/2019 20:40
Waimarino	40.74	0.03	7.45	0.11	51.45	0.12	0.55	0.00	100.44	76.88	02/08/2019 20:46
Waimarino	40.82	0.02	7.15	0.11	51.30	0.11	0.55	0.01	100.07	102.5	02/08/2019 20:52
Waimarino	40.63	0.02	7.25	0.11	51.37	0.12	0.56	0.00	100.06	128.13	02/08/2019 20:57
Waimarino	40.60	0.02	7.18	0.11	51.41	0.12	0.56	0.00	100.00	153.76	02/08/2019 21:03
Waimarino	41.12	0.03	7.57	0.10	50.43	0.12	0.55	0.00	99.92	179.38	02/08/2019 21:09
Waimarino	40.42	0.03	7.35	0.10	50.90	0.11	0.55	0.01	99.47	205.01	02/08/2019 21:15
Waimarino	40.96	0.02	7.88	0.11	51.18	0.12	0.54	0.00	100.82	230.63	02/08/2019 21:21
Waimarino	40.57	0.03	7.64	0.11	50.99	0.11	0.55	0.00	99.99	256.26	02/08/2019 21:27
Waimarino	40.88	0.02	7.81	0.08	50.78	0.12	0.54	0.00	100.24	281.89	02/08/2019 21:33
Waimarino	40.88	0.04	8.09	0.11	50.94	0.12	0.52	0.00	100.69	307.51	02/08/2019 21:39
Waimarino	40.41	0.03	7.71	0.11	51.10	0.12	0.52	0.01	100.01	333.14	02/08/2019 21:45
Waimarino	40.63	0.02	8.19	0.11	50.66	0.12	0.51	0.00	100.25	358.76	02/08/2019 21:51
Waimarino	40.77	0.18	8.08	0.11	50.51	0.13	0.51	0.01	100.31	410.02	02/08/2019 21:57
Waimarino	40.58	0.02	8.60	0.11	50.53	0.12	0.49	-0.01	100.45	435.64	02/08/2019 22:03
Waimarino	40.63	0.03	8.33	0.12	50.29	0.12	0.48	0.00	100.00	461.27	02/08/2019 22:09
Waimarino	40.36	0.03	8.54	0.12	49.79	0.12	0.47	0.00	99.44	486.9	02/08/2019 22:15
Waimarino	40.40	0.15	8.26	0.11	49.78	0.13	0.45	0.00	99.31	512.52	02/08/2019 22:20
Waimarino	40.88	0.02	8.53	0.11	49.87	0.13	0.47	-0.01	100.02	538.15	02/08/2019 22:26
Waimarino	40.48	0.02	8.43	0.11	50.44	0.14	0.45	0.00	100.08	563.77	02/08/2019 22:33
Waimarino	40.57	0.02	8.42	0.11	50.23	0.13	0.45	0.00	99.93	589.4	02/08/2019 22:38
Waimarino	41.08	0.02	8.55	0.12	50.16	0.13	0.45	0.00	100.53	615.03	02/08/2019 22:44

Waimarino	40.34	0.02	8.35	0.12	50.43	0.13	0.44	0.00	99.84	640.65	02/08/2019 22:50
Waimarino	40.91	0.02	8.39	0.12	50.30	0.13	0.42	-0.01	100.28	666.28	02/08/2019 22:56
Waimarino	40.68	0.02	8.42	0.11	50.48	0.13	0.43	0.00	100.29	691.9	02/08/2019 23:02
Waimarino	40.79	0.02	8.08	0.11	50.49	0.13	0.42	0.00	100.05	717.53	02/08/2019 23:08
Waimarino	40.88	0.07	7.83	0.12	50.20	0.13	0.43	0.00	99.68	743.15	02/08/2019 23:14
Waimarino	40.51	0.02	8.26	0.12	50.77	0.13	0.42	-0.01	100.22	768.78	02/08/2019 23:20
Waimarino	40.29	0.60	8.32	0.10	50.56	0.14	0.40	0.01	100.45	794.41	02/08/2019 23:26
Waimarino	40.42	0.03	8.21	0.12	50.12	0.13	0.41	0.01	99.45	820.03	02/08/2019 23:32
Waimarino	40.41	0.02	8.70	0.11	50.18	0.13	0.39	0.01	99.96	845.66	02/08/2019 23:38
Waimarino	40.65	0.02	9.07	0.12	49.89	0.13	0.37	0.00	100.26	871.29	02/08/2019 23:44
Waimarino	40.65	0.02	9.04	0.12	49.85	0.13	0.36	0.00	100.18	896.91	02/08/2019 23:50
Waimarino	39.97	0.02	9.41	0.12	50.04	0.14	0.37	0.00	100.08	922.54	02/08/2019 23:56
Waimarino	41.31	1.56	9.30	0.13	49.64	0.18	0.33	0.01	102.51	948.16	03/08/2019 00:02
Waimarino	39.99	0.02	9.63	0.13	49.37	0.14	0.32	0.00	99.60	973.79	03/08/2019 00:08
Waimarino	40.25	0.01	9.87	0.14	49.18	0.15	0.32	0.00	99.92	999.42	03/08/2019 00:14
Waimarino	40.13	0.02	9.86	0.15	49.04	0.15	0.30	0.00	99.66	1025.04	03/08/2019 00:20
Waimarino	40.11	0.02	10.31	0.14	48.60	0.15	0.28	0.00	99.63	1050.67	03/08/2019 00:26
Waimarino	40.27	0.02	11.08	0.15	48.20	0.15	0.26	0.00	100.14	1076.3	03/08/2019 00:32
Waimarino	39.63	0.02	12.03	0.16	47.70	0.15	0.24	0.00	99.93	1101.92	03/08/2019 00:38
Waimarino	39.76	0.01	12.90	0.18	46.75	0.15	0.21	0.00	99.98	1127.55	03/08/2019 00:44
Waimarino	39.75	0.03	13.79	0.20	46.03	0.15	0.18	0.00	100.14	1153.17	03/08/2019 00:50
Waimarino	39.63	0.02	14.67	0.22	45.36	0.17	0.14	0.00	100.20	1178.8	03/08/2019 00:56
Waimarino	39.65	0.01	14.91	0.22	44.91	0.16	0.12	0.00	99.99	1230.05	03/08/2019 01:08
Waimarino	39.53	0.02	15.59	0.24	44.25	0.18	0.12	0.00	99.93	1255.68	03/08/2019 01:14
Waimarino	41.39	0.02	10.66	0.15	48.92	0.15	0.29	0.00	101.59	core	18/03/2019 20:08
Waimarino	41.51	0.02	10.14	0.15	48.67	0.15	0.32	0.00	100.96	core	18/03/2019 20:21
Waimarino	41.65	0.02	10.08	0.14	49.05	0.13	0.30	0.00	101.38	0	18/03/2019 20:27
Waimarino	41.09	0.02	9.64	0.14	48.30	0.13	0.32	0.01	99.64	39.52	18/03/2019 20:33
Waimarino	40.54	0.02	9.61	0.15	48.32	0.14	0.31	0.00	99.10	79.05	18/03/2019 20:39
Waimarino	40.23	0.01	11.60	0.17	47.26	0.16	0.22	0.00	99.66	118.57	18/03/2019 20:45
Waimarino	52.81	2.06	15.20	0.35	22.85	6.27	0.04	0.00	99.99	158.09	18/03/2019 20:51
Waimarino	41.16	0.02	8.92	0.13	49.63	0.13	0.39	0.00	100.38	core	18/03/2019 21:40
Waimarino	40.56	0.02	14.02	0.18	46.71	0.16	0.20	0.00	101.85	mid	18/03/2019 22:00
Waimarino	39.96	0.02	14.99	0.22	45.38	0.19	0.13	0.01	100.92	rim	18/03/2019 22:06
Ohakune											
Ohakune	40.88	0.01	14.01	0.19	45.49	0.10	0.14	0.01	100.85	core	19/03/2019 12:37
Ohakune	41.01	0.01	10.69	0.16	47.44	0.11	0.19	0.00	99.64	core	19/03/2019 13:11
Ohakune	40.74	0.01	10.81	0.16	47.71	0.11	0.17	0.00	99.71	core	19/03/2019 13:24

Ohakune	40.96	0.01	10.66	0.16	47.05	0.11	0.19	0.01	99.16	0	19/03/2019 13:30
Ohakune	40.51	0.01	10.99	0.17	47.45	0.11	0.18	0.01	99.44	50	19/03/2019 13:36
Ohakune	40.38	0.01	11.63	0.17	46.52	0.11	0.19	0.00	99.02	100	19/03/2019 13:42
Ohakune	40.89	0.02	12.36	0.19	46.87	0.17	0.14	0.00	100.64	core	19/03/2019 21:10
Ohakune	40.24	0.01	11.90	0.17	46.70	0.11	0.14	0.00	99.29	core	19/03/2019 21:23
Ohakune	41.16	0.02	12.30	0.17	47.13	0.13	0.15	0.00	101.07	core	19/03/2019 21:36
Ohakune	40.12	0.01	11.95	0.18	46.63	0.12	0.14	0.00	99.16	core	19/03/2019 21:49
Ohakune	40.94	0.01	12.44	0.17	47.03	0.12	0.12	0.00	100.85	mid	19/03/2019 22:03
Ohakune	39.77	0.01	14.05	0.19	45.02	0.12	0.11	0.00	99.26	rim	19/03/2019 22:09
Ohakune	40.14	0.01	12.34	0.17	47.88	0.12	0.14	0.00	100.81	0	02/08/2019 17:12
Ohakune	39.67	0.01	12.64	0.17	47.75	0.12	0.14	0.00	100.51	20.58	02/08/2019 17:18
Ohakune	39.60	0.01	12.21	0.18	47.59	0.12	0.15	0.02	99.88	41.16	02/08/2019 17:24
Ohakune	39.89	0.01	12.28	0.18	47.67	0.12	0.14	0.01	100.31	61.74	02/08/2019 17:30
Ohakune	39.46	0.04	12.20	0.18	47.22	0.19	0.14	0.00	99.44	82.32	02/08/2019 17:36
Ohakune	39.46	0.01	12.89	0.18	47.64	0.12	0.14	0.01	100.45	102.9	02/08/2019 17:42
Ohakune	39.84	0.01	12.83	0.17	47.46	0.12	0.13	0.01	100.57	123.48	02/08/2019 17:48
Ohakune	40.03	0.01	12.96	0.18	46.50	0.12	0.12	0.00	99.94	185.22	02/08/2019 17:54
Ohakune	39.13	0.01	13.85	0.20	46.88	0.12	0.13	0.01	100.33	205.8	02/08/2019 17:59
Ohakune	39.71	0.01	14.07	0.18	46.46	0.12	0.14	0.00	100.70	226.38	02/08/2019 18:05
Ohakune	39.92	0.01	13.66	0.18	46.68	0.12	0.14	0.00	100.71	246.96	02/08/2019 18:11
Ohakune	39.47	0.02	13.38	0.18	46.58	0.12	0.13	0.00	99.88	267.54	02/08/2019 18:17
Ohakune	39.16	0.01	12.80	0.17	47.29	0.12	0.12	0.01	99.67	288.12	02/08/2019 18:23
Ohakune	39.72	0.02	13.31	0.18	47.24	0.12	0.13	0.00	100.73	308.71	02/08/2019 18:29
Ohakune	39.75	0.02	12.65	0.18	47.41	0.12	0.14	0.00	100.27	329.29	02/08/2019 18:35
Ohakune	39.79	0.02	12.54	0.18	47.20	0.12	0.13	0.00	99.97	349.87	02/08/2019 18:41
Ohakune	40.09	0.06	12.44	0.17	47.38	0.12	0.12	0.00	100.39	370.45	02/08/2019 18:47
Ohakune	39.44	0.05	12.63	0.18	47.45	0.12	0.13	0.01	100.01	391.03	02/08/2019 18:53
Ohakune	39.89	0.02	12.18	0.18	47.12	0.12	0.12	0.00	99.63	411.61	02/08/2019 18:59
Ohakune	40.51	0.02	11.97	0.18	47.24	0.12	0.13	0.00	100.15	432.19	02/08/2019 19:05
Ohakune	39.55	0.02	12.83	0.19	47.23	0.12	0.14	0.00	100.08	452.77	02/08/2019 19:11
Ohakune	39.85	0.01	12.57	0.18	47.46	0.13	0.13	0.01	100.34	473.35	02/08/2019 19:17
Ohakune	39.90	0.02	12.25	0.17	47.45	0.12	0.14	0.01	100.05	493.93	02/08/2019 19:23
Ohakune	40.36	0.02	12.67	0.17	47.16	0.12	0.13	0.00	100.63	514.51	02/08/2019 19:28
Ohakune	40.51	0.01	12.69	0.17	46.82	0.13	0.12	0.00	100.46	535.09	02/08/2019 19:34
Ohakune	40.09	0.02	13.11	0.18	46.31	0.12	0.12	0.00	99.95	555.67	02/08/2019 19:40
Ohakune	39.42	0.03	14.20	0.21	45.29	0.12	0.13	0.01	99.39	576.25	02/08/2019 19:46
Ohakune	39.19	0.01	15.87	0.21	44.35	0.11	0.13	0.00	99.87	596.83	02/08/2019 19:52
Ohakune	53.60	2.90	11.42	0.23	29.94	1.24	0.04	0.00	99.53	617.41	02/08/2019 19:58

Ohakune	41.11	0.01	10.93	0.17	47.71	0.11	0.16	0.00	100.21	0	31/07/2018 17:16
Ohakune	40.52	0.01	11.20	0.16	48.08	0.11	0.18	0.01	100.28	92	31/07/2018 17:23
Ohakune	41.09	0.01	10.91	0.16	47.66	0.11	0.17	0.01	100.12	186	31/07/2018 17:29
Ohakune	40.71	0.01	11.14	0.16	47.95	0.11	0.17	0.00	100.26	538	31/07/2018 17:36
Ohakune	41.03	0.01	11.05	0.15	48.07	0.11	0.17	0.01	100.60	664	31/07/2018 17:42
Ohakune	41.17	0.01	10.84	0.16	47.67	0.11	0.18	0.00	100.13	751	31/07/2018 17:49
Ohakune	40.80	0.01	12.18	0.18	46.96	0.11	0.18	0.01	100.45	942	31/07/2018 17:55
Ohakune	40.78	0.01	11.21	0.16	48.09	0.11	0.19	0.01	100.56	1044	31/07/2018 18:02
Ohakune	41.04	0.01	11.09	0.15	48.34	0.11	0.18	0.00	100.92	1164	31/07/2018 18:08
Ohakune	40.78	0.01	11.54	0.16	48.00	0.11	0.17	0.01	100.79	1252	31/07/2018 18:14
Ohakune	40.79	0.01	10.67	0.16	47.78	0.11	0.18	0.00	99.71	2140	31/07/2018 18:21
Ohakune	40.46	0.01	11.50	0.16	48.23	0.11	0.18	0.00	100.66	2194	31/07/2018 18:27
Ohakune	40.70	0.03	10.90	0.15	48.42	0.11	0.19	0.00	100.49	2492	31/07/2018 18:34
Ohakune	40.40	0.02	12.31	0.16	47.65	0.11	0.18	0.01	100.84	2591	31/07/2018 18:40

A.3 Spinel EPMA analyses

Table A.5: **Spinel analyses**

Sample	SiO2	TiO2	Al2O3	Cr2O3	Fe2O3	FeO	MnO	MgO	total	Position	comment
Ongaroto											
Ongaroto	0.10	0.57	20.75	40.43	7.17	16.82	0.26	11.86	98.12	core	20/03/2019 10:20
Ongaroto	0.10	0.41	13.95	48.78	6.70	18.96	0.30	9.88	99.19	core	20/03/2019 10:36
Ongaroto	0.10	0.80	20.87	34.99	10.94	19.40	0.30	10.22	97.91	core	20/03/2019 11:16
Ongaroto	0.09	0.54	14.36	47.80	6.96	18.76	0.28	10.09	99.09	core	20/03/2019 11:31
Ongaroto	0.08	0.79	17.19	40.75	9.05	20.37	0.34	9.17	97.96	core	20/03/2019 11:46
Ongaroto	0.14	0.56	18.80	44.16	6.55	17.96	0.27	11.32	100.01	core	20/03/2019 12:55
Ongaroto	0.14	0.30	13.42	48.77	6.75	19.04	0.32	9.57	98.55	mid	20/03/2019 13:10
Ongaroto	0.08	8.73	7.42	18.82	24.36	33.64	0.43	3.87	97.46	rim	20/03/2019 13:33
Ongaroto	0.08	0.71	14.60	44.40	9.25	22.31	0.33	8.00	99.69	core	22/03/2019 12:21
Ongaroto	0.16	2.15	12.56	30.22	20.12	27.29	0.39	4.91	97.80	rim	22/03/2019 12:36
Ongaroto	0.12	3.42	8.76	25.96	23.78	29.74	0.41	3.04	95.23	rim	22/03/2019 13:22
Ongaroto	0.08	0.98	17.08	35.64	15.16	21.81	0.33	8.70	99.78	core	22/03/2019 13:37
Ongaroto	0.08	5.58	9.33	24.78	21.94	31.99	0.44	3.34	97.48	inner rim	22/03/2019 13:53
Ongaroto	0.09	22.64	1.87	0.04	52.82	17.87	0.40	1.23	96.96	outer rim	22/03/2019 14:08
Waimarino											
Waimarino	0.11	0.18	10.21	58.58	3.93	12.13	0.24	13.95	99.52	core	18/03/2019 17:05

Waimarino	0.11	0.20	10.11	58.20	3.91	11.69	0.22	14.08	98.72	core	18/03/2019 17:59
Waimarino	0.12	0.28	12.08	52.21	6.98	14.60	0.26	12.48	99.14	mid	18/03/2019 18:51
Waimarino	0.09	0.40	11.00	48.64	9.33	19.94	0.30	8.76	98.51	rim	18/03/2019 19:05
Waimarino	0.12	0.22	9.63	58.49	4.90	13.50	0.23	13.23	100.49	core/mid	18/03/2019 19:37
Waimarino	0.00	0.27	11.65	51.79	7.64	14.66	0.27	12.16	98.55	core	18/03/2019 20:01
Waimarino	0.12	0.23	10.28	54.44	6.65	14.79	0.27	12.12	99.02	core	18/03/2019 20:14
Waimarino	0.12	0.22	10.80	54.56	5.95	13.87	0.23	12.71	98.60	core	18/03/2019 21:47
Ohakune											
Ohakune	0.08	0.38	8.77	51.35	8.93	19.87	0.32	8.50	98.25	core	19/03/2019 12:18
Ohakune	0.09	0.43	9.02	51.96	8.94	16.22	0.27	10.90	97.91	core	19/03/2019 13:00
Ohakune	0.07	0.44	9.72	51.25	8.87	16.49	0.28	10.80	98.00	core	19/03/2019 13:17
Ohakune	0.11	0.57	9.18	50.42	9.89	17.98	0.30	9.96	98.47	core	19/03/2019 21:03
Ohakune	0.10	0.59	9.20	51.90	9.82	18.09	0.30	10.29	100.35	core	19/03/2019 21:16
Ohakune	0.14	0.56	9.17	50.35	10.07	18.04	0.30	9.98	98.67	core	19/03/2019 21:29
Ohakune	0.08	0.55	9.30	50.10	10.33	17.97	0.30	9.98	98.66	core	19/03/2019 21:42
Ohakune	0.12	0.48	9.34	48.41	11.31	17.58	0.29	10.00	97.59	mid	19/03/2019 21:56

A.4 Clinopyroxene EPMA analyses

Table A.6: **Clinopyroxene analyses**

	SiO_2	**TiO_2**	**Al_2O_3**	**FeO**	**MnO**	**MgO**	**CaO**	**Na_2O**	**Cr_2O_3**	**Total**	
Waimarino											
	50.74	0.25	3.12	5.06	0.13	16.55	21.28	0.17	0.90	98.22	85.36
	53.86	0.12	1.58	4.46	0.13	18.73	21.28	0.17	0.73	101.07	88.22
	53.18	0.17	2.05	5.46	0.16	18.37	20.88	0.14	0.59	101.02	85.71
	52.68	0.17	2.00	5.07	0.16	18.19	21.00	0.15	0.60	100.03	86.49
	53.17	0.16	1.67	5.04	0.15	18.28	21.23	0.13	0.51	100.35	86.60
	52.77	0.18	2.10	5.25	0.16	17.81	21.09	0.14	0.52	100.04	85.82
	52.11	0.17	1.75	4.86	0.14	17.69	21.00	0.14	0.55	98.42	86.66
	53.07	0.17	1.62	5.22	0.15	18.14	21.30	0.13	0.46	100.29	86.10
	53.37	0.17	1.71	5.01	0.15	18.08	21.56	0.14	0.47	100.68	86.55
	52.75	0.18	1.72	6.04	0.17	18.34	20.74	0.12	0.41	100.49	84.40
	53.01	0.19	1.75	5.42	0.15	18.20	21.29	0.13	0.40	100.54	85.70
	52.02	0.99	2.69	11.92	0.29	15.90	15.77	0.38	0.02	100.61	70.40
	51.45	0.69	2.47	10.20	0.27	16.73	18.04	0.48	0.03	100.68	74.51

53.50	0.18	1.51	8.08	0.25	20.00	16.53	0.10	0.15	100.31	81.52
52.16	0.25	3.06	5.41	0.09	16.61	21.54	0.00	0.00	99.12	84.54
52.43	0.30	1.54	11.71	0.32	16.82	16.66	0.00	0.00	99.79	71.89
52.74	0.15	2.39	4.92	0.07	17.02	21.68	0.00	0.00	98.97	86.03
52.45	0.37	2.11	10.33	0.32	16.18	18.41	0.00	0.00	100.17	73.61
52.61	0.30	1.52	12.30	0.32	16.90	16.39	0.00	0.00	100.32	70.99
52.48	0.36	2.11	9.86	0.15	16.08	18.81	0.00	0.00	99.86	74.39
53.64	0.15	1.30	5.50	0.13	15.88	23.88	0.00	0.00	100.48	83.72
51.31	0.30	3.94	6.51	0.13	15.93	21.16	0.00	0.00	99.29	81.33
53.81	0.14	1.49	5.30	0.18	17.59	21.21	0.00	0.00	99.72	85.53
52.09	0.22	3.03	5.35	0.14	16.55	21.28	0.00	0.00	98.66	84.64
52.30	0.32	2.28	9.80	0.31	16.47	18.19	0.00	0.00	99.66	74.95
51.64	0.36	3.17	6.18	0.15	16.45	21.08	0.00	0.00	99.03	82.58
53.35	0.16	1.52	5.83	0.22	18.19	20.40	0.00	0.00	99.66	84.75
53.66	0.18	1.00	9.96	0.31	19.46	14.76	0.00	0.00	99.32	77.68
52.72	0.31	2.47	10.38	0.23	18.98	14.77	0.00	0.00	99.86	76.50
50.80	0.45	3.96	7.62	0.21	16.62	18.98	0.00	0.00	98.66	79.53
51.13	0.34	3.73	6.10	0.24	15.63	21.91	0.00	0.00	99.09	82.02
54.21	0.14	1.06	9.56	0.36	22.69	11.39	0.00	0.00	99.41	80.87
52.36	0.24	2.86	6.34	0.25	17.26	20.32	0.00	0.00	99.63	82.90
53.20	0.26	1.19	10.57	0.30	17.45	16.62	0.00	0.00	99.60	74.62
52.25	0.26	2.82	6.45	0.16	15.09	21.85	0.25	0.31	99.45	80.64
54.14	0.11	1.27	4.14	0.12	16.79	22.03	0.19	0.80	99.60	87.83
53.68	0.13	1.33	4.13	0.14	16.92	21.90	0.20	0.73	99.17	87.95
52.07	0.27	2.37	6.19	0.14	15.45	21.69	0.19	0.32	98.71	81.64
52.19	0.25	2.28	6.11	0.16	15.47	21.65	0.20	0.30	98.62	81.84
51.99	0.25	2.40	6.31	0.16	15.62	21.55	0.21	0.31	98.83	81.51
52.26	0.24	2.63	6.24	0.16	15.51	21.34	0.24	0.30	98.93	81.57
52.49	0.25	2.52	6.18	0.17	15.65	21.53	0.20	0.28	99.28	81.86
51.66	0.24	2.76	6.30	0.14	15.63	20.74	0.22	0.29	98.00	81.56
53.02	0.23	2.46	6.30	0.16	15.93	21.57	0.23	0.28	100.20	81.83
52.34	0.22	2.49	6.24	0.17	15.94	21.18	0.23	0.31	99.16	81.98
52.43	0.24	2.43	6.11	0.15	15.83	21.42	0.21	0.31	99.14	82.19
49.88	0.61	4.08	8.21	0.19	14.69	20.73	0.20	0.08	98.68	76.11

	49.86	0.54	4.48	8.98	0.20	14.41	20.38	0.21	0.04	99.14	74.07
	52.39	0.16	2.21	4.48	0.13	16.41	21.94	0.19	0.96	98.88	86.72
	51.84	0.18	2.58	4.51	0.12	16.12	22.19	0.19	0.95	98.70	86.42
	51.92	0.23	2.77	4.93	0.11	15.75	22.12	0.19	0.77	98.81	85.05
	51.70	0.25	2.79	5.05	0.13	15.58	22.03	0.16	0.80	98.50	84.59
	51.96	0.21	2.93	5.09	0.13	15.88	22.05	0.19	0.80	99.27	84.76
	52.39	0.20	2.53	4.73	0.12	16.05	22.28	0.18	0.85	99.36	85.79
	52.46	0.29	3.41	5.84	0.15	15.24	21.78	0.17	0.50	99.86	82.30
	53.00	0.21	2.57	4.72	0.12	15.84	21.98	0.19	0.79	99.44	85.67
	52.09	0.24	2.78	5.10	0.12	15.53	22.27	0.17	0.77	99.10	84.42
	52.16	0.23	2.81	5.01	0.12	15.70	22.44	0.17	0.78	99.43	84.80
	52.14	0.20	2.54	4.90	0.12	15.98	22.45	0.18	0.86	99.39	85.31
	52.84	0.23	2.79	4.97	0.13	15.77	22.43	0.17	0.74	100.08	84.96
	52.57	0.23	2.78	5.05	0.13	15.67	22.35	0.18	0.71	99.70	84.66
	53.22	0.17	1.85	5.37	0.15	16.75	21.02	0.14	0.51	99.20	84.73
	52.98	0.17	1.65	5.35	0.17	16.96	21.07	0.13	0.50	99.00	84.95
	51.77	0.23	2.96	5.08	0.13	15.65	22.00	0.17	0.73	98.76	84.58
	52.34	0.23	2.98	5.14	0.12	15.59	22.11	0.17	0.81	99.51	84.37
	52.26	0.24	2.95	5.14	0.12	15.40	22.18	0.17	0.78	99.26	84.22
Ohakune											
	49.90	0.45	3.54	7.75	0.17	15.34	20.67	0.20	0.08	98.10	77.91
	50.48	0.39	3.17	7.37	0.18	15.64	20.65	0.20	0.09	98.19	79.09
	50.28	0.38	3.39	7.32	0.15	15.39	20.94	0.21	0.08	98.12	78.94
	50.42	0.35	3.31	7.07	0.15	15.60	21.13	0.21	0.10	98.37	79.72
	51.87	0.26	2.34	6.11	0.16	16.96	21.16	0.18	0.30	99.37	83.18
	51.47	0.23	2.36	6.25	0.15	16.70	20.82	0.23	0.25	98.49	82.66
	52.62	0.21	2.21	6.15	0.15	17.15	21.08	0.21	0.37	100.17	83.24
	51.93	0.23	2.51	6.12	0.15	16.64	20.65	0.21	0.25	98.71	82.90
	52.78	0.09	1.07	3.91	0.12	18.15	21.17	0.18	0.65	98.14	89.21
	52.23	0.18	2.04	5.50	0.14	16.81	20.86	0.21	0.42	98.42	84.50
	51.15	0.26	2.61	6.50	0.15	16.32	20.74	0.21	0.28	98.23	81.75
	50.73	0.24	2.45	6.30	0.17	16.70	20.72	0.22	0.25	97.82	82.53
	51.03	0.26	2.57	6.53	0.16	16.45	20.83	0.19	0.25	98.30	81.78
	51.25	0.23	2.61	6.43	0.18	16.54	20.75	0.22	0.31	98.54	82.10
	51.45	0.24	2.57	6.31	0.18	16.53	20.69	0.24	0.31	98.55	82.36
	51.20	0.24	2.46	6.25	0.15	16.48	20.85	0.21	0.27	98.13	82.46
	51.15	0.25	2.69	6.37	0.15	16.38	20.49	0.23	0.32	98.06	82.08
	52.19	0.25	2.80	6.64	0.18	16.74	20.99	0.23	0.24	100.29	81.80
	50.90	0.24	2.55	6.33	0.17	16.42	20.72	0.24	0.27	97.85	82.21
	51.55	0.21	2.36	6.05	0.15	16.59	20.91	0.21	0.36	98.40	83.01

51.48	0.33	3.03	7.00	0.18	16.67	21.02	0.18	0.24	100.16	80.92
50.89	0.28	2.82	6.76	0.17	16.16	20.61	0.23	0.24	98.18	80.99
51.00	0.28	2.81	6.67	0.16	16.31	20.76	0.22	0.27	98.50	81.33
52.10	0.27	2.68	6.63	0.18	16.92	21.13	0.21	0.30	100.45	81.97
50.89	0.26	2.73	6.42	0.16	16.40	20.58	0.23	0.32	97.99	81.98
51.19	0.23	2.54	6.15	0.15	16.72	20.51	0.23	0.41	98.14	82.88
52.15	0.25	2.57	6.33	0.17	17.00	21.24	0.21	0.33	100.26	82.72
51.99	0.26	2.80	6.78	0.15	16.87	20.89	0.23	0.32	100.30	81.61
52.36	0.26	2.63	6.37	0.15	16.98	21.22	0.22	0.30	100.51	82.60
52.20	0.25	2.52	6.54	0.17	17.10	21.14	0.22	0.31	100.47	82.33
53.86	0.64	5.21	10.19	0.21	12.32	15.83	0.49	0.02	99.04	68.30
53.15	0.20	1.82	6.36	0.18	17.65	20.88	0.18	0.22	100.65	83.18
53.05	0.19	1.22	5.34	0.16	17.71	21.09	0.15	0.09	99.02	85.53
52.49	0.21	2.38	6.54	0.17	17.10	20.81	0.22	0.27	100.21	82.34
50.75	0.46	3.62	8.54	0.22	16.46	19.62	0.19	0.18	100.05	77.46
50.71	0.51	3.53	9.11	0.19	16.82	18.99	0.18	0.09	100.16	76.71
51.15	0.43	3.14	9.50	0.22	15.60	19.16	0.21	0.06	99.49	74.55
53.32	0.16	1.46	6.08	0.17	17.51	20.73	0.17	0.18	99.79	83.71
53.72	0.15	1.47	6.07	0.17	17.84	20.94	0.17	0.22	100.76	83.98
53.13	0.15	1.44	6.06	0.17	17.63	20.80	0.17	0.20	99.76	83.83
53.60	0.16	1.45	6.15	0.18	17.65	21.19	0.17	0.17	100.73	83.64
52.07	0.16	1.41	5.96	0.17	17.41	20.46	0.17	0.17	97.99	83.90
53.18	0.16	1.46	6.28	0.18	17.79	20.84	0.16	0.18	100.24	83.48
53.12	0.16	1.51	5.89	0.18	17.51	20.58	0.16	0.16	99.30	84.12
52.60	0.16	1.61	6.15	0.17	17.38	20.33	0.18	0.16	98.77	83.42
53.65	0.14	1.38	6.38	0.19	18.05	20.30	0.16	0.23	100.50	83.45
53.16	0.18	1.56	6.65	0.17	17.45	20.60	0.15	0.11	100.05	82.39
53.36	0.21	1.48	7.31	0.19	17.48	20.15	0.13	0.09	100.41	80.99
53.85	0.17	1.49	6.48	0.19	17.74	20.57	0.15	0.16	100.81	82.99
52.24	0.16	1.57	6.27	0.19	17.33	20.29	0.17	0.14	98.38	83.13
53.09	0.17	1.67	6.28	0.18	17.65	20.80	0.19	0.19	100.22	83.35
53.34	0.14	1.51	5.79	0.17	17.82	20.80	0.18	0.26	100.03	84.57
53.80	0.12	1.18	5.49	0.17	18.16	20.46	0.17	0.33	99.89	85.50
53.76	0.12	1.20	5.28	0.16	18.36	20.65	0.17	0.35	100.09	86.11
53.35	0.21	1.89	6.70	0.18	17.12	20.61	0.18	0.12	100.38	82.00
53.06	0.19	1.68	6.51	0.20	17.37	20.61	0.16	0.11	99.90	82.62
53.26	0.18	1.57	6.60	0.19	17.59	20.55	0.17	0.13	100.25	82.61
53.29	0.15	1.42	6.09	0.18	17.84	20.49	0.19	0.24	99.90	83.93

	53.12	0.16	1.58	6.37	0.16	17.38	20.34	0.18	0.16	99.47	82.94
	52.28	0.16	1.50	6.19	0.18	17.31	20.34	0.18	0.19	98.36	83.30
	53.33	0.18	1.57	6.43	0.19	17.53	20.49	0.16	0.13	100.02	82.93
	53.19	0.17	1.68	6.41	0.17	17.35	20.92	0.19	0.17	100.26	82.84
	53.06	0.17	1.68	6.19	0.17	17.32	20.99	0.18	0.18	99.97	83.30
	53.11	0.16	1.62	5.68	0.16	17.46	20.96	0.19	0.23	99.58	84.56
	53.03	0.18	1.67	6.73	0.18	17.39	20.74	0.17	0.12	100.22	82.15
	52.44	0.18	1.69	6.39	0.17	17.18	20.78	0.18	0.15	99.19	82.72
	52.24	0.18	2.45	6.17	0.18	16.45	20.05	0.18	0.16	98.11	82.61
	52.65	0.20	1.60	6.54	0.19	17.36	20.35	0.14	0.16	99.20	82.56
	53.10	0.17	1.73	6.24	0.18	17.32	20.82	0.18	0.19	99.94	83.19
	53.20	0.17	1.57	6.29	0.17	17.35	21.00	0.18	0.19	100.14	83.10
	52.44	0.16	1.48	6.53	0.17	17.17	20.31	0.18	0.16	98.62	82.42
	53.90	0.16	1.60	6.36	0.17	17.40	20.69	0.18	0.19	100.67	82.99
	53.70	0.23	1.52	6.70	0.22	17.48	20.02	0.11	0.09	100.07	82.31
	52.54	0.23	2.25	6.55	0.19	16.67	21.08	0.00	0.00	99.51	81.92
	53.72	0.10	1.13	5.30	0.17	18.06	20.57	0.00	0.00	99.05	85.85
	53.23	0.16	1.56	6.34	0.17	16.99	20.66	0.00	0.00	99.11	82.68
	53.98	0.09	1.07	3.76	0.11	17.49	22.31	0.00	0.00	98.81	89.23
	52.92	0.15	1.63	7.02	0.23	16.17	20.46	0.00	0.00	98.57	80.40
	53.18	0.19	1.72	5.66	0.23	17.72	20.41	0.00	0.00	99.11	84.79
	53.95	0.06	1.03	3.88	0.14	18.44	21.30	0.00	0.00	98.79	89.43
	53.29	0.16	1.67	6.23	0.17	17.56	19.72	0.00	0.00	98.80	83.39
	53.23	0.15	1.23	5.26	0.17	16.54	21.77	0.00	0.00	98.34	84.85
	53.23	0.12	1.54	6.52	0.16	17.23	20.51	0.00	0.00	99.31	82.47
Ongaroto											
	53.61	0.34	0.70	20.53	0.49	22.11	3.34	0.06	0.00	101.21	
	51.04	0.96	2.16	11.73	0.36	15.43	14.84	0.29	0.00	96.85	
Orakeikorako											
	51.15	0.64	4.06	6.69	0.18	16.14	20.50	0.40	0.07	99.84	81.14
	52.05	0.51	2.44	6.54	0.19	17.09	20.46	0.26	0.11	99.65	82.32
	50.41	0.81	4.13	7.52	0.22	16.43	19.60	0.33	0.07	99.55	79.57
	51.53	1.15	2.87	15.90	0.49	11.72	15.40	1.20	0.00	100.47	56.77
	49.39	1.08	4.57	8.50	0.22	14.25	20.90	0.43	0.01	99.38	74.92
	49.52	0.90	5.02	7.68	0.19	15.04	20.35	0.41	0.05	99.16	77.73
	49.88	1.16	3.64	9.42	0.26	14.73	19.75	0.43	0.03	99.32	73.59

	51.80	0.51	2.91	6.84	0.20	16.60	20.43	0.37	0.03	99.70	81.24
	50.31	1.03	2.67	10.75	0.30	15.26	18.45	0.41	0.01	99.20	71.67
	51.84	0.56	2.38	6.77	0.19	17.04	20.48	0.26	0.09	99.62	81.78
	50.27	1.04	2.31	11.75	0.33	14.65	18.56	0.46	0.02	99.40	68.97
	50.95	0.63	3.40	6.87	0.18	15.94	20.71	0.37	0.02	99.07	80.52
	51.70	0.76	1.79	9.68	0.29	16.30	18.69	0.26	0.02	99.53	75.01
	51.12	0.89	2.06	11.35	0.34	15.81	17.59	0.29	0.01	99.44	71.29
	51.37	0.82	1.93	11.30	0.35	16.16	17.12	0.34	0.01	99.41	71.83
Rotokawau											
	51.89	0.38	3.30	6.12	0.15	15.96	22.30	0.20	0.07	100.37	82.29
	52.07	0.38	3.34	5.98	0.13	15.74	23.03	0.20	0.18	101.06	82.42
	52.29	0.39	3.56	5.75	0.12	15.97	22.58	0.19	0.19	101.06	83.19
	51.48	0.39	3.56	6.00	0.13	15.95	22.87	0.20	0.20	100.79	82.57
	51.52	0.38	3.39	5.87	0.14	16.02	22.47	0.20	0.16	100.16	82.94
	51.79	0.36	3.29	5.57	0.12	16.00	22.79	0.19	0.29	100.41	83.66
	53.24	0.36	2.41	6.53	0.18	16.50	21.73	0.15	0.13	101.23	81.83
	52.29	0.40	2.27	7.53	0.19	16.46	21.23	0.14	0.06	100.57	79.57
	51.53	0.34	2.42	6.31	0.16	16.68	22.09	0.19	0.06	99.78	82.50
	51.02	0.34	2.62	6.31	0.17	16.47	22.18	0.20	0.06	99.37	82.31
	51.56	0.35	2.63	6.42	0.18	16.50	21.77	0.19	0.05	99.66	82.08
	51.23	0.34	2.50	6.42	0.16	16.28	21.78	0.19	0.05	98.96	81.87
	51.44	0.37	2.78	6.67	0.17	16.24	22.26	0.20	0.06	100.21	81.27
	51.27	0.44	3.34	6.59	0.15	15.92	22.32	0.21	0.07	100.32	81.14
	50.73	0.44	3.50	6.22	0.14	15.83	22.36	0.20	0.12	99.54	81.95
	50.61	0.44	3.50	6.00	0.12	15.95	22.65	0.20	0.20	99.68	82.58
	48.28	0.96	5.18	8.69	0.21	14.62	20.82	0.24	0.07	99.08	75.00
	51.86	0.34	2.40	6.21	0.17	16.33	21.53	0.19	0.09	99.11	82.41
	52.60	0.34	2.46	6.53	0.18	16.65	22.08	0.20	0.06	101.10	81.96
	51.75	0.36	2.47	6.33	0.17	16.35	21.57	0.20	0.05	99.26	82.14
	52.64	0.39	2.67	6.62	0.16	16.45	21.87	0.20	0.06	101.07	81.58
	50.95	0.45	3.36	6.34	0.15	15.99	22.16	0.20	0.14	99.77	81.81
	51.89	0.44	3.47	6.13	0.15	16.05	22.47	0.20	0.14	100.94	82.35
	51.02	0.72	2.96	10.13	0.28	15.47	19.49	0.22	0.02	100.30	73.14
	52.75	0.31	2.36	6.74	0.17	16.79	20.75	0.00	0.00	99.87	81.60
	50.47	0.67	4.72	7.53	0.24	14.68	21.90	0.00	0.00	100.22	77.64

	53.23	0.33	2.25	7.77	0.28	16.45	20.19	0.00	0.00	100.50	79.04
	52.52	0.29	3.13	5.22	0.12	15.98	23.00	0.00	0.00	100.25	84.50
	50.67	0.51	4.14	8.71	0.24	15.52	20.44	0.00	0.00	100.24	76.04
	53.16	0.28	1.92	7.71	0.27	17.27	19.42	0.00	0.00	100.03	79.96
	52.99	0.32	2.28	8.59	0.27	17.10	19.03	0.00	0.00	100.57	78.00
	52.92	0.34	2.16	8.32	0.18	16.85	19.24	0.00	0.00	100.02	78.29
	50.32	0.54	4.96	6.03	0.12	15.31	22.03	0.00	0.00	99.31	81.89
	52.95	0.33	1.95	8.09	0.27	16.99	19.67	0.00	0.00	100.24	78.90
	52.94	0.29	2.76	5.46	0.18	16.42	22.29	0.00	0.00	100.35	84.27
	51.38	0.43	4.22	5.57	0.11	15.44	22.74	0.00	0.00	99.89	83.15
	51.36	0.51	4.83	6.64	0.09	14.75	22.48	0.00	0.00	100.64	79.82
Kakuki											
	50.92	1.14	3.41	7.79	0.21	17.35	18.23	0.33	0.02	99.41	79.89
	49.11	1.23	4.49	9.25	0.24	14.67	20.21	0.30	0.14	99.64	73.88
Tarawera											
	49.41	0.66	6.18	6.66	0.15	15.05	21.22	0.17	0.21	99.73	80.10
	48.30	1.03	7.34	7.40	0.17	14.53	20.88	0.18	0.24	100.08	77.77
	49.13	0.89	5.85	7.21	0.17	15.39	20.63	0.18	0.17	99.62	79.17
	48.81	0.92	5.81	7.83	0.16	15.24	20.48	0.19	0.20	99.65	77.62
	48.54	0.72	5.70	7.73	0.15	15.46	20.04	0.59	0.12	99.08	78.09
HJR											
	51.59	0.53	2.46	6.42	0.17	16.33	21.65	0.25	0.23	99.66	81.93
	51.76	0.47	2.62	7.30	0.18	16.74	20.45	0.26	0.16	99.97	80.34
	46.92	1.58	7.28	8.18	0.18	13.58	21.01	0.27	0.13	99.13	74.74
	47.75	1.32	5.76	8.73	0.18	14.30	21.01	0.27	0.19	99.52	74.49
	51.32	0.74	3.22	8.68	0.27	14.87	21.07	0.32	0.00	100.50	75.32
	50.80	0.82	3.40	8.92	0.31	14.41	20.92	0.34	0.00	99.92	74.22
	50.68	0.77	3.10	8.86	0.31	14.72	20.72	0.32	0.00	99.48	74.75
	50.37	1.15	3.30	7.76	0.17	16.15	20.47	0.27	0.12	99.77	78.77
	46.04	2.02	7.19	9.20	0.16	12.27	21.35	0.31	0.05	98.62	70.39
	51.45	0.59	2.34	7.58	0.20	16.26	20.82	0.19	0.11	99.54	79.26
Terrace Rd											
	49.97	0.73	5.37	8.63	0.25	15.41	19.65	0.18	0.08	100.27	76.08
	51.67	0.62	2.82	7.59	0.19	16.31	21.09	0.19	0.08	100.56	79.29
	50.98	0.77	3.70	10.06	0.24	14.53	20.24	0.21	0.03	100.76	72.03
	50.05	0.89	3.61	10.98	0.27	14.00	20.28	0.22	0.01	100.31	69.45
	50.35	0.92	3.96	9.94	0.24	14.63	19.89	0.21	0.03	100.16	72.41

	50.63	0.78	2.79	11.89	0.31	13.43	20.18	0.27	0.00	100.29	66.81
	50.80	0.78	2.69	11.93	0.32	13.33	20.08	0.27	0.00	100.19	66.57
	51.21	0.51	2.67	10.87	0.29	13.83	20.37	0.23	0.01	100.00	69.41
	50.90	0.62	2.81	12.19	0.32	13.13	19.89	0.26	0.00	100.13	65.74
	51.56	0.50	2.34	10.10	0.26	14.55	20.99	0.22	0.01	100.52	71.98
	51.49	0.53	4.03	6.88	0.15	15.58	21.79	0.20	0.11	100.76	80.15
	51.79	0.45	2.98	7.29	0.20	16.03	21.14	0.23	0.06	100.19	79.68
	52.28	0.47	3.06	7.11	0.19	15.98	21.27	0.23	0.11	100.72	80.02
	51.93	0.45	3.47	6.29	0.15	15.65	21.69	0.21	0.15	99.99	81.59
	49.97	0.85	3.95	9.36	0.21	14.40	20.92	0.21	0.03	99.90	73.29
	48.49	1.13	6.10	8.72	0.21	13.80	19.85	0.24	0.02	98.57	73.82
	50.92	0.99	3.57	13.21	0.36	15.18	15.86	0.20	0.01	100.32	67.20
	50.88	0.61	4.02	8.36	0.23	16.34	19.24	0.20	0.08	99.97	77.70
RMR											
	52.40	0.49	2.15	19.78	0.48	23.67	2.09	0.02	0.00	101.08	68.08
	51.16	0.67	2.93	9.12	0.29	15.16	20.33	0.26	0.00	99.94	74.77
	50.97	0.71	2.86	9.24	0.29	15.07	20.07	0.26	0.00	99.47	74.40
	50.44	0.72	2.81	9.15	0.28	15.04	20.14	0.26	0.00	98.83	74.55
	51.23	0.50	3.03	7.07	0.20	16.22	20.73	0.22	0.20	99.40	80.35
	50.64	0.55	2.98	8.20	0.22	15.72	20.16	0.25	0.15	98.88	77.36
	51.20	0.56	2.74	8.84	0.23	16.10	20.44	0.27	0.10	100.48	76.45
	50.75	0.56	2.66	8.74	0.26	15.90	19.65	0.27	0.10	98.88	76.42
	50.58	0.59	1.85	9.85	0.30	15.26	19.37	0.25	0.01	98.11	73.42
	50.15	0.36	3.94	4.67	0.12	16.39	21.93	0.20	0.76	98.53	86.21
	51.33	0.30	3.21	4.67	0.12	16.72	22.13	0.20	0.71	99.41	86.45
	51.34	0.30	3.27	4.52	0.13	16.78	21.66	0.19	0.72	98.91	86.86
	51.21	0.33	3.75	4.78	0.12	16.61	21.91	0.19	0.70	99.61	86.10
	50.82	0.35	3.78	4.75	0.13	16.51	21.95	0.19	0.72	99.20	86.11
	50.19	0.34	3.73	4.74	0.12	16.30	21.98	0.20	0.70	98.32	85.98
	50.89	0.35	3.91	4.84	0.13	16.33	21.97	0.19	0.72	99.33	85.74
	50.90	0.35	3.89	4.97	0.13	16.11	21.67	0.21	0.75	98.98	85.24
	49.56	0.74	3.66	8.63	0.24	15.00	20.11	0.27	0.17	98.40	75.59
	50.69	0.66	1.96	11.06	0.34	14.48	18.86	0.26	0.01	98.32	70.00
	52.66	0.44	2.83	7.19	0.19	16.51	20.57	0.22	0.00	100.59	80.37
	52.62	0.45	2.81	6.56	0.19	16.66	20.72	0.22	0.00	100.23	81.90
	51.64	0.44	2.78	6.80	0.20	16.19	20.56	0.22	0.00	98.84	80.94
	52.81	0.46	2.72	6.79	0.19	16.41	20.50	0.22	0.00	100.09	81.16
	52.25	0.45	2.84	6.45	0.19	16.42	20.80	0.22	0.00	99.62	81.95

52.38	0.45	2.79	6.42	0.18	16.61	20.81	0.21	0.00	99.84	82.17
52.72	0.44	2.78	6.37	0.19	16.49	20.75	0.22	0.00	99.97	82.19
52.13	0.44	2.66	7.02	0.21	16.49	20.27	0.22	0.00	99.44	80.71
52.27	0.53	2.95	7.65	0.21	15.99	20.26	0.23	0.00	100.09	78.83
51.89	0.61	2.78	9.89	0.27	15.12	19.36	0.28	0.00	100.21	73.15
52.10	0.69	2.45	10.18	0.28	14.93	19.25	0.26	0.00	100.15	72.33

A.5 Orthopyroxene EPMA analyses

Table A.7: **Orthopyroxene analyses**

	SiO_2	**TiO_2**	**Al_2O_3**	**FeO**	**MnO**	**MgO**	**CaO**	**Total**	**Mg#**
Waimarino									
	55.12	0.13	1.06	13.18	0.31	27.52	2.39	99.73	78.81
	54.56	0.21	1.31	14.86	0.34	24.67	4.08	100.03	74.72
	53.59	0.25	1.77	13.69	0.43	22.27	6.89	98.88	74.34
	50.74	0.22	1.72	14.81	0.32	26.16	5.59	99.58	75.88
	54.45	0.16	0.85	15.51	0.36	23.81	4.64	99.76	73.22
	53.11	0.21	1.54	15.86	0.29	21.89	6.85	99.74	71.08

	55.33	0.11	0.64	13.96	0.41	24.60	4.90	99.95	75.83
Ohakune									
	54.85	0.10	1.02	14.92	0.30	27.76	1.35	100.32	76.84
	54.79	0.10	1.05	14.65	0.29	27.64	1.36	99.92	77.08
	53.89	0.11	0.94	14.71	0.29	27.20	1.36	98.54	76.72
	53.38	0.18	2.83	15.45	0.30	26.84	1.40	100.43	75.58
	55.86	0.10	1.37	11.54	0.25	30.04	1.34	100.56	82.27
	55.69	0.11	1.49	11.64	0.24	29.88	1.45	100.55	82.06
	56.54	0.10	1.20	11.07	0.23	29.80	1.45	100.43	82.75
	56.46	0.08	0.79	11.25	0.25	30.12	1.49	100.47	82.68
	56.52	0.08	0.80	12.26	0.26	29.84	1.43	101.23	81.27
	56.00	0.09	0.83	11.86	0.26	29.29	1.60	99.97	81.49
	56.78	0.08	0.98	11.91	0.25	29.82	1.39	101.26	81.70
	56.82	0.07	0.77	10.60	0.23	30.59	1.52	100.65	83.72
	56.37	0.09	0.94	11.92	0.26	29.66	1.39	100.66	81.60
	55.98	0.09	0.98	12.46	0.28	29.34	1.41	100.60	80.75
	55.93	0.08	0.94	12.11	0.25	29.47	1.46	100.29	81.26
	56.09	0.08	0.94	11.86	0.25	29.45	1.46	100.16	81.57
	56.43	0.10	1.07	12.00	0.26	29.50	1.51	100.89	81.42
	56.12	0.12	0.90	14.52	0.31	26.90	1.57	100.46	76.75
	53.69	0.15	2.80	12.57	0.25	27.99	1.60	99.10	79.88
	54.37	0.14	1.96	12.46	0.25	28.51	1.50	99.24	80.31
	55.35	0.08	0.87	12.34	0.27	29.18	1.46	99.61	80.83
	54.27	0.13	1.84	11.95	0.26	28.85	1.41	98.74	81.15
	54.11	0.24	2.37	15.51	0.31	25.99	2.07	100.75	74.92
	56.62	0.08	1.27	9.43	0.22	31.34	1.41	100.42	85.56
	56.69	0.07	1.18	9.42	0.21	31.34	1.39	100.34	85.57
	56.85	0.07	1.10	9.54	0.21	31.52	1.41	100.74	85.48
	57.34	0.07	1.21	9.47	0.21	31.58	1.44	101.36	85.60
	56.44	0.08	1.15	9.26	0.21	31.43	1.49	100.09	85.82
	56.80	0.08	1.31	9.43	0.23	31.21	1.48	100.59	85.50
	56.15	0.09	1.30	9.64	0.22	31.07	1.45	99.97	85.18
	56.22	0.08	1.32	9.79	0.23	31.14	1.46	100.27	85.01
	56.18	0.08	1.37	10.00	0.23	30.85	1.45	100.22	84.62
	56.00	0.09	1.56	10.71	0.23	30.12	1.42	100.19	83.38
	55.99	0.09	1.66	11.61	0.24	29.75	1.34	100.71	82.04
	56.02	0.10	1.48	11.45	0.23	29.76	1.30	100.38	82.25
	55.60	0.10	1.72	11.27	0.23	29.76	1.42	100.16	82.47
	55.49	0.11	1.76	12.21	0.24	29.23	1.36	100.45	81.02

55.53	0.14	2.24	12.52	0.27	28.69	1.50	100.93	80.33
54.88	0.13	1.90	12.75	0.25	28.81	1.45	100.22	80.11
55.22	0.11	1.83	13.05	0.25	28.79	1.40	100.71	79.72
55.15	0.14	2.02	13.02	0.26	28.63	1.38	100.64	79.68
54.78	0.14	2.27	13.42	0.27	28.46	1.52	100.91	79.09
55.49	0.13	1.92	13.04	0.26	28.86	1.44	101.17	79.78
54.73	0.14	2.22	13.05	0.26	28.66	1.44	100.55	79.64
55.02	0.12	1.89	12.82	0.27	28.84	1.38	100.37	80.03
55.22	0.13	1.91	12.72	0.26	28.87	1.44	100.60	80.18
55.55	0.12	1.84	12.61	0.26	28.91	1.40	100.73	80.34
55.23	0.11	1.93	12.63	0.24	28.81	1.43	100.43	80.27
55.15	0.11	1.78	12.49	0.26	28.99	1.44	100.25	80.53
55.44	0.09	1.24	11.82	0.26	29.03	1.46	99.38	81.41
56.73	0.08	0.88	12.18	0.25	29.61	1.49	101.29	81.25
55.56	0.09	1.19	11.84	0.26	29.86	1.48	100.32	81.81
55.87	0.09	1.14	12.17	0.25	29.64	1.50	100.70	81.28
53.88	0.18	1.19	17.26	0.38	25.51	1.86	100.33	72.48
55.07	0.11	2.05	11.94	0.25	27.70	1.45	98.66	80.52
53.81	0.17	1.22	15.81	0.35	25.88	1.66	98.95	74.48
53.79	0.14	0.80	16.02	0.35	26.20	1.67	99.01	74.46
55.19	0.12	1.41	11.28	0.27	29.81	1.44	99.55	82.48
54.88	0.11	1.44	11.59	0.24	29.57	1.35	99.22	81.98
54.37	0.13	1.60	11.93	0.25	29.07	1.47	98.84	81.29
54.70	0.12	1.49	11.97	0.25	29.16	1.32	99.04	81.28
55.78	0.12	1.54	12.20	0.25	29.31	1.37	100.60	81.07
54.69	0.12	1.58	11.74	0.24	29.00	1.35	98.78	81.49
55.14	0.11	1.59	11.62	0.26	29.41	1.38	99.56	81.85
55.02	0.11	1.53	11.80	0.25	29.31	1.31	99.38	81.58
55.19	0.12	1.61	12.00	0.24	29.23	1.35	99.77	81.27
54.89	0.12	1.69	11.92	0.26	29.06	1.33	99.32	81.29
54.71	0.11	1.66	12.26	0.25	29.14	1.39	99.57	80.91
55.15	0.10	1.57	11.84	0.26	29.16	1.35	99.47	81.45
55.13	0.13	1.84	13.06	0.26	28.60	1.41	100.47	79.61
54.77	0.12	1.71	12.17	0.26	29.12	1.36	99.55	81.01
54.84	0.11	1.78	12.00	0.24	29.01	1.37	99.39	81.17
55.10	0.10	1.56	10.92	0.23	29.95	1.44	99.34	83.02
54.81	0.09	1.53	10.28	0.23	29.87	1.43	98.29	83.82
55.51	0.09	1.53	10.04	0.24	30.22	1.48	99.16	84.30
55.54	0.09	1.52	10.62	0.24	30.15	1.43	99.64	83.51
55.11	0.10	1.53	11.11	0.25	30.00	1.36	99.50	82.79

	55.69	0.12	1.85	12.85	0.24	29.42	1.32	101.54	80.32
	54.56	0.11	1.78	11.95	0.24	28.92	1.34	98.96	81.18
	54.60	0.11	1.74	12.31	0.25	28.91	1.33	99.32	80.72
	54.53	0.11	1.71	11.96	0.25	28.99	1.33	98.91	81.20
	54.47	0.11	1.87	12.57	0.24	28.93	1.33	99.56	80.40
	55.63	0.12	1.83	12.68	0.25	29.31	1.32	101.18	80.47
	54.02	0.13	1.93	12.21	0.25	28.43	1.32	98.32	80.59
	54.55	0.13	1.96	12.62	0.26	28.46	1.33	99.34	80.07
	54.19	0.12	2.01	12.73	0.25	28.39	1.35	99.08	79.90
	55.45	0.12	2.04	12.21	0.25	29.05	1.37	100.54	80.91
	54.29	0.12	1.80	11.87	0.26	27.95	1.33	97.68	80.76
	54.67	0.12	1.77	12.12	0.26	28.84	1.35	99.16	80.92
	55.52	0.12	1.88	12.00	0.25	29.03	1.44	100.28	81.18
	55.49	0.12	1.93	12.33	0.25	29.20	1.40	100.75	80.85
	54.15	0.18	2.47	14.68	0.30	26.54	1.57	99.91	76.32
	54.63	0.10	1.59	11.75	0.31	29.57	1.36	99.32	81.76
	54.27	0.15	2.11	12.82	0.32	28.34	1.38	99.38	79.74
	54.53	0.12	2.16	12.15	0.26	29.52	1.57	100.30	81.23
	53.94	0.12	1.60	11.79	0.27	30.22	1.54	99.49	82.03
	54.35	0.10	1.89	11.90	0.34	29.37	1.45	99.42	81.46
	53.86	0.12	2.00	13.07	0.24	28.57	1.39	99.25	79.56
	55.13	0.08	1.47	9.86	0.23	30.61	1.61	99.00	84.68
	55.14	0.10	1.95	12.12	0.28	28.38	1.39	99.35	80.66
	54.56	0.14	1.78	13.26	0.27	28.17	1.37	99.56	79.09
	54.50	0.11	1.67	12.73	0.33	28.83	1.46	99.62	80.13
	55.04	0.10	2.02	12.43	0.28	28.87	1.38	100.12	80.53
	55.00	0.13	1.96	12.31	0.25	28.92	1.38	99.95	80.71
	55.36	0.09	1.58	11.42	0.23	29.64	1.47	99.80	82.21
	53.44	0.22	3.12	14.59	0.33	26.45	1.96	100.12	76.35
	53.29	0.18	2.65	15.77	0.35	26.53	1.42	100.19	74.97
	54.48	0.19	2.29	16.69	0.34	24.98	1.77	100.75	72.72
Ongaroto									
	53.19	0.37	0.63	19.08	0.51	22.39	3.19	99.48	67.65
	53.06	0.39	0.59	18.20	0.50	23.36	3.44	99.65	69.58
Terrace Rd									
	53.04	0.26	2.42	15.05	0.33	26.42	1.59	99.13	75.79

	53.53	0.25	2.03	15.09	0.33	26.75	1.57	99.57	75.96
	53.07	0.25	2.11	14.77	0.32	26.26	1.61	98.41	76.01
Rotomakariri									
	52.75	0.30	2.68	14.43	0.34	26.77	1.61	98.92	
	54.09	0.20	1.71	15.93	0.34	27.16	1.54	101.01	75.23
	53.55	0.25	2.52	15.12	0.32	27.29	1.63	100.71	76.29
	53.37	0.25	2.62	15.92	0.34	26.83	1.65	101.01	75.03
	53.58	0.33	1.31	18.17	0.46	25.44	1.72	101.03	71.39
	52.62	0.32	1.33	20.13	0.53	23.21	1.87	100.04	67.27
	52.68	0.42	1.42	19.98	0.51	23.15	2.27	100.46	67.38
	54.38	0.24	1.27	16.83	0.44	25.92	1.64	100.72	73.29
	53.87	0.27	1.48	17.30	0.45	25.81	1.59	100.80	72.67
	53.06	0.33	1.81	19.81	0.51	24.42	1.68	101.64	68.72
	52.30	0.31	1.30	19.26	0.54	23.53	1.61	98.87	68.53
	53.14	0.36	1.02	20.72	0.53	22.92	1.89	100.58	66.35
	51.73	0.42	1.16	21.85	0.58	21.02	1.95	98.75	63.16
	53.60	0.33	2.72	15.26	0.34	26.85	1.93	101.07	75.83
	51.54	0.43	2.81	6.68	0.19	16.45	20.54	98.86	81.44
	52.59	0.32	3.01	15.77	0.34	26.28	1.76	100.10	74.82
	52.95	0.29	2.36	17.62	0.42	24.83	1.55	100.05	71.53
	53.15	0.29	1.34	18.40	0.44	25.06	1.67	100.40	70.82
	52.84	0.23	1.74	14.17	0.31	28.83	0.78	98.96	78.39
	53.10	0.30	2.40	16.51	0.39	26.17	1.63	100.53	73.86
	52.82	0.29	2.13	17.34	0.41	25.36	1.62	100.00	72.27
	52.59	0.43	1.26	20.67	0.50	23.36	2.06	100.91	66.83

A.6 Plagioclase EPMA analyses

Table A.8: **Plagioclase analyses**

	SiO2	**Al2O3**	**FeO**	**MgO**	**CaO**	**Na2O**	**K2O**	**Total**	**Spacing (um)**	**An#**
Waimarino										
	51.31	29.38	0.75	0.35	14.29	3.30	0.13	99.51	gm	82.35
	49.50	30.63	1.14	0.19	14.87	3.12	0.13	99.59	gm	83.68
	50.44	30.37	0.99	0.22	14.72	2.90	0.14	99.78	gm	84.47

	49.72	31.05	1.07	0.16	15.26	2.67	0.11	100.05	gm	86.01
	51.80	29.75	1.25	0.11	13.88	3.33	0.17	100.31	gm	81.68
	49.26	31.19	1.02	0.26	15.53	2.53	0.10	99.88	gm	86.86
	50.03	30.50	0.90	0.23	15.23	2.87	0.11	99.88	gm	85.12
	49.45	31.42	0.91	0.17	15.53	2.65	0.09	100.21	gm	86.37
	49.15	31.38	0.79	0.23	16.15	2.36	0.08	100.15	gm	88.09
	49.91	30.73	0.94	0.33	15.63	2.64	0.06	100.25	gm	86.57
	51.60	29.81	1.06	0.20	14.23	3.31	0.16	100.37	gm	82.16
	47.45	32.26	0.79	0.20	16.89	2.03	0.07	99.67	gm	89.99
	49.28	31.39	0.91	0.19	15.88	2.48	0.10	100.24	gm	87.33
	47.32	32.38	0.70	0.21	17.14	1.89	0.04	99.69	gm	90.81
	50.76	30.66	1.05	0.23	14.82	3.09	0.12	100.72	gm	83.79
	50.28	29.09	1.10	0.14	14.30	3.10	0.23	98.23	gm	82.94
	49.15	30.79	0.92	0.24	15.61	2.60	0.07	99.38	gm	86.70
Ohakune										
	50.48	30.96	1.02	0.17	14.57	3.20	0.08	100.63	gm	83.19
	50.01	30.79	0.92	0.20	14.91	2.94	0.07	99.99	gm	84.65
Ongaroto										
	50.78	29.05	1.20	0.12	12.93	4.11	0.22	98.59	gm	77.07
Orakeikorako										
	54.33	28.48	0.55	0.09	11.61	4.94	0.13	100.27	0.00	71.85
	54.56	28.36	0.54	0.07	11.28	5.36	0.15	100.46	11.88	69.57
	56.54	26.92	0.54	0.07	9.86	6.23	0.18	100.48	23.76	63.20
	54.98	28.15	0.51	0.07	11.03	5.33	0.15	100.36	35.65	69.21
	53.80	29.38	0.53	0.11	12.25	4.80	0.10	101.12	47.53	73.55
	50.26	30.92	0.53	0.15	14.65	3.48	0.06	100.16	59.41	82.14
	50.41	30.94	0.56	0.14	14.53	3.56	0.06	100.33	71.30	81.70
	50.53	30.73	0.62	0.14	14.71	3.48	0.06	100.39	83.18	82.22
	50.88	30.96	0.70	0.14	14.49	3.54	0.06	100.92	95.06	81.71
	53.33	29.21	0.82	0.13	12.45	4.47	0.14	100.71	106.94	75.10
	55.23	28.27	0.49	0.06	11.29	5.34	0.15	100.98	core	69.66
	51.11	30.23	0.81	0.17	13.51	3.88	0.09	99.97	gm	79.12
	55.08	26.48	1.08	0.09	10.05	5.94	0.25	99.21	gm	64.57
	50.71	30.08	0.85	0.15	13.83	3.86	0.08	99.73	gm	79.64
	55.38	27.08	1.52	0.10	10.48	5.88	0.37	101.06	gm	65.44
	55.93	28.07	0.36	0.04	10.36	5.94	0.17	101.00	0.00	65.44
	56.47	27.65	0.38	0.04	9.91	6.15	0.17	100.90	16.68	63.66
	56.31	27.55	0.36	0.04	9.83	5.97	0.18	100.37	33.36	64.07

	54.92	28.37	0.36	0.07	10.87	5.46	0.17	100.36	50.04	68.31
	48.92	29.75	0.52	0.14	13.95	3.46	0.07	96.93	66.72	81.49
	47.06	28.63	0.51	0.14	13.72	3.20	0.06	93.44	83.40	82.39
	50.39	30.90	0.57	0.14	14.42	3.60	0.06	100.21	100.08	81.41
	51.06	30.98	0.62	0.14	14.41	3.59	0.06	101.00	116.76	81.44
	51.13	30.42	0.70	0.13	14.19	3.68	0.06	100.48	133.44	80.81
	50.85	30.22	0.70	0.13	14.07	3.63	0.06	99.82	150.12	80.89
	52.15	29.32	0.78	0.14	13.08	4.34	0.09	100.04	166.80	76.67
	56.65	26.17	0.98	0.11	9.58	6.26	0.22	100.15	183.48	62.31
	55.61	27.72	1.07	0.14	10.96	5.44	0.20	101.31	gm	68.49
Rotokawau										
	44.53	34.37	0.53	0.10	18.67	1.20	0.01	99.50	0.00	94.47
	44.92	34.66	0.54	0.10	18.76	1.14	0.02	100.24	29.79	94.72
	44.51	34.60	0.54	0.10	18.52	1.13	0.02	99.52	59.57	94.73
	44.98	34.38	0.56	0.11	18.55	1.06	0.02	99.77	89.35	95.03
	37.57	28.17	0.55	0.12	13.26	0.77	0.06	80.57	119.14	94.74
	45.35	34.77	0.55	0.11	18.66	1.10	0.02	100.66	148.92	94.86
	44.39	34.54	0.53	0.11	18.74	1.08	0.02	99.52	178.71	94.97
	44.60	34.86	0.50	0.09	19.17	0.83	0.01	100.14	208.49	96.21
	44.43	34.59	0.49	0.09	19.23	0.85	0.01	99.79	238.27	96.11
	44.62	34.91	0.48	0.10	19.04	0.94	0.01	100.20	268.06	95.68
	44.11	34.91	0.50	0.09	19.11	0.80	0.01	99.60	297.84	96.33
	44.81	34.76	0.52	0.09	18.98	0.87	0.01	100.12	327.63	96.00
	44.83	34.91	0.59	0.09	18.97	0.83	0.01	100.32	357.41	96.16
	48.20	31.90	0.93	0.19	16.08	2.43	0.06	99.92	387.20	87.81
	45.77	33.71	0.59	0.10	17.96	1.46	0.03	99.72	0.00	93.07
	46.72	34.20	0.59	0.10	18.52	1.36	0.03	101.59	17.75	93.71
	45.36	34.41	0.58	0.11	18.31	1.28	0.02	100.18	35.50	93.98
	45.61	33.84	0.61	0.11	18.44	1.32	0.02	100.04	53.25	93.87
	51.11	30.25	1.02	0.25	14.46	3.35	0.11	100.71	71.00	82.34
	50.04	31.49	0.95	0.18	15.38	3.03	0.08	101.27	gm	84.65
	49.97	31.26	0.93	0.19	15.48	2.94	0.08	101.00	gm	85.10
	49.34	31.18	0.95	0.19	15.50	2.85	0.08	100.23	gm	85.51
	49.05	30.87	0.95	0.22	15.41	2.85	0.08	99.58	gm	85.43
	50.70	30.50	1.03	0.22	14.86	3.24	0.09	100.81	gm	83.26
										84.79
	45.19	34.48	0.50	0.10	18.69	1.06	0.02	100.13	0.00	95.06
	45.20	34.68	0.49	0.09	18.61	1.03	0.02	100.21	18.92	95.19
	44.94	34.72	0.50	0.09	18.85	0.96	0.01	100.17	37.84	95.56

44.98	34.39	0.49	0.09	18.82	0.93	0.01	99.82	56.76	95.67
45.27	34.71	0.49	0.10	18.80	1.02	0.02	100.48	75.69	95.29
45.04	34.83	0.49	0.10	19.38	0.94	0.01	100.89	94.61	95.76
44.61	34.56	0.49	0.09	19.22	0.87	0.01	99.95	113.53	96.02
45.37	35.09	0.51	0.10	19.13	0.94	0.01	101.24	132.45	95.72
45.22	34.65	0.54	0.09	19.22	0.91	0.01	100.74	151.37	95.88
45.64	32.42	0.66	0.13	17.15	1.56	0.04	97.71	170.29	92.27
49.69	30.97	0.88	0.19	15.46	2.94	0.08	100.35	189.21	85.10
49.46	31.77	0.85	0.20	16.06	2.75	0.07	101.29	0.00	86.39
49.69	31.45	0.90	0.16	15.18	2.96	0.09	100.56	15.00	84.75
50.20	30.94	0.94	0.17	15.09	3.14	0.09	100.71	30.00	83.91
45.62	34.22	0.42	0.09	18.87	1.07	0.04	100.32	core	95.01
49.65	31.64	0.78	0.21	15.79	2.93	0.09	101.10	rim	85.38
45.27	34.64	0.51	0.09	19.12	0.84	0.00	100.46	core	96.18
48.16	32.42	0.89	0.17	16.83	2.10	0.05	100.63	rim	89.71
45.66	34.58	0.42	0.10	18.63	1.05	0.03	100.47	core	95.06
44.72	34.83	0.44	0.13	19.19	0.83	0.01	100.16	mid	96.21
49.23	31.64	0.87	0.18	15.93	2.54	0.09	100.47	rim	87.14
45.49	34.98	0.44	0.11	19.11	0.78	0.01	100.91	core	96.41
47.43	33.02	0.76	0.16	17.43	1.73	0.03	100.56	rim	91.67
45.68	34.08	0.54	0.09	18.52	1.10	0.03	100.04	core	94.81
45.06	34.37	0.52	0.11	18.76	1.06	0.03	99.92	core	95.05
48.25	32.29	0.65	0.13	16.92	2.19	0.04	100.47	mid	89.40
49.59	31.39	0.98	0.20	15.72	2.71	0.10	100.68	rim	86.23
49.58	31.43	0.79	0.23	15.81	2.63	0.10	100.57	rim	86.63
45.29	34.92	0.40	0.07	19.12	0.82	0.02	100.64	core	96.21
47.96	32.21	0.91	0.14	16.65	2.21	0.06	100.14	rim	89.11
45.90	34.49	0.46	0.09	19.05	0.99	0.02	100.99	core	95.45
48.66	32.52	0.69	0.16	16.67	2.12	0.07	100.88	rim	89.48
45.28	34.88	0.44	0.13	19.07	0.84	0.02	100.65	core	96.11
49.86	30.92	0.95	0.26	15.57	2.97	0.12	100.64	rim	84.95
45.48	34.77	0.50	0.10	19.16	0.91	0.02	100.93	core	95.82

	44.85	34.59	0.81	0.09	19.00	0.92	0.03	100.28	rim	95.72
	45.45	34.65	0.44	0.10	19.02	1.33	0.02	101.03	core	93.99
	48.54	32.21	0.88	0.16	16.37	2.32	0.04	100.53	rim	88.52
	45.06	34.72	0.48	0.10	19.16	0.89	0.04	100.46	core	95.85
	48.99	32.28	0.74	0.20	16.56	2.32	0.08	101.18	rim	88.52
	46.12	34.06	0.57	0.13	18.38	1.32	0.01	100.59	core	93.87
	49.71	30.98	0.90	0.22	15.62	3.09	0.09	100.62	rim	84.57
	46.10	34.53	0.48	0.14	18.87	1.09	0.02	101.24	core	94.98
	48.56	31.95	0.88	0.19	16.69	2.25	0.06	100.58	rim	88.96
	45.26	34.35	0.52	0.11	18.84	0.99	0.04	100.11	core	95.35
	48.93	31.61	0.77	0.21	15.93	2.56	0.08	100.11	rim	87.08
	48.84	32.30	0.68	0.20	16.45	2.18	0.07	100.72	core	89.09
	48.66	32.05	0.93	0.19	16.48	2.45	0.08	100.84	rim	87.92
	45.24	34.75	0.47	0.10	19.07	0.88	0.01	100.53	core	95.96
	48.63	31.90	0.83	0.20	16.31	2.26	0.08	100.22	rim	88.63
Kakuki										
	49.16	32.43	0.43	0.18	16.08	2.73	0.04	101.16	rim	86.59
	50.65	30.72	0.63	0.11	14.20	3.73	0.09	100.25	core	80.54
	49.33	31.02	1.06	0.29	15.09	3.06	0.13	100.22	core	84.11
	48.71	32.54	0.51	0.18	16.33	2.46	0.04	100.90	rim	87.89
	52.68	29.37	0.86	0.21	13.13	4.29	0.12	100.82	gm	76.89
	48.93	32.46	0.60	0.19	15.79	2.56	0.05	100.70	core	87.07
	51.52	30.27	0.81	0.25	14.23	3.59	0.10	100.92	rim	81.14
	49.34	32.31	0.50	0.14	15.87	2.77	0.06	101.07	0.00	86.21
	47.51	33.19	0.50	0.13	16.82	2.08	0.05	100.37	24.11	89.81
	50.13	31.36	0.49	0.14	15.19	3.07	0.07	100.57	48.21	84.34
	48.19	32.87	0.43	0.17	16.41	2.41	0.04	100.62	72.32	88.16
	50.11	30.74	0.62	0.21	14.94	3.13	0.07	99.95	96.42	83.88
	51.56	29.92	0.93	0.23	13.54	3.89	0.11	100.36	gm	79.05
	53.10	28.47	0.60	0.09	12.13	4.85	0.16	99.54	core	73.03
	51.58	29.42	0.64	0.20	13.50	4.27	0.08	99.84	mid	77.55

50.62	29.81	0.66	0.22	14.23	3.69	0.07	99.45	rim	80.81
51.16	29.73	1.30	0.29	13.93	3.77	0.12	100.53	gm	80.01
52.61	28.25	1.11	0.26	12.49	4.54	0.14	99.63	gm	74.88
52.56	29.36	2.11	0.37	12.98	4.29	0.18	102.19	gm	76.48
49.05	31.48	0.49	0.13	15.46	2.98	0.08	99.80	core	85.13
49.56	31.81	0.50	0.14	15.57	3.06	0.08	100.83	core	84.90
49.43	31.79	0.50	0.14	15.23	3.04	0.08	100.33	core	84.69
49.46	31.47	0.51	0.13	15.39	2.97	0.08	100.14	core	85.14
49.04	31.47	0.52	0.13	15.46	2.99	0.07	99.79	core	85.13
48.99	31.54	0.54	0.11	15.50	2.92	0.07	99.81	core	85.43
48.41	32.17	0.46	0.19	16.37	2.54	0.04	100.29	core	87.68
48.62	32.71	0.48	0.18	16.54	2.40	0.04	101.10	core	88.39
47.90	32.77	0.52	0.18	16.79	2.30	0.05	100.62	core	88.97
47.74	32.29	0.62	0.19	16.25	2.48	0.04	99.73	core	87.89
50.97	30.45	0.85	0.27	14.33	3.78	0.09	100.90	core	80.75
51.57	29.80	0.81	0.21	13.94	3.89	0.11	100.49	gm	79.85
48.66	31.37	0.64	0.28	15.10	2.90	0.04	99.01	core	85.08
50.86	30.47	0.84	0.23	14.18	3.48	0.07	100.15	mid	81.63
50.97	29.73	0.94	0.21	13.89	3.64	0.08	99.45	rim	80.61
47.88	32.55	0.54	0.18	16.35	2.36	0.03	99.89	core	88.36
50.49	30.07	0.85	0.29	14.12	3.49	0.07	99.39	rim	81.53
48.11	31.87	0.67	0.20	15.96	2.73	0.04	99.58	core	86.49
49.62	30.66	0.78	0.23	14.81	3.00	0.06	99.18	mid	84.34
51.46	28.90	0.97	0.28	13.26	3.80	0.12	98.81	rim	79.07
49.09	31.49	0.60	0.20	15.24	2.75	0.04	99.39	core	85.85
51.28	30.43	0.88	0.25	13.94	3.44	0.09	100.31	rim	81.49
48.10	30.41	1.60	0.64	15.15	2.45	0.11	98.46	core	86.91
50.61	30.17	0.78	0.31	14.29	3.23	0.07	99.44	rim	82.82
49.26	31.35	0.66	0.19	15.34	2.75	0.06	99.61	core	85.87
49.13	31.84	0.67	0.20	15.53	2.71	0.06	100.14	rim	86.19
50.88	30.12	0.78	0.28	13.21	3.70	0.18	99.15	core	79.27
49.75	25.91	3.64	2.77	14.19	2.85	0.14	99.25	mid	84.20
53.56	26.84	2.61	0.51	11.04	4.67	0.27	99.51	rim	71.57

	48.98	31.49	0.47	0.19	15.27	2.64	0.05	99.09	core	86.33
	48.63	31.55	0.53	0.19	15.46	2.58	0.04	98.98	mid	86.77
	48.62	32.12	0.63	0.21	15.67	2.51	0.05	99.81	rim	87.20
	49.39	31.55	0.55	0.19	15.06	2.78	0.04	99.56	core	85.57
	49.04	31.77	0.60	0.22	15.37	2.65	0.03	99.68	mid	86.42
	51.68	29.45	0.98	0.19	13.40	3.82	0.13	99.66	rim	79.13
	49.39	31.55	0.55	0.19	15.06	2.78	0.04	99.56	core	85.57
	49.04	31.77	0.60	0.22	15.37	2.65	0.03	99.68	mid	86.42
	51.68	29.45	0.98	0.19	13.40	3.82	0.13	99.66	rim	79.13
	51.05	30.25	0.79	0.26	13.97	3.37	0.07	99.76	rim	81.88
	48.98	31.53	0.58	0.19	14.85	2.83	0.05	99.02	core	85.15
	48.88	31.57	0.48	0.23	15.54	2.52	0.05	99.26	mid	87.06
	51.49	30.14	0.76	0.22	14.00	3.59	0.06	100.27	rim	81.00
	49.03	31.82	0.47	0.18	15.33	2.82	0.05	99.71	core	85.59
	49.39	31.55	0.61	0.19	15.56	2.71	0.05	100.06	rim	86.25
	49.19	31.54	0.47	0.12	15.00	2.48	0.07	98.87	core	86.78
	49.26	31.65	0.46	0.20	15.10	2.81	0.04	99.52	mid	85.47
	50.26	30.69	0.73	0.26	14.69	2.97	0.05	99.67	rim	84.39
	48.79	31.55	0.55	0.18	15.41	2.66	0.04	99.18	core	86.38
	51.26	28.53	1.15	0.47	13.48	3.83	0.10	98.82	rim	79.27
	49.17	32.01	0.52	0.17	15.37	2.68	0.05	99.98	core	86.23
	49.02	32.01	0.52	0.19	15.58	2.58	0.05	99.95	mid	86.83
	49.51	31.37	0.79	0.22	15.52	2.66	0.05	100.12	rim	86.43
	49.96	31.52	0.73	0.25	14.95	3.02	0.03	100.47	core	84.46
	52.02	26.05	3.33	1.34	12.18	3.75	0.21	98.88	rim	77.59
	56.13	27.32	0.23	0.02	9.97	5.44	0.43	99.53	core	65.82
	48.98	31.91	0.59	0.16	15.60	2.84	0.03	100.11	rim	85.77
	50.62	30.34	0.71	0.20	13.95	3.17	0.08	99.07	rim	82.71
Tarawera										
	48.93	31.54	0.99	0.31	15.58	2.81	0.08	100.37		85.73
	48.05	31.42	0.95	0.33	16.45	2.37	0.07	99.77		88.25

	48.42	31.73	0.77	0.25	16.08	2.40	0.05	99.82		87.97
	48.66	31.74	0.89	0.30	16.35	2.29	0.06	100.39		88.58
	48.11	31.99	2.22	0.66	16.35	2.36	0.12	102.08		88.09
	47.80	31.73	0.93	0.33	16.14	2.40	0.06	99.52	gm	87.96
	49.05	31.63	0.88	0.28	15.76	2.65	0.07	100.46	gm	86.60
	49.19	30.88	0.88	0.27	15.57	2.80	0.09	99.80	gm	85.74
	48.05	31.31	1.05	0.38	16.23	2.41	0.07	99.65	gm	87.94
	48.81	31.49	0.99	0.34	16.03	2.45	0.07	100.31	gm	87.63
HJR										
	46.31	34.30	0.50	0.11	18.13	1.30	0.02	100.76	0.00	93.83
	46.13	34.08	0.46	0.12	17.97	1.44	0.02	100.31	49.59	93.20
	46.20	34.31	0.46	0.11	18.35	1.34	0.02	100.91	99.19	93.73
	45.67	34.53	0.48	0.11	18.23	1.17	0.02	100.30	148.78	94.44
	46.49	34.40	0.50	0.11	18.23	1.34	0.02	101.18	198.38	93.70
	48.86	31.95	0.68	0.16	15.88	2.66	0.05	100.36	247.97	86.72
	51.27	28.49	1.07	0.31	13.32	3.81	0.11	98.59	0.00	79.12
	50.72	29.99	0.75	0.12	13.86	4.05	0.10	99.75	10.83	78.83
	48.33	31.81	0.72	0.14	15.93	2.63	0.06	99.73	21.65	86.85
	49.72	30.89	0.80	0.14	14.96	3.42	0.07	100.14	32.48	82.67
	48.38	31.93	0.81	0.16	15.73	2.77	0.06	99.99	43.30	86.07
	50.65	29.48	2.89	1.03	14.01	3.66	0.21	102.46	54.13	80.30
	50.32	31.21	0.62	0.10	14.83	3.23	0.09	100.52	0.00	83.29
	51.74	30.09	0.68	0.13	13.65	4.09	0.13	100.67	19.54	78.30
	51.92	29.68	0.92	0.19	13.49	4.10	0.16	100.71	39.08	78.02
	52.10	29.50	0.65	0.10	13.12	4.27	0.15	100.04	58.62	76.86
	52.67	29.94	0.78	0.11	13.23	4.17	0.14	101.21	78.16	77.43
	48.40	32.23	0.75	0.23	16.22	2.43	0.06	100.45	97.70	87.89
	48.76	32.04	0.64	0.15	16.09	2.57	0.06	100.45	117.24	87.23
	49.39	30.98	0.69	0.16	15.31	3.18	0.07	99.92	136.78	83.99
	51.36	30.05	0.76	0.18	14.36	3.68	0.10	100.64	156.32	80.90
	51.17	30.05	0.67	0.08	13.52	4.27	0.17	100.09	0.00	77.32
	51.92	29.17	0.85	0.11	12.74	4.19	0.15	99.30	15.17	76.67
	53.09	28.10	0.98	0.16	12.19	4.48	0.21	99.44	30.33	74.48
	44.77	24.36	3.23	0.27	10.55	2.29	0.15	86.00	45.50	83.01
	50.52	29.19	1.56	0.20	13.50	3.21	0.15	98.57	60.67	81.84
	48.81	32.02	0.66	0.16	16.00	2.60	0.05	100.44	75.83	87.03
	49.70	31.47	0.70	0.17	15.52	2.88	0.06	100.62	91.00	85.44
	50.15	31.11	0.78	0.17	14.89	3.19	0.08	100.49	106.17	83.56

	51.09	30.60	0.86	0.20	14.11	3.58	0.10	100.70	121.33	81.04
	50.15	30.78	1.02	0.22	14.65	3.30	0.10	100.39	gm	82.81
	51.10	30.61	1.42	0.66	14.52	3.50	0.12	102.18	gm	81.78
	49.95	31.25	0.81	0.17	15.15	3.04	0.07	100.59	gm	84.46
Terrace Rd										
	46.33	33.65	0.53	0.12	18.00	1.67	0.05	100.44	0.00	92.10
	45.45	34.41	0.51	0.09	18.52	1.06	0.03	100.17	19.60	94.98
	45.31	34.71	0.51	0.09	18.66	1.13	0.03	100.54	39.20	94.72
	45.14	33.90	0.53	0.10	18.40	1.27	0.04	99.46	58.80	94.03
	45.90	34.30	0.55	0.09	18.55	1.13	0.03	100.65	78.40	94.66
	48.59	32.40	0.81	0.14	16.27	2.56	0.09	100.99	98.01	87.27
	48.32	32.17	0.80	0.15	16.29	2.46	0.08	100.39	105.00	87.78
	50.44	30.76	1.03	0.21	14.64	3.32	0.16	100.75	gm	82.55
	50.00	31.75	0.85	0.17	15.65	2.91	0.09	101.57	gm	85.34
	48.28	31.52	0.69	0.14	15.49	2.49	0.08	98.81	rim	87.06
	44.22	34.15	0.50	0.09	18.49	0.92	0.03	98.46	core	95.62
	47.20	31.85	0.75	0.13	16.51	2.08	0.06	98.70	rim	89.61
	44.94	33.75	0.50	0.10	17.84	1.24	0.04	98.53	core	93.96
	45.53	34.56	0.49	0.09	18.49	1.08	0.03	100.37	core	94.88
	47.67	31.86	0.72	0.13	15.64	2.41	0.08	98.63	rim	87.53
	45.14	35.00	0.47	0.09	18.80	0.96	0.02	100.56	core	95.57
	49.10	30.46	0.90	0.18	14.98	3.00	0.11	98.86	gm	84.67
	49.86	30.73	0.99	0.20	14.62	3.05	0.14	99.75	gm	84.11
rotomakariri										
	45.79	34.21	0.53	0.10	17.43	1.66	0.03	99.83	0.00	91.97
	45.86	34.30	0.51	0.08	18.21	1.33	0.02	100.40	50.00	93.74
	46.69	33.48	0.60	0.07	17.12	1.92	0.05	100.01	100.00	90.65
	50.78	29.36	0.71	0.10	12.75	4.14	0.14	98.10	110.00	76.91
	52.16	29.48	0.74	0.11	12.94	4.33	0.16	100.05	120.00	76.33
	53.40	28.49	0.87	0.13	11.81	4.63	0.17	99.65	gm	73.82
	47.92	32.44	0.68	0.07	15.84	2.51	0.07	99.62	0.00	87.29
	47.32	32.90	0.67	0.07	16.26	2.36	0.07	99.73	15.92	88.18
	48.22	32.19	0.67	0.08	15.67	2.69	0.09	99.72	31.80	86.32
	48.78	30.19	0.69	0.09	13.88	3.32	0.12	97.18	47.68	81.88

48.36	30.00	0.70	0.08	13.62	3.35	0.11	96.37	63.59	81.50
49.88	29.42	0.72	0.09	13.16	3.61	0.14	97.15	79.48	79.72
50.79	28.80	0.73	0.09	12.24	4.22	0.16	97.14	95.36	75.79
53.19	28.51	0.77	0.09	11.48	4.80	0.19	99.16	111.25	72.03
46.04	33.91	0.54	0.08	17.69	1.66	0.03	100.06	0.00	92.09
45.83	33.81	0.54	0.09	17.77	1.61	0.03	99.77	16.54	92.33
45.68	34.01	0.52	0.08	17.65	1.49	0.03	99.55	33.04	92.80
46.07	33.61	0.52	0.08	17.64	1.64	0.03	99.68	49.55	92.15
46.31	34.07	0.53	0.08	17.75	1.59	0.03	100.45	66.07	92.42
45.66	33.97	0.54	0.08	17.96	1.49	0.03	99.83	82.58	92.95
45.35	33.96	0.53	0.08	17.50	1.57	0.03	99.11	99.11	92.40
44.42	34.99	0.53	0.07	18.42	1.19	0.02	99.73	115.62	94.40
45.40	34.23	0.53	0.07	17.97	1.57	0.03	99.89	132.13	92.62
44.96	34.59	0.57	0.06	18.08	1.28	0.03	99.64	148.65	93.89
44.27	33.52	0.58	0.06	17.69	1.42	0.03	97.66	165.16	93.13
48.82	31.76	0.68	0.09	15.30	2.86	0.09	99.70	181.67	85.29

Analyses of SJI Ol from the 9th and 10th May 2019 drift to 0.5wt.% higher MgO, however, at high MgO contents for olivine, this results in a negligible shift in forsterite content. Samples analysed on these days are high-alumina basalt with olivines of Fo_{72-85} and are not involved in the interpretation of mantle-derived vs. non mantle-derived olivine. There is drift in SJI olivine at the end of the run on 03/08/2019, where MgO is 96% of the reference value. This only affects the traverse of a high forsterite olivine in WM sample. As the secondary standards and unknowns are of high MgO content, the drift on detectors results in only a 0.3 mol.% shift in forsterite on SJI olivine. We applied a correction to the WM olivine data, based on MgO concentrations being 96% of the reference value. For the unknowns, as these are of high forsterite content, this correction results in a shift of 0.2 mol.% to higher forsterite. The uncorrected core values are $Fo_{92.5}$. With the correction, the core values are $Fo_{92.7}$. This is in line with forsterite contents of olivines from WM sample analysed on days with no drift. There is a weak negative correlation between NiO and MgO, where NiO is lower at higher MgO in SJI olivine analyses. Uncertainty on individual NiO analyses is 0.01 wt.%. 2 standard deviations from the compilation of SJI olivine secondary standard analyses is 0.02 wt.%. This is the error reported on NiO values used for interpretation of high NiO populations. NiO concentrations range from 0.56 - 0.12 wt.% within WM sample, and from 0.37 - 0.11 wt.% in

OG sample. The difference between the NiO concentration in the cores of olivines in these samples is 0.19 wt.%, an order of magnitude larger than the calculated error in NiO concentrations.

A.7 Fractionation and Magma mixing models

Our fractional crystallisation model was conducted in *Petrolog* (Danyushevsky and Plechov, 2011) and run under the conditions highlighted in tableA.9. We chose to simulate crystallisation of olivine only from the melt as this is the only macrocryst phase in Ongaroto, and the first phase to form in all other eruptions, and also reduces discrepancies in the model by allowing $D_{bulk} = D_{Ol}^{Ni}$. $D_{Ol}^{Ni} = 8$ was calculated from an average of 18 published partition coefficients from the *GERM* K_d database. The input composition is listed in table A.10. HMB is a natural composition from Gust and Perfit (1987) adapted to be in Fe-Mg equilibrium (Roeder and Emslie, 1970) with the most primitive non-mantle olivines from the TVZ. The model was run at 5kbar as a representative depth for the mid crust in the TVZ, however was also run at 10kbar and 1kbar and was insensitive to changes in pressure. The model was run until 30% fractionation had occurred.

The magma mixing model simulates the effect of repeated intrusions of high-Mg basalt on a magma that had the same initial composition but has subsequently undergone fractionation in the crust. The model starts with the first iteration of fractionation, which was identical to that described above. The model again was set to run until 30% fractionation had occurred, which always required >200°C of temperature decrease. The composition of the magma at the 200°C interval from the starting temperature was selected as the fractionated end-member for the first iteration of magma mixing. In this first iteration, the HMB and fractionated end-member compositions were mixed in a 1:1 ratio. The resultant composition was used as the next input into *Petrolog*, where the fractionation model was run again and the next fractionated melt was selected at the 200°C interval. As the amount of HMB magma used for the recharge events was kept constant, on the 2nd iteration of mixing, the ratio of fractionated melt : HMB melt was 2:1. Throughout the iterations this meant that the ratio of fractionated melt : HMB increased, and so the effect of the HMB recharge events on the overall composition decreased. The same model was also run at 150°C recharge intervals, with the effect of producing a slightly steeper trend and less pronounced NiO enrichment at lower forsterite.

Table A.9: Output from *Petrolog* showing Parameters for fractional crystallisation modelling.

Modelling Crystallisation	
Minerals chosen for calculations are:	Olv
The model used for Olv is:	Beattie 1993
Olv fractionation is:	100.00%
Fe_2O_3 in the melt:	Fe = FeO_t
Initial Pressure:	5 kbar
During calculations Pressure is kept constant	
Kds for minerals:	
Name: Olv	Ni: 8
Melt density is calculated following the model of Lange & Carmichael 1987	
Melt viscosity is calculated following the model of Bottinga & Weill 1972	
Parameters to stop calculations at:	
Final degree of fractionation:	30%
The amount of a mineral phase which will be extracted from 100% of melt on each step is:	1%

A.8 MELTS model - mantle depletion

Our MELTS model (Asimow and Ghiorso, 1998; Ghiorso and Sack, 1995) simulates the effect of mantle melting and melt extraction on residual mantle olivine composition. The initial composition input into the model was of Workman and Hart (2005), for the depleted MORB mantle. The model was set at 1 GPa, a pressure corresponding to the base of the crust beneath the TVZ (Harrison and White, 2006; Stratford and Stern, 2006), and fO_2 of QFM+1, corresponding to fO_2 values using the spinel oxygen barometer of Ballhaus et al. (1991). T was increased at 1°C intervals from 1340-1420°C, over which, the melt fraction increases from 0.33-19.8%. At 15% melt, all clinopyroxene had melted out, resulting in a harzburgitic residue, at which point, the forsterite content of olivine increases more rapdily. The NiO of the residual olivine was calculated using a D_{Ol}^{Ni}=8 from the melt NiO at each step of the model. For this reason, we did not fractionate liquids, in order to best approximate batch melting. A detailed approach to using MELTS to calculate peridotite melting can be found in Hirschmann

Table A.10: high-Mg basalt (HMB), representing a primary mantle melt composition, used for *Petrolog* models. HMB is a natural composition from Gust and Perfit (1987) adapted to be in Fe-Mg equilibrium (Roeder and Emslie, 1970) with the most primitive not mantle-derived olivines from the TVZ.

HMB	Wt.%
SiO_2	48.53
Al_2O_3	13.14
FeO	8.97
MnO	0.16
MgO	16.92
CaO	9.87
Na_2O	1.49
Cr_2O_3	0.11
TiO_2	0.10
NiO	0.05
K_2O	0.45
P_2O_5	0.21

et al. (1998) The model produces the observed increases in Fo and NiO, offset to aprroximately 0.5 mol.% lower Fo. Decreasing the availability of Fe^{2+}, and therefore the total Fe available to incorporate into the olivine structure, by increasing fO_2 to QFM+2, produces similar increases in Fo and NiO, at 1mol.% higher Fo for a given melt fraction.

Appendix A

Appendix B

A.1 EDS Secondary Standards

Table A.1: **Andradite secondary standard analyses**

SiO2	Al2O3	FeO	CaO	Total	Project Path
36.95	1.52	27.89	32.99	99.25	XP051120/Andradite/Site 1
36.65	1.75	28.09	33.31	99.81	XP051120/Andradite/Site 1
36.62	1.93	27.77	33.5	99.83	XP051120/Andradite/Site 1
36.64	1.7	27.68	32.93	99.04	XP051120/Andradite/Site 1
36.74	1.78	27.76	33.11	99.53	XP051120/Andradite/Site 1
36.64	1.79	27.53	33.36	99.31	XP051120/Andradite/Site 1
36.69	1.79	27.58	32.96	99.09	XP051120/Andradite/Site 1
37.04	1.66	27.86	33.37	100.08	XP051120/Andradite/Site 1
36.38	1.71	27.57	33.21	98.96	XP051120/Andradite/Site 2
36.42	1.76	27.43	32.97	98.68	XP051120/Andradite/Site 2
36.39	1.62	27.66	33	98.76	XP051120/Andradite/Site 2
36.31	1.85	27.13	32.89	98.17	XP051120/Andradite/Site 2
36.43	1.75	27.23	33.04	98.46	XP051120/Andradite/Site 2
36.22	1.81	27.4	32.96	98.38	XP051120/Andradite/Site 2
36.84	1.84	27.52	33.2	99.35	XP051120/Andradite/Site 3
36.8	1.67	27.49	33.39	99.57	XP051120/Andradite/Site 3
36.67	1.69	27.13	33.32	98.88	XP051120/Andradite/Site 3
36.79	1.67	27.89	33.48	99.83	XP051120/Andradite/Site 3
36.56	1.92	27.98	33.12	99.68	XP051120/Andradite/Site 3
36.69	1.72	27.52	32.85	98.84	XP051120/Andradite/Site 4
36.62	1.73	27.24	33.03	98.68	XP051120/Andradite/Site 4
36.32	1.8	27.47	32.9	98.54	XP051120/Andradite/Site 4
36.49	1.79	27.16	32.96	98.38	XP051120/Andradite/Site 4

36.14	1.69	27.32	32.71	98.01	XP051120/Andradite/Site 4
36.33	1.74	27.28	32.89	98.27	XP051120/Andradite/Site 5
36.46	1.88	27.44	32.96	98.8	XP051120/Andradite/Site 5
36.56	1.74	27.31	33.05	98.67	XP051120/Andradite/Site 5
36.37	1.67	27.28	32.54	97.9	XP051120/Andradite/Site 5
36.34	1.81	27.43	32.93	98.53	XP051120/Andradite/Site 5
36.25	1.65	27.58	32.79	98.44	XP051120/Andradite/Site 5

Table A.2: **Clinopyroxene secondary standard analyses**

SiO2	Al2O3	FeO	MgO	CaO	Na2O	Total	Project Path
52.08	0.55	16.92	8.29	23.3	0.87	101.97	XP051120/Pyroxene/Site 1
52.2	0.47	17.18	8.21	23.18	0.69	101.91	XP051120/Pyroxene/Site 1
52.25	0.8	17.27	8.26	23.14	0.76	102.46	XP051120/Pyroxene/Site 1
52.2	0.61	17.34	8.27	23.51	0.79	102.73	XP051120/Pyroxene/Site 1
52.62	0.66	16.81	8.27	23.43	0.8	102.57	XP051120/Pyroxene/Site 1
52.51	0.66	17.15	8.3	23.58	0.75	102.98	XP051120/Pyroxene/Site 1
52.11	0.64	17.02	8.35	23.24	0.81	102.14	XP051120/Pyroxene/Site 1
52.05	0.67	17.13	8.09	23.27	0.71	101.89	XP051120/Pyroxene/Site 2
52.16	0.66	17.11	8.08	23.39	0.69	102.03	XP051120/Pyroxene/Site 2
52.12	0.64	16.7	8.14	23.17	0.71	101.48	XP051120/Pyroxene/Site 2
52.09	0.63	16.85	8.18	23.2	0.8	101.73	XP051120/Pyroxene/Site 2
52.01	0.54	16.92	8.19	23.26	0.58	101.51	XP051120/Pyroxene/Site 2
51.94	0.53	17.08	8.1	23.24	0.84	101.75	XP051120/Pyroxene/Site 2
51.76	0.6	16.43	8.16	23.35	0.76	101.04	XP051120/Pyroxene/Site 2
51.85	0.65	17.31	8.11	23.6	0.63	102.15	XP051120/Pyroxene/Site 3
52.04	0.62	16.92	8.17	23.32	0.84	101.91	XP051120/Pyroxene/Site 3
51.87	0.61	17.18	8.17	22.97	0.76	101.59	XP051120/Pyroxene/Site 3
52.13	0.65	17.2	8.13	23.49	0.82	102.45	XP051120/Pyroxene/Site 3
52.05	0.73	16.82	8.1	23.58	0.73	102.13	XP051120/Pyroxene/Site 3
51.94	0.7	16.91	8.11	23.32	0.73	101.69	XP051120/Pyroxene/Site 3
52.23	0.66	17.23	8.02	23.45	0.68	102.28	XP051120/Pyroxene/Site 3
51.91	0.61	16.93	8.29	23.35	0.81	101.88	XP051120/Pyroxene/Site 4
51.55	0.68	16.94	8.19	23.22	0.82	101.39	XP051120/Pyroxene/Site 4
52.15	0.63	17.22	8.31	23.33	0.75	102.41	XP051120/Pyroxene/Site 4
52.07	0.53	17.19	8.02	23.07	0.8	101.66	XP051120/Pyroxene/Site 4
51.99	0.48	17.23	8.13	23.28	0.72	101.81	XP051120/Pyroxene/Site 4
51.69	0.58	16.9	8.25	23.39	0.76	101.63	XP051120/Pyroxene/Site 5
51.94	0.57	17.06	8.03	23.28	0.81	101.67	XP051120/Pyroxene/Site 5
51.88	0.61	17.18	8.1	23.32	0.74	101.85	XP051120/Pyroxene/Site 5
51.85	0.75	16.97	8.18	23.38	0.62	101.76	XP051120/Pyroxene/Site 5
51.97	0.65	17.04	8.05	23.21	0.74	101.67	XP051120/Pyroxene/Site 5

52.18	0.58	16.93	8.18	23.18	0.73	101.81	XP051120/Pyroxene/Site 5
51.86	0.66	17.11	8.23	23.39	0.77	102.03	XP051120/Pyroxene/Site 5
52.17	0.64	16.94	8.03	23.17	0.8	101.72	XP051120/Pyroxene/Site 7
51.96	0.61	16.82	8.18	23.38	0.77	101.73	XP051120/Pyroxene/Site 7
52.11	0.67	17.2	8.17	23.39	0.79	102.37	XP051120/Pyroxene/Site 7
51.6	0.56	16.94	7.89	23.49	0.75	101.23	XP051120/Pyroxene/Site 7
51.56	0.63	16.92	8.03	23.13	0.66	100.94	XP051120/Pyroxene/Site 7
51.64	0.66	16.9	8.05	23.26	0.81	101.38	XP051120/Pyroxene/Site 8
51.78	0.63	16.88	7.87	23.24	0.72	101.09	XP051120/Pyroxene/Site 8
51.13	0.53	16.59	8.02	23.09	0.7	100.07	XP051120/Pyroxene/Site 8
52.08	0.5	17.19	7.95	23.29	0.81	101.79	XP051120/Pyroxene/Site 8
51.65	0.69	17.09	8.06	23.2	0.76	101.48	XP051120/Pyroxene/Site 8

Table A.3: **St. John's Island Olivine secondary standard analyses**

SiO2	FeO	MgO	Total	Project Path
42.17	9.78	51.57	103.49	XP051120/SJI Ol/Site 1
42.04	10.06	51.12	103.31	XP051120/SJI Ol/Site 1
42.16	9.92	51.45	103.48	XP051120/SJI Ol/Site 1
42.09	9.99	51.76	103.84	XP051120/SJI Ol/Site 1
41.83	9.85	51.54	103.24	XP051120/SJI Ol/Site 1
41.96	9.86	51.32	103.2	XP051120/SJI Ol/Site 1
41.99	9.56	51.5	102.95	XP051120/SJI Ol/Site 1
41.73	9.99	51.58	103.24	XP051120/SJI Ol/Site 1
41.49	9.77	51.09	102.51	XP051120/SJI Ol/Site 2
42.12	9.71	51.13	103.04	XP051120/SJI Ol/Site 2
41.7	9.96	51.15	102.75	XP051120/SJI Ol/Site 2
41.84	10.05	51.13	102.85	XP051120/SJI Ol/Site 2
41.3	9.77	51.05	102.03	XP051120/SJI Ol/Site 2
42.02	9.92	51.48	103.33	XP051120/SJI Ol/Site 2
41.96	9.77	51.58	103.23	XP051120/SJI Ol/Site 2
41.99	9.94	51.87	103.81	XP051120/SJI Ol/Site 3
42.52	10.08	51.63	104.11	XP051120/SJI Ol/Site 3
42.17	9.95	51.71	103.81	XP051120/SJI Ol/Site 3
42.19	9.91	51.66	103.78	XP051120/SJI Ol/Site 3
42.44	10.19	51.53	104.06	XP051120/SJI Ol/Site 3
42.08	9.81	51.46	103.3	XP051120/SJI Ol/Site 3
42.32	10.03	51.53	103.88	XP051120/SJI Ol/Site 3
41.78	9.94	51.06	102.71	XP051120/SJI Ol/Site 4
41.72	9.88	51.1	102.7	XP051120/SJI Ol/Site 4
41.53	9.81	51.47	102.64	XP051120/SJI Ol/Site 4
41.61	9.94	51.73	103.38	XP051120/SJI Ol/Site 4

42.03	9.79	51.12	103.1	XP051120/SJI Ol/Site 4
42.22	10.03	51.54	103.77	XP051120/SJI Ol/Site 4
41.92	9.94	51.26	103.18	XP051120/SJI Ol/Site 4
41.9	9.73	50.78	102.19	XP051120/SJI Ol/Site 5
41.71	9.96	50.98	102.77	XP051120/SJI Ol/Site 5
41.38	9.84	50.97	102.26	XP051120/SJI Ol/Site 5
41.62	9.92	51.02	102.35	XP051120/SJI Ol/Site 5
41.97	9.86	51.18	102.93	XP051120/SJI Ol/Site 5
41.75	9.79	50.97	102.5	XP051120/SJI Ol/Site 5
41.94	9.96	50.97	102.84	XP051120/SJI Ol/Site 6
41.72	9.79	50.98	102.43	XP051120/SJI Ol/Site 6
41.35	9.7	50.91	102.01	XP051120/SJI Ol/Site 6
41.5	9.59	50.66	101.73	XP051120/SJI Ol/Site 6
41.63	9.78	51.11	102.37	XP051120/SJI Ol/Site 6
41.31	9.66	50.86	101.85	XP051120/SJI Ol/Site 6

Table A.4: **Wollastonite secondary standard analyses**

SiO2	CaO	Total	Project Path
52.98	49.11	102.55	XP051120/Wollastonite/Site 1
53.43	48.98	102.89	XP051120/Wollastonite/Site 1
52.71	49.16	102.52	XP051120/Wollastonite/Site 1
52.9	49.16	102.58	XP051120/Wollastonite/Site 1
52.78	49.24	102.83	XP051120/Wollastonite/Site 1
52.99	49.12	102.5	XP051120/Wollastonite/Site 1
52.43	49.27	102.46	XP051120/Wollastonite/Site 1
53.22	48.97	102.99	XP051120/Wollastonite/Site 2
53.09	49.33	103.04	XP051120/Wollastonite/Site 2
52.71	48.88	102.09	XP051120/Wollastonite/Site 2
52.91	49.02	102.54	XP051120/Wollastonite/Site 2
52.47	48.93	102.04	XP051120/Wollastonite/Site 3
52.8	48.87	102.25	XP051120/Wollastonite/Site 3
52.4	48.53	101.49	XP051120/Wollastonite/Site 3
53.11	48.7	102.31	XP051120/Wollastonite/Site 3
52.38	48.64	101.78	XP051120/Wollastonite/Site 3
52.97	48.85	102.52	XP051120/Wollastonite/Site 3

Table A.5: **Jadeite secondary standard analyses**

SiO2	Al2O3	Na2O	Total	Project Path
61.35	26.79	15.65	103.9	XP051120/Jadeite/Site 1
60.75	26.64	15.44	103.05	XP051120/Jadeite/Site 1

60.74	26.43	15.42	102.96	XP051120/Jadeite/Site 1
60.49	26.15	15.43	102.66	XP051120/Jadeite/Site 1
61.37	26.84	15.60	104.02	XP051120/Jadeite/Site 1
60.71	26.17	15.27	102.69	XP051120/Jadeite/Site 1
60.58	26.77	15.71	103.12	XP051120/Jadeite/Site 1
60.18	25.13	15.07	101.86	XP051120/Jadeite/Site 1
60.74	25.52	15.24	102.98	XP051120/Jadeite/Site 1
60.51	26.26	15.21	101.96	XP051120/Jadeite/Site 2
60.68	26.14	15.5	102.28	XP051120/Jadeite/Site 2
60.99	26.41	15.44	102.8	XP051120/Jadeite/Site 2
60.39	26.37	15.7	102.45	XP051120/Jadeite/Site 2
60.57	26.32	15.41	102.16	XP051120/Jadeite/Site 2
60.95	26.38	15.56	102.89	XP051120/Jadeite/Site 3
60.73	26.63	15.49	102.97	XP051120/Jadeite/Site 3
60.55	26.46	15.37	102.43	XP051120/Jadeite/Site 3
60.71	26.76	15.48	103.04	XP051120/Jadeite/Site 3
60.76	26.44	15.50	102.63	XP051120/Jadeite/Site 3
60.49	25.94	15.29	101.66	XP051120/Jadeite/Site 4
60.19	26.23	15.23	101.57	XP051120/Jadeite/Site 4
60.71	26.14	15.43	102.23	XP051120/Jadeite/Site 4
60.99	26.14	15.41	102.6	XP051120/Jadeite/Site 4
60.41	26.31	15.28	101.99	XP051120/Jadeite/Site 4
59.95	26.21	15.34	101.44	XP051120/Jadeite/Site 4

A.2 2 wt.% H_2O basalt analyses

Table A.6: **2 wt.% H_2O basalt olivine analyses**

SiO2	TiO2	Al2O3	FeO	MnO	MgO	CaO	Na2O	NiO	Total	Comment
40.92	0.01	0.11	7.49	-0.01	48.76	0.17	0.02	1.44	98.96	H_1250_1_Ol
40.58	0.01	0.10	8.27	-0.01	48.14	0.19	0.03	1.31	98.62	H_1250_1_Ol2
40.46	0.01	0.09	7.15	0.00	50.27	0.21	0.01	1.10	99.29	H1225_08_Ol1
40.54	0.01	0.09	7.05	0.00	51.08	0.21	0.01	1.02	100.03	H1225_08_Ol2
41.05	0.01	0.10	6.42	0.00	50.64	0.20	0.01	1.30	99.73	H1225_08_Ol3c
40.80	0.01	0.08	6.92	0.00	50.94	0.22	0.01	1.07	100.06	H1225_08_Ol3r
40.80	0.02	0.08	6.80	0.00	50.08	0.26	0.07	1.16	99.27	H_1200_07_Ol1
40.34	0.02	0.09	6.67	0.00	50.16	0.29	0.06	1.17	98.82	H_1200_07_Ol2
40.65	0.03	0.24	5.74	0.01	51.73	0.36	0.03	1.02	99.82	H_1225_07_Ol1

41.63	0.03	0.16	5.48	0.01	51.71	0.30	0.07	1.03	100.42	H_1225_07_Ol2
40.83	0.01	0.07	5.66	-0.01	51.84	0.19	0.01	1.04	99.66	H_1225_07_Ol3
40.89	0.02	0.10	5.72	0.00	51.42	0.27	0.01	0.93	99.37	H1250_07_Ol1
40.81	0.02	0.09	5.83	0.01	51.66	0.25	0.01	0.94	99.62	H1250_07_Ol2
41.21		0.11	9.39		50.42	0.22	0.11		101.51	XP051120/H-1125-05/Site 1
41.50		0.11	9.62		50.81	0.33	0.08		102.42	XP051120/H-1125-05/Site 1
41.48		0.29	8.52		50.87	0.66	0.13		101.98	XP051120/H-1125-05/Site 2
41.81		0.02	8.41		51.67	0.31	0.03		102.35	XP051120/H-1125-05/Site 2
42.01		0.02	8.53		51.54	0.20	0.06		102.41	XP051120/H-1125-05/Site 2
41.58		0.46	8.90		51.01	0.66	0.11		102.77	XP051120/H-1125-05/Site 2
41.54		0.10	9.56		50.70	0.19	0.11		102.27	XP051120/H-1125-05/Site 4
41.49		0.01	9.82		50.92	0.25	0.02		102.55	XP051120/H-1125-05/Site 4
41.85		-0.08	9.70		50.92	0.23	0.04		102.66	XP051120/H-1125-05/Site 4
41.76		0.11	9.62		50.17	0.30	0.07		102.10	XP051120/H-1125-05/Site 4
41.15		0.06	9.76		50.59	0.24	0.00		101.83	XP051120/H-1125-05/Site 4
40.77		0.14	9.65		50.35	0.29	-0.05		101.15	XP051120/H-1125-05/Site 4
41.18		0.11	9.95		50.65	0.33	0.08		102.33	XP051120/H-1125-05/Site 4
40.03	0.06	0.56	8.76	0.00	48.95	0.55	0.10	0.75	99.77	H1175_05_Ol1
40.85	0.14	0.07	8.51	0.00	49.36	0.29	0.04	0.79	100.08	H1175_05_Ol2
40.34	0.09	0.17	8.71	0.00	49.74	0.32	0.04	0.83	100.26	H1175_05_Ol3
40.42	0.03	0.07	8.88	0.00	48.94	0.27	0.02	0.81	99.44	H1175_05_Ol4
42.37		0.04	5.55		54.23	0.32	-0.09		102.44	XP051120/H-1225-05/Site 1
42.04		-0.02	5.79		54.55	0.24	0.05		102.66	XP051120/H-1225-05/Site 2
42.22		0.08	5.80		54.33	0.25	-0.03		102.68	XP051120/H-1225-05/Site 2
42.28		-0.02	5.57		54.29	0.26	0.06		102.49	XP051120/H-1225-05/Site 2
42.20		0.01	5.43		54.49	0.24	0.07		102.52	XP051120/H-1225-05/Site 2
42.22		0.03	5.70		54.41	0.28	-0.02		102.61	XP051120/H-1225-05/Site 2
41.94		0.18	5.49		54.31	0.23	-0.02		102.21	XP051120/H-1225-05/Site 2
42.26		0.15	5.77		54.17	0.17	0.11		102.66	XP051120/H-1225-05/Site 2
42.04		0.16	5.61		54.30	0.18	0.08		102.42	XP051120/H-1225-05/Site 3
42.04		0.10	5.64		53.99	0.25	-0.08		101.94	XP051120/H-1225-05/Site 3
42.23		0.05	5.63		54.17	0.20	0.02		102.35	XP051120/H-1225-05/Site 3
41.82		0.13	5.48		53.77	0.17	0.07		101.45	XP051120/H-1225-05/Site 3
41.87		0.07	5.70		53.77	0.19	0.06		101.72	XP051120/H-1225-05/Site 3
42.17		0.04	5.69		54.24	0.22	0.06		102.46	XP051120/H-1225-05/Site 3
41.89		-0.03	5.49		54.03	0.27	-0.02		101.68	XP051120/H-1225-05/Site 4
41.97		0.07	5.40		54.13	0.20	0.06		101.86	XP051120/H-1225-05/Site 4
42.50		0.11	5.46		54.34	0.24	0.09		102.78	XP051120/H-1225-05/Site 4

42.36	0.09	5.86	54.09	0.25	0.00	102.63	XP051120/H-1225-05/Site 4
42.15	0.10	5.74	54.32	0.16	0.13	102.60	XP051120/H-1225-05/Site 4
41.95	0.05	5.51	54.31	0.27	0.11	102.22	XP051120/H-1225-05/Site 5
41.93	0.10	5.51	54.32	0.22	0.09	102.26	XP051120/H-1225-05/Site 5
42.00	0.00	5.57	54.10	0.28	0.03	102.04	XP051120/H-1225-05/Site 5
41.77	0.12	5.35	54.24	0.22	-0.05	101.66	XP051120/H-1225-05/Site 5
41.75	0.17	5.44	53.80	0.32	0.05	101.55	XP051120/H-1225-05/Site 5
42.26	0.07	5.44	54.15	0.20	0.06	102.17	XP051120/H-1225-05/Site 5

Table A.7: **2 wt.% H_2O basalt clinopyroxene analyses**

SiO2	TiO2	Al2O3	FeO	MgO	CaO	Na2O	K2O	Total	Comment
48.17	0.75	8.57	9.00	15.85	17.19	1.17	0.05	100.97	H1100_10_px1
47.80	0.69	7.55	7.97	16.25	18.20	1.26	0.10	99.98	H_1200_10_Px2
48.81	0.99	6.83	7.53	16.18	17.84	0.76	0.19	99.33	H_1200_10_Px7
46.84	0.58	9.75	7.52	15.19	18.49	0.56	0.01	99.19	H-1225-10
48.22	0.57	9.42	7.60	16.01	17.99	0.52	0.01	100.60	H-1225-10
50.06		5.64	7.75	16.50	19.58	0.64	0.05	100.22	XP051120/H-1175-07/Site 1
49.28		5.55	7.25	16.60	20.05	0.40	0.02	99.16	XP051120/H-1175-07/Site 1
54.54		3.40	6.58	32.94	2.41	0.14	0.03	100.03	XP051120/H-1175-07/Site 1
53.01		3.38	5.59	19.45	19.17	0.34	0.03	100.97	XP051120/H-1175-07/Site 1
49.52		5.72	7.52	17.42	19.40	0.45	-0.01	100.01	XP051120/H-1175-07/Site 1
49.36		5.41	7.35	16.73	19.76	0.46	0.01	99.09	XP051120/H-1175-07/Site 1
48.58		6.16	8.38	16.16	19.48	0.59	0.05	99.40	XP051120/H-1175-07/Site 2
50.05		6.87	7.60	17.88	18.79	0.43	0.02	101.65	XP051120/H-1175-07/Site 3
49.79		6.86	7.55	17.90	18.67	0.47	0.11	101.34	XP051120/H-1175-07/Site 3
48.60		7.76	8.08	16.57	19.40	0.54	0.00	100.95	XP051120/H-1175-07/Site 3
49.22	0.55	6.44	7.40	16.78	17.86	0.45	0.02	98.97	H_1200_07_px
48.67	0.51	7.26	8.04	16.91	17.36	0.42	0.01	99.45	H_1200_07_px2
48.56	0.67	7.36	7.76	16.29	18.02	0.44	0.02	99.35	H_1200_07_px3
54.61		2.93	4.56	20.26	19.53	0.23	0.02	102.15	XP051120/H-1125-05/Site 1
54.00		2.35	4.27	20.73	19.21	0.29	-0.03	100.81	XP051120/H-1125-05/Site 1
55.54		1.60	5.71	20.63	18.24	0.57	0.04	102.33	XP051120/H-1125-05/Site 1
54.42		2.18	5.11	19.31	19.80	0.47	0.05	101.35	XP051120/H-1125-05/Site 2
54.89		2.83	4.00	19.59	19.93	0.28	0.05	101.56	XP051120/H-1125-05/Site 2
54.96		1.84	5.44	17.06	21.24	1.35	0.03	101.92	XP051120/H-1125-05/Site 2
55.09		2.90	4.91	17.91	18.77	1.22	0.09	100.89	XP051120/H-1125-05/Site 2

54.94	1.16	5.94	18.57	20.92	0.80	0.03	102.35	XP051120/H-1125-05/Site 2
54.68	2.65	3.82	20.23	19.95	0.22	0.09	101.65	XP051120/H-1125-05/Site 2
55.97	2.35	5.07	21.19	17.85	0.36	0.09	102.88	XP051120/H-1125-05/Site 3
55.54	2.00	4.77	20.70	18.42	0.41	0.05	101.90	XP051120/H-1125-05/Site 3

Table A.8: **2 wt.% H_2O basalt orthopyroxene analyses**

SiO2	TiO2	Al2O3	FeO	MgO	CaO	Na2O	K2O	Total	Comment
53.13	0.26	5.25	7.93	30.17	2.37	0.12	0.04	99.69	H_1200_10_Px1
52.74	0.28	8.89	7.12	26.20	3.47	0.40	0.04	99.50	H_1200_10_Px5
54.29		4.03	7.13	32.76	2.29	-0.02	0.03	100.52	XP051120/H-1175-07/Site 1
54.87		3.19	6.58	32.31	3.18	0.04	0.05	100.21	XP051120/H-1175-07/Site 1
53.31		5.10	7.25	32.16	2.15	0.03	0.04	100.05	XP051120/H-1175-07/Site 1
56.25		2.17	5.79	34.52	2.10	0.11	0.02	100.97	XP051120/H-1175-07/Site 1
54.44		4.03	7.11	32.71	2.27	0.04	0.09	100.69	XP051120/H-1175-07/Site 1
55.72		2.53	6.18	33.36	2.23	0.06	0.05	100.13	XP051120/H-1175-07/Site 1
56.28		2.95	6.48	34.09	2.13	0.08	-0.03	101.97	XP051120/H-1175-07/Site 1
55.86		3.46	7.24	32.61	2.81	0.14	0.07	102.20	XP051120/H-1175-07/Site 1
54.03		4.26	6.93	32.37	2.57	-0.01	0.08	100.22	XP051120/H-1175-07/Site 1
55.05		2.81	6.76	32.89	2.47	0.09	0.05	100.13	XP051120/H-1175-07/Site 1
53.88		4.34	6.81	32.66	2.15	0.05	0.06	99.96	XP051120/H-1175-07/Site 2
53.74		4.67	6.95	33.97	2.62	0.13	0.00	102.08	XP051120/H-1175-07/Site 3
52.12	0.48	7.64	7.37	28.78	4.79	0.26	0.00	101.78	H_1200_07_opx1
57.39		1.30	7.54	33.45	2.43	0.00	-0.03	102.09	XP051120/H-1125-05/Site 1
57.22		1.69	7.62	33.54	2.64	0.09	0.03	102.83	XP051120/H-1125-05/Site 2
56.26		2.50	8.04	32.46	2.68	0.11	0.02	102.07	XP051120/H-1125-05/Site 2
57.11		2.35	7.45	33.20	2.25	0.01	0.07	102.44	XP051120/H-1125-05/Site 2
57.95		1.35	6.47	34.54	2.60	-0.04	0.06	102.93	XP051120/H-1125-05/Site 3
58.20		1.28	5.94	34.84	2.33	0.09	0.01	102.68	XP051120/H-1125-05/Site 3
58.11		1.75	5.42	34.91	2.29	0.03	0.06	102.57	XP051120/H-1125-05/Site 3
58.07		1.56	6.92	34.21	2.35	0.02	0.04	103.17	XP051120/H-1125-05/Site 3
57.48		1.59	7.28	33.81	2.38	0.04	0.10	102.68	XP051120/H-1125-05/Site 3

Table A.9: **2 wt.% H_2O basalt plagioclase analyses**

SiO2	Al2O3	FeO	MgO	CaO	Na2O	K2O	Total	Comment
51.70	29.61	1.60	0.43	12.95	3.50	0.14	100.06	H_1200_10_Px6
50.65	30.89	1.74	0.30	14.59	3.29	0.08	101.54	XP051120/H-1175-07/Site 1

50.41	30.85	1.76	0.13	14.66	3.29	0.05	101.14	XP051120/H-1175-07/Site 1
52.33	29.48	1.66	0.26	13.45	3.84	0.07	101.09	XP051120/H-1175-07/Site 1
51.38	30.85	1.85	0.15	14.50	3.40	0.04	102.18	XP051120/H-1175-07/Site 1
50.80	30.77	1.68	0.24	14.43	3.26	0.06	101.25	XP051120/H-1175-07/Site 1
51.02	29.55	1.74	0.26	13.73	3.60	0.03	99.93	XP051120/H-1175-07/Site 2
51.74	29.80	1.79	0.25	13.74	3.76	0.13	101.20	XP051120/H-1175-07/Site 2
51.55	29.54	1.79	0.40	13.32	3.67	0.11	100.40	XP051120/H-1175-07/Site 2
49.99	30.41	1.72	0.21	14.67	3.08	0.07	100.16	XP051120/H-1175-07/Site 2
51.82	29.75	1.69	0.21	13.71	3.73	0.06	100.96	XP051120/H-1175-07/Site 2
52.12	31.33	1.64	0.24	14.54	3.46	0.02	103.36	XP051120/H-1175-07/Site 3
52.13	31.10	1.76	0.24	14.15	3.51	0.07	102.95	XP051120/H-1175-07/Site 3
51.02	30.65	1.78	0.56	13.70	3.32	0.11	101.41	H_1200_07_pl
50.66	30.30	1.55	0.72	13.87	3.39	0.09	100.80	H_1200_07_pl2
50.53	30.45	1.46	0.34	13.64	3.41	0.09	100.15	H_1200_07_pl3
48.14	33.94	0.73	0.48	16.37	2.18	0.11	101.96	XP051120/H-1125-05/Site 2
49.44	31.59	0.96	1.39	15.38	2.34	0.03	101.13	XP051120/H-1125-05/Site 2
48.13	34.21	0.55	0.31	16.92	1.90	0.04	102.06	XP051120/H-1125-05/Site 2
48.88	32.65	0.77	0.61	16.22	2.16	0.13	101.41	XP051120/H-1125-05/Site 2
49.35	32.60	0.55	0.42	15.93	2.43	0.06	101.36	XP051120/H-1125-05/Site 2
51.19	29.13	2.35	2.98	14.44	2.70	0.07	102.86	XP051120/H-1125-05/Site 2
49.87	31.02	0.92	0.34	14.51	3.03	0.07	99.95	H1175_05_PL
50.12	30.58	1.21	2.06	14.24	3.05	0.06	101.50	H1175_05_PL2
49.91	31.12	0.98	0.23	14.47	2.98	0.08	99.99	H1175_05_PL3
50.01	31.15	1.05	1.41	14.43	3.09	0.07	101.42	H1175_05_PL5

Table A.10: **2 wt.% H_2O basalt glass analyses**

SiO2	TiO2	Al2O3	FeO	MgO	CaO	Na2O	K2O	Total	Comment
49.79	1.82	16.46	9.16	7.61	9.01	3.58	0.56	98.26	H_1200_10_Gl1
49.21	1.00	17.81	8.48	8.44	10.60	2.77	0.28	98.87	h1225-1gl
49.35	0.94	17.76	8.28	8.94	10.56	2.80	0.29	99.15	h1225-1gl
49.30	0.90	17.94	7.95	8.71	10.74	2.84	0.31	98.92	h1225-1gl
50.11	1.02	18.39	8.27	8.47	10.84	2.80	0.28	100.40	h1225-1gl
50.22	1.06	17.92	8.14	8.62	10.56	2.98	0.32	100.02	H_1225_1_Gl1
50.12	1.06	17.68	8.02	8.74	10.63	2.83	0.33	99.60	H_1225_1_Gl2
49.34	0.71	14.91	7.78	14.84	8.80	1.61	0.17	98.33	h1250-1gl
49.55	0.75	18.45	7.25	8.79	9.19	2.67	0.30	97.17	h1250-1gl

49.66	0.84	19.14	7.13	7.19	9.17	2.98	0.34	96.65	h1250-1gl
49.32	0.72	15.84	7.48	12.29	9.51	2.16	0.24	97.80	h1250-1gl
51.54	0.80	16.00	6.90	10.06	9.62	3.47	0.23	98.84	h1225-8gl
50.35	0.79	16.39	6.92	10.05	9.83	3.36	0.22	98.07	h1225-8gl
50.83	0.80	16.36	7.26	10.06	9.88	3.42	0.21	98.92	h1225-8gl
50.89	0.82	16.93	7.24	9.78	10.17	3.25	0.20	99.48	h1225-8gl
51.11	0.87	17.53	7.43	9.14	10.30	3.43	0.23	100.17	h1225-8gl
51.84	0.95	17.77	7.51	9.47	10.27	3.58	0.27	101.81	H1225_08_gl1
52.92		15.32	8.46	6.34	9.31	3.21	0.48	96.05	XP051120/H-1175-07/Site 1
52.65		15.28	8.59	6.48	9.54	2.97	0.43	95.93	XP051120/H-1175-07/Site 1
52.57		15.38	8.74	6.50	9.33	3.22	0.45	96.20	XP051120/H-1175-07/Site 1
52.34		15.28	8.36	6.42	9.38	3.16	0.46	95.39	XP051120/H-1175-07/Site 1
52.78		15.33	8.82	6.61	9.32	2.94	0.47	96.28	XP051120/H-1175-07/Site 2
52.53		15.12	8.54	6.58	9.26	3.17	0.38	95.59	XP051120/H-1175-07/Site 2
52.09		16.52	8.36	8.14	10.66	2.90	0.36	99.03	XP051120/H-1175-07/Site 3
52.43		16.74	8.17	8.58	10.49	2.97	0.29	99.68	XP051120/H-1175-07/Site 3
52.14		16.47	8.15	8.39	10.71	2.97	0.26	99.10	XP051120/H-1175-07/Site 3
52.44		16.53	8.04	8.31	10.85	2.95	0.33	99.47	XP051120/H-1175-07/Site 3
52.32		16.24	8.27	8.20	10.71	2.90	0.26	98.89	XP051120/H-1175-07/Site 3
49.94	1.10	16.39	8.93	8.34	10.78	2.86	0.32	98.78	h1200-7gl
50.12	1.30	15.59	9.25	8.45	10.99	2.68	0.34	98.97	H_1200_07_gl1
50.96	1.22	16.82	8.99	7.70	10.40	2.89	0.37	99.52	H_1200_07_gl2
50.38	1.22	16.42	8.91	8.45	10.57	2.80	0.28	99.22	H_1200_07_gl3
50.69	1.23	15.92	9.09	8.63	10.38	2.79	0.35	99.30	H_1200_07_gl4
51.14	0.83	17.02	7.74	9.58	10.23	2.30	0.23	99.23	h1225-7gl
51.28	0.78	17.32	7.44	9.56	10.57	2.32	0.23	99.63	h1225-7gl
51.05	0.83	17.53	7.78	9.51	10.59	2.31	0.22	100.01	h1225-7gl
50.84	0.77	17.55	7.47	9.80	10.66	2.26	0.22	99.83	h1225-7gl
51.38	0.83	17.87	7.40	9.41	10.74	2.24	0.22	100.24	h1225-7gl
50.76	0.85	17.54	7.75	9.77	10.58	2.22	0.19	99.80	h1225-7gl
50.83	0.81	17.33	7.90	9.81	10.60	2.28	0.22	100.01	h1225-7gl
50.12	0.94	17.05	7.99	8.94	10.23	2.28	0.21	97.91	H_1225_07_Gl1
50.33	0.82	16.73	6.94	10.13	10.58	2.31	0.21	98.19	h1250-7gl
50.65	0.80	16.89	7.03	10.07	10.67	2.41	0.24	98.95	h1250-7gl
50.67	0.79	16.79	7.09	10.12	10.83	2.37	0.20	99.02	h1250-7gl
50.80	0.80	16.88	7.08	9.98	10.84	2.28	0.23	99.13	h1250-7gl
50.81	0.83	16.80	7.13	9.95	10.87	2.38	0.23	99.14	h1250-7gl

49.48	0.80	16.57	7.15	10.01	10.78	2.39	0.24	97.62	h1250-7gl
50.74	0.90	16.61	7.26	9.88	10.63	2.55	0.20	98.87	H1250_07_gl1
55.72		16.96	5.27	7.10	10.45	2.90	0.30	98.71	XP051120/H-1125-05/Site 1
55.14		17.33	5.26	7.08	10.28	2.74	0.32	98.16	XP051120/H-1125-05/Site 1
56.28		17.64	4.79	6.66	10.12	2.84	0.28	98.61	XP051120/H-1125-05/Site 2
55.31		17.53	4.74	6.91	10.21	2.96	0.32	97.99	XP051120/H-1125-05/Site 2
56.09		17.35	4.73	6.82	10.36	2.88	0.30	98.52	XP051120/H-1125-05/Site 2
56.01		17.32	4.96	6.89	10.42	2.94	0.38	98.92	XP051120/H-1125-05/Site 2
56.05		17.49	4.82	6.77	10.30	3.01	0.30	98.72	XP051120/H-1125-05/Site 3
56.09		17.29	4.81	6.90	10.25	3.06	0.24	98.64	XP051120/H-1125-05/Site 3
56.52		17.29	4.54	6.90	10.09	3.11	0.30	98.74	XP051120/H-1125-05/Site 3
54.06		16.82	5.89	8.71	9.60	2.73	0.28	98.09	XP051120/H-1125-05/Site 4
54.92		17.28	5.39	7.26	10.54	2.79	0.26	98.43	XP051120/H-1125-05/Site 4
55.34		17.28	5.52	7.53	10.62	2.76	0.33	99.37	XP051120/H-1125-05/Site 4
55.13		17.54	5.58	7.36	10.80	2.82	0.31	99.54	XP051120/H-1125-05/Site 4
53.39	1.17	15.07	8.31	7.24	10.42	2.57	0.33	98.69	h1175-5gl
52.89	1.12	14.88	8.29	7.53	10.25	2.51	0.32	97.91	h1175-5gl
52.64	1.13	15.40	7.94	7.69	10.47	2.55	0.32	98.26	h1175-5gl
52.99	1.13	15.41	7.95	7.74	10.55	2.54	0.31	98.62	h1175-5gl
53.49	1.29	14.32	8.68	7.24	9.87	2.71	0.37	98.06	h1175-5gl
52.91	1.13	14.85	8.34	7.82	10.04	2.40	0.34	98.06	h1175-5gl
51.14	1.74	14.47	9.95	7.06	9.11	3.03	0.56	97.20	H1175_05_gl2
51.92		16.82	6.82	11.18	10.42	2.08	0.26	99.50	XP051120/H-1225-05/Site 1
51.44		16.63	6.72	11.04	10.41	2.13	0.21	98.59	XP051120/H-1225-05/Site 1
51.92		16.91	6.86	10.94	10.57	2.12	0.24	99.57	XP051120/H-1225-05/Site 1
51.24		16.89	6.86	10.91	10.50	2.00	0.25	98.64	XP051120/H-1225-05/Site 1
51.89		17.19	6.68	10.72	10.53	2.17	0.18	99.36	XP051120/H-1225-05/Site 2
51.84		17.16	6.78	10.53	10.34	2.15	0.29	99.10	XP051120/H-1225-05/Site 2
51.13		17.25	6.96	10.47	10.54	2.07	0.27	98.69	XP051120/H-1225-05/Site 2
51.37		17.08	7.09	10.33	10.76	2.11	0.23	98.97	XP051120/H-1225-05/Site 2
51.56		17.14	6.94	10.40	10.82	2.17	0.25	99.28	XP051120/H-1225-05/Site 2
51.92		17.11	7.03	10.29	10.83	2.07	0.23	99.47	XP051120/H-1225-05/Site 3
51.56		17.08	6.71	10.47	10.86	2.24	0.22	99.14	XP051120/H-1225-05/Site 3
51.41		16.90	6.79	10.53	10.42	2.22	0.25	98.53	XP051120/H-1225-05/Site 3
51.55		16.91	6.81	10.36	10.68	2.18	0.26	98.76	XP051120/H-1225-05/Site 3
52.10		17.05	6.90	10.66	10.44	2.28	0.19	99.63	XP051120/H-1225-05/Site 4
51.75		17.34	6.80	10.47	10.64	2.31	0.22	99.51	XP051120/H-1225-05/Site 4
51.76		17.30	6.68	10.65	10.53	2.16	0.27	99.35	XP051120/H-1225-05/Site 4
51.44		17.15	6.68	10.59	10.72	2.24	0.25	99.06	XP051120/H-1225-05/Site 4

51.50	17.10	6.85	10.69	10.58	2.23	0.23	99.18	XP051120/H-1225-05/Site 4
51.54	17.13	6.66	10.61	10.59	2.27	0.22	99.02	XP051120/H-1225-05/Site 5
51.78	17.36	6.26	10.41	9.87	2.34	0.25	98.26	XP051120/H-1225-05/Site 5
51.35	17.11	6.56	9.95	10.60	2.18	0.26	98.01	XP051120/H-1225-05/Site 5
51.60	17.06	6.56	10.56	10.52	2.11	0.30	98.70	XP051120/H-1225-05/Site 5

A.3 5 wt.% basalt analyses

Table A.11: **5 wt.% H_2O basalt olivine analyses**

SiO2	Al2O3	FeO	MgO	CaO	Na2O	K2O	Total	Comment
42.76	0.40	7.31	43.39	0.79	0.00	0.00	96.16	W-1200-10 ol2
42.30	0.15	5.50	52.84	0.25	0.17	0.06	101.26	XP041120/W-1225-10/Site 1
41.98	0.05	5.37	52.59	0.23	0.10	0.02	100.34	XP041120/W-1225-10/Site 1
42.20	0.12	5.47	52.81	0.30	0.15	0.04	101.09	XP041120/W-1225-10/Site 1
42.16	0.11	5.34	52.96	0.24	0.17	-0.04	100.93	XP041120/W-1225-10/Site 4
42.16	0.10	5.29	52.57	0.17	0.16	0.04	100.50	XP041120/W-1225-10/Site 4
42.23	0.13	5.57	52.74	0.25	0.15	0.01	101.07	XP041120/W-1225-10/Site 4
42.12	0.08	5.51	52.72	0.23	0.14	0.08	100.88	XP041120/W-1225-10/Site 4
42.07	0.01	8.19	50.78	0.30	0.00	0.06	101.42	XP051120/W-1250-10/Site 2
41.36	0.04	8.36	51.09	0.29	-0.01	0.07	101.19	XP051120/W-1250-10/Site 2
41.85	0.06	7.96	51.06	0.28	0.11	0.02	101.33	XP051120/W-1250-10/Site 2
41.37	-0.03	8.34	50.35	0.26	-0.03	0.00	100.25	XP051120/W-1250-10/Site 2
41.44	0.11	8.41	51.26	0.27	0.12	0.01	101.62	XP051120/W-1250-10/Site 2
41.45	0.04	8.35	51.12	0.27	0.03	0.11	101.37	XP051120/W-1250-10/Site 2
41.92	0.14	8.12	51.13	0.33	0.01	0.04	101.69	XP051120/W-1250-10/Site 2
41.65	0.08	8.16	50.77	0.30	0.00	0.07	101.03	XP051120/W-1250-10/Site 2
41.45	0.12	8.28	50.82	0.23	-0.02	0.05	100.93	XP051120/W-1250-10/Site 2
41.37	0.06	9.12	49.36	0.37	0.11	-0.02	100.36	XP041120/W-1150-07/Site 1
41.36	0.11	9.27	49.46	0.34	0.06	0.07	100.66	XP041120/W-1150-07/Site 1
40.88	0.08	9.23	48.51	0.39	0.04	0.03	99.17	XP041120/W-1150-07/Site 1
41.53	0.15	8.39	50.32	0.29	0.14	-0.01	100.81	XP041120/W-1150-07/Site 2
41.72	0.65	8.61	49.32	0.59	0.12	0.09	101.09	XP041120/W-1150-07/Site 3
41.18	0.24	8.80	50.11	0.24	0.08	0.05	100.69	XP041120/W-1150-07/Site 3
41.64	0.08	9.14	49.81	0.28	0.03	0.06	101.04	XP041120/W-1150-07/Site 1
41.25	0.07	8.14	49.55	0.27	0.00	0.00	100.44	W-1175-07 ol1
41.64	0.05	8.11	49.35	0.25	0.00	0.00	100.52	W-1175-07 ol2

41.63	0.07	8.25	49.56	0.26	0.00	0.00	100.90	W-1175-07 ol3
41.66	0.05	8.38	49.50	0.26	0.00	0.00	100.97	W-1175-07 ol4
41.76	0.07	6.44	50.44	0.26	0.00	0.00	100.16	W-1200-07 ol1
41.70	0.08	6.66	49.86	0.27	0.00	0.00	99.70	W-1200-07 ol2
41.83	0.06	6.61	50.25	0.27	0.00	0.00	100.14	W-1200-07 ol3
41.86	0.06	6.72	50.68	0.24	0.00	0.00	100.75	W-1200-07 ol4
40.14	0.09	6.73	49.15	0.24	0.00	0.00	97.71	W-1225-07 ol1
41.33	0.09	6.67	50.52	0.24	0.00	0.00	100.18	W-1225-07 ol2
41.28	0.08	6.88	50.28	0.24	0.00	0.00	99.98	W-1225-07 ol3
40.77	0.09	7.15	50.22	0.25	0.00	0.00	99.78	W-1225-07 ol4
40.82	0.03	11.08	49.10	0.38	0.04	0.02	101.47	XP041120/W-1150-05/Site 1
41.01	0.16	10.90	48.46	0.37	0.07	0.04	101.01	XP041120/W-1150-05/Site 1
41.13	0.08	11.06	49.07	0.31	0.04	0.08	101.76	XP041120/W-1150-05/Site 1
41.11	0.59	10.91	48.14	0.71	0.04	-0.04	101.45	XP041120/W-1150-05/Site 1
40.77	0.12	10.92	48.77	0.43	-0.01	0.00	100.99	XP041120/W-1150-05/Site 1
41.12	0.27	10.71	48.73	0.33	0.05	0.02	101.23	XP041120/W-1150-05/Site 2
41.66	0.35	10.82	48.74	0.34	0.02	0.04	101.96	XP041120/W-1150-05/Site 2
42.25	0.10	7.77	51.42	0.38	0.03	0.02	101.96	XP041120/W-1200-05/Site 1
41.50	0.01	7.78	51.32	0.28	0.12	0.05	101.06	XP041120/W-1200-05/Site 1
42.30	0.58	7.86	51.01	0.61	0.09	0.06	102.49	XP041120/W-1200-05/Site 1
41.48	0.08	8.13	51.67	0.29	0.03	0.00	101.68	XP041120/W-1200-05/Site 2
41.74	0.11	7.92	51.12	0.33	0.14	0.02	101.40	XP041120/W-1200-05/Site 2
42.08	0.04	8.05	51.22	0.22	0.07	0.08	101.76	XP041120/W-1200-05/Site 2
42.31	0.17	7.98	51.22	0.25	0.22	0.13	102.28	XP041120/W-1200-05/Site 3
41.72	0.01	6.20	52.46	0.24	0.00	0.06	100.70	XP041120/W-1225-05/Site 1
42.12	0.05	6.33	52.84	0.29	0.11	0.04	101.78	XP041120/W-1225-05/Site 1
42.13	0.16	6.22	52.83	0.32	0.13	0.02	101.82	XP041120/W-1225-05/Site 1
42.03	0.08	6.10	52.24	0.21	-0.01	0.02	100.68	XP041120/W-1225-05/Site 2
41.45	0.10	6.15	52.78	0.26	0.17	0.06	100.96	XP041120/W-1225-05/Site 2
42.27	0.04	6.19	53.07	0.24	-0.02	0.10	101.90	XP041120/W-1225-05/Site 2
42.35	0.02	6.17	53.02	0.31	0.14	0.05	102.05	XP041120/W-1225-05/Site 2
42.07	0.20	6.18	52.81	0.28	0.05	0.03	101.62	XP041120/W-1225-05/Site 3
41.87	0.09	6.21	52.74	0.25	0.13	0.08	101.37	XP041120/W-1225-05/Site 3
42.23	0.09	6.14	52.65	0.22	-0.07	0.04	101.29	XP041120/W-1225-05/Site 4
41.70	0.12	6.00	52.90	0.25	0.10	0.00	101.07	XP041120/W-1225-05/Site 4
41.53	0.10	6.19	52.44	0.21	0.06	0.06	100.59	XP041120/W-1225-05/Site 4
42.30	0.10	6.19	53.05	0.31	0.06	0.06	102.07	XP041120/W-1225-05/Site 4

Table A.12: **5 wt.% H_2O basalt clinopyroxene analyses**

SiO2	TiO2	Al2O3	FeO	MgO	CaO	Na2O	K2O	Total	Comment
49.54	0.91	7.33	7.99	15.65	17.32	0.52	0.01	99.48	W1175-10 cpx
46.61	0.74	6.67	7.69	14.41	17.28	0.52	0.01	94.14	W1175-10 cpx2
47.51	0.88	7.35	8.41	14.09	18.79	0.49	0.01	97.73	W1175-10 cpx3
48.83	0.64	7.13	7.65	16.68	17.10	0.52	0.01	98.83	W-1200-10 cpx1
48.33	0.50	6.46	8.22	15.93	16.94	0.46	0.01	97.10	W-1200-10 cpx2
47.96	0.55	7.00	7.80	13.99	19.33	0.44	0.01	97.34	W-1200-10 cpx3
46.63	0.79	8.48	8.93	13.09	19.44	0.50	0.00	98.15	W-1200-10 cpx4
47.25		11.00	8.19	15.10	19.45	0.56	0.06	101.62	XP041120/W-1225-10/Site 2
51.99		6.43	6.25	20.85	16.28	0.45	0.07	102.32	XP041120/W-1225-10/Site 2
45.89		10.97	8.44	14.72	20.03	0.49	0.03	100.58	XP041120/W-1225-10/Site 2
51.17		7.30	6.53	18.06	19.06	0.62	0.11	102.85	XP041120/W-1225-10/Site 2
47.02		10.74	8.35	14.76	19.93	0.58	0.10	101.49	XP041120/W-1225-10/Site 2
52.15		6.09	6.18	20.48	16.98	0.50	0.05	102.42	XP041120/W-1225-10/Site 2
46.95		10.91	7.85	15.23	19.63	0.52	0.02	101.11	XP041120/W-1225-10/Site 2
51.82		6.63	6.25	20.57	17.04	0.50	0.04	102.86	XP041120/W-1225-10/Site 7
47.22		10.81	8.01	15.67	19.36	0.63	0.07	101.77	XP041120/W-1225-10/Site 7
46.96		10.61	7.63	15.57	19.54	0.57	0.06	100.94	XP041120/W-1225-10/Site 7
52.57		5.72	5.59	20.96	16.77	0.34	0.02	101.98	XP041120/W-1225-10/Site 7
50.51		5.22	7.68	18.36	18.27	0.40	0.09	100.53	XP041120/W-1150-07/Site 1
51.01		5.33	7.76	17.78	19.15	0.45	0.02	101.50	XP041120/W-1150-07/Site 1
50.59		6.03	8.00	17.63	19.04	0.39	0.05	101.73	XP041120/W-1150-07/Site 1
49.84		6.27	7.67	16.99	19.71	0.44	0.02	100.94	XP041120/W-1150-07/Site 1
49.79		5.61	7.83	17.04	19.42	0.31	0.06	100.06	XP041120/W-1150-07/Site 1
52.25		5.49	6.39	18.95	17.49	0.36	0.09	101.03	XP041120/W-1150-07/Site 2
51.26		5.82	7.00	18.37	19.20	0.41	0.03	102.08	XP041120/W-1150-07/Site 2
51.38		5.19	6.95	18.70	18.39	0.40	0.09	101.11	XP041120/W-1150-07/Site 2
51.54		5.93	6.74	17.85	18.74	0.40	0.09	101.29	XP041120/W-1150-07/Site 2
50.68		5.46	7.04	17.67	20.04	0.36	0.06	101.32	XP041120/W-1150-07/Site 3
51.55		5.19	6.79	18.29	18.20	0.29	0.11	100.41	XP041120/W-1150-07/Site 3
54.49		3.61	5.48	19.41	18.77	0.34	0.11	102.20	XP041120/W-1150-05/Site 1
54.27		5.37	5.39	17.68	18.55	0.49	0.11	101.87	XP041120/W-1150-05/Site 1
53.89		2.72	5.77	19.79	19.45	0.18	-0.01	101.79	XP041120/W-1150-05/Site 2
53.76		2.68	5.22	19.59	19.31	0.26	0.08	100.91	XP041120/W-1150-05/Site 2
54.53		3.30	5.36	19.32	19.24	0.27	0.08	102.10	XP041120/W-1150-05/Site 2
53.97		4.71	5.26	18.14	19.20	0.34	0.16	101.77	XP041120/W-1150-05/Site 2

Table A.13: **5 wt.% H_2O basalt orthopyroxene analyses**

SiO2	Al2O3	FeO	MgO	CaO	Na2O	K2O	Total	Comment
51.00	4.39	8.88	30.26	2.01	0.00	0.00	96.94	W1175-10 opx1
52.44	5.37	8.35	30.98	2.34	0.00	0.00	99.87	W-1200-10 opx2
52.52	6.55	8.38	30.22	1.95	0.00	0.00	100.06	W-1200-10 opx3
52.76	5.98	7.82	31.58	2.08	0.00	0.00	100.63	W-1200-10 opx4
51.38	4.29	8.54	30.32	2.41	0.00	0.00	97.36	W-1200-10 ol1
53.30	7.22	6.67	33.14	1.89	0.02	0.06	102.31	XP041120/W-1225-10/Site 1
57.18	3.84	5.00	35.34	1.65	0.18	0.05	103.23	XP041120/W-1225-10/Site 1
56.27	3.70	5.11	35.00	1.64	0.06	-0.01	101.77	XP041120/W-1225-10/Site 1
53.85	7.31	6.45	33.09	1.65	0.09	0.00	102.45	XP041120/W-1225-10/Site 2
53.73	7.56	6.88	33.16	1.59	0.12	0.12	103.17	XP041120/W-1225-10/Site 2
53.27	7.71	6.93	32.87	1.74	0.05	0.03	102.59	XP041120/W-1225-10/Site 2
53.57	7.14	6.69	33.19	1.69	0.14	0.04	102.47	XP041120/W-1225-10/Site 2
53.99	7.29	6.76	32.81	1.85	0.14	0.04	102.88	XP041120/W-1225-10/Site 3
56.55	4.51	5.38	34.80	1.93	0.05	0.02	103.25	XP041120/W-1225-10/Site 3
52.93	8.78	7.22	32.31	1.86	0.13	0.04	103.27	XP041120/W-1225-10/Site 3
56.22	4.47	5.58	34.63	1.76	0.15	0.08	102.88	XP041120/W-1225-10/Site 3
50.00	5.54	8.74	31.36	3.57	0.42	0.14	99.78	XP041120/W-1150-07/Site 1
54.32	4.19	8.58	31.63	2.51	0.14	0.01	101.39	XP041120/W-1150-07/Site 1
54.88	3.82	8.42	32.30	2.18	0.11	0.04	101.75	XP041120/W-1150-07/Site 1
54.35	4.60	8.88	31.31	2.55	0.12	0.07	101.87	XP041120/W-1150-07/Site 1
54.64	3.98	8.33	31.62	2.26	0.08	0.03	100.94	XP041120/W-1150-07/Site 1
54.91	4.05	8.10	32.46	2.41	0.12	0.00	102.05	XP041120/W-1150-07/Site 2
55.58	3.79	8.10	32.87	2.21	0.12	0.05	102.71	XP041120/W-1150-07/Site 2
54.86	4.27	8.06	32.00	2.73	-0.01	0.05	101.96	XP041120/W-1150-07/Site 2
54.65	4.36	8.40	31.86	2.37	0.03	0.05	101.73	XP041120/W-1150-07/Site 2
54.39	4.68	8.50	31.86	2.29	0.04	0.05	101.82	XP041120/W-1150-07/Site 3
53.48	5.20	8.62	30.35	2.05	0.00	0.00	100.02	W-1175-07 opx1
52.41	4.99	8.47	31.43	1.88	0.00	0.00	99.53	W-1175-07 opx2
51.75	7.08	8.11	30.81	1.75	0.00	0.00	99.91	W-1225-07 opx1

Table A.14: **5 wt.% H_2O basalt plagioclase analyses**

SiO2	Al2O3	FeO	MgO	CaO	Na2O	K2O	Total	Comment
51.10	29.30	1.94	0.87	13.56	3.67	0.26	101.35	W1175-10 plag1

51.06	29.36	1.53	0.36	13.79	3.88	0.15	100.46	W1175-10 plag3
51.08	29.33	1.73	0.61	13.68	3.77	0.20	100.90	
0.02	0.03	0.21	0.26	0.12	0.11	0.05	0.45	
51.56	30.34	1.74	0.23	14.12	3.59	0.11	101.90	W-1200-10 plag2
51.59	30.02	1.81	0.22	14.58	3.54	0.11	102.13	W-1200-10 plag3
50.59	29.93	1.67	0.23	14.34	3.46	0.11	100.53	W-1200-10 plag4
51.24	30.10	1.74	0.23	14.35	3.53	0.11	101.52	
0.46	0.17	0.06	0.00	0.19	0.05	0.00	0.71	
48.27	32.53	2.02	0.42	16.81	1.96	0.08	102.09	XP041120/W-1150-07/Site 1
51.00	28.79	2.28	0.84	13.80	3.21	0.18	100.11	XP041120/W-1150-07/Site 1
45.91	33.78	1.97	0.49	17.87	1.00	0.09	101.11	XP041120/W-1150-07/Site 1
51.67	30.08	1.99	0.65	14.08	3.37	0.11	101.94	XP041120/W-1150-07/Site 2
51.43	28.98	3.16	1.06	13.44	3.43	0.22	101.73	XP041120/W-1150-07/Site 3
51.12	29.32	2.30	0.83	13.88	3.25	0.14	100.84	XP041120/W-1150-07/Site 3
49.90	30.58	2.29	0.72	14.98	2.70	0.14	101.30	
2.11	1.90	0.41	0.22	1.71	0.91	0.05	0.69	
51.10	27.75	1.46	0.26	14.40	3.05	0.07	98.30	W-1175-07 pl1
50.50	30.01	1.45	0.24	14.82	3.21	0.07	100.48	W-1175-07 pl2
50.18	31.03	1.42	0.28	15.54	2.98	0.06	101.73	W-1175-07 pl3
51.05	29.96	1.74	0.28	14.91	3.13	0.07	101.38	W-1175-07 pl4
50.71	29.69	1.52	0.26	14.92	3.09	0.07	100.47	
0.38	1.20	0.13	0.02	0.41	0.09	0.00	1.33	
50.48	30.63	1.31	0.24	15.12	2.94	0.07	100.98	W-1200-07 pl1
49.94	29.79	1.28	0.85	14.85	2.83	0.06	99.79	W-1200-07 pl3
51.03	31.55	1.30	0.20	15.41	2.90	0.07	102.64	W-1200-07 pl4
50.48	30.65	1.30	0.43	15.13	2.89	0.07	101.14	
0.45	0.72	0.01	0.30	0.23	0.05	0.00	1.17	
49.89	30.40	1.32	0.24	14.96	3.07	0.08	100.12	W-1225-07 pl1
50.68	29.87	1.42	0.25	14.45	3.22	0.09	100.15	W-1225-07 pl2
50.47	29.98	1.34	0.23	14.84	3.16	0.08	100.29	W-1225-07 plag3
50.67	30.12	1.42	0.24	14.69	3.16	0.08	100.57	W-1225-07 plag4

50.43	30.09	1.37	0.24	14.74	3.15	0.08	100.28	
0.32	0.20	0.04	0.01	0.19	0.06	0.00	0.18	
51.64	29.94	1.87	1.00	14.30	3.22	0.08	102.06	XP041120/W-1150-05/Site 1
47.67	32.86	1.55	0.55	17.05	1.81	0.08	101.58	XP041120/W-1150-05/Site 1
50.95	25.96	3.25	3.85	12.64	3.13	0.18	99.98	XP041120/W-1150-05/Site 1
51.96	29.34	1.99	1.11	13.98	3.19	0.14	101.72	XP041120/W-1150-05/Site 1
47.31	33.14	1.52	0.91	16.94	1.58	0.05	101.46	XP041120/W-1150-05/Site 2
51.25	29.09	2.26	1.36	14.48	2.94	0.14	101.52	XP041120/W-1150-05/Site 2
50.13	30.06	2.07	1.46	14.90	2.65	0.11	101.39	
1.90	2.44	0.58	1.09	1.60	0.68	0.04	0.66	
51.02	28.51	2.98	1.96	14.17	2.89	0.17	101.70	XP041120/W-1200-05/Site 1
48.58	32.24	2.11	0.72	16.69	2.06	0.11	102.52	XP041120/W-1200-05/Site 2
51.19	31.04	1.88	0.52	14.76	3.07	0.13	102.59	XP041120/W-1200-05/Site 2
51.08	31.97	1.64	0.62	15.29	3.00	0.10	103.70	XP041120/W-1200-05/Site 3
51.08	31.14	1.94	0.46	15.48	2.94	0.24	103.29	XP041120/W-1200-05/Site 3

Table A.15: **5 wt.% H_2O basalt glass analyses**

SiO2	**TiO2**	**Al2O3**	**FeO**	**MgO**	**CaO**	**Na2O**	**K2O**	**Total**	**Comment**
50.00	2.30	17.34	7.03	5.95	7.91	4.71	0.92	96.45	W1175-10 melt1
50.08	2.26	17.14	7.21	5.70	8.22	4.60	1.03	96.51	W1175-10 melt2
49.98	2.25	17.33	6.91	5.83	8.46	4.68	0.90	96.66	W1175-10 melt3
50.02	2.27	17.27	7.05	5.82	8.20	4.67	0.95	96.54	
0.05	0.02	0.09	0.12	0.10	0.23	0.05	0.05	0.09	
49.25	1.83	17.37	8.40	6.26	9.42	3.73	0.68	97.20	W-1200-10 melt1
50.60	1.85	17.10	8.20	6.68	9.33	3.76	0.69	98.49	W-1200-10 melt2
50.07	1.84	17.27	8.31	6.77	9.05	3.67	0.71	97.96	W-1200-10 melt3
49.08	1.91	16.64	8.37	6.76	9.70	3.70	0.60	97.02	W-1200-10 melt4
50.17	1.95	17.13	8.68	6.98	9.24	3.71	0.61	98.77	W-1200-10 melt5
49.83	1.88	17.10	8.39	6.69	9.35	3.71	0.66	97.89	
0.58	0.05	0.25	0.16	0.24	0.21	0.03	0.04	0.69	
49.34		17.80	8.05	9.99	11.18	2.55	0.32	99.23	XP041120/W-1225-10/Site 1
49.48		17.68	8.32	9.96	11.26	2.49	0.37	99.54	XP041120/W-1225-10/Site 1
49.56		17.78	8.38	9.73	11.48	2.55	0.40	99.87	XP041120/W-1225-10/Site 1
49.88		18.73	8.41	8.84	11.01	2.47	0.35	99.69	XP041120/W-1225-10/Site 2

49.72	18.74	8.17	9.13	10.92	2.45	0.40	99.55	XP041120/W-1225-10/Site 2
49.86	18.50	8.03	9.29	11.32	2.68	0.37	100.05	XP041120/W-1225-10/Site 3
49.50	18.60	8.03	9.20	11.34	2.64	0.39	99.70	XP041120/W-1225-10/Site 3
49.50	18.35	8.40	9.44	11.26	2.50	0.37	99.81	XP041120/W-1225-10/Site 4
49.15	18.50	7.95	9.80	11.14	2.52	0.39	99.44	XP041120/W-1225-10/Site 4
49.72	18.62	8.37	9.52	11.33	2.61	0.41	100.57	XP041120/W-1225-10/Site 4
49.36	18.50	8.29	9.01	11.62	2.52	0.42	99.73	XP041120/W-1225-10/Site 4
49.94	18.71	8.23	9.82	11.34	2.78	0.28	101.08	XP041120/W-1225-10/Site 5
49.21	18.13	8.05	9.64	11.30	2.57	0.36	99.26	XP041120/W-1225-10/Site 7
49.51	18.23	8.26	9.79	11.44	2.60	0.38	100.21	XP041120/W-1225-10/Site 7
49.55	18.35	8.21	9.51	11.28	2.57	0.37	99.84	
0.24	0.36	0.16	0.35	0.17	0.09	0.04	0.49	
50.60	18.14	6.72	8.84	10.71	3.63	0.40	99.03	XP051120/W-1250-10/Site 2
50.89	18.35	6.72	8.60	10.63	3.70	0.36	99.25	XP051120/W-1250-10/Site 2
51.17	18.46	6.61	8.80	10.77	3.83	0.38	100.02	XP051120/W-1250-10/Site 2
51.18	18.41	6.79	8.72	10.67	3.75	0.36	99.89	XP051120/W-1250-10/Site 2
50.88	18.08	6.45	8.95	10.92	3.70	0.37	99.36	XP051120/W-1250-10/Site 2
51.12	18.40	6.83	8.80	10.70	3.80	0.36	100.01	XP051120/W-1250-10/Site 2
50.58	18.27	6.48	8.75	10.51	3.69	0.37	98.64	XP051120/W-1250-10/Site 2
50.91	18.15	6.84	8.58	10.62	3.84	0.38	99.32	XP051120/W-1250-10/Site 2
50.77	18.09	6.46	8.53	10.63	3.70	0.42	98.62	XP051120/W-1250-10/Site 2
51.25	18.47	6.61	8.77	10.69	3.80	0.35	99.95	XP051120/W-1250-10/Site 2
50.94	18.28	6.65	8.73	10.69	3.74	0.38	99.41	
0.23	0.15	0.14	0.12	0.10	0.07	0.02	0.51	
51.05	15.04	10.16	6.89	9.51	2.36	0.64	95.65	XP041120/W-1150-07/Site 1
50.80	15.21	10.71	7.09	10.02	2.44	0.52	96.80	XP041120/W-1150-07/Site 1
50.24	14.52	10.33	7.84	9.46	2.23	0.50	95.12	XP041120/W-1150-07/Site 1
51.33	16.09	9.18	8.35	10.26	2.54	0.66	98.40	XP041120/W-1150-07/Site 1
51.68	16.70	8.44	7.46	10.46	2.85	0.48	98.07	XP041120/W-1150-07/Site 2
52.42	16.67	8.36	7.75	10.00	2.64	0.58	98.42	XP041120/W-1150-07/Site 2
51.68	16.56	8.29	7.87	10.34	2.61	0.51	97.86	XP041120/W-1150-07/Site 2
51.38	14.96	10.14	7.92	10.22	2.39	0.52	97.52	XP041120/W-1150-07/Site 3
52.18	16.96	8.62	6.89	10.20	2.71	0.60	98.15	XP041120/W-1150-07/Site 3
51.42	16.43	8.66	8.81	9.55	2.71	0.39	97.98	XP041120/W-1150-07/Site 3
51.42	15.91	9.29	7.69	10.00	2.55	0.54	97.40	
0.60	0.84	0.90	0.59	0.35	0.18	0.08	1.11	

52.00	1.28	15.23	8.71	6.82	11.08	2.50	0.33	98.13	W-1175-07 melt1
51.35	1.28	15.80	8.00	7.01	10.73	2.76	0.43	97.54	W-1175-07 melt2
51.17	1.29	15.54	7.93	6.71	11.02	2.57	0.39	96.78	W-1175-07 melt3
51.96	1.28	15.97	8.17	7.01	10.89	2.63	0.38	98.47	W-1175-07 melt4
51.62	1.28	15.63	8.20	6.89	10.93	2.62	0.38	97.73	
0.36	0.00	0.28	0.31	0.13	0.13	0.10	0.04	0.64	
51.17	1.15	16.12	8.64	7.15	11.31	2.45	0.26	98.41	W-1200-07 melt1
51.06	1.16	15.63	8.74	7.30	10.81	2.64	0.31	97.82	W-1200-07 melt2
51.15	1.16	16.20	8.33	7.18	10.97	2.43	0.31	97.90	W-1200-07 melt3
51.99	1.17	15.75	9.06	7.14	11.01	2.67	0.29	99.25	W-1200-07 melt4
51.34	1.16	15.93	8.69	7.19	11.02	2.55	0.29	98.35	
0.38	0.00	0.24	0.26	0.06	0.18	0.11	0.02	0.57	
49.45	1.04	16.62	8.37	7.90	10.60	2.43	0.27	96.88	W-1225-07 melt2
50.55	1.07	16.18	8.76	8.36	10.61	2.11	0.28	98.12	W-1225-07 melt3
49.54	1.12	16.20	8.39	7.80	10.69	2.44	0.34	96.68	W-1225-07 melt4
49.71	1.10	16.40	8.72	8.09	10.28	2.29	0.31	97.11	W-1225-07 melt5
49.81	1.08	16.35	8.56	8.04	10.54	2.32	0.30	97.20	
0.44	0.03	0.18	0.18	0.21	0.16	0.13	0.03	0.55	
53.85		16.65	7.31	6.25	10.56	2.42	0.49	97.51	XP041120/W-1150-05/Site 1
53.67		16.90	7.35	7.27	10.93	2.34	0.51	98.97	XP041120/W-1150-05/Site 1
53.77		16.10	7.26	7.53	9.73	2.37	0.57	97.33	XP041120/W-1150-05/Site 1
53.65		16.10	7.47	6.70	10.83	2.27	0.56	97.58	XP041120/W-1150-05/Site 2
53.35		17.46	6.43	6.73	11.20	2.27	0.39	97.83	XP041120/W-1150-05/Site 2
53.90		16.63	7.08	6.99	11.29	2.23	0.50	98.62	XP041120/W-1150-05/Site 2
52.95		15.06	7.58	7.02	11.13	2.19	0.48	96.40	XP041120/W-1150-05/Site 2
53.59		16.41	7.21	6.93	10.81	2.30	0.50	97.75	
0.31		0.70	0.35	0.39	0.50	0.08	0.06	0.79	
52.60		16.46	8.67	8.77	11.06	2.34	0.40	100.30	XP041120/W-1200-05/Site 1
52.43		16.58	8.67	8.50	11.20	2.34	0.44	100.16	XP041120/W-1200-05/Site 1
52.07		16.52	8.63	8.68	11.11	2.32	0.38	99.70	XP041120/W-1200-05/Site 2
51.91		16.41	8.42	8.70	11.14	2.32	0.44	99.34	XP041120/W-1200-05/Site 2
52.20		16.49	8.38	8.91	11.01	2.31	0.43	99.73	XP041120/W-1200-05/Site 2
54.07		15.77	8.11	8.51	10.20	2.52	0.53	99.72	XP041120/W-1200-05/Site 3
53.65		16.39	8.33	7.75	10.92	2.36	0.62	100.01	XP041120/W-1200-05/Site 3

53.51	16.16	7.97	7.70	11.13	2.48	0.53	99.47	XP041120/W-1200-05/Site 3
52.81	16.35	8.40	8.44	10.97	2.37	0.47	99.80	
0.77	0.25	0.24	0.43	0.30	0.07	0.08	0.31	
51.18	17.56	7.35	10.85	10.97	2.39	0.30	100.59	XP041120/W-1225-05/Site 1
51.61	17.30	7.40	10.76	10.87	2.39	0.28	100.61	XP041120/W-1225-05/Site 1
51.31	17.56	7.36	10.72	10.70	2.42	0.43	100.51	XP041120/W-1225-05/Site 1
51.25	17.56	7.15	10.66	10.97	2.29	0.28	100.17	XP041120/W-1225-05/Site 2
51.44	17.55	7.41	10.74	10.93	2.29	0.30	100.66	XP041120/W-1225-05/Site 2
51.49	17.59	7.43	10.78	11.06	2.33	0.35	101.03	XP041120/W-1225-05/Site 2
50.94	17.66	7.37	10.92	10.95	2.18	0.33	100.35	XP041120/W-1225-05/Site 2
51.40	17.48	7.19	10.75	10.87	2.31	0.33	100.33	XP041120/W-1225-05/Site 3
51.53	17.83	7.38	10.60	11.08	2.27	0.36	101.05	XP041120/W-1225-05/Site 3
51.36	17.75	7.29	10.72	11.14	2.41	0.28	100.94	XP041120/W-1225-05/Site 3
51.20	17.60	7.22	10.71	10.99	2.29	0.33	100.33	XP041120/W-1225-05/Site 3
51.86	17.49	7.37	10.72	10.99	2.21	0.32	100.95	XP041120/W-1225-05/Site 4
51.54	18.00	7.27	10.94	10.76	2.26	0.32	101.09	XP041120/W-1225-05/Site 4
51.51	17.57	7.31	10.69	10.95	2.27	0.30	100.61	XP041120/W-1225-05/Site 4

A.4 2 wt.% HMBA analyses

Table A.16: **2 wt.% H_2O HMBA clinopyroxene analyses**

SiO2	Al2O3	FeO	MgO	CaO	Na2O	K2O	Total	Project Path
53.09	2.78	5.73	18.73	19.68	0.57	0.06	100.65	XP051120/BA-1150-07/Site 3
54.46	1.89	5.03	19.95	18.88	0.45	0.05	100.71	XP051120/BA-1150-07/Site 3
53.76	1.99	5.26	20.99	17.65	0.48	-0.04	100.10	XP051120/BA-1150-07/Site 3
52.96	3.11	5.92	18.79	18.53	0.45	0.04	99.81	XP051120/BA-1150-07/Site 3
53.87	2.09	5.22	20.11	18.37	0.49	0.04	100.20	XP051120/BA-1150-07/Site 3
53.24	3.27	5.97	17.95	18.70	0.77	0.06	99.95	XP051120/BA-1150-07/Site 3
52.58	3.19	6.03	18.49	19.18	0.62	0.08	100.16	XP051120/BA-1150-07/Site 3
53.83	1.99	4.76	17.90	21.48	0.84	0.06	100.86	XP051120/BA-1150-07/Site 4
51.75	4.09	7.31	17.73	19.50	0.53	0.08	101.00	XP051120/BA-1150-07/Site 4
51.25	3.53	9.50	17.82	18.34	0.44	0.07	100.94	XP051120/BA-1150-07/Site 4
53.20	4.05	6.64	18.96	17.63	0.85	0.06	101.38	XP051120/BA-1175-10/Site 1
55.36	1.32	6.39	18.43	18.63	1.49	0.00	101.63	XP051120/BA-1175-10/Site 1
53.66	4.29	6.63	19.14	17.11	0.75	0.02	101.60	XP051120/BA-1175-10/Site 1
53.43	3.71	6.58	18.77	17.23	0.92	0.01	100.66	XP051120/BA-1175-10/Site 1

51.10	5.85	8.12	16.54	18.47	0.94	0.06	101.07	XP051120/BA-1175-10/Site 2
53.89	3.08	6.56	19.42	18.11	0.92	0.02	102.00	XP051120/BA-1175-10/Site 2
54.02	3.39	6.74	19.19	17.07	0.95	0.04	101.41	XP051120/BA-1175-10/Site 2
50.26	5.85	8.22	16.26	18.64	0.80	0.08	100.12	XP051120/BA-1175-10/Site 2
55.12	1.74	5.61	19.63	18.64	0.93	0.06	101.73	XP051120/BA-1175-10/Site 3
53.92	2.53	6.06	19.38	17.67	0.79	-0.04	100.31	XP051120/BA-1175-10/Site 4
55.52	1.36	5.70	17.63	18.80	2.14	0.03	101.18	XP051120/BA-1175-10/Site 6
53.20	6.05	7.47	15.94	17.54	1.07	0.09	101.35	XP051120/BA-1175-10/Site 7
56.26	1.30	6.21	22.06	16.43	0.55	0.05	102.87	XP051120/BA-1090-10/Site 1
56.25	1.05	5.86	21.20	17.51	0.61	0.06	102.53	XP051120/BA-1090-10/Site 1
55.88	1.27	5.51	19.51	18.70	0.63	0.09	101.59	XP051120/BA-1090-10/Site 1
56.58	1.13	5.67	20.46	17.88	0.64	0.07	102.43	XP051120/BA-1090-10/Site 2
54.62	3.91	5.90	16.73	18.14	1.00	0.16	100.46	XP051120/BA-1090-10/Site 3
51.93	2.90	5.96	18.67	18.34	0.47	0.09	98.35	XP051120/BA-1090-10/Site 3
55.74	1.22	5.55	19.82	17.94	0.52	0.06	100.85	XP051120/BA-1090-10/Site 3
56.60	1.47	6.24	21.44	16.43	0.66	0.11	102.95	XP051120/BA-1090-10/Site 3
55.06	1.28	5.66	19.16	18.59	0.69	0.05	100.49	XP051120/BA-1090-10/Site 3
56.12	0.82	6.25	18.31	18.25	1.99	0.04	101.78	XP051120/BA-1090-10/Site 4
56.07	2.20	5.64	20.95	16.75	0.59	0.04	102.25	XP051120/BA-1090-10/Site 4
54.16	2.62	5.88	19.09	18.96	0.55	0.03	101.29	XP051120/BA-1090-10/Site 4
54.47	2.17	5.62	18.50	19.27	0.82	0.03	100.88	XP051120/BA-1090-10/Site 5
55.87	1.19	5.14	21.26	17.65	0.50	0.05	101.65	XP051120/BA-1090-10/Site 5
54.36	3.07	5.75	18.99	18.73	0.62	0.07	101.59	XP051120/BA-1090-10/Site 5
55.81	2.09	5.75	20.56	16.94	0.52	0.11	101.78	XP051120/BA-1090-10/Site 5
56.72	1.08	5.71	22.52	15.72	0.89	-0.01	102.64	XP051120/BA-1090-10/Site 5
55.60	1.43	5.88	18.93	18.10	1.20	0.03	101.17	XP051120/BA-1065-05/Site 1
54.42	1.90	6.19	18.70	18.52	0.63	0.04	100.39	XP051120/BA-1065-05/Site 1
55.78	0.74	5.47	19.06	19.66	0.83	0.11	101.65	XP051120/BA-1065-05/Site 1
54.62	1.11	6.15	18.30	19.42	0.91	0.07	100.58	XP051120/BA-1065-05/Site 1
54.66	0.99	6.60	20.83	16.62	0.26	0.07	100.03	XP051120/BA-1065-05/Site 2
53.36	3.88	5.69	19.11	17.94	0.34	0.04	100.36	XP051120/BA-1065-05/Site 3
56.79	1.17	6.32	20.31	17.96	0.32	0.11	102.98	XP051120/BA-1065-05/Site 4
55.30	0.71	5.88	20.10	18.62	0.33	0.03	100.96	XP051120/BA-1065-05/Site 4
55.86	0.70	5.52	19.86	19.02	0.48	0.10	101.55	XP051120/BA-1065-05/Site 4
55.08	0.79	5.98	18.66	19.67	0.55	0.01	100.74	XP051120/BA-1065-05/Site 4
54.93	0.89	4.12	19.89	20.27	0.25	0.08	100.42	XP041120/BA-1110-05/Site 1
56.22	1.02	3.08	20.69	19.84	0.32	0.06	101.23	XP041120/BA-1110-05/Site 1
56.35	0.65	4.85	22.93	16.83	0.30	0.05	101.96	XP041120/BA-1110-05/Site 1
55.22	1.51	4.73	20.25	19.39	0.43	0.10	101.64	XP041120/BA-1110-05/Site 3

55.55	0.75	5.21	18.19	19.47	1.43	0.01	100.62	XP041120/BA-1110-05/Site 3
55.43	1.21	5.66	21.52	17.54	0.40	0.07	101.83	XP041120/BA-1110-05/Site 3
54.99	1.27	5.13	19.35	19.57	0.90	0.07	101.29	XP041120/BA-1110-05/Site 3
55.13	1.94	5.57	19.53	19.30	0.65	0.00	102.11	XP041120/BA-1150-05/Site 1
54.90	2.09	5.30	19.80	19.05	0.48	-0.01	101.60	XP041120/BA-1150-05/Site 2
54.38	2.30	5.48	19.32	19.27	0.65	0.05	101.43	XP041120/BA-1150-05/Site 2
53.38	2.47	5.67	18.29	19.69	0.85	0.02	100.37	XP041120/BA-1150-05/Site 2
53.43	1.52	6.03	16.89	18.24	2.74	-0.03	98.82	XP041120/BA-1200-10/Site 1
52.88	4.56	7.10	16.54	17.58	0.93	0.07	99.65	XP041120/BA-1200-10/Site 2
53.29	3.71	6.88	17.82	18.95	0.94	0.01	101.59	XP041120/BA-1200-10/Site 2
52.21	4.03	6.94	18.35	18.78	0.95	0.05	101.31	XP041120/BA-1200-10/Site 3
52.71	3.07	6.40	17.96	19.13	1.17	0.04	100.47	XP041120/BA-1200-10/Site 3
51.53	3.94	6.71	17.77	18.58	0.84	0.00	99.36	XP041120/BA-1200-10/Site 4
51.58	4.51	7.81	17.34	19.48	0.81	0.06	101.59	XP041120/BA-1200-10/Site 5
50.88	4.75	7.17	17.78	18.31	0.88	0.02	99.78	XP041120/BA-1225-10/Site 1
52.47	3.74	6.52	18.21	18.76	0.79	0.00	100.49	XP041120/BA-1225-10/Site 1
52.82	3.78	6.44	18.70	17.91	0.84	0.05	100.54	XP041120/BA-1225-10/Site 1
51.61	4.54	7.13	17.67	18.60	0.91	0.07	100.52	XP041120/BA-1225-10/Site 2
53.77	3.34	6.29	19.27	17.94	0.78	0.03	101.41	XP041120/BA-1225-10/Site 2
53.65	3.26	6.19	19.75	17.93	0.81	0.04	101.64	XP041120/BA-1225-10/Site 2
52.45	4.15	6.86	18.13	18.27	0.91	0.03	100.80	XP041120/BA-1225-10/Site 2
50.98	4.72	7.19	17.35	19.02	0.81	0.03	100.09	XP041120/BA-1225-10/Site 2
51.83	3.71	6.62	18.07	19.80	0.62	0.06	100.70	XP041120/BA-1175-07/Site 1
54.97	1.34	5.39	19.48	18.74	0.80	0.03	100.76	XP041120/BA-1175-07/Site 1
54.94	1.67	6.06	19.85	18.40	0.93	0.01	101.85	XP041120/BA-1175-07/Site 3
54.18	1.66	5.89	19.72	18.79	0.93	0.02	101.21	XP041120/BA-1175-07/Site 3
53.07	2.82	6.05	18.77	18.55	0.72	0.03	100.01	XP041120/BA-1175-07/Site 3
53.55	3.17	5.74	19.38	18.70	0.58	0.07	101.20	XP041120/BA-1175-07/Site 4
53.84	2.47	5.74	20.67	17.89	0.46	0.07	101.15	XP041120/BA-1175-07/Site 4
52.54	3.67	6.57	19.00	19.03	0.54	0.09	101.44	XP041120/BA-1175-07/Site 5

Table A.17: **2 wt.% H_2O HMBA orthopyroxene analyses**

SiO2	Al2O3	FeO	MgO	CaO	Total	Project Path
56.97	2.75	4.44	36.66	1.79	102.74	XP051120/BA-1250-07/Site 1
58.17	1.89	5.17	35.72	1.66	102.74	XP051120/BA-1250-07/Site 1
58.40	1.67	3.70	37.47	1.49	102.83	XP051120/BA-1250-07/Site 1
57.43	2.02	5.08	36.22	1.57	102.36	XP051120/BA-1250-07/Site 1

58.21	1.97	3.99	37.07	1.50	102.83	XP051120/BA-1250-07/Site 3
57.32	2.42	4.77	35.97	1.45	101.92	XP051120/BA-1250-07/Site 3
57.53	1.96	4.48	35.96	1.68	101.68	XP051120/BA-1250-07/Site 4
58.03	1.76	3.87	36.43	1.48	101.66	XP051120/BA-1250-07/Site 4
58.11	1.72	4.24	36.60	1.42	102.10	XP051120/BA-1250-07/Site 4
57.15	2.19	4.60	36.19	1.40	101.63	XP051120/BA-1250-07/Site 4
57.19	2.33	4.43	35.50	1.29	100.85	XP051120/BA-1250-07/Site 5
57.56	1.69	4.08	35.37	1.63	100.57	XP051120/BA-1250-07/Site 5
58.59	1.53	4.24	36.73	1.42	102.64	XP051120/BA-1250-07/Site 5
57.09	2.13	4.86	35.72	1.52	101.45	XP051120/BA-1250-07/Site 5
57.77	1.91	5.09	35.93	1.62	102.35	XP051120/BA-1250-07/Site 5
58.41	0.90	3.48	36.29	1.83	101.05	XP051120/BA-1250-07/Site 5
58.10	1.64	5.77	34.59	2.66	102.86	XP051120/BA-1150-07/Site 2
57.89	1.35	5.44	34.91	2.32	102.10	XP051120/BA-1150-07/Site 2
56.62	1.95	5.75	34.18	2.25	100.93	XP051120/BA-1150-07/Site 2
57.21	2.24	5.75	34.32	2.20	101.82	XP051120/BA-1150-07/Site 2
56.11	3.16	5.56	34.15	1.91	100.96	XP051120/BA-1150-07/Site 2
56.89	1.65	6.56	33.74	2.04	100.98	XP051120/BA-1150-07/Site 3
57.28	1.45	6.25	34.07	2.20	101.55	XP051120/BA-1150-07/Site 3
55.59	2.24	6.36	32.69	2.93	100.02	XP051120/BA-1150-07/Site 3
57.93	0.94	5.97	34.27	2.07	101.22	XP051120/BA-1150-07/Site 3
58.08	2.36	5.85	31.32	2.93	100.81	XP051120/BA-1150-07/Site 3
57.15	1.95	6.39	33.15	2.16	100.94	XP051120/BA-1150-07/Site 3
55.93	2.77	6.63	33.33	2.67	101.29	XP051120/BA-1150-07/Site 4
58.00	1.07	6.12	34.26	2.32	101.93	XP051120/BA-1150-07/Site 4
57.40	2.02	6.30	34.39	2.04	102.38	XP051120/BA-1175-10/Site 1
57.66	1.89	6.17	33.93	2.30	102.11	XP051120/BA-1175-10/Site 1
56.18	3.90	6.44	33.49	2.25	102.47	XP051120/BA-1175-10/Site 1
56.84	2.82	6.51	33.62	2.07	101.99	XP051120/BA-1175-10/Site 1
58.01	2.20	5.74	34.49	2.00	102.55	XP051120/BA-1175-10/Site 2
56.76	2.57	6.66	33.59	2.62	102.46	XP051120/BA-1175-10/Site 2
56.35	3.08	7.22	33.57	1.80	102.32	XP051120/BA-1175-10/Site 2
56.53	2.26	6.22	33.09	2.95	101.31	XP051120/BA-1175-10/Site 3
55.71	3.38	6.63	32.60	2.83	101.22	XP051120/BA-1175-10/Site 3
58.04	1.38	6.12	34.67	2.30	102.74	XP051120/BA-1175-10/Site 3
57.52	2.00	6.11	34.17	2.06	102.10	XP051120/BA-1175-10/Site 3
55.39	3.35	6.86	33.16	1.92	100.80	XP051120/BA-1175-10/Site 3
57.26	2.29	6.30	33.84	2.34	102.17	XP051120/BA-1175-10/Site 3
58.36	1.18	6.02	34.57	2.31	102.64	XP051120/BA-1175-10/Site 4
55.81	4.26	5.78	33.44	2.39	101.87	XP051120/BA-1175-10/Site 7

57.30	2.86	4.82	35.92	2.00	102.98	XP051120/BA-1250-10/Site 1
57.75	2.27	3.90	36.01	2.23	102.33	XP051120/BA-1250-10/Site 1
58.29	1.92	3.83	36.83	1.60	102.62	XP051120/BA-1250-10/Site 1
56.75	2.43	4.63	35.67	1.65	101.23	XP051120/BA-1250-10/Site 1
57.16	2.57	4.90	35.51	1.94	102.33	XP051120/BA-1250-10/Site 1
58.88	1.38	3.94	36.97	1.64	102.87	XP051120/BA-1250-10/Site 2
58.58	1.61	3.93	36.55	1.76	102.61	XP051120/BA-1250-10/Site 2
56.72	2.85	4.16	34.68	2.41	101.07	XP051120/BA-1250-10/Site 2
58.12	1.91	4.10	36.00	1.72	102.14	XP051120/BA-1250-10/Site 2
58.32	1.52	3.76	36.50	1.69	102.04	XP051120/BA-1250-10/Site 2
57.20	2.17	4.73	35.98	1.78	101.95	XP051120/BA-1250-10/Site 3
56.18	3.04	4.60	36.08	2.06	102.05	XP051120/BA-1250-10/Site 3
56.98	2.59	4.50	35.79	2.14	102.11	XP051120/BA-1250-10/Site 3
57.63	2.01	4.08	35.71	2.08	101.76	XP051120/BA-1250-10/Site 3
56.89	2.59	4.16	35.97	2.01	101.60	XP051120/BA-1250-10/Site 3
58.41	1.62	3.91	36.12	2.17	102.45	XP051120/BA-1250-10/Site 3
57.96	2.05	4.48	35.85	1.80	102.17	XP051120/BA-1250-10/Site 4
58.42	1.45	4.13	36.82	1.82	102.65	XP051120/BA-1250-10/Site 4
58.10	1.51	3.96	36.30	1.85	101.97	XP051120/BA-1250-10/Site 4
58.08	1.62	3.85	36.05	1.97	101.85	XP051120/BA-1250-10/Site 4
58.11	1.91	4.15	36.02	1.76	102.12	XP051120/BA-1250-10/Site 4
58.57	1.49	4.33	36.29	1.75	102.61	XP051120/BA-1250-10/Site 4
56.22	4.30	8.25	31.73	2.23	102.94	XP051120/BA-1090-10/Site 1
55.42	3.02	8.35	32.74	1.90	101.60	XP051120/BA-1090-10/Site 1
56.70	2.51	6.98	32.74	2.38	101.44	XP051120/BA-1090-10/Site 3
55.22	3.74	8.81	32.14	2.05	102.21	XP051120/BA-1090-10/Site 3
54.69	3.21	9.54	31.60	1.93	101.09	XP051120/BA-1090-10/Site 3
55.30	3.39	8.14	30.99	2.89	100.82	XP051120/BA-1090-10/Site 3
55.41	3.65	8.54	30.97	2.76	101.39	XP051120/BA-1090-10/Site 4
57.01	2.71	6.78	33.47	2.23	102.30	XP051120/BA-1090-10/Site 4
53.62	5.93	9.17	31.53	1.55	101.91	XP051120/BA-1090-10/Site 4
56.79	2.46	7.11	32.96	2.54	102.02	XP051120/BA-1090-10/Site 4
53.42	4.60	8.44	31.46	1.94	100.05	XP051120/BA-1090-10/Site 4
56.58	1.66	8.65	31.93	2.95	102.07	XP051120/BA-1065-05/Site 1
57.29	1.52	8.60	32.25	2.20	102.04	XP051120/BA-1065-05/Site 1
56.49	1.48	8.80	31.45	2.52	100.87	XP051120/BA-1065-05/Site 1
56.69	1.23	9.53	32.21	2.11	101.88	XP051120/BA-1065-05/Site 1
56.59	1.50	8.63	32.35	2.55	101.74	XP051120/BA-1065-05/Site 1
56.39	1.03	8.57	32.10	2.31	100.45	XP051120/BA-1065-05/Site 1

57.12	0.76	9.11	31.74	2.30	101.17	XP051120/BA-1065-05/Site 2
56.27	1.65	8.47	32.25	2.20	100.85	XP051120/BA-1065-05/Site 2
55.92	1.71	9.66	31.55	2.44	101.35	XP051120/BA-1065-05/Site 2
56.32	1.14	9.48	31.58	2.37	100.90	XP051120/BA-1065-05/Site 2
58.44	2.96	7.75	29.87	2.76	102.21	XP051120/BA-1065-05/Site 3
55.45	2.29	8.58	31.58	2.54	100.44	XP051120/BA-1065-05/Site 3
55.84	2.26	8.40	31.92	2.01	100.56	XP051120/BA-1065-05/Site 3
56.39	1.80	8.76	31.58	3.09	101.72	XP051120/BA-1065-05/Site 3
56.54	1.40	9.29	31.98	2.13	101.44	XP051120/BA-1065-05/Site 4
56.34	1.48	9.33	31.34	2.71	101.32	XP051120/BA-1065-05/Site 4
57.01	0.80	9.13	32.19	1.90	101.11	XP051120/BA-1065-05/Site 4
57.01	1.27	8.91	31.54	2.43	101.24	XP051120/BA-1065-05/Site 4
57.87	0.96	8.52	33.27	1.85	102.61	XP051120/BA-1065-05/Site 5
56.39	2.28	7.80	32.21	2.40	101.29	XP051120/BA-1065-05/Site 5
58.84	1.10	3.45	37.20	1.22	101.98	XP041120/BA-1300-06/Site 1
58.12	1.22	3.56	37.01	1.18	101.13	XP041120/BA-1300-06/Site 1
58.20	1.41	3.76	36.87	1.24	101.58	XP041120/BA-1300-06/Site 1
58.67	0.97	3.63	37.26	1.26	101.95	XP041120/BA-1300-06/Site 1
57.76	1.44	3.68	36.46	1.00	100.43	XP041120/BA-1300-06/Site 2
57.61	1.78	4.16	36.28	1.31	101.33	XP041120/BA-1300-06/Site 2
57.93	1.38	3.83	36.59	1.20	101.06	XP041120/BA-1300-06/Site 2
58.28	1.05	3.62	36.70	1.07	100.80	XP041120/BA-1300-06/Site 2
58.38	0.98	3.39	36.98	1.14	100.98	XP041120/BA-1300-06/Site 2
57.53	2.69	4.25	32.96	2.01	99.82	XP041120/BA-1300-06/Site 2
58.06	1.67	3.84	36.71	1.14	101.53	XP041120/BA-1225-05/Site 1
57.53	1.62	4.02	36.37	1.11	100.65	XP041120/BA-1225-05/Site 1
58.46	1.06	4.23	36.62	1.33	101.73	XP041120/BA-1225-05/Site 1
58.43	1.11	4.23	36.67	1.22	101.74	XP041120/BA-1225-05/Site 1
58.16	1.55	4.87	35.84	1.16	101.73	XP041120/BA-1225-05/Site 2
57.65	1.54	4.91	35.88	1.21	101.15	XP041120/BA-1225-05/Site 2
58.20	1.32	4.73	36.28	1.28	101.93	XP041120/BA-1225-05/Site 2
57.50	1.82	4.71	35.70	1.34	101.07	XP041120/BA-1225-05/Site 2
58.56	1.72	4.75	36.06	1.27	102.54	XP041120/BA-1225-05/Site 2
57.24	1.53	6.34	32.75	2.33	100.35	XP041120/BA-1110-05/Site 1
57.07	1.47	6.15	33.24	2.39	100.38	XP041120/BA-1110-05/Site 1
58.26	1.03	6.02	34.32	2.15	101.79	XP041120/BA-1110-05/Site 1
58.04	0.97	6.75	33.84	2.19	101.96	XP041120/BA-1110-05/Site 1
57.47	1.28	7.42	33.31	2.18	101.78	XP041120/BA-1110-05/Site 3
58.11	0.71	7.62	33.12	2.51	102.11	XP041120/BA-1110-05/Site 3

56.38	1.00	7.28	33.61	2.57	100.95	XP041120/BA-1110-05/Site 3
58.19	0.74	6.39	34.27	2.26	101.98	XP041120/BA-1110-05/Site 3
55.80	3.11	8.25	31.74	1.96	100.99	XP041120/BA-1110-05/Site 5
56.98	2.89	5.40	35.11	2.45	102.87	XP041120/BA-1150-05/Site 1
56.41	2.96	6.18	34.44	2.38	102.46	XP041120/BA-1150-05/Site 1
55.91	3.55	6.41	34.18	2.16	102.45	XP041120/BA-1150-05/Site 2
57.78	1.96	4.64	35.66	2.15	102.26	XP041120/BA-1225-07/Site 1
58.60	1.11	4.86	35.61	2.15	102.46	XP041120/BA-1225-07/Site 1
57.54	2.25	5.49	34.64	2.50	102.44	XP041120/BA-1225-07/Site 2
57.91	1.94	5.08	35.71	1.89	102.57	XP041120/BA-1225-07/Site 2
57.48	2.05	5.05	35.68	1.95	102.35	XP041120/BA-1225-07/Site 3
58.68	1.34	4.94	35.90	1.91	102.85	XP041120/BA-1225-07/Site 3
58.18	1.31	5.03	35.67	1.97	102.24	XP041120/BA-1225-07/Site 3
56.97	2.58	5.63	34.99	1.81	102.11	XP041120/BA-1225-07/Site 3
57.00	2.44	5.44	35.23	2.01	102.30	XP041120/BA-1225-07/Site 3
58.48	1.56	5.05	35.25	2.27	102.76	XP041120/BA-1200-10/Site 1
57.30	1.76	5.17	35.14	2.18	101.70	XP041120/BA-1200-10/Site 1
56.98	2.09	5.58	34.01	2.38	101.29	XP041120/BA-1200-10/Site 1
56.95	1.98	5.46	34.73	2.14	101.49	XP041120/BA-1200-10/Site 2
57.74	1.62	3.85	35.81	2.04	101.15	XP041120/BA-1200-10/Site 3
54.93	4.73	5.82	33.93	2.07	101.56	XP041120/BA-1200-10/Site 4
56.73	3.04	4.60	35.69	2.12	102.33	XP041120/BA-1200-10/Site 5
56.61	2.74	5.84	34.06	2.49	101.93	XP041120/BA-1200-10/Site 5
56.90	2.66	4.07	35.97	2.13	101.95	XP041120/BA-1225-10/Site 1
57.77	1.19	4.60	34.83	2.67	101.24	XP041120/BA-1225-10/Site 2
57.83	1.47	4.70	35.71	2.31	102.22	XP041120/BA-1225-10/Site 3
58.61	1.15	4.25	35.62	2.34	102.20	XP041120/BA-1225-10/Site 3
58.61	1.06	4.03	36.19	2.83	102.92	XP041120/BA-1225-10/Site 3
57.73	1.72	5.28	34.59	2.73	102.18	XP041120/BA-1225-10/Site 6
57.38	1.45	5.29	34.48	2.36	101.11	XP041120/BA-1225-10/Site 6
57.02	2.41	4.20	35.75	2.52	102.03	XP041120/BA-1200-07/Site 1
57.70	1.73	3.62	36.33	2.43	101.91	XP041120/BA-1200-07/Site 1
57.85	1.76	4.03	36.16	2.22	102.25	XP041120/BA-1200-07/Site 1
57.72	1.89	4.40	35.46	2.62	102.26	XP041120/BA-1200-07/Site 3
57.99	1.59	3.55	36.52	2.53	102.25	XP041120/BA-1200-07/Site 3
57.87	1.69	4.41	35.51	2.74	102.36	XP041120/BA-1200-07/Site 3
57.04	2.12	5.59	34.98	2.04	101.94	XP041120/BA-1200-07/Site 4

57.05	2.48	5.71	33.50	2.31	101.48	XP041120/BA-1200-07/Site 4
57.69	1.68	4.78	35.43	2.62	102.31	XP041120/BA-1200-07/Site 4
58.53	1.05	4.03	36.24	2.06	102.09	XP041120/BA-1200-07/Site 4
57.96	1.28	5.77	34.26	2.56	102.03	XP041120/BA-1175-07/Site 1
57.60	1.12	5.63	34.50	2.52	101.56	XP041120/BA-1175-07/Site 1
57.75	1.24	6.30	33.76	2.31	101.55	XP041120/BA-1175-07/Site 1
57.84	1.94	5.59	34.24	2.49	102.33	XP041120/BA-1175-07/Site 3
55.97	2.99	6.28	33.57	2.58	101.60	XP041120/BA-1175-07/Site 4
56.76	1.96	5.88	33.97	2.78	101.52	XP041120/BA-1175-07/Site 4
56.28	2.85	6.34	34.22	2.19	102.11	XP041120/BA-1175-07/Site 4
58.28	1.16	5.97	34.83	2.49	102.98	XP041120/BA-1175-07/Site 5

Table A.18: **2 wt.% H_2O HMBA plagioclase analyses**

SiO2	Al2O3	FeO	MgO	CaO	Na2O	K2O	Total	Project Path
56.35	27.70	1.87	0.34	11.13	5.10	0.19	102.68	XP051120/BA-1150-07/Site 4
56.08	27.56	1.78	0.37	10.95	5.08	0.08	101.90	XP051120/BA-1150-07/Site 4
55.46	28.34	1.72	0.17	11.95	4.92	0.05	102.62	XP051120/BA-1150-07/Site 4
55.81	28.60	1.69	0.21	11.72	4.83	0.07	102.92	XP051120/BA-1150-07/Site 5
53.23	28.74	3.71	1.07	11.13	4.76	0.16	102.80	XP051120/BA-1175-10/Site 6
58.48	27.94	1.02	0.18	9.79	6.12	0.04	103.57	XP051120/BA-1090-10/Site 2
59.35	27.98	1.03	0.15	9.57	6.37	0.09	104.54	XP051120/BA-1090-10/Site 2
58.83	27.93	1.00	-0.02	9.88	6.16	0.14	103.92	XP051120/BA-1090-10/Site 2
58.29	27.70	0.97	0.15	9.74	5.99	0.16	103.00	XP051120/BA-1090-10/Site 2
59.39	26.72	1.33	0.16	8.98	6.65	0.06	103.28	XP051120/BA-1090-10/Site 2
61.01	27.02	1.11	0.08	8.71	6.99	0.18	105.09	XP051120/BA-1090-10/Site 2
58.81	28.13	1.10	0.17	9.79	6.23	0.07	104.29	XP051120/BA-1090-10/Site 2
60.94	26.63	1.26	0.14	8.39	6.87	0.17	104.39	XP051120/BA-1090-10/Site 2
60.86	26.30	1.35	0.71	8.31	6.79	0.14	104.45	XP051120/BA-1090-10/Site 2
58.06	27.71	1.11	0.04	9.62	6.04	0.10	102.68	XP051120/BA-1090-10/Site 3
59.38	24.40	1.33	1.15	8.06	6.98	0.09	101.40	XP051120/BA-1090-10/Site 3
60.74	23.99	1.28	0.60	7.39	7.32	0.19	101.51	XP051120/BA-1090-10/Site 3
61.06	25.24	1.16	0.09	7.09	7.40	0.10	102.13	XP051120/BA-1090-10/Site 4
59.38	26.57	1.21	0.18	8.79	6.57	0.11	102.82	XP051120/BA-1090-10/Site 4
59.59	26.03	1.28	0.23	8.63	6.67	0.14	102.57	XP051120/BA-1090-10/Site 4
57.54	27.79	0.96	0.20	10.34	5.60	0.06	102.49	XP051120/BA-1090-10/Site 4
60.16	26.60	1.21	0.19	8.78	6.62	0.12	103.68	XP051120/BA-1090-10/Site 4
62.58	25.04	1.14	0.14	6.97	7.57	0.09	103.54	XP051120/BA-1090-10/Site 5

56.00	26.74	1.41	1.37	12.09	4.38	0.17	102.15	XP051120/BA-1065-05/Site 3
55.93	28.34	1.04	0.84	11.27	4.60	0.18	102.20	XP051120/BA-1065-05/Site 3
51.33	32.50	1.55	1.19	12.69	3.93	0.05	103.25	XP051120/BA-1065-05/Site 3
56.55	28.22	0.66	0.45	11.59	4.84	0.13	102.44	XP051120/BA-1065-05/Site 3
53.25	31.44	0.57	0.38	13.80	3.90	0.02	103.35	XP041120/BA-1110-05/Site 4
51.80	32.27	0.57	0.82	12.55	4.10	0.10	102.21	XP041120/BA-1110-05/Site 4
52.79	31.38	0.51	0.46	13.70	3.65	0.06	102.56	XP041120/BA-1110-05/Site 4
54.70	30.38	0.57	0.30	12.66	4.36	0.12	103.08	XP041120/BA-1110-05/Site 4
54.22	30.62	0.48	0.22	12.57	4.38	0.05	102.54	XP041120/BA-1110-05/Site 5
54.55	30.59	0.59	0.23	13.00	4.25	0.13	103.36	XP041120/BA-1110-05/Site 5
54.07	30.24	0.58	0.47	12.80	4.31	0.15	102.61	XP041120/BA-1110-05/Site 5
56.56	26.57	2.69	0.78	10.93	4.72	0.13	102.38	XP041120/BA-1175-07/Site 2
56.55	25.61	3.08	0.89	10.29	5.00	0.39	101.80	XP041120/BA-1175-07/Site 2
54.63	28.59	1.84	0.19	11.96	4.54	0.07	101.81	XP041120/BA-1175-07/Site 2
54.55	28.37	1.78	0.29	11.80	4.77	0.08	101.63	XP041120/BA-1175-07/Site 5
54.33	27.60	1.99	0.44	11.67	4.59	0.14	100.76	XP041120/BA-1175-07/Site 5
56.81	27.63	1.80	0.30	11.03	5.30	0.15	103.02	XP041120/BA-1175-07/Site 5

Table A.19: **2 wt.% H_2O HMBA glass analyses**

SiO2	Al2O3	FeO	MgO	CaO	Na2O	K2O	Total	Project Path
58.39	13.04	7.61	8.19	8.52	3.29	0.39	99.43	XP051120/BA-1250-07/Site 1
58.21	13.01	7.81	8.23	8.48	3.20	0.36	99.30	XP051120/BA-1250-07/Site 1
57.92	13.04	7.65	7.95	8.61	3.39	0.44	99.01	XP051120/BA-1250-07/Site 1
58.27	13.09	7.99	8.07	8.59	3.42	0.35	99.79	XP051120/BA-1250-07/Site 2
58.64	13.28	7.96	8.28	8.58	3.41	0.34	100.49	XP051120/BA-1250-07/Site 2
58.67	13.29	7.63	8.33	8.37	3.28	0.45	100.02	XP051120/BA-1250-07/Site 2
58.30	13.20	8.02	8.03	8.47	3.48	0.45	99.93	XP051120/BA-1250-07/Site 2
58.90	13.10	7.85	8.17	8.46	3.39	0.40	100.27	XP051120/BA-1250-07/Site 2
58.97	13.08	7.92	8.17	8.49	3.51	0.42	100.57	XP051120/BA-1250-07/Site 2
58.01	13.25	7.71	8.14	8.35	3.48	0.41	99.36	XP051120/BA-1250-07/Site 3
58.24	13.12	7.90	7.94	8.56	3.43	0.50	99.69	XP051120/BA-1250-07/Site 3
58.52	13.08	7.94	8.04	8.35	3.42	0.39	99.74	XP051120/BA-1250-07/Site 3
58.34	13.18	7.60	8.09	8.52	3.47	0.35	99.54	XP051120/BA-1250-07/Site 4
58.85	13.07	8.09	8.06	8.52	3.55	0.35	100.49	XP051120/BA-1250-07/Site 4
58.33	12.98	7.75	8.15	8.47	3.28	0.43	99.39	XP051120/BA-1250-07/Site 4
58.59	13.05	7.82	8.07	8.47	3.32	0.39	99.71	XP051120/BA-1250-07/Site 4
58.66	13.20	7.81	7.97	8.48	3.41	0.36	99.89	XP051120/BA-1250-07/Site 4
58.53	13.03	7.72	8.00	8.53	3.33	0.43	99.56	XP051120/BA-1250-07/Site 5

63.92	15.10	5.45	3.78	6.60	3.87	0.59	99.31	XP051120/BA-1150-07/Site 2
63.98	14.60	5.63	3.91	6.64	3.77	0.55	99.09	XP051120/BA-1150-07/Site 2
63.30	15.06	5.62	3.97	6.69	3.77	0.58	98.99	XP051120/BA-1150-07/Site 2
64.18	15.28	5.29	3.43	6.01	4.05	0.59	98.83	XP051120/BA-1150-07/Site 4
64.54	14.70	5.22	3.19	5.93	4.00	0.62	98.21	XP051120/BA-1150-07/Site 4
64.04	14.68	5.31	3.34	6.21	4.15	0.57	98.31	XP051120/BA-1150-07/Site 4
64.00	14.59	5.33	3.15	5.93	4.07	0.59	97.66	XP051120/BA-1150-07/Site 4
64.66	14.51	5.32	3.31	5.92	4.24	0.66	98.61	XP051120/BA-1150-07/Site 4
61.20	15.50	5.99	4.48	7.35	3.79	0.46	98.77	XP051120/BA-1175-10/Site 1
61.38	15.39	6.12	4.53	7.36	3.63	0.46	98.87	XP051120/BA-1175-10/Site 1
61.52	15.29	6.31	4.47	7.29	3.67	0.43	98.99	XP051120/BA-1175-10/Site 1
61.60	15.42	6.19	4.32	7.26	3.61	0.39	98.79	XP051120/BA-1175-10/Site 1
61.46	15.27	6.10	4.57	7.23	3.49	0.47	98.59	XP051120/BA-1175-10/Site 2
61.87	14.95	6.21	4.41	7.04	3.63	0.48	98.56	XP051120/BA-1175-10/Site 2
61.22	15.29	6.14	4.43	7.16	3.59	0.55	98.39	XP051120/BA-1175-10/Site 2
61.96	15.49	6.04	4.36	6.99	3.60	0.51	98.96	XP051120/BA-1175-10/Site 3
61.79	15.30	6.08	4.37	7.11	3.81	0.46	98.92	XP051120/BA-1175-10/Site 3
61.39	15.01	5.88	4.45	7.09	3.68	0.48	97.98	XP051120/BA-1175-10/Site 3
61.94	15.48	6.06	4.25	6.88	3.96	0.52	99.09	XP051120/BA-1175-10/Site 6
62.03	15.30	5.80	4.16	7.02	3.96	0.51	98.79	XP051120/BA-1175-10/Site 6
61.66	15.17	5.90	4.19	6.81	3.82	0.51	98.06	XP051120/BA-1175-10/Site 7
62.08	14.77	6.05	4.36	6.83	3.65	0.46	98.19	XP051120/BA-1175-10/Site 7
58.72	13.01	7.87	7.97	8.24	3.16	0.43	99.41	XP051120/BA-1250-10/Site 1
58.79	13.27	7.74	7.93	8.43	3.26	0.39	99.80	XP051120/BA-1250-10/Site 1
58.69	13.01	7.93	7.83	8.47	3.21	0.35	99.51	XP051120/BA-1250-10/Site 1
58.71	13.23	8.04	7.99	8.69	3.27	0.37	100.28	XP051120/BA-1250-10/Site 1
59.66	13.16	7.99	7.83	8.31	3.32	0.39	100.67	XP051120/BA-1250-10/Site 2
59.12	13.14	7.82	7.83	8.53	3.54	0.40	100.39	XP051120/BA-1250-10/Site 2
59.66	13.32	7.79	7.92	8.41	3.45	0.44	100.99	XP051120/BA-1250-10/Site 2
59.55	13.02	7.78	8.02	8.12	3.42	0.41	100.32	XP051120/BA-1250-10/Site 2
59.48	13.34	7.97	7.76	8.40	3.22	0.39	100.56	XP051120/BA-1250-10/Site 3
59.61	13.17	7.97	7.72	8.38	3.34	0.42	100.61	XP051120/BA-1250-10/Site 3
59.07	13.24	7.99	7.87	8.24	3.15	0.42	99.98	XP051120/BA-1250-10/Site 3
58.63	13.17	7.95	7.58	8.25	3.17	0.41	99.16	XP051120/BA-1250-10/Site 3
59.43	13.14	7.73	7.63	8.38	3.36	0.43	100.10	XP051120/BA-1250-10/Site 3
59.97	13.37	7.72	7.65	8.15	3.29	0.43	100.58	XP051120/BA-1250-10/Site 4
59.72	13.29	7.77	7.51	8.01	3.33	0.43	100.05	XP051120/BA-1250-10/Site 4
59.22	13.12	7.49	7.52	8.16	3.33	0.39	99.24	XP051120/BA-1250-10/Site 4
59.30	13.25	7.80	7.65	8.37	3.22	0.43	100.02	XP051120/BA-1250-10/Site 4

59.45	13.15	7.82	7.46	8.13	3.18	0.44	99.64	XP051120/BA-1250-10/Site 4
73.84	12.93	2.32	1.03	2.17	4.30	0.86	97.45	XP051120/BA-1090-10/Site 2
73.19	13.47	2.33	0.97	2.22	4.49	0.88	97.56	XP051120/BA-1090-10/Site 2
73.67	12.89	2.35	1.45	2.24	4.49	0.89	97.98	XP051120/BA-1090-10/Site 2
73.64	13.38	2.59	1.12	2.24	4.36	0.89	98.23	XP051120/BA-1090-10/Site 3
70.81	14.23	2.34	1.25	2.96	4.30	0.71	96.59	XP051120/BA-1090-10/Site 3
71.07	12.49	2.53	1.45	2.21	4.26	0.93	94.94	XP051120/BA-1090-10/Site 3
72.66	12.94	2.38	0.99	2.10	4.39	0.92	96.39	XP051120/BA-1090-10/Site 3
72.04	13.05	2.50	1.24	2.45	4.33	0.88	96.49	XP051120/BA-1090-10/Site 3
72.63	13.35	2.39	1.16	2.23	4.23	0.97	96.96	XP051120/BA-1090-10/Site 4
72.30	12.86	2.60	1.20	2.64	4.27	0.90	96.77	XP051120/BA-1090-10/Site 4
72.37	13.01	2.37	1.19	2.59	4.36	0.88	96.78	XP051120/BA-1090-10/Site 5
67.23	14.47	3.80	2.52	5.04	3.72	0.54	97.32	XP051120/BA-1065-05/Site 1
66.93	14.87	4.06	2.43	5.20	3.67	0.59	97.74	XP051120/BA-1065-05/Site 1
67.17	14.82	4.06	2.65	5.26	3.81	0.58	98.36	XP051120/BA-1065-05/Site 1
66.24	14.81	3.91	2.47	5.38	3.70	0.55	97.05	XP051120/BA-1065-05/Site 1
67.70	14.60	3.69	2.34	4.74	3.94	0.62	97.62	XP051120/BA-1065-05/Site 2
68.36	14.35	3.28	2.30	4.81	4.01	0.65	97.76	XP051120/BA-1065-05/Site 2
68.08	14.14	3.50	2.28	4.78	3.51	0.60	96.88	XP051120/BA-1065-05/Site 2
67.29	14.74	4.05	2.26	4.58	4.40	0.69	98.02	XP051120/BA-1065-05/Site 5
68.22	14.51	3.95	2.21	4.48	4.32	0.69	98.38	XP051120/BA-1065-05/Site 5
67.83	14.61	4.07	2.39	4.70	4.17	0.65	98.41	XP051120/BA-1065-05/Site 5
67.68	14.61	4.17	2.51	4.86	4.22	0.63	98.67	XP051120/BA-1065-05/Site 5
67.45	14.71	4.00	2.33	4.69	4.21	0.61	98.01	XP051120/BA-1065-05/Site 5
67.98	14.85	3.97	2.30	4.78	4.35	0.69	98.93	XP051120/BA-1065-05/Site 5
58.35	12.11	7.48	11.12	7.39	2.91	0.36	99.73	XP041120/BA-1300-06/Site 1
57.81	11.86	7.18	11.26	7.40	3.06	0.40	98.97	XP041120/BA-1300-06/Site 1
58.33	12.06	7.39	10.85	7.80	3.16	0.32	99.91	XP041120/BA-1300-06/Site 1
57.98	11.95	7.35	11.30	7.44	2.97	0.29	99.28	XP041120/BA-1300-06/Site 1
58.37	12.05	7.27	11.20	7.37	2.88	0.43	99.58	XP041120/BA-1300-06/Site 2
58.09	11.79	7.48	11.39	7.33	3.05	0.40	99.53	XP041120/BA-1300-06/Site 2
57.96	11.65	7.24	11.14	7.39	2.97	0.27	98.60	XP041120/BA-1300-06/Site 2
58.32	11.90	7.42	11.66	7.45	3.00	0.44	100.18	XP041120/BA-1300-06/Site 2
58.29	11.92	7.31	11.25	7.54	2.92	0.34	99.55	XP041120/BA-1300-06/Site 2
60.83	10.65	5.34	8.97	6.35	3.29	0.47	95.90	XP041120/BA-1225-05/Site 1
60.84	10.64	5.63	8.93	6.58	3.30	0.32	96.23	XP041120/BA-1225-05/Site 1
60.40	10.84	5.46	8.74	6.72	3.11	0.36	95.62	XP041120/BA-1225-05/Site 1
60.30	10.87	5.58	8.90	6.57	3.03	0.44	95.69	XP041120/BA-1225-05/Site 1

58.60	11.87	6.00	8.73	6.93	3.24	0.45	95.81	XP041120/BA-1225-05/Site 2
59.34	11.96	5.88	8.96	6.96	3.12	0.36	96.58	XP041120/BA-1225-05/Site 2
59.05	12.23	5.86	8.84	6.90	3.32	0.33	96.53	XP041120/BA-1225-05/Site 2
59.38	11.97	6.08	9.04	6.83	3.42	0.37	97.10	XP041120/BA-1225-05/Site 2
59.41	12.30	6.18	8.95	7.28	3.23	0.39	97.74	XP041120/BA-1225-05/Site 2
58.54	12.49	6.07	8.63	7.32	3.26	0.37	96.68	XP041120/BA-1225-05/Site 2
70.33	6.36	3.25	6.90	3.51	3.00	0.40	93.77	XP041120/BA-1225-05/Site 3
69.58	6.49	3.10	7.01	3.65	2.96	0.51	93.30	XP041120/BA-1225-05/Site 3
67.38	6.84	3.83	7.80	4.11	2.83	0.48	93.26	XP041120/BA-1225-05/Site 3
65.50	7.42	4.39	8.16	4.84	2.99	0.41	93.72	XP041120/BA-1225-05/Site 3
65.67	7.37	4.10	8.20	4.93	2.87	0.42	93.56	XP041120/BA-1225-05/Site 3
68.24	6.66	3.34	7.34	4.10	2.79	0.45	92.91	XP041120/BA-1225-05/Site 3
67.75	6.81	3.43	7.46	3.87	2.93	0.48	92.73	XP041120/BA-1225-05/Site 3
66.18	7.27	3.75	7.84	4.38	2.98	0.43	92.83	XP041120/BA-1225-05/Site 3
64.84	7.54	4.44	8.28	4.91	2.93	0.37	93.33	XP041120/BA-1225-05/Site 3
66.26	15.59	1.46	3.07	5.55	3.92	0.65	96.50	XP041120/BA-1110-05/Site 1
66.96	15.81	1.58	3.18	5.52	4.17	0.66	97.88	XP041120/BA-1110-05/Site 1
67.66	15.34	1.77	3.11	5.40	3.96	0.65	97.88	XP041120/BA-1110-05/Site 1
65.43	16.41	1.75	3.28	5.97	3.92	0.60	97.36	XP041120/BA-1110-05/Site 1
65.38	16.15	2.75	3.77	6.28	3.90	0.61	98.84	XP041120/BA-1110-05/Site 3
64.69	15.87	2.60	3.73	6.26	3.68	0.62	97.46	XP041120/BA-1110-05/Site 3
64.74	16.17	2.68	3.64	6.24	3.82	0.53	97.82	XP041120/BA-1110-05/Site 3
63.63	16.29	2.51	3.78	6.48	3.89	0.56	97.14	XP041120/BA-1110-05/Site 3
64.34	15.99	2.49	3.76	6.31	3.72	0.53	97.14	XP041120/BA-1110-05/Site 3
64.94	15.85	2.85	3.62	6.22	3.94	0.57	97.98	XP041120/BA-1110-05/Site 3
63.04	16.46	2.47	3.94	6.82	3.95	0.54	97.22	XP041120/BA-1110-05/Site 4
63.07	16.54	2.47	4.04	7.00	3.91	0.53	97.55	XP041120/BA-1110-05/Site 4
62.38	16.90	2.78	4.17	7.12	3.77	0.55	97.67	XP041120/BA-1110-05/Site 5
58.83	15.83	7.15	5.49	8.63	3.75	0.46	100.15	XP041120/BA-1150-05/Site 1
59.36	15.29	6.04	5.25	8.05	3.59	0.48	98.07	XP041120/BA-1150-05/Site 2
60.05	15.64	6.24	5.25	8.15	3.70	0.45	99.49	XP041120/BA-1150-05/Site 2
60.58	15.68	5.89	5.31	8.02	3.64	0.46	99.58	XP041120/BA-1150-05/Site 2
59.87	15.16	6.13	5.57	8.67	3.71	0.44	99.55	XP041120/BA-1150-05/Site 2
60.07	15.71	6.25	5.24	7.94	3.56	0.48	99.25	XP041120/BA-1150-05/Site 2
58.49	13.97	7.67	7.41	8.62	3.23	0.40	99.79	XP041120/BA-1225-07/Site 1
59.79	13.85	7.64	7.30	8.81	3.45	0.38	101.22	XP041120/BA-1225-07/Site 1
59.13	13.71	7.62	7.46	8.61	3.26	0.37	100.17	XP041120/BA-1225-07/Site 1
58.93	13.92	7.64	7.28	8.75	3.38	0.50	100.39	XP041120/BA-1225-07/Site 2
59.41	14.02	7.65	7.18	8.89	3.29	0.38	100.81	XP041120/BA-1225-07/Site 2

58.56	13.77	7.51	7.20	8.66	3.17	0.46	99.34	XP041120/BA-1225-07/Site 3
58.74	14.02	7.81	7.24	8.77	3.44	0.37	100.40	XP041120/BA-1225-07/Site 3
58.66	13.65	7.67	7.23	8.70	3.32	0.41	99.64	XP041120/BA-1225-07/Site 3
61.46	13.84	6.60	4.85	7.47	3.63	0.53	98.38	XP041120/BA-1200-10/Site 1
61.28	13.92	6.50	4.94	7.30	3.55	0.51	98.01	XP041120/BA-1200-10/Site 1
61.69	14.05	6.60	4.84	7.47	3.81	0.42	98.88	XP041120/BA-1200-10/Site 1
61.44	14.05	6.68	4.98	7.48	3.52	0.46	98.61	XP041120/BA-1200-10/Site 3
61.78	14.09	6.62	4.98	7.41	3.71	0.54	99.13	XP041120/BA-1200-10/Site 3
60.71	14.45	6.63	4.76	7.50	3.62	0.53	98.20	XP041120/BA-1200-10/Site 4
60.82	14.16	6.35	4.92	7.41	3.59	0.49	97.74	XP041120/BA-1200-10/Site 4
60.16	14.78	6.94	5.05	7.80	3.54	0.42	98.69	XP041120/BA-1200-10/Site 5
60.24	14.57	6.75	5.13	7.69	3.38	0.46	98.22	XP041120/BA-1200-10/Site 5
59.38	14.26	7.47	5.73	8.42	3.60	0.44	99.31	XP041120/BA-1225-10/Site 1
59.27	14.10	7.46	5.90	8.29	3.38	0.47	98.87	XP041120/BA-1225-10/Site 1
59.33	14.41	7.26	5.74	8.18	3.63	0.45	99.00	XP041120/BA-1225-10/Site 2
59.60	14.34	7.28	5.53	8.15	3.62	0.48	99.01	XP041120/BA-1225-10/Site 2
60.15	14.03	7.27	5.62	8.07	3.55	0.45	99.14	XP041120/BA-1225-10/Site 3
59.73	14.46	7.23	5.64	8.08	3.51	0.40	99.04	XP041120/BA-1225-10/Site 3
58.83	14.55	7.12	6.53	7.50	3.61	0.37	98.49	XP041120/BA-1225-10/Site 6
59.11	13.36	7.60	6.54	8.70	3.45	0.44	99.21	XP041120/BA-1200-07/Site 1
58.69	13.57	7.44	6.48	8.77	3.66	0.45	99.06	XP041120/BA-1200-07/Site 1
59.07	13.58	7.64	6.58	8.69	3.56	0.39	99.52	XP041120/BA-1200-07/Site 2
58.36	13.60	7.41	6.71	8.74	3.53	0.43	98.78	XP041120/BA-1200-07/Site 2
59.01	13.41	7.61	6.45	8.78	3.49	0.41	99.16	XP041120/BA-1200-07/Site 3
58.92	13.58	7.42	6.62	8.50	3.55	0.48	99.06	XP041120/BA-1200-07/Site 4
59.00	13.62	7.37	6.45	8.50	3.79	0.45	99.18	XP041120/BA-1200-07/Site 4
58.67	13.69	7.51	6.50	8.82	3.72	0.45	99.35	XP041120/BA-1200-07/Site 4
62.13	15.34	6.16	4.12	7.13	4.12	0.51	99.51	XP041120/BA-1175-07/Site 1
62.84	15.23	6.00	4.14	7.03	4.15	0.53	99.92	XP041120/BA-1175-07/Site 1
61.99	15.46	6.07	4.03	7.15	4.01	0.55	99.26	XP041120/BA-1175-07/Site 1
60.50	15.27	6.62	4.58	7.62	3.79	0.57	98.94	XP041120/BA-1175-07/Site 2
61.07	15.41	6.47	4.63	7.39	3.98	0.50	99.45	XP041120/BA-1175-07/Site 3
61.44	15.15	6.27	4.43	7.33	3.76	0.52	98.91	XP041120/BA-1175-07/Site 3
60.61	15.11	6.37	4.76	7.88	3.65	0.52	98.91	XP041120/BA-1175-07/Site 4
61.09	15.30	6.42	4.80	7.71	3.62	0.52	99.45	XP041120/BA-1175-07/Site 4
61.15	14.87	6.68	4.92	7.83	3.82	0.48	99.76	XP041120/BA-1175-07/Site 4
61.83	15.35	6.52	4.42	7.27	4.13	0.48	99.99	XP041120/BA-1175-07/Site 5